TRANSIENT FOUR-WAVE MIXING STUDIES OF GaAs, LOW-TEMPERATURE-GROWN GaAs, AND $CH_3NH_3PbI_3$

by

Daniel Webber

Submitted in partial fulfillment of the
requirements for the degree of
Doctor of Philosophy

at

Dalhousie University
Halifax, Nova Scotia
December 2017

Table of Contents

List of Tables . . . . . **vi**

List of Figures . . . . . **vii**

Abstract . . . . . **x**

List of Abbreviations and Symbols Used . . . . . **xi**

Acknowledgements . . . . . **xvi**

Chapter 1 Introduction **1**

1.1 Overview 1

1.2 Electronic Structure and Optical Properties of Direct-Band Gap Semiconductors 4

1.3 Defects 7

1.4 Carrier Relaxation Processes in Semiconductors 9

1.5 Material Systems under Investigation 10
1.5.1 $CH_3NH_3PbI_3$ 10
1.5.2 GaAs 12
1.5.3 LT-GaAs 13

1.6 Four-wave Mixing Spectroscopy 16
1.6.1 Two Pulse Self Diffraction Four-wave Mixing 17
1.6.2 Two-dimensional Fourier Transform Spectroscopy 21
1.6.3 Transient Grating Four-wave Mixing 23

1.7 Literature Review 26
1.7.1 Overview 26
1.7.2 Carrier Transport Properties of $CH_3NH_3PbI_3$ 27
1.7.3 Optical and Electronic Properties of Annealed LT-GaAs . . . 31
1.7.4 FWM Studies of Exciton-Exciton and Exciton-Carrier Scattering in GaAs 36

1.8 Summary of the Thesis 39

Chapter 2 Optical Bloch Equation Analysis of Four-Wave Mixing Experiments **43**

2.1 Chapter Overview 43
2.2 FWM for a Two-Level System without Interactions 44
2.3 Free Polarization Decay from a Homogeneously-Broadened Two-Level System 48
2.4 Photon Echo from an Inhomogeneously Broadened System 49
2.5 Phase-Dependent Detection of the Complex FWM Response 51
2.6 Effect of Many-Body Interactions on the FWM Signal 52
2.7 Influence of the Spin State of the Excited Carriers 54
2.8 Simultaneous Excitation of Exciton and Continuum Transitions . . . 54

Chapter 3 Apparatus and Experimental Techniques 58

3.1 Overview 58
3.2 Samples 58
3.2.1 GaAs and LT-GaAs 58
3.2.2 $CH_3NH_3PbI_3$ 62
3.3 Sample Cooling 63
3.4 Pulse Measurement, Characterization, and Optimization 64
3.4.1 Excited Carrier Density 65
3.4.2 Laser Spot Size Measurement 66
3.4.3 Pulse Compression 66
3.5 Two-Pulse Self-Diffracted FWM 68
3.6 Two-Dimensional Fourier Transform Spectroscopy 71
3.7 Transient Grating Technique 74

Chapter 4 Carrier Diffusion in Thin-Film $CH_3NH_3PbI_3$ Perovskite Measured using Four-Wave Mixing 78

4.1 Abstract 78
4.2 Introduction 79
4.3 Materials and Methods 82
4.3.1 Transient Grating Technique 82
4.3.2 Experiment Details 85
4.3.3 Sample 85

4.4 Results and Discussion . . . 86
4.4.1 Transient Grating Results: Evidence of Ambipolar Carrier Diffusion . . . 86
4.4.2 Influence of Grain Size on Carrier Transport . . . 87
4.5 Conclusions . . . 89
Chapter 5 Control of the Urbach band tail and Interband Dephasing Time with Post-Growth Annealing in Low-Temperature-Grown GaAs . . . 90
5.1 Abstract . . . 90
5.2 Introduction . . . 91
5.3 Experimental Methods . . . 92
5.4 Results and Discussion . . . 93
5.5 Conclusions . . . 99
Chapter 6 Signatures of four-particle correlations associated with exciton-carrier interactions in coherent spectroscopy on bulk GaAs . . . 101
6.1 Abstract . . . 101
6.2 Introduction . . . 102
6.3 Materials and Methods . . . 106
6.3.1 TFWM . . . 106
6.3.2 2DFTS . . . 107
6.3.3 Samples . . . 108
6.4 Numerical Simulations . . . 108
6.5 Results and Discussion . . . 111
6.5.1 TFWM on Bulk GaAs: Exciton Enhancement Through Non-degenerate Interactions . . . 111
6.5.2 2DFTS Results: Separation of Signals Tied to Exciton-Exciton and Exciton-Continuum Coupling . . . 116
6.5.3 Simulations of 2DFTS Experimental Results . . . 119
6.5.4 Polarization dependence . . . 121
6.5.5 Dependence on Excited Carrier Density . . . 122
6.6 Conclusions . . . 122

Chapter 7 Conclusion **125**

Bibliography **128**

Appendix A Discussion of Experimental Uncertainties **147**

Appendix B Choice of Ordinary Differential Integrator for Simulating the Optical Bloch Equations **149**

Appendix C Bányai Projection Method **152**

Appendix D Derivation of the Ambipolar Diffusion Equation **154**

Appendix E Rights and Permissions **156**

List of Tables

Table 3.1 A table of the five LT-GaAs samples studied in this work and their corresponding annealing temperatures. 59

Table 6.1 Many-body coefficients ($\gamma^{\mathrm{X}}_{\mathrm{EID/EIS}}$ and $\gamma^{\mathrm{C}}_{\mathrm{EID/EIS}}$) found in numerical simulations of the 2DFTS results to provide the best agreement with the experimental data. 118

List of Figures

Figure 1.1 Schematic diagram of a three pulse FWM experiment. 2

Figure 1.2 A pictorial representation of many-body interactions in an optically-excited semiconductor. 3

Figure 1.3 Simplified band structure of GaAs. 5

Figure 1.4 Linear absorption spectrum of GaAs. 7

Figure 1.5 Crystal structure and band structure of $CH_3NH_3PbI_3$. 10

Figure 1.6 Crystal and electronic band structure for GaAs. 13

Figure 1.7 Crystal structure, electronic band structure, and linear absorption spectrum of LT-GaAs. 15

Figure 1.8 Calculated TR-FWM and TI-FWM response for a homogeneously- and inhomogeneously-broadened transition. 19

Figure 1.9 Bloch sphere representation of a photon-echo response of an inhomogeneously broadened two-level transition. 19

Figure 1.10 SR-FWM results on bulk GaAs from Wehner *et al.* 21

Figure 1.11 2DFTS results from Siemens *et al.* 23

Figure 1.12 Transient grating measurements from Schwab *et al.* 26

Figure 1.13 Hall Effect, PL, and TAM transport measurements in perovskite. 28

Figure 1.14 Annealing-induced changes to the electronic and optical properties of LT-GaAs. 33

Figure 1.15 SR-FWM results on Ge from Rappen *et al.* 34

Figure 1.16 Optical selection rules and carrier occupation grating in FWM experiments. 35

Figure 1.17 Calculated 2DFTS response of GaAs multiple quantum wells from Li *et al.* 39

Figure 2.1 The SR-FWM signal for a homogeneously- and inhomogeneously-broadened transition. 50

Figure 3.1 The three step process used to produce the GaAs samples for transmission measurements. 60

Figure 3.2 Linear absorption and electronic band structure of GaAs and LT-GaAs. 61

Figure 3.3 Linear absorption spectrum for $CH_3NH_3PbI_3$. 63

Figure 3.4 A schematic of the experiment used to measure the zero-background autocorrelation. 64

Figure 3.5 A schematic of the knife edge experiment. 66

Figure 3.6 A schematic diagram of the prism compressor. 67

Figure 3.7 A schematic diagram of the prism compressor. 69

Figure 3.8 CAD and simple schematic of the 2DFTS experiment used in this thesis work. 73

Figure 3.9 A schematic diagram of the three-pulse FWM apparatus used in this thesis. 75

Figure 3.10 Measured values of the angle between the three pulses and the optical axis. 77

Figure 4.1 Crystal structure and linear absorption spectrum of $CH_3NH_3PbI_3$. 80

Figure 4.2 FWM signal intensity on a logarithmic scale as a function of delay T for a range of grating constants. 81

Figure 4.3 (a) Inverse signal decay time T_s^{-1} as a function of $8\pi^2/d^2$. (b) Scanning electron microscopy image of the $CH_3NH_3PbI_3$ sample. 84

Figure 4.4 Results of differential transmission measurements. 87

Figure 5.1 SR-FWM results of LT-GaAs. 94

Figure 5.2 Spectral cuts of the SR-FWM response of LT-GaAs. 95

Figure 5.3 Spectral cuts of the SR-FWM response at zero delay. 97

Figure 5.4 Spectral cuts showing the dip in exciton response. 98

Figure 5.5 SR-FWM results of as-grown LT-GaAs. 100

Figure 6.1 Linear absorption and SR-FWM response of GaAs. 105

Figure 6.2 Results of 2DFTS experiments on GaAs. 110

Figure 6.3 Results of simulations of the 2DFTS response of GaAs. 113

Figure 6.4 Results of simulations of the 2DFTS response of GaAs for varying EID and EIS. 114

Figure 6.5 Results of 2DFTS experiments for collinear and cross-linearly polarized pulses. 116

Figure 6.6 Normalized amplitude results of 2DFTS experiments and simulations for varying excited carrier density. 117

Figure B.1 The time-resolved four-wave mixing signal alongside the reference signal (black dashed line) calculated with (a) ODE23, (b) ODE45, (c) ODE87. 151

Abstract

Understanding the mechanisms responsible for the relaxation of charge carriers in semiconductor systems is crucial for the development of novel devices based on these materials. Transient four-wave mixing (FWM) is a powerful technique used to study relaxation processes as it is intimately connected to these mechanisms. In this thesis work, three different experimental implementations of FWM were used to study three different semiconductor systems relevant for optoelectronic applications.

FWM was used to probe charge diffusion in $CH_3NH_3PbI_3$. $CH_3NH_3PbI_3$ is an attractive material for solar cell devices due in part to its large charge diffusion length. In this work, charge transport in $CH_3NH_3PbI_3$ was directly measured resulting in a calculated ambipolar diffusion length of 0.95 μm. Relative to the measured grain size in this sample, the larger diffusion length suggests that grain boundaries do not significantly impact charge transport.

The properties of GaAs grown at lower than conventional temperatures can be tailored via post-growth annealing. Spectrally-resolved FWM (SR-FWM) was used to study the effect of annealing on the coherent response of LT-GaAs. For low annealing temperatures, an observed dip in the SR-FWM response was found to stem from a polarization interference between the many-body exciton response and that of the band tail response. The interband dephasing time was observed to increase for increasing annealing temperatures. Extracted values for the Urbach energy of band tail states revealed a dramatic decrease at 550°C.

SR-FWM and two-dimensional Fourier transform spectroscopy (2DFTS) were used to study the interactions between bound and unbound electron-hole pairs in GaAs. Through comparison with numerical simulations of the 2DFTS response it was determined that exciton-carrier scattering was ten-fold stronger than exciton-exciton scattering, and that excitation-induced dephasing manifested in the real part of the 2DFTS spectra stronger than excitation-induced shift.

List of Abbreviations and Symbols Used

$\vec{\mu_k}$	Dipole moment of transition with wavevector k
$\varepsilon_{\vec{k}}$	Energy of an electron with wavevector k
ω_k	Angular frequency of transition with wavevector k
ω_C	Angular frequency of continuum transition
ω_{HH}	Angular frequency of heavy-hole exciton transition
ω_{LH}	Angular frequency of light-hole exciton transition
λ	Wavelength
θ	Beam angle
ω	Angular frequency
ω_0	Angular frequency of two-level transition
$\Delta\omega$	Frequency detuning
ρ	Density matrix
ϕ	Phase angle
ψ	Phase angle
Ψ	Electron wave function
μ_{ex}	Exciton transition dipole moment
μ_{a}	Ambipolar mobility
$\sigma_+(\sigma_-)$	Left (Right) circularly-polarized light
$\Theta()$	Heaviside step function
ξ	Electron-hole pair density distribution
2DFTS	Two-dimensional Fourier transform spectroscopy
$\alpha(\omega)$	Absorption coefficient at frequency ω
Al_2O_3	Sapphire
AlGaAs	Aluminum gallium arsenide
$\mathrm{As_{Ga}}$	Arsenic antisite
$\mathrm{As^0_{Ga}}$	Neutral arsenic antisite state
$\mathrm{As^+_{Ga}}$	Ionized arsenic antisite state
As_i	Arsenic Interstitial

BBO	Beta-Barium Borate
BS	Beamsplitter
C	Conduction band
CC	Continuum contribution
CdS	Cadmium Sulfide
$CdS_{1-x}Se_x$	Cadmium sulfide selenide
CdSe	Cadmium Selenide
$CH_3NH_3PbI_3$	Methylammonium lead iodide
d	Grating period
D	Ambipolar diffusion coefficient
DFT	Density functional theory
DS	Delay stage
E_b	Exciton binding energy
E_g	Band gap energy
E_1	Electric field of pulse 1
E_2	Electric field of pulse 2
E_3	Electric field of pulse 3
E_{PP}	Electric field of prepulse
EID	Excitation-induced dephasing
EIS	Excitation-induced shift
eV	Electron Volts (units of energy)
F	Neutral density filter
F_1	Focal length of lens 1
F_2	Focal length of lens 2
γ_{EID}	EID coefficient
γ_{EIS}	EIS coefficient
GaAs	Gallium arsenide
GaMnAs	Gallium manganese arsenide
GaNAsSb	Gallium Nitride Arsenide Antimonide
GVD	Group velocity dispersion
$\hbar$	Planck's constant

H	Hamiltonian
H_0	Unperturbed Hamiltonian
H_{int}	Interaction Hamiltonian
H_R	Relaxation Hamiltonian
HH	Heavy hole
HWP	Half-wave plate
InGaAs	Indium Gallium Arsenide
InP	Indium phosphide
InSe	Indium Selenide
$\vec{k}$	Electron wave vector
$\vec{k}_1$	Pulse E_1 wavevector
$\vec{k}_2$	Pulse E_2 wavevector
$\vec{k}_3$	Pulse E_3 wavevector
L_D	Ambipolar diffusion length
LF	Local field
LH	Light hole
LO	Longitudinal-optical
LP	Low-pass filter
LT-GaAs	Low-temperature grown gallium arsenide
OBE	Optical Bloch equations
M	Mirror
MBE	Molecular beam epitaxy
MQW	Multiple Quantum Well
m_r	Reduced mass
N	Excited population density
N_X	Exciton population density
N_C	Continuum population density
n	Occupation
n_{ex}	Exciton occupation
p	Coherence
p_{ex}	Exciton coherence

P_1	Prism one
P_2	Prism two
P_{ex}	Macroscopic exciton polarization
PC	Pulse compressor
PCBM	[6,6]-Phenyl C61 butyric acid methyl ester
$\Psi_{\nu,\vec{k}}(\vec{r})$	Bloch function
PL	Photoluminescence
PMT	Photomultiplier tube
q	Charge
SF	Spatial filter
SLM	Spatial Light Modulator
SO	Spin-orbit split-off
SR-FWM	Spectrally-resolved four-wave mixing
S_{SR}	Spectrally-resolved four-wave mixing signal
S_{TR}	Time-resolved four-wave mixing signal
S_{TI}	Time-integrated four-wave mixing signal
τ	Pulse delay between pulses $\vec{E}_1$ and $\vec{E}_2$
T	Pulse delay between pulses $\vec{E}_2$ and $\vec{E}_3$
$T_{lattice}$	Lattice temperature
TAM	Transient Absorption Microscopy
TFWM	Transient Four-Wave Mixing
THz	Terahertz
TRTHz	Time-resolved terahertz
Ti:Sapphire	Titanium sapphire
TI-FWM	Time-integrated four-wave mixing
T_L	Recombination lifetime
T_s	Four-wave mixing signal lifetime
TR-FWM	Time-resolved four-wave mixing
T_2	Coherence decay time
T_2^0	Coherence decay time in absence of excitation
TAM	Transient absorption microscopy

TRTHz	Time-resolved terahertz
TS	Linear translation stage
V	Valence band
$u_{\nu,\vec{r}}$	Cell function
z	Distance between the two lenses F_1 and F_2

Acknowledgements

First and foremost, I would like to thank my girlfriend Ellen Patrick for her patient support during my PhD studies. I would like to thank my supervisor Kimberley C. Hall for her guidance over the duration of my graduate studies. I wish to thank Jacek Furdyna and his group at the University of Notre Dame for growing the GaAs samples investigated in this thesis work, as well as Ian G. Hill and his group for producing the perovskite sample.

I would like to acknowledge my past and present fellow group members Tristan de Boer, Eric Dilcher, Sam March, Allister Mason, Angela Gamouras, Luke Hacquebard, Reuble Mathew, Ajan Ramachandran, Drew Riley, and Seth Todd for their assistance in the lab and in life. In particular, I would like to acknowledge Luke Hacquebard and Allister Mason who assisted me in collecting the data presented in this thesis work.

Finally, I would like to thank my family for their past, present, and continuing support throughout my studies.

Chapter 1

Introduction

1.1 Overview

Understanding the mechanisms responsible for the relaxation of charge carriers in a semiconductor after photoexcitation is essential for the development of novel optoelectronic devices based on these materials. The optimization of the material properties is dependent on the specific application being targeted. For example, for solar cells a large carrier lifetime and long diffusion length are important in achieving high solar conversion efficiency as these properties partly determine the thickness of the absorbing material. On the other hand, devices such as high-speed photoconductive switches require materials with short lifetimes, which can be obtained by making materials with large densities of crystal defects. As well, devices that utilize the ultrafast coherent response such as saturable absorbers for laser mode locking applications must cope with excitation-induced interactions that manifest for these excitation conditions. The timescales of these mechanisms are extremely short (on the order of a millionth of a billionth of a second) and are only accessible via ultrafast optical means. A diverse range of experimental approaches utilizing short optical pulses have permitted the detailed study of these interactions.

The technique of transient four-wave mixing (FWM) provides a valuable tool for investigating the complex interplay of charge carrier interactions in a semiconductor. Fig. 1.1 shows a simple schematic of a FWM experiment. In this *nonlinear* optical technique, the electric field of three optical pulses causes the excitation of a coherent polarization response in the material, leading to the generation of a fourth field (hence the name FWM) that carries information regarding the nature of the polarization that generated it. The groundbreaking work by Yajima and Taira [1] established FWM as a powerful tool to study ultrafast relaxation mechanisms. In this work, they described the first and simplest variant of FWM, namely the two-pulse self-diffracted geometry, that used two delayed optical pulses (shown in Fig. 1.1 as $\vec{E}_1$

and $\vec{E}_2$) to probe the system. Their work illustrated how one can obtain important information about the excited system by measuring the FWM signal as a function of delay τ, such as the coherence time T_2 (*i.e.* how long the ensemble of oscillators remain in phase, or *coherent* with each other and the optical pulse used to generate them) and the degree and type of optical state broadening (*e.g.* homogeneous vs. inhomogeneous). FWM studies utilizing a third delayed pulse ($\vec{E}_3$ in Fig. 1.1) have also shown that information about the *incoherent* response of the material can be obtained by measuring the FWM signal as a function of delay T. For instance, the population lifetime T_L (*i.e.* how long it takes for electrons to relax back into valence band states, restoring the system to equilibrium) and the diffusion length of charge carriers (*i.e.* the distance these carriers diffuse before the electrons relax to the valence states) may be measured [2,3]. More recent FWM experiments have also focused on understanding the nature of interactions between the excited species generated by the optical pulses [4–6].

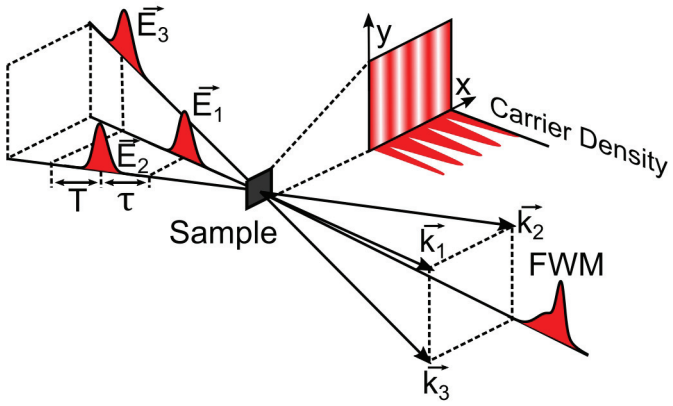

Figure 1.1: Schematic diagram of a three pulse FWM experiment. Three laser pulses with electric fields $\vec{E}_1$, $\vec{E}_2$, and $\vec{E}_3$ along directions $\vec{k}_1$, $\vec{k}_2$, and $\vec{k}_3$ and separated by delays τ and T are focused onto the sample. Excitation by $\vec{E}_1$ and $\vec{E}_2$ leads to the generation of a coherent carrier modulation laterally across the sample. The FWM signal consists of the diffraction of $\vec{E}_3$ from this transient grating. Due to momentum conservation, this diffraction is along $\vec{k}_3 + \vec{k}_2 - \vec{k}_1$.

Optical excitation in a semiconductor leads to the generation of electrons and holes (*i.e.* a missing electron in the valence band), which are pictorially shown in Fig. 1.2. These charge carriers can interact with each other via the Coulomb interaction in numerous ways: i) free carriers (e.g. electrons and holes) can interact with

each other through a process known as carrier-carrier scattering; ii) electrons and holes can bind together forming bound states known as excitons; iii) Excitons can interact with electrons and holes via exciton-carrier scattering; iv) Excitons can interact with other excitons via exciton-exciton scattering; v) excitons and free carriers can interact with defects in the material. Together, these interactions lead to large deviations from the expected behavior of charge carriers and their transport properties. Therefore, to improve the performance of optoelectronic materials, we need to improve our understanding of these interactions.

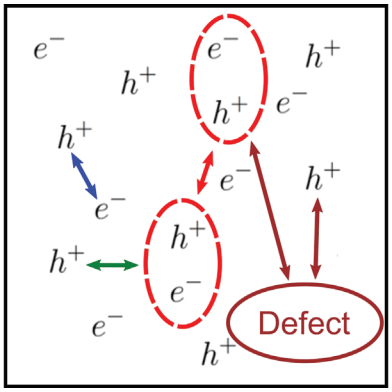

Figure 1.2: A pictorial representation of many-body interactions in an optically-excited semiconductor. Electrons and holes are denoted by e^- and h^+ respectively. The interactions between charge carriers are given by coloured arrows: i) carrier-carrier scattering (blue); ii) exciton-carrier scattering (green); iii) exciton-exciton scattering (red); and iv) defect scattering (brown).

In this thesis work, three different experimental implementations of FWM have been used to explore three semiconductor systems. The first project uses the transient grating technique to study charge carrier diffusion in $CH_3NH_3PbI_3$. The second project examines the coherent response of annealed low-temperature-grown GaAs using spectrally-resolved FWM (SR-FWM). The third project aims to further our understanding of exciton-carrier and exciton-exciton interactions in the direct band gap semiconductor GaAs using SR-FWM and two-dimensional Fourier transform spectroscopy (2DFTS).

1.2 Electronic Structure and Optical Properties of Direct-Band Gap Semiconductors

A bulk semiconductor is composed of a three-dimensional periodic arrangement of atoms, forming what is known as a crystal lattice. The wave function $\Psi(\vec{r})$ for an electron in the crystal is obtained from the time-independent Schrödinger Equation, where the potential the electron experiences stems from the electrostatic potential of each ion core at every atom site. The solutions to this equation $\Psi(\vec{r})$ are the Bloch Functions which are a product of a plane wave with a function that shares the periodicity of the crystal.

$$\Psi_{\nu,\vec{k}}(\vec{r}) = \frac{1}{\sqrt{V}} u_{\nu,\vec{k}}(\vec{r}) e^{i\vec{k}\cdot\vec{r}}. \tag{1.1}$$

Here $u_{\nu,\vec{k}}(r)$ is the cell function, where ν indicates the band, $\vec{k}$ is the electron wave vector, and V is the volume of the semiconductor. The possible electron energies as a function of wave vector are given by a series of bands. For instance, the full electronic band structure of GaAs is shown in Fig. 1.3(a). The highest occupied bands are called the valence bands and the lowest unoccupied band is the conduction band. The energy separation between these bands is the band gap energy (E_g). For a direct band gap semiconductor like GaAs, the minimum of the conduction band lies at the same wave vector as the maximum of the valence band.

The top three valence bands and the lowest conduction band correspond to $\nu =$ HH (heavy-hole valence band), LH (light-hole valence band), SO (spin-orbit split off valence band), C (conduction band). The cell functions have a unique character that reflects the corresponding bonding or anti-bonding orbital of the GaAs molecule at each lattice site. For instance, near zone centre ($\vec{k} = \vec{0}$) the cell functions for the three valence bands resemble p hydrogenic orbitals, whereas the conduction band possesses s hydrogenic character. Restricting our attention to states near $\vec{k} = \vec{0}$ results in a simplified band diagram (Fig. 1.3(b)), in which the band edges are treated as nearly parabolic. In this case, the dispersion relation resembles that for a free electron, but with the bare mass (m_0) replaced by an effective mass(m^*_ν). The effective mass takes into account the coupling of the electron with the lattice of ion cores. The names of the three valence bands are derived from the curvature of the band and thus the associated effective mass.

The value of E_g is dependent on the constituent atoms that make up the crystal. For example, GaAs and InAs have band gap energies of 1.519 eV and 0.415 eV at absolute zero respectively. Electrons can be promoted from the valence to the conduction band if a photon of sufficient energy ($\hbar\omega \geq E_g$) is absorbed in the material. During this process, an electron vacancy, or *hole* is left in the valence band. The electrons and holes resulting from optical excitation are the charge carriers in the system until they ultimately recombine, returning the system to equilibrium.

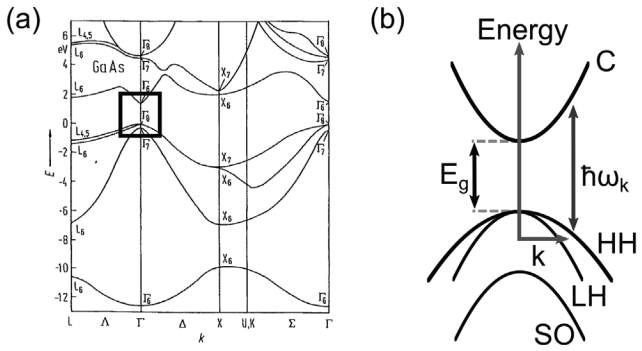

Figure 1.3: (a) The full electronic band structure of GaAs. Modified with permission from [7]. (b) A simple diagram of the electronic band structure shown in the black box of (a). A photon with energy $\hbar\omega_k$ can excite an electron with wave momentum k from the valence band (V) to the conduction band (C).

Restricting our attention to the top most valence band (V = HH) and the conduction band (C), the energy of an electron in the conduction band ($\varepsilon_{c,\vec{k}}$) or a hole in the valence band ($\varepsilon_{v,\vec{k}}$) is given by:

$$\varepsilon_{C,\vec{k}} = \frac{\hbar^2 k^2}{2m_e^*} + E_g \quad \varepsilon_{V,\vec{k}} = -\frac{\hbar^2 k^2}{2m_h^*} \tag{1.2}$$

where the zero of energy has been taken at the top of the valence band, and E_g is the band gap energy. $m_e^*(m_h^*)$ represents the effective mass of the electron (hole) in the conduction (valence) bands respectively. An optical transition in a semiconductor can be described by Fermi's Golden rule which depends on the optical joint density of states $\rho(\omega)$, the coupling strength to the light field (given by the optical dipole moment), and the density of photons in the applied electromagnetic field. A transition can only occur if two conditions are satisfied: i) the photon has sufficient energy to excite an electron from an occupied valence band state $\left|V, \vec{k_V}\right\rangle$ to an unoccupied conduction band state $\left|C, \vec{k_C}\right\rangle$, and ii) momentum is conserved such that the final

electron momentum $\vec{k_C}$ is equal to the sum of the initial electron momentum $\vec{k_V}$, the photon momentum, as well as any additional collisions that may impart momentum to the electron. For example, at finite temperature crystal lattice vibrations, referred to as phonons, can scatter with electrons and satisfy the above constraint. We will restrict our attention to the case of no phonon interactions. In this case, optical transitions are approximately vertical between the valence and conduction band in momentum space because photons have negligible momentum relative to the electron momentum. We can see this because for electrons at the zone boundary $k = \frac{\pi}{a}$, where a is the atomic spacing (a $\sim$ Å) and the photon momentum is $k = \frac{2\pi}{\lambda}$ ($\lambda \sim \mu$m), which is several orders of magnitude smaller. For this reason, optical transitions at each wave vector $\vec{k}$ represent an effective two-level system within the semiconductor. Each of these two-level systems represents an optical dipole, with corresponding transition dipole moment $\vec{\mu_k}$ and angular frequency ω_k.

As shown in Fig. 1.3(b), since energy and momentum are conserved in an optical transition, a photon with energy $\hbar\omega_k$ can excite an electron from the valence band to the conduction band if the energy separation between those states is equal to the energy of the photon, *i.e.*

$$\hbar\omega_k = \varepsilon_{C,\vec{k}} - \varepsilon_{V,\vec{k}} \tag{1.3}$$

This constraint leads to the following relation between the wave vector k and the transition energy $\hbar\omega_k$:

$$k^2 = \frac{2m_r}{\hbar^2}\left(\hbar\omega_k - E_g\right) \tag{1.4}$$

where $\frac{1}{m_r} = \frac{1}{m_e^*} + \frac{1}{m_h^*}$ is the reduced mass of the electron-hole pair. The optical joint density of states for interband transitions in a direct band gap semiconductor is then given by:

$$\rho(\omega) = \Theta\left(\hbar\omega - E_g\right)\frac{\left(2m_r\right)^{3/2}}{\pi\hbar^2}\left(\hbar\omega - E_g\right)^{1/2} \tag{1.5}$$

where $\Theta\left(\hbar\omega - E_g\right)$ is the Heaviside step function. The corresponding linear optical absorption spectrum is given by:

$$\alpha(\omega) \propto \Theta\left(\hbar\omega - E_g\right)\frac{\left(\hbar\omega - E_g\right)^{1/2}}{\left(\hbar\omega\right)^2} \tag{1.6}$$

The linear optical absorption (Eqn. 1.6) is plotted as the dashed black line in Fig. 1.4 taking into account the band gap of GaAs at 10 K.

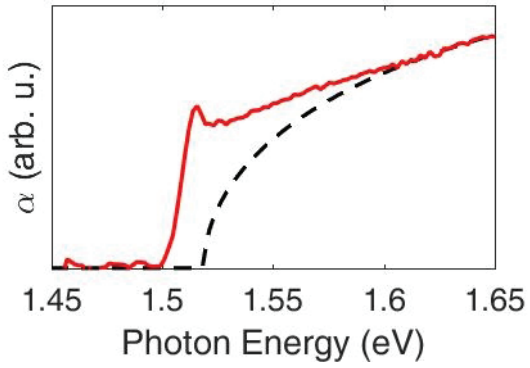

Figure 1.4: Eqn. 1.6 is plotted as a dashed line, with a $E_g = 1.5187$ eV corresponding to the band gap energy of GaAs at 10K (The linear absorption of GaAs was reproduced with permission from [8]).

So far in this development, the Coulomb interaction between excited carriers has been neglected. However, in a semiconductor as a result of the Coulomb interaction electrons and holes can bind together forming an exciton which is similar to a hydrogen atom albeit with a much smaller binding energy ($\sim$ 4 meV) due to the influence of screening by the ion cores and other electrons in the crystal. Like the hydrogen atom, the exciton has a series of bound states (1s, 2p, etc.) In a semiconductor, the optical transitions for bound excitons have energies below the band gap. For the unbound states above the band gap, the attractive interaction between the electron and hole enhances the dipole moment of the transition. As a result, exciton states dominate the linear optical properties of direct band gap semiconductors near the band gap [9]. This can be observed in Fig. 1.4 where the solid line is the linear absorption spectrum for GaAs taken at 10 K. The sharp resonance below the band gap energy stems from absorption at the heavy-hole and light-hole exciton resonance. These ground exciton states as well as excited excitonic states appear as a single peak due to the limited spectral resolution. The enhancement of optical absorption for states close to but above the band gap energy due to the Coulomb interaction between electrons and holes is known as Sommerfeld Enhancement [10].

1.3 Defects

The optical and electronic properties of a semiconductor can be drastically changed

when the local composition and/or structure of the crystal lattice is altered. In this section, a brief overview of two categories of defects are discussed. The class of defects that modify the periodicity of the crystal structure are known as crystal defects. The second class of defects are called point defects, and they primarily modify the electronic properties of the material.

Crystal Defects

Defects that primarily modify the structure of the crystal are grouped based on the dimensionality of the defect [11]. In one dimension these are called dislocations, and examples of these include edge dislocations and screw dislocations. Interfaces are two-dimensional structural defects, and represent surfaces between different materials. Polycrystalline materials are composed of many smaller crystals, or grains. The interfaces between these grains play an important role in the properties of the material. Finally, there are volume defects which result in the grouping of atoms or atom vacancies in a three-dimensional shape. Examples of these types of defects include precipitates (small, sub-micron clusters of atoms), inclusions (large, undesirable clusters that stem from precipitation of foreign contaminants) and voids (large empty spaces in the crystal structure).

Point Defects

Defects that modify the material at an isolated site (zero-dimensional) are known as point defects, and are categorized based on whether the defect is due to a local species of atom (intrinsic) or due to a foreign species of atom (extrinsic). The three most common types of point defects are: i) an interstitial, where an atom resides in space in the lattice that is not occupied by an atom in the perfect crystal. This can occur as an intrinsic defect or as an extrinsic defect. ii) a vacancy defect, where an atom is missing from its position in the periodic crystal lattice and is only an intrinsic defect. iii) A substitutional defect or anti-site defect, where an atom in the crystal lattice is replaced with a different species of atom. For example, for a compound semiconductor composed of two species of atoms, labeled A and B. An intrinsic defect could correspond to A (B) being replaced by B (A). Conversely, a foreign species of atom can replace either A or B leading to an extrinsic anti-site

defect.

1.4 Carrier Relaxation Processes in Semiconductors

Following excitation by a short laser pulse, excited electron-hole pairs in a semiconductor will undergo a cascade of relaxation processes until they energetically return to thermal equilibrium through recombination of the electron and hole. Immediately following excitation, the ensemble of electron-hole pairs, which represent a collection of oscillating dipoles, are in phase with one another, resulting in a macroscopic polarization density that persists until a scattering process causes the phase of these oscillators to change. The phase-breaking scattering process can involve scattering with carriers, defects in the crystal lattice, or phonons depending on the type of semiconductor and the experimental conditions (*e.g.* sample temperature, excitation density, density/type of defects present, etc.) The decay of the macroscopic polarization density is known as dephasing, and the decay time associated with this process is called the T_2 time. Prior to dephasing, the state of the system is said to be within the *coherent regime*. This regime is important for applications utilizing the coherent properties of semiconductors (*e.g.* quantum computation).

In addition to causing dephasing, the initial scattering processes also result in the formation of a thermalized distribution. Immediately after excitation, the excited electrons will have an energetic distribution determined by the centre frequency and band width of the laser pulse. Within the first 100 fs of excitation, electron-hole pairs redistribute energy and momentum, and ultimately form a distribution governed by Fermi-Dirac statistics but at an elevated temperature with respect to the lattice. These carriers are referred to as hot-carriers. The electrons and holes exchange energy and momentum with the lattice through the absorption and emission of phonons. Eventually the hot distribution of electron-hole pairs cools to the lattice temperature. This is known as the *cooling regime* [12]. After the electron-hole pairs have thermalized with the lattice, they undergo recombination. The lifetime of the population of electrons and holes is denoted by T_L, which is commonly referred to as the recombination time. (for instance, for interband electron-hole pairs in bulk GaAs, $T_2 \sim 100$ fs and $T_L \sim 1 - 2$ ns. [13–15])

1.5 Material Systems under Investigation

1.5.1 $CH_3NH_3PbI_3$

The material class known as perovskites are characterized by a material structure comprised of corner-sharing octahedra. These materials exhibit extraordinary properties and have seen widespread usage across several fields. For instance, the compound $YBa_2Cu_3O_7$ exhibits a perovskite structure and was the first superconductor discovered with a transition temperature exceeding the boiling point of nitrogen. This *high critical temperature* (high T_c) superconductor was such a breakthrough in the field that it led to the awarding of the 1987 Nobel Prize in Physics to Johannes Georg Bednorz and Karl Alexander Muller. Furthermore, perovskites have seen widespread usage in ferroelectric devices, with the perovskite $BaTiO_3$ as one of the most widely used materials [16].

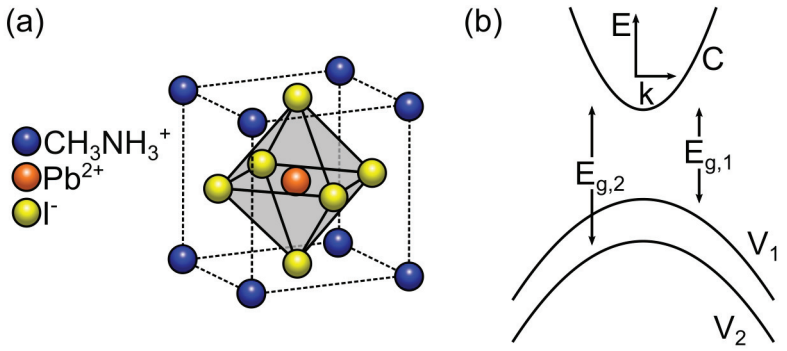

Figure 1.5: (a) The tetragonal crystal structure of $CH_3NH_3PbI_3$ perovskite. (b) The simplified band structure of $CH_3NH_3PbI_3$ relevant for optical transitions.

A class of compounds of interest for applications in optoelectronic devices are the organic-inorganic perovskite compounds of chemical structure ABX_3, where the A-cations are organic, B-cations are metallic and usually divalent (Pb^{2+}, Sn^{2+}, Cu^{2+}) and the X-anions are halides (Cl^-, Br^-, I^-). The prototypical perovskite for optoelectronic applications is methyl-ammonium lead iodide ($CH_3NH_3PbI_3$), where B = Pb^{2+}, A = $CH_3NH_3^+$, and X = I^-. The first synthesis of $CH_3NH_3PbI_3$ was performed by Weber in 1978 [17] as an analog of another perovskite material, $CsPbI_3$. The first solar cell device using $CH_3NH_3PbI_3$ as a photovoltaic absorber material was made in 2009 by Kojima *et al.* with a power conversion efficiency of 3.8 % [18]. This

finding, together with the ready availability and low cost of the constituent materials as well as convenience of solution processing, stimulated a concerted research effort into the development of perovskite solar cell materials. Device efficiencies using perovskite materials have rapidly increased in a short time period, reaching record values exceeding parity with conventional polycrystalline silicon at 22 % [19]. This high efficiency in perovskite is linked to several factors: (i) large, broadband absorption across the the solar spectrum [20]; (ii) long charge diffusion lengths on the order of microns [21], stemming from high charge mobilities and low recombination rates; and (iii) low exciton binding energy at room temperature relative to other solution-processed materials [22].

The crystal structure of $CH_3NH_3PbI_3$ is sensitive to lattice temperature. This material transitions through several phases from absolute zero to temperatures experienced during normal solar cell operation. For temperatures exceeding 327 K, the high-temperature phase has a cubic Pm-3m structure. Between 160 K and 327 K, the range in which most solar cell applications operate, $CH_3NH_3PbI_3$ exhibits a tetragonal I4/mcm structure. Finally, for temperatures below 160 K, the low-temperature phase is orthorhombic pnma [23]. In the discussion that follows, the focus will be on the intermediate tetragonal phase since experiments were conducted at room temperature in this thesis work.

The unit cell for $CH_3NH_3PbI_3$ in the tetragonal phase is shown in Fig. 1.5(a). The tetragonal phase is favoured at room temperature over the cubic phase due to a relatively lower free energy [24] as shown by DFT calculations with the quasiharmonic approximation in which temperature effects are implicitly included due to the dependence of the phonon frequencies on structural parameters. Methylammonium ions reside on each of the eight corners of the unit cell. Pb^{2+} lies at the body centre, and surrounding it are six I^- that are located at the faces of the unit cell. Binding of Pb^{2+} to the six I^- leads to the creation of PbI_6^{-4} octahedra [25]. PbI_6^{-4} octahedron form a three-dimensional network, with the $CH_3NH_3^+$ cations residing in the voids. There also exist layered perovskites (called 2D perovskites) in which one or more layers of PbI_6^{-4} octahedra are separated by organic layers. This thesis work focuses on the bulk perovskite $CH_3NH_3PbI_3$.

A simplified schematic of the band structure of $CH_3NH_3PbI_3$ is shown in Fig. 1.5(b).

$CH_3NH_3PbI_3$ has dual valence bands that contribute to optical absorption [26, 27]. These are labeled V_1 and V_2, and at room temperature their respective band gap energies are $E_{g,1} = 1.631$eV and $E_{g,2} = 2.583$eV. The cell functions for V_1 is composed of the Pb 6p-I5p σ anti-bonding orbital, while the conduction conduction band minimum is the Pb 6p-I 5s σ anti-bonding and Pb 6p-I 5p π anti-bonding orbitals as found by DFT calculations in [28]

An attractive property of $CH_3NH_3PbI_3$ is that it can be solution-processed while maintaining good crystallinity [29], providing a low-cost and efficient means of device production. Methods of producing solar cells utilizing solution processed perovskites include spin coating [29], slot dye coating [30], and blade coating [31]. Spin coating, which was the technique used to prepare the $CH_3NH_3PbI_3$ sample in this work (details of the procedure are described later in Chapter 3), works by applying a solution of the desired material to a substrate in either a one-step or two-step deposition procedure, which is subsequently spun so that a thin, uniform film is formed across the substrate.

In addition to functioning as a standalone absorber, another promising application of perovskites is as a top cell in tandem crystalline-Si (c-Si) solar cells [32, 33]. Si strongly absorbs photons with energies exceeding 1.1 eV (corresponding to the indirect band gap). Photons with energy exceeding 1.1 eV are also absorbed, but the energy difference is wasted as heat (due to intraband relaxation). A tandem cell circumvents this issue by placing another solar absorbing material with a larger band gap on top of the c-Si. The larger band gap of solution-processed mixed halide perovskites permits the collection of these higher energy photons. For example, Bush *et al.* demonstrated a 23.7 % collection efficiency in a caesium formamidinium lead halide perovskite on top of c-Si in a two-terminal configuration [33].

1.5.2 GaAs

Gallium arsenide (GaAs) is one of the most well studied semiconductors in history, second only to silicon (Si). The production of high purity GaAs has been a concerted research effort spanning several decades. Molecular beam epitaxy (MBE) is a technique used for making high purity single crystal samples due to its ability to selectively deposit individual layers of atoms. For example, MBE grown GaAs can be made to a purity such that the residual defect density per unit volume is $\leq 10^{13}\text{cm}^{-3}$

(*i.e.* one defect per 1×10^9 unit cells) with the remnant defect density tied to carbon contamination [34, 35].

The crystal structure for GaAs is shown in Fig. 1.6(a). GaAs has a zinc-blende crystal structure which is composed of two offset face-centred cubic structures of As and Ga. The electronic bands relevant for optical transitions in the near-infrared range are shown in Fig. 1.3(b) and are comprised of three doubly-spin degenerate valence bands and one doubly-spin degenerate conduction band as discussed in Sec. 1.2.

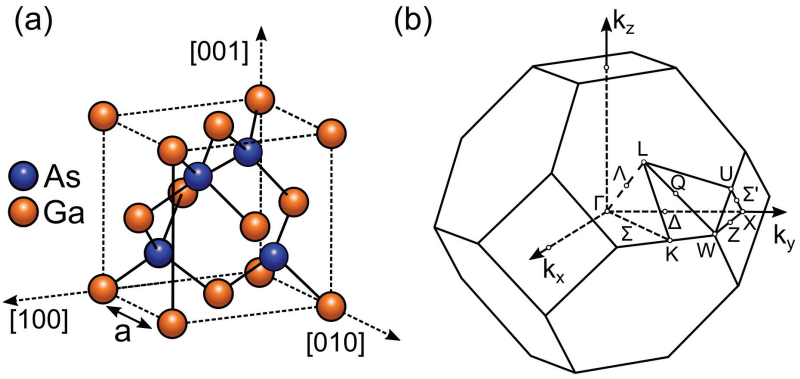

Figure 1.6: (a) The zinc-blende crystal structure of GaAs. The lattice constant for GaAs is a = 5.65 Å. (b) The first Brillouin zone for GaAs.

1.5.3 LT-GaAs

Many of the attractive properties GaAs possesses are derived from its high purity. To achieve this level of purity the substrate is typically held at 600°C during growth. However, when GaAs is grown at lower than typical temperatures (*e.g.* 250°C) imperfections emerge in the crystal leading to dramatic changes in the optical and electrical properties. The most notable of these changes are a higher dark resistivity [36], high breakdown field [37], and a short carrier lifetime [38–43]. Due to these attractive properties, this so-called low-temperature-grown (LT) GaAs has been the material of choice in the design of ultrafast photodetectors [44–46], laser mode locking elements [47, 48], and terahertz (THz) photonics applications [49–53].

One of the most popular applications of LT-GaAs are THz sources. A THz source (10^{12} Hz) is a device that emits an electromagnetic wave with a frequency in the THz

frequency range. The configuration and operation of a typical THz source based on LT-GaAs is described as follows: two metal strips are placed on top of a semiconductor with a gap separating the strips. A DC voltage is applied across the strips, generating an electric field within the semiconductor layer. A temporally-short laser pulse (femtosecond duration) is then focused onto the semiconductor, generating electrons and holes which drift to the anode and cathode respectively. The ensuing pulse of photocurrent is the source of electromagnetic radiation with frequency determined by the lifetime of photoexcited carriers in the material. To generate THz pulses, the carrier lifetime must be on the femtosecond scale. The ability to achieve subpicosecond carrier lifetimes in LT-GaAs with low-temperature growth is the primary reason why LT-GaAs is the material of choice for these applications.

Low-temperature growth of GaAs (*i.e.* with the substrate held at 200°C - 300°C) leads to the incorporation excess As (up to 1%) [54,55]. Fig. 1.7(a) shows the crystal structure of LT-GaAs. (For reference, the crystal structure of defect-free GaAs is shown in Fig. 1.6(a).) Growth at lower substrate temperatures leads to an increase in the residence time of As atoms on the growth surface, resulting in trapping of As atoms in nonstoichiometric bonding configurations [56]. As well, large arsenic overpressure (As/Ga>1) required for crystalline growth of GaAs is responsible for the high density of As incorporated into LT-GaAs. In as-grown LT-GaAs, the majority of excess As atoms are incorporated as point defects and small clusters which lead to dramatic changes in the electronic structure. In Fig. 1.7(b) is shown the band structure for as-grown LT-GaAs. For instance, As can be incorporated into the crystal structure by replacing a Ga atom, leading to the substitutional defect As_{Ga}. Because As is a type V atom, when it replaces the type III atom Ga, two electrons are left over from bonding (*i.e.* As_{Ga} is a double donor) and can contribute to conduction leading to a band of energy states that are located 0.5 eV above the valence band in GaAs (shown as the horizontal bar in Fig. 1.7(b)). Ga vacancies (V_{Ga}) are also formed under these conditions. Due to the presence of Ga vacancies V_{Ga}, As_{Ga} is present in two electronic configurations: an unionized state As^{0}_{Ga} as well as an ionized state As^{+}_{Ga} where an electron has been captured by a V_{Ga}. Due to the large potential these defects exhibit, excited electrons can be trapped by As^{+}_{Ga} leading to localization of the electron. Since these states are localized, these midgap states are represented as

horizontal lines in the electronic band structure. As can also reside in an unoccupied space in the crystal lattice. These are referred to as As interstitials (As_i) which act as electron donors, and reside in two locations in the crystal: i) As resides in the largest empty space in the lattice so as to minimize strain in the crystal (shown in Fig. 1.7(a)), and ii) two As atoms can form a bond-centered or split interstitial configuration that is centred over a Ga site. The former As interstitial has formation energies several eV above the conduction band edge, whereas the split As interstitial is energetically located close to As_{Ga} [57].

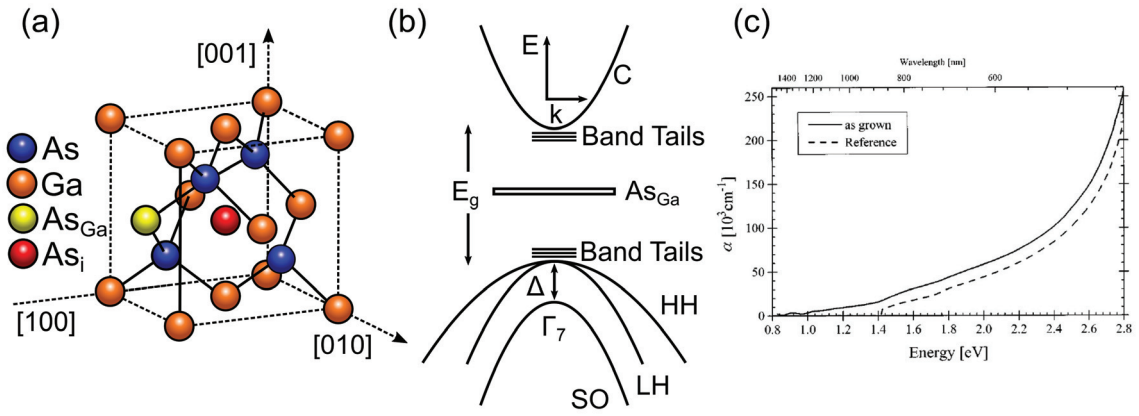

Figure 1.7: (a) The zinc-blende crystal structure of LT-GaAs with substitutional As (As_{Ga}) and interstitial As (As_i). (b) The band structure of LT-GaAs near the band edge with band tails and As_{Ga} defect states. (c) The linear absorption spectrum of as-grown GaAs at room temperature alongside GaAs. Reproduced with permission from Streb *et al.* [58]

Collectively, the distribution of point defects throughout the material causes fluctuations in the local potential experienced by electrons, leading to smearing of the valence and conduction bands and the creation of localized states that reside within the band gap but near the band edges. These are called band tails, and are represented as closely-spaced lines in the band structure shown in Fig. 1.7(b). [40, 59]. Due to localization, these electronic states are represented as flat horizontal lines in the electronic band structure. A spread of energies exist for the band tail states due to the varying potential landscape (*i.e.* variations in the local potential depth and width) within the crystal.

Optical absorption experiments have provided considerable insight into the electronic structure near the band edge of LT-GaAs. In contrast to the linear absorption spectrum for GaAs at room temperature (shown by the black dashed line in Fig. 1.7(c)), absorption in LT-GaAs starts at 0.8 eV and increases smoothly across the band edge, as shown by the absorption spectrum for an as-grown LT-GaAs sample in Fig. 1.7(c). This strong sub-gap absorption has been studied extensively using transmission [36, 58, 60, 61], magnetic circular dichroism [62], and ellipsometry techniques [63], and is caused by transitions from the mid-gap As_{Ga} band to conduction band. Additionally, transitions between band tail states can contribute to absorption near the band edge, and is referred to as the Urbach absorption tail [59]. Empirically, the absorption edge is modeled by the following equation:

$$\alpha(\omega) \propto e^{\frac{\hbar\omega - \hbar\omega_0}{E_U}} \tag{1.7}$$

$\hbar\omega_0$ is the effective band gap energy of the disordered system and E_U is called the Urbach parameter which characterizes the disorder. In optical absorption experiments, E_U is extracted by taking the slope of the log of the absorption curve. In a material with low disorder such as GaAs, E_U is approximately 7 meV [64].

The short carrier lifetimes in LT-GaAs is one of the primary reasons why this material is attractive for high speed photodetectors and THz sources. Carrier lifetimes on the sub-picosecond time scale have been measured using ultrafast pump-probe techniques [38–43, 56, 65] and time-resolved THz spectroscopy [66, 67]. The source of these short lifetimes is the large density of As-related point defects present in low-temperature-grown films. Following excitation, electrons in the material are rapidly trapped on these defects [38, 67].

1.6 Four-wave Mixing Spectroscopy

Four-wave mixing spectroscopy techniques probe the dynamics of electron-hole pairs within the coherent regime by measuring the coherent emission from the macroscopic polarization that persists until dephasing occurs. These techniques can therefore be used to measure the coherence lifetime (T_2) and to study the interactions between the electron-hole pairs through the modifications these interactions make to the polarization. They can also be used to study diffusion of charge carriers by probing the

magnitude of the polarization as a function of the separation between the exciting pulses. A brief introduction to four-wave mixing is provided in this section. This is followed by an introduction to each of the three experimental geometries used in this thesis work: (i) two pulse self-diffraction FWM (Sec. 1.6.1); (ii) Two-dimensional Fourier transform spectroscopy (Sec. 1.6.2); and (iii) Transient grating technique (Sec. 1.6.3).

1.6.1 Two Pulse Self Diffraction Four-wave Mixing

In a two-pulse FWM experiment, two short optical pulses with electric fields $\vec{E_1}$ and $\vec{E_2}$ with wave vectors $\vec{k_1}$ and $\vec{k_2}$ are focused onto a sample. In the simplest case, all three pulses are linearly polarized in the same direction. We first consider the case in which the pulses arrive at the same time ($i.e\ \tau = 0$). Interference between the electric fields $\vec{E_1}$ and $\vec{E_2}$ in the material can lead to a spatial modulation in the density of electron-hole pairs across the sample, which in turn changes the local absorption and index of refraction for energies resonant with these transitions. This can be viewed physically as an optical grating, or population grating. This grating will cause a portion of both pulses $\vec{E_1}$ and $\vec{E_2}$ to diffract. In the experiment, we measure the diffraction of pulse $\vec{E_2}$.

It is also possible to generate a grating for times when $\vec{E_1}$ and $\vec{E_2}$ are not mutually overlapped in time. For example, excitation by pulse $\vec{E_1}$ will lead to coherent oscillation of dipoles associated with many electron-hole pairs in the material, leading to a macroscopic polarization that persists on a timescale set by the coherence lifetime. As long as these electron-hole pairs are still coherent when $\vec{E_2}$ arrives, the electric field can interfere with the polarization excited by the first pulse, and is possible to generate a population grating. By measuring the FWM signal resulting from self-diffraction of pulse $\vec{E_2}$ as a function of the time delay τ between pulses $\vec{E_1}$ and $\vec{E_2}$, one can extract the coherence relaxation time T_2. Since the total FWM signal is measured as a function of delay τ between the pulses $\vec{E_1}$ and $\vec{E_2}$, this is known as time-integrated FWM (TI-FWM).

Two-pulse FWM experiments (TR-FWM and TI-FWM) can be used to distinguish whether the optical transition that generated the light is a homogeneously-broadened transition (*e.g.* an exciton transition with discrete energy levels) or an

inhomogeneously-broadened transition (*e.g.* the interband continuum of transitions, which form a set of closely-spaced two-level systems). Homogeneous broadening reflects the natural line shape of a discrete transition due to interactions such as electron-hole collisions, collisions with defects, etc. For an inhomogeneously broadened transition, the line width is further broadened by the presence of transitions with closely spaced energies. These two transitions are shown pictorially in Fig. 1.8(a,d) respectively. The FWM signal versus time for a homogeneously-broadened transition monoexponentially decays with time after arrival of $\vec{E_2}$, and is called *free polarization decay* (shown in Fig. 1.8(b)). In contrast, for an inhomogeneously-broadened transition the FWM signal versus time peaks at a time τ after arrival of $\vec{E_2}$ (shown in Fig. 1.8(e)). This is commonly called a *photon echo* and is analogous to the spin-echo observed in nuclear magnetic resonance, except that a photon-echo is produced by the rephasing of dipoles of electron-hole pair transitions. In Fig. 1.9 a diagram of the photon echo process for a two-level system in the Bloch sphere representation within the rotating wave approximation is shown above the time order of the exciting pulses. The optical Bloch vector lies on the sphere of radius 1. The z-component of the Bloch vector indicates the difference in the occupation of the valence and conduction states, which we refer to as $|0\rangle$ and $|1\rangle$. The angle that the in plane component of the Bloch vector makes with the x-axis indicates the phase accumulation of each electron-hole pair versus time relative to the centre frequency of the laser pulse.

Prior to excitation, the system is in the ground state as indicated by the Bloch vector pointing in the negative z-direction. Excitation by pulse $\vec{E_1}$ at time t_1 excites the system. (Note: For clarity, a pulse with area $\pi/2$ has been assumed. In this thesis work, the Bloch vector would point much closer to the z-axis due to the low excitation powers used.) Due to the spread of frequencies excited in an inhomogeneously broadened transition, the different frequency components of the Bloch vector will spread out in the x-y plane until arrival of pulse $\vec{E_2}$ at time t_2 (given by the different coloured arrows in Fig. 1.9). Pulse $\vec{E_2}$ causes a phase reversal of the different frequency components. In particular, due to the phase matching conditions imposed by the FWM process and path chosen to measure the FWM signal (*i.e.* $2\vec{k}_2 - \vec{k}_1$), the phase of pulse $\vec{E_2}$ is conjugated with respect to pulse $\vec{E_1}$. For this reason, $\vec{E_2}$ causes a reversal of the phase accrual in the coherence. These components then rephase at

time τ producing a photon echo. In the time-integrated method applied here, the total amount of FWM signal (*i.e.* integrated over time) is measured as a function of interpulse delay.

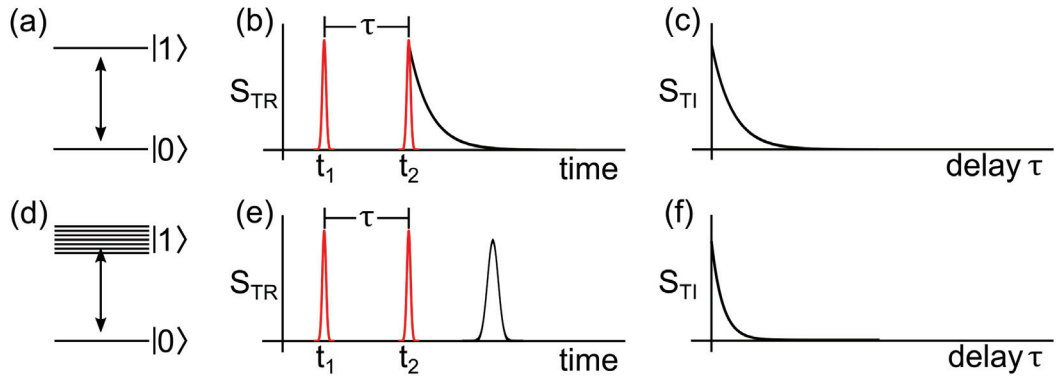

Figure 1.8: (a) a homogeneously-broadened two-level transition. (b) The corresponding TR-FWM (S_{TR}) signal and (c) TI-FWM (S_{TI}) for a homogeneously-broadened transition excited by Delta-shaped pulses. (d) an inhomogeneously-broadened transition. (e) The corresponding TR-FWM (S_{TR}) signal and (f) TI-FWM (S_{TI}) for an inhomogenously-broadened transition excited by Delta-shaped pulses.

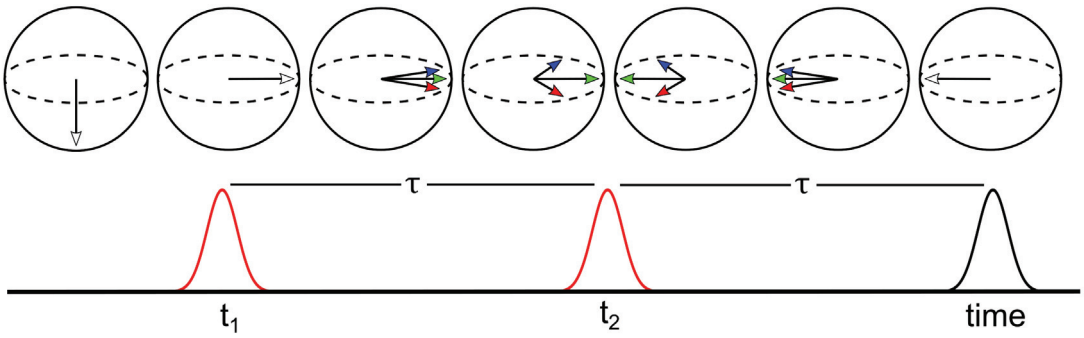

Figure 1.9: Shown here is the Bloch sphere representation of an inhomogeneously broadened two-level transition with states $|0\rangle$ and $|1\rangle$ excited in a two-pulse FWM experiment. On the top is the Bloch sphere at different points of time, and on the bottom is a time axis showing the excitation pulses at t_1 and t_2. Excitation by pulse $\vec{E}_1$ at time t_1 generates a coherence in the system. Different frequency components of the transition spread out in the Bloch sphere (given by the different coloured vectors) until they are reversed a time τ later by pulse $\vec{E}_2$. Approximately a time τ later, the different frequency components rephase, generating a photon-echo signal.

The two-pulse FWM signal for a homogeneously broadened and inhomogeneously broadened transition ($S_{TI,homo}$ and $S_{TI,inhomo}$ respectively) are given by [1]:

$$S_{TI,homo} \propto e^{-\frac{2\tau}{T_2}} \quad S_{TI,inhomo} \propto e^{-\frac{4\tau}{T_2}} \left(1 + \mathrm{erf}\left(\frac{\delta\omega\tau}{\sqrt{\pi}}\right)\right) \tag{1.8}$$

where erf is the error function, and $\delta\omega$ is the amount of inhomogeneous broadening (*i.e.* the range of energies within the transition). The minimum range of delay τ required in TI-FWM experiments is determined by the coherence time T_2 as it reflects the $1/e$ decay of the coherence, and in practice is taken to be several times larger to ensure complete coherence decay. For a homogeneously broadened transition, the time-integrated FWM signal decays versus τ at a rate $T_2/2$, while for the inhomogeneously broadened case it decays at a rate $T_2/4$, and are shown in Fig. 1.8(c) and Fig. 1.8(f) respectively.

The work of Yajima and Taira stimulated a broad research effort utilizing four-wave mixing to study relaxation in bulk materials like GaAs [4, 8, 13, 68–72], InP [73, 74], CdSe [75–77] , Ge [78–80], and nanostructured materials like GaAs quantum wells [5, 6, 76, 77, 81–86], InGaAs multiple quantum well [87], and ZnSe multiple quantum well [88]. This also motivated new experimental geometries of FWM. FWM geometries utilizing three spatially separate pulses expanded the utility of these techniques. The delay between the second and third pulse could now be adjusted (in the two pulse self-diffraction geometry, this delay was equal to zero because the second pulse played the role of the third pulse) providing a means to examine excited-state population relaxation. After excitation by the first two pulses, photoexcited charge carriers will relax on a timescale set by the population lifetime T_L. Interaction with a third pulse produces the FWM signal, and is a direct reflection of the amount of excited carriers remaining in the system at that particular time.

Spectral resolution of the FWM signal makes it possible to distinguish between different types of electronic states that contribute to the optical response. In particular, one can distinguish between the FWM response of excitons and loosely bound electron-hole pairs above the band gap. By detecting the dependence of the FWM signal on both the interpulse delay and detection photon energy, one can separately probe the type and rate of the relevant scattering mechanisms that result in the relaxation of these electron-hole pairs. The results of spectrally-resolved four-wave mixing experiments are presented as a 3D plot showing the amplitude of the FWM signal as

a function of interpulse delay τ and the detection photon energy ($\hbar\omega_t$). An example of such a measurement, showing the results of Wehner *et al.* on bulk GaAs at 77 K is shown in Fig. 1.10.

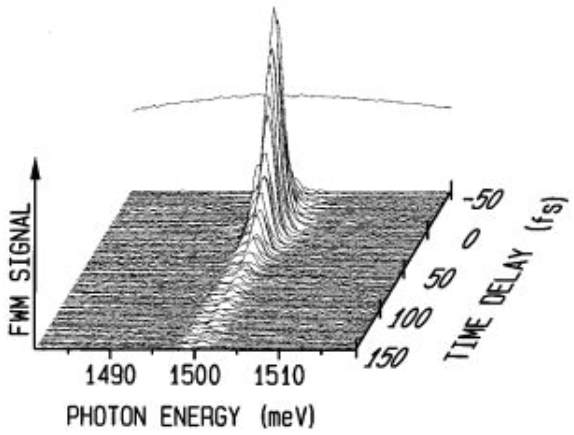

Figure 1.10: SR-FWM results on bulk GaAs held at 77 K. Modified with permission from Wehner *et al.* [70]. The contour represents the FWM amplitude for each interpulse delay and photon energy.

1.6.2 Two-dimensional Fourier Transform Spectroscopy

2DFTS differs from the two pulse self diffraction technique in two ways: (i) three pulses are used instead of two; and (ii) the phase of the four-wave mixing signal is detected in addition to the amplitude. The first demonstration of this technique [89] ushered forth a new era in the realm of FWM. In the experiment of Chen *et al.* [89], the amplitude and phase was detected using spectral interferometry. Spectral interferometry involves interfering the FWM signal with a reference pulse and using the resulting coherent interferogram versus pulse energy to deduce the amplitude and phase of the FWM signal. The interferogram is only stable provided that the path lengths of the individual beams do not change. Since vibrations of optical mounts would destroy the interferogram, phase stabilization techniques are used. Advancements in phase-stabilization techniques (both passive and active) permitted new implementations of *phase-resolved* FWM, resulting in what is known as two-dimensional Fourier transform spectroscopy. These experiments have permitted the observation of complex quantum coupling mechanisms in excited systems [90], measurement of

homogeneous and inhomogeneous line widths for a transition [91,92], and provided a means to distinguish between different types of many-body interactions [93–95].

The presentation of data in a 2DFTS experiment is distinguished from FWM studies as the FWM signal is shown as a function of absorption and emission energies in the system. Similar to spectrally-resolved FWM, the emission energy in 2DFTS is obtained via spectral resolution of the FWM signal. However, instead of presenting the data as a function of interpulse delay τ, the second frequency axis (absorption) is obtained by performing a Fourier transform of the complex FWM signal with respect to the interpulse delay since the rate of phase accrual between the first two pulses reflects the absorption frequency.

Fig. 1.11 shows calculated 2DFTS results for varying levels of inhomogeneity by Siemens *et al.* [96]. In 2DFTS, the diagonal and cross-diagonal line shapes of a resonance (shown in Fig. 1.11(a)) are important as they are used to determine the inhomogeneous and homogeneous line width of the transition. In 2DFTS, homogeneous broadening manifests as an elongation parallel to the diagonal line. Fig. 1.11(a) shows the 2DFTS response for a homogeneously-broadened transition (such as an exciton transition). The diagonal and cross-diagonal line shape for this transition (shown in Fig. 1.11(d)) is a Lorentzian. Fig. 1.11(c) shows the 2DFTS response for an inhomogeneously-broadened transition. Each point along the diagonal corresponds to a resonant interaction (*i.e.* absorption and emission at the same frequency) and so the width of the 2DFTS signal along this line directly reflects the spread of resonant frequencies within that transition. For example, interband-continuum transitions in GaAs can be modeled as an inhomogeneously-broadened transition where the spread in frequencies reflects the continuum of energies an electron-hole pair can possess. A line through the cross-diagonal of a resonance reflects the degree of homogeneous broadening for that transition. In this case, the 2DFTS response is elongated along the diagonal and has a Gaussian line shape (shown in Fig. 1.11(f)) reflecting the energy range of transitions excited.

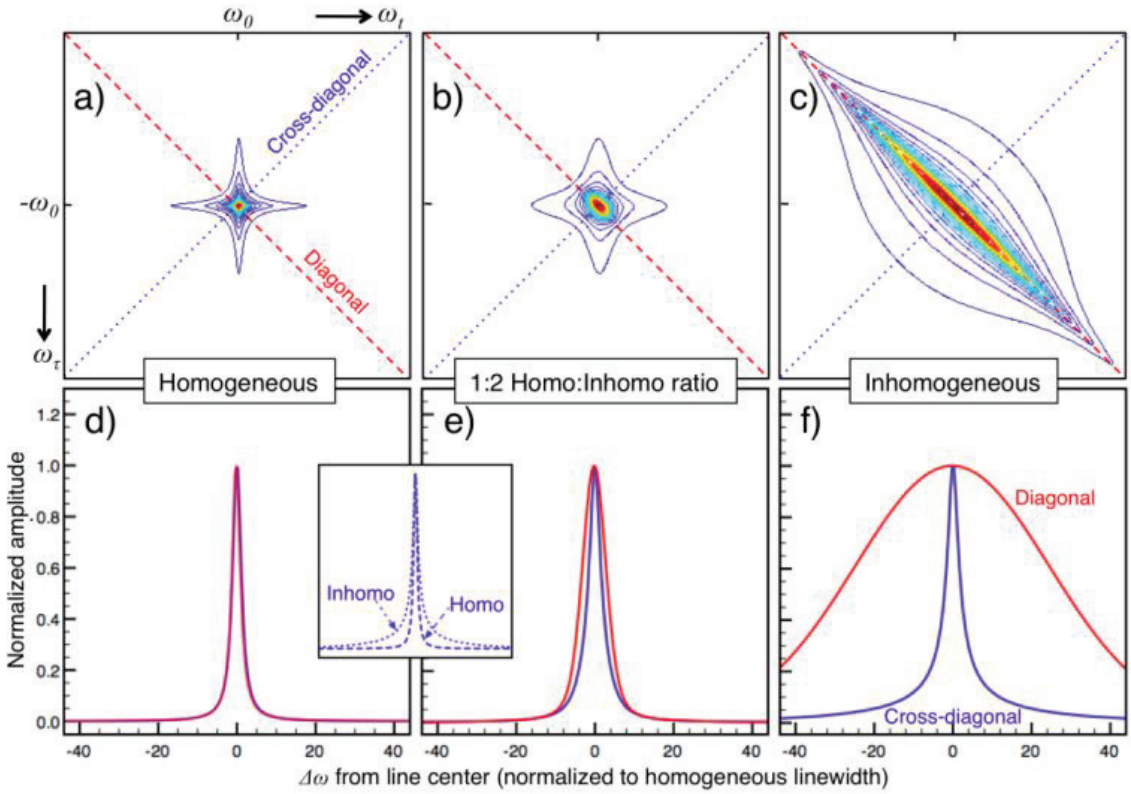

Figure 1.11: The amplitude 2DFTS response for a two-level system that is (a,d) purely homogeneous broadened, (b,e) partially inhomogeneously-broadened, and (c,f) purely inhomogeneously-broadened. Modified with permission from Siemens *et al.* [96]

1.6.3 Transient Grating Four-wave Mixing

FWM can also be used to probe the transport of photoexcited carriers. The transport properties of electron-hole pairs are described by ambipolar diffusion. Diffusive transport is driven by a concentration gradient. For ambipolar transport, the motion of one species of charge (*e.g* electrons) results in an electric field that influences the motion of the oppositely-charge species (holes), leading to a collective motion of both charge species. The version of a FWM experiment that is sensitive to carrier diffusion is called the transient grating technique. In this method, the first two pulses are coincident ($\tau = 0$) and together excite a carrier grating in the material (across the x-direction in Fig. 1.1). The third pulse is used to study the amplitude of the carrier grating as a function of delay T. The grating decays via both carrier diffusion away from the maxima and minima of the grating and due to recombination. These two

timescales can be disentangled by varying the initial period of the grating by changing the direction of the incoming excitation beams. The transient grating technique has been used to study the diffusion of electron-hole pairs in molecular systems [2,3] and semiconductor systems [97]. The first implementation of the transient grating technique was by Salcedo *et al.* [2]. It wasn't until the work of Schwab *et al.* [97] that the transient grating technique was applied to the study of a material system suitable for solar cell applications. In this work, Schwab *et al.* examined the diffusion of electron-hole pairs in $CdS_{1-x}Se_x$, a mixed crystal between the binary compounds of CdS and CdSe. In addition to obtaining values for the diffusion coefficient and lifetime using a purely continuum-diffusion model, Schwab *et al.* demonstrated the efficacy of this technique as a tool to study charge transport in solar cell materials.

After excitation, electron-hole pairs forming the transient carrier grating will diffuse laterally (in the x direction in Fig. 1.1). Since the first two pulses are mutually overlapped in time ($\tau = 0$), the delay T of the third pulse serves as the time axis (*i.e.* $t \rightarrow T$). After excitation, the distribution of electron-hole pairs $\zeta(x,T)$ can be modeled using the following equation (a brief derivation is shown in Appendix D):

$$\frac{d\zeta(x,T)}{dT} = D\frac{\partial^2\zeta(x,T)}{\partial x^2} - \frac{\zeta(x,T)}{T_L} \tag{1.9}$$

where D is the ambipolar diffusion coefficient, and T_L is the population lifetime of excited electron-hole pairs. The ambipolar mobility μ_a and the diffusion coefficient D are related via the well-known Einstein relation:

$$D = \frac{\mu_a k_B T_{\text{lattice}}}{e} \tag{1.10}$$

where k_B is the Boltzmann constant, e is the electron charge, and T_{lattice} is the temperature of the crystal lattice. Following the treatment in Wong *et al.* [3], at the instant the population grating is formed, the population distribution of electron-hole pairs is given by:

$$\zeta(x,0) = 1/2\left[1 + \cos\left(\Delta x\right)\right] \tag{1.11}$$

$\Delta = 2\pi/d$, where $d = \lambda/2\sin\left(\theta/2\right)$ is the grating constant, and depends on the wavelength λ of the excitation laser, and the angle θ between the two excitation beams. This description of the population grating is adequate, since the spot-size (and therefore the macroscopic extent of the grating) is much larger than the wavelength

of the laser. In ultrafast optical experiments, the transient behavior is measured by varying the delay between optical pulses. The solution to the diffusion equation in the limit of short optical pulses with the initial condition in Eqn. 1.11 is:

$$\zeta(x,T) = 1/2e^{-T/T_L}\left[1 + e^{-\Delta^2 DT}\cos(\Delta x)\right] \tag{1.12}$$

The observed signal in a transient grating measurement is proportional to the square of the difference in grating amplitude, i.e.

$$\mathrm{S}(t) \propto |\zeta(0,T) - \zeta(d/2,T)|^2 \tag{1.13}$$

The resulting signal is given as

$$\mathrm{S}(t) \propto e^{-T/T_s} \tag{1.14}$$

where

$$\frac{1}{T_s} = \frac{2}{T_L} + \Delta^2 D \tag{1.15}$$

Inspection of Eqn. 1.15 reveals that the FWM signal lifetime, T_s, depends on the carrier lifetime T_L, the diffusion coefficient D, and the grating period (through $\Delta = 2\pi/d$). The form of Eqn. 1.15 is a linear equation, where $\frac{1}{T_s}$ and Δ^2 represent the dependent and independent variables, D is the slope of the line, and $\frac{2}{T_L}$ is the intercept of the line with the y-axis. An example of results of transient grating experiments on CdSSe mixed crystals by Schwab *et al.* [97] is shown in Fig. [ADD]. In this thesis work, the FWM signal lifetime T_s was measured as a function of Δ for several grating periods, and the data was fitted using Eqn. 1.15 to extract D and T_L. Using the values for D and T_L, the diffusion length in one-dimension can be calculated by:

$$L_D = \sqrt{DT_L} \tag{1.16}$$

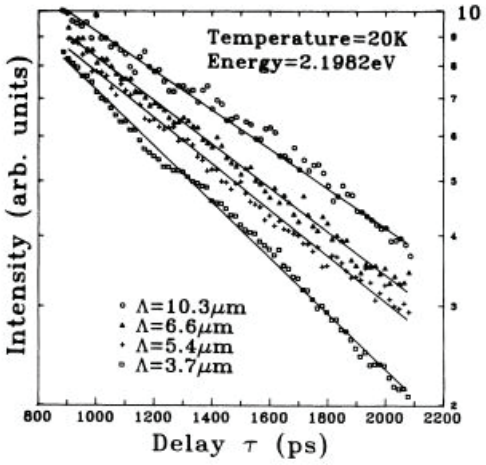

Figure 1.12: Transient grating measurements on CdSSe mixed crystals for different grating periods. For increasing grating period, the lifetime of the transient grating signal increased. Note: the grating period d in this thesis work is denoted by Λ in Ref. [97]. Reproduced with permission from Schwab *et al.*.

The transient grating technique is attractive over other methods used to measure charge transport as it is an all-optical technique (does not require electrical contact layers). This implies that it can be used to study a whole host of optoelectronic materials without the need to identify suitable electrode materials that permit ohmic contacts. The transient grating technique also does not require sophisticated modeling to extract the carrier lifetime and ambipolar diffusion length.

1.7 Literature Review

1.7.1 Overview

The relevant literature associated with each of the three projects pursued in this thesis work is presented in this section. For the first project, the present thesis work fits within the context of earlier studies of diffusion lengths in $CH_3NH_3PbI_3$, for which the large variation of reported values reflects both the breadth of techniques used and uncertainties in the models used to extract the diffusion length. For the second project, the study of the change in the density and type of defects in LT-GaAs with annealing using four-wave mixing spectroscopy for the first time builds upon prior studies of these annealing-induced changes with X-ray diffraction, infrared absorption,

and other techniques. For the third project, this thesis work builds upon the current understanding of many-body interactions that has been built up over two decades in four-wave mixing experiments on a range of group IV and III-V semiconductors. Whereas previous work had focused on exciton-exciton interactions, this work sheds light on non-degenerate exciton-carrier interactions using two-dimensional Fourier transform spectroscopy.

1.7.2 Carrier Transport Properties of $CH_3NH_3PbI_3$

Understanding the charge transport properties within a semiconductor is vital for the development of new devices, as well as the improvement of existing devices based on these materials. Due to the attractive properties of $CH_3NH_3PbI_3$ for optoelectronic applications, a massive research effort has been carried out to determine the nature of charge transport (whether occurring via excitons vs unbound electron-hole pairs) as well as to determine the value of the carrier diffusion length. One of the reasons for the uncertainty in the diffusion length is the range and type of diffusion being reported in the experiments [98]. For example, photoluminescence experiments which probe the light resulting from carriers undergoing radiative recombination, probe only the transport of radiative species. Time-domain THz (TDTHz) is a pump-probe technique in which the pump photon energy is above the band gap and the probe is a THz pulse. In these techniques, both the electron motion and hole motion contribute to this photocurrent and so such techniques probe the sum of the electron and hole mobilities. In the case of optical excitation of an undoped semiconductor in the absence of external bias, the transport of electron-hole pairs is described by ambipolar diffusion, in which case the mobility probed is $\mu_a = \frac{2\mu_e\mu_h}{\mu_e+\mu_h}$ where μ_e and μ_h are the electron and hole mobilities respectively.

Experimental approaches used to measure the diffusion length in $CH_3NH_3PbI_3$ can be organized into three groups: all-electrical, electrical-optical, and all-optical. All-electrical techniques used to study perovskites include space-charge limited current [99], photo-Hall effect [100], impedance spectroscopy [101], and spatially-resolved electron beam induced current [102]. For instance, a schematic of the experiment used by Chen *et al.* in Hall effect studies of carrier transport in perovskite is shown in Fig. 1.13(a) [100]. A current injects electrons into the source terminal. A magnetic

field, oriented along the vertical direction, causes the injected charges to be steered into the page (via the Lorentz force), leading to electron buildup on the side of the sample (on the opposite side of the sample are holes). This charge separation leads to the formation of an electric field and a corresponding voltage across the sample that reflects the density of charge carriers. Together with the charge conductivity between the source and drain (labeled S and D in Fig. 1.13(a)), the charge mobility can be determined. In the experiment by Chen *et al.*, a low frequency magnetic field was applied to oscillate the Lorentz force on charge carriers. Due to the time-varying magnetic field, Faraday induction effects in the semiconductor were taken into account by measuring the Hall voltage across the sample in the absence of applied current, and subtracting this signal from the measured Hall voltage in the presence of current injection. This subtraction improves the signal to noise of the measurement, which is essential in perovskite materials since they have higher resistances and lower mobilities than conventional inorganic semiconductors. This method is therefore referred to as artefact-corrected Hall effect.

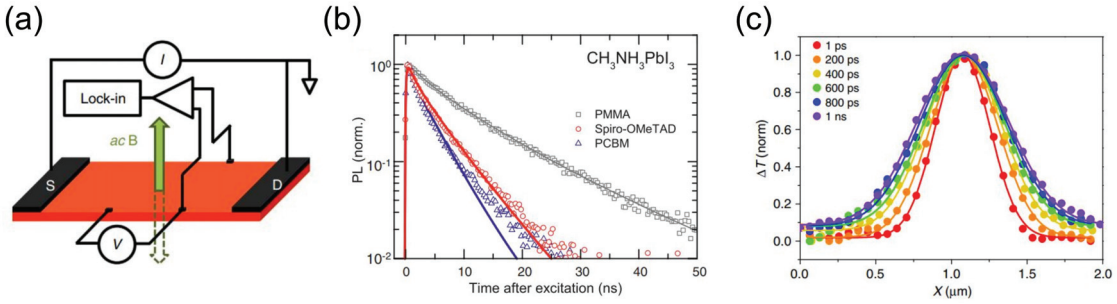

Figure 1.13: (a) Schematic of the AC Hall Effect apparatus. Reproduced with permission from Chen *et al.* [100] (b) PL decay curves for $CH_3NH_3PbI_3$ attached to different charge transport layers. Reproduced with permission from Stranks *et al.* [21] (c) TAM measurements of $CH_3NH_3PbI_3$ as a function of pulse delay. Reproduced with permission from Guo *et al.* [103].

A technique using both optical excitation and electrical contact layers is photoluminescence (PL) quenching. The earliest diffusion studies in perovskite were carried out by Stranks *et al.* [21] using this approach. The perovskite layer is deposited onto a charge quenching layer. In an operating solar cell, these layers are called electron (or hole) transport layers. Relative to perovskite, conduction (valence) bands are

lower (higher) such that electrons (holes) are selectively able to pass through the interface. The removal of either electrons or holes quenches the photoluminescence. After photoexcitation, the electrons and holes diffuse to their respective collection layers, where either the electron or hole is removed from the perovskite layer, reducing the rate of radiative recombination and photoluminescence emission. By comparing the time-resolved photoluminscence for neat perovskite and perovskite deposited onto an electron acceptor layer, or hole acceptor layer, one can obtain information about the nature of transport for each charge carrier type [21, 104]. Using PCBM ($C_{72}H_{14}O_2$) and Spiro-OMeTAD ($C_{81}H_{68}N_4O_8$) as electron and hole quenchers, respectively, Stranks *et al.* [21] examined the rate of PL decay with each type of layer. As shown in Fig. 1.13(b), both electron and hole quenching layers lead to a dramatic decrease in PL lifetime. Together with the recombination lifetime extracted from the PL decay for neat $CH_3NH_3PbI_3$ (without a quenching layer), Stranks *et al.* calculated diffusion lengths of 105 nm and 129 nm for holes and electrons respectively.

Another experiment utilizing both optical and electrical means to probe transport is the steady-state grating technique [105]. In this approach, two non-collinear continuous-wave laser beams are focused onto the same spot of the material, and the polarization of the beams are alternated between colinearlly polarized and cross-linearly polarized. Collinear polarized excitation leads to carrier grating formation in the sample, whereas cross-linear does not. For collinear excitation, the carrier grating causes a spatial change in the photoconductivity which is measured by electrical contacts. The diffusion length is determined by measuring the change in photoconductivity as a function of grating period (as determined by the angle between the two exciting beams).

The third category of techniques employed to study charge transport in $CH_3NH_3PbI_3$ are referred to as all-optical. In contrast to the previous techniques, all-optical experiments utilize only an optical probe, thereby avoiding the need to identify suitable contact layers and to consider the influence of interface effects imposed by the contact layers. These experiments include TRTHz [106–109], transient absorption microscopy (TAM) [103], and time-resolved microwave conductivity (TRMC) [106]. Several TDTHz spectroscopy studies have looked at $CH_3NH_3PbI_3$ [106–109]. TRTHz

spectroscopy techniques probe the photoconductivity of the material in the THz frequency range. This technique is performed by first using a visible infrared femtosecond laser pulse to excite electron-hole pairs in the sample, followed by a delayed THz probe pulse. The THz probe transmitted through the sample carries information on the photoconductive response of the material. To extract important parameters related to transport, the material response to the THz field must be assumed. Several studies have used a Drude-like response [107,108]. The use of charge extraction layers to understand electron or hole transport has also seen usage in TRTHz. Ponseca *et al.* [106] measured near balanced THz electron and hole mobilities of 12.5 $cm^2V^{-1}s^{-1}$ and 7.5 $cm^2V^{-1}s^{-1}$. Ponseca *et al.* performed complementary transient absorption experiments and found that the transient absorption response matched the TRTHz response, leading them to conclude that the charge mobility remains constant for the first 1 ns after excitation.

Transient absorption microscopy is a newer all-optical technique, and is advantageous over other techniques discussed thus far because it is a direct probe of carrier transport [103]. In this technique, a pump pulse excites electron-hole pairs. A time-delayed probe measures the transient absorption (*i.e.* the change in absorption of the probe pulse due to the excited carriers injected by the pump pulse) as a function of lateral position across the sample. Since the transient absorption signal reflects the electron-hole concentration, the spatial profile of the signal directly reflects the movement of electron-hole pairs (shown in Fig. 1.13(c)). Using this method, Guo *et al.* obtained an ambipolar diffusion length of approximately 1 μm in a $CH_3NH_3PbI_3$ thin film. However, due to the necessity of a tightly focused beam (≈ 0.5 μm) in these experiments, the diffusion length is reflective of the local environment, and does not represent the macroscopic properties of the material.

As discussed above, a broad range of experimental approaches have been used to investigate carrier diffusion in methylammonium lead iodide perovskite. All-optical techniques are attractive because they do not require the attachment of contacts, however the current array of techniques either require modeling (*e.g.* TDTHz) or are experimentally challenging (*e.g.* requires a difficult focusing geometry, such as in TAM). The all-optical FWM technique known as the transient grating technique circumvents these issues by directly measuring carrier diffusion (without the need for

modeling) in a simple optical configuration that probes the macroscopic transport properties of the thin-film under study. Such a technique is suitable for rapidly surveying a wide range of solar cell materials. In this thesis work, the transient grating technique was used to extract the ambipolar diffusion length in $CH_3NH_3PbI_3$.

1.7.3 Optical and Electronic Properties of Annealed LT-GaAs

The influence of annealing on the structural, dynamic, and optical properties of LT-GaAs has been studied by a number of techniques [36,58,61,62,110–114]. Post-growth annealing refers to the process by which LT-GaAs is heated to high temperature (*e.g.* 600°C) for a short period of time (on the order of seconds to minutes). Using Hall effect measurements, Look *et al.* showed that after post-growth annealing at 600°C the resistivity of as-grown LT-GaAs increases by five orders of magnitude [36, 115] as shown Fig. 1.14(a). The change in the conduction properties of LT-GaAs with annealing stems from structural changes within the material. Post-growth annealing causes As point defects (*e.g.* As_{Ga}, As_i) to agglomerate into clusters because these defects are not stable against the annealing process for temperatures exceeding 400°C. For example, in a LT-GaAs sample grown at 200°C, the density of As_{Ga} defects was observed to drop by a factor of 9 after annealing at 600°C for ten minutes [36].

In addition to changing the conduction properties, post-growth annealing of LT-GaAs causes an increase in the carrier lifetime [39,65–67] due to a reduction in carrier trapping at As_{Ga} point defects as these defects precipitate into As clusters. For annealing temperatures between 700°C and 1000°C, Harmon *et al.* [39] observed an increase in carrier lifetime from 2.1 ps to 10.3 ps. This result was further corroborated by Prabhu *et al.* [66] who observed a similar trend over the same temperature range. In contrast, for annealing temperatures below 550°C there is no strong dependence of carrier lifetime on annealing temperature. Pump-probe experiments by Youn *et al.* [65] observed that the pump-probe signal lifetime (which directly reflects the carrier lifetime) was shorter than their temporal resolution of 30 fs for all samples annealed below 550°C. Above 550°C, the carrier lifetime increases rapidly with annealing temperature with measured lifetimes of 100 fs and 824 fs for annealing temperatures of 600°C and 800°C respectively.

The optical properties of LT-GaAs also change drastically with post-growth annealing. Measurements of the linear absorption for varying annealing temperature in LT-GaAs have been reported by Streb *et al.* [58] and are shown in Fig. 1.14(c). For annealing temperatures up to 400°C, no change in absorption was observed within the experimental error of their setup. For temperatures between 400°C - 500°C, the overall absorption was observed to drastically decrease, however the spectroscopic shape did not change significantly with annealing. The decrease in absorption was therefore linked to the agglomeration of As-related point defects into As clusters. For annealing temperatures exceeding 500°C the overall absorption coefficient did not change significantly. The broadband absorption from 0.8 eV to energies above E_g in Fig. 1.14(c) is due to promotion of electrons from the As_{Ga} defect levels to the conduction band. However, fine structure in the absorption spectrum for photon energies around the band edge (1.42 eV) began to emerge. For the sample with the highest annealing temperature (600°C), the absorption spectrum began to recover the sharp band edge of their reference GaAs sample.

FWM experiments (carried out by the author as part of MSc work) on as-grown LT-GaAs has uncovered new insights regarding the band edge response [8, 13, 71, 72]. The FWM response of as-grown LT-GaAs is shown in Fig. 1.14(b). A large spectrally narrow FWM response at 1.518 eV was observed and attributed to the response of the exciton. The observation of an exciton response (in contrast to linear absorption experiments in which no exciton response is observed) was attributed to an exciton-carrier coupling mechanism between exciton and free-carrier continuum states. The spectrally-broad response for photon energies above the exciton and at positive time delays corresponded to the photon-echo response of interband continuum transitions similar to observations in GaAs films grown at elevated temperatures. These experiments also revealed a FWM signal for photon energies below 1.46 eV tied to band tail transitions. The band edge response could therefore be treated like an Urbach absorption tail, where an effective band gap energy of 1.46 eV was obtained in as-grown LT-GaAs.

The origin of the strong FWM signal at the exciton, despite its absence in linear absorption, was surprising. In traditional GaAs grown at elevated temperatures the exciton response in four-wave mixing experiments is dominated by many-body effects.

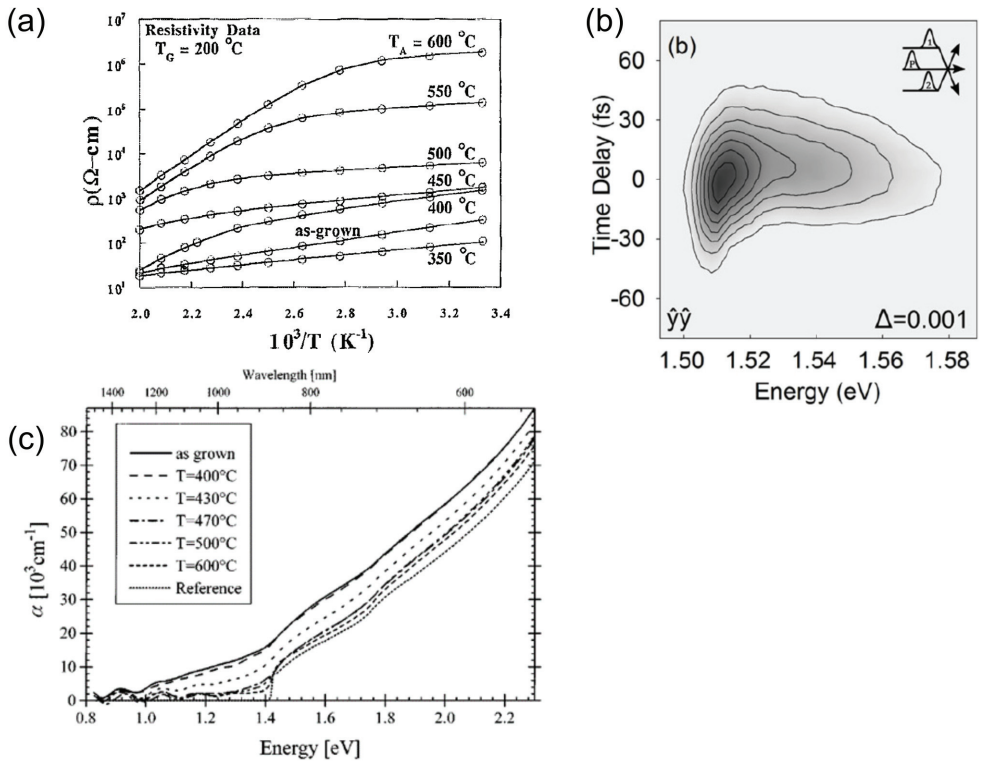

Figure 1.14: (a) Resistivity as a function of sample temperature for a range of LT-GaAs samples annealed at different temperatures. Modified from Look *et al.* [36] (b) The SR-FWM response of as-grown GaAs held at 10K. Modified from Webber *et al.* [8] (c) Linear absorption spectra for LT-GaAs annealed over a range of temperatures. Modified from Streb *et al.* [58]

In particular, if the dephasing rate of the exciton depends on the number density of electron-hole pairs, then the polarization excited at the exciton can diffract from the free carrier density grating via this Coulomb coupling. This produces an extra contribution to the FWM signal at the exciton in addition to the free-polarization decay response. This additional signal is proportional to the slope of the density-dependent dephasing rate. There are also analogous contributions to the exciton signal tied to the excitation density-dependent shift of the exciton transition energy. In traditional GaAs, these signal contributions are very strong causing the exciton to show up more prominently than in linear absorption. This enhancement is shown in Fig. 1.15 for experiments on bulk Ge, where the weak bump in the linear absorption (top) is replaced by a pronounced exciton peak in FWM (bottom). The observation of such a many-body related signal in LT-GaAs offers a possible explanation as to

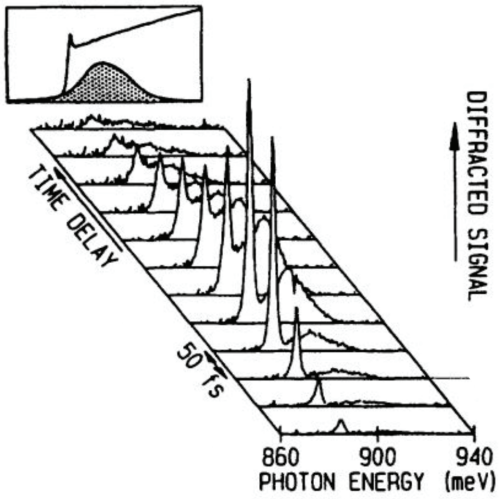

Figure 1.15: Results of SR-FWM experiments on bulk Ge. The laser spectrum used for each tuning condition is shown alongside the linear absorption spectrum in the background. Modified from Rappen *et al.* [80]

why the exciton signal shows up in FWM, while not appearing in linear absorption.

In order to test this assertion FWM experiments were carried out under conditions in which this additional many-body exciton signal is suppressed. Due to the optical selection rules, excitation by collinearly polarized pulses results in the occupation gratings for each spin state (given by n_{σ_+} and n_{σ_-}) to be in phase, as shown pictorally in Fig. 1.16(a). But if the polarization of the two excitation pulses is orthogonal, then no grating in the total carrier occupation exists, as shown in Fig. 1.16(c). This is due to the fact that the optical gratings tied to the two spin-states of the carriers are out of phase by 90°. The Coulomb interactions are spin independent, and the additional signal contribution associated with these effects corresponds to diffraction of the exciton polarization from a grating in the total population (including spin). In Webber *et al.*, polarization-dependent experiments showed that the exciton FWM response vanishes when the two excitation pulses have orthogonal linear polarizations. Since no grating in the total population exists for orthogonal pulse polarizations, this confirmed the fact that the exciton response in LT-GaAs was indeed linked to many-body-related coupling between the exciton and the other excited carriers.

The above experiments on LT-GaAs were limited to as-grown LT-GaAs films.

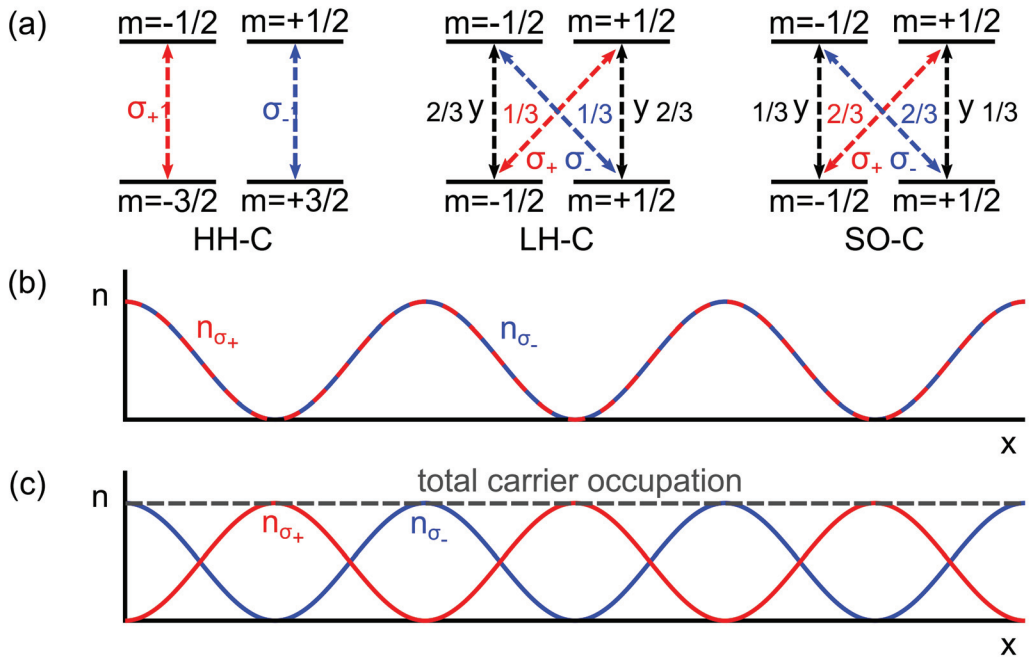

Figure 1.16: (a) Optical selection rules and transition probabilities for GaAs. σ_+ and σ_- correspond to left-circularly polarized and right-circularly polarized light respectively, and y is the linear polarization. The carrier occupation grating as a function of lateral position x created in the sample for (b) collinearly polarized and (c) cross-linearly polarized optical pulses. n_{σ_+} and n_{σ_-} is the carrier occupation excited for σ_+ and σ_- polarized pulses respectively.

Measurements of the FWM response as a function of annealing temperature on LT-GaAs will further enhance our understanding of the near band edge optical response of this material. This is important since annealing of LT-GaAs is required to achieve the performance characteristics suitable for high-speed optoelectronic devices. Such experiments will also improve our understanding of other low-temperature-grown materials. One such example is GaMnAs, an attractive material for spintronics applications where both the electronic properties of the host crystal (GaAs) and the magnetic properties of the metallic dopant (Mn) are exploited to make devices that use the electron property spin, in addition to or instead of the charge property, to store and manipulate information. To dope GaAs with Mn, the lattice must be held at temperatures similar to LT-GaAs during growth. In addition, other examples of low-temperature-grown materials include LT-InGaAs [116] which is of interest for the development of ultrafast photoconductive switches and other optoelectronic devices

operating at 1.55 μm. The application of four-wave mixing spectroscopy to a series of annealed LT-GaAs films provides new insight into the influence of annealing on the optical response of such systems.

1.7.4 FWM Studies of Exciton-Exciton and Exciton-Carrier Scattering in GaAs

The Coulomb interaction between charge carriers plays a major role in the behavior of particles in a condensed matter system, or *many-body system*, and can lead to the formation of new particles that only exist in this many-body state. These so-called quasiparticles are shaped by their environment, and can be found as Cooper pairs in superconductors [117], Wannier excitons in inorganic semiconductors and Frenkel excitons in organic semiconductors [118], as well as polarons [119, 120] in semiconductors. The Coulomb interaction is also responsible for interactions between these newly formed quasiparticles, resulting in a plethora of many-body phenomena which has been a topic of considerable interest in condensed matter physics.

The semiconductor GaAs is an excellent platform to study many-body effects for several reasons. The linear and nonlinear (although to a lesser degree) optical properties are well understood. In addition, refinement in growth techniques have permitted the epitaxial growth of GaAs to extremely high purity so that defect-related phenomena (such as defect-carrier binding or scattering) can be safely excluded in the interpretation of experimental results. Finally, GaAs is the host material for a variety of derived compounds, such as AlGaAs, InGaAs, GaMnAs, and LT-GaAs, and so understanding the underlying physics in GaAs will assist in understanding the physics in these relatively more complicated systems.

The optical properties of GaAs for photon energies near the band edge are dominated by the response of the exciton, an electron-hole pair bound together by the Coulomb interaction. The strength of this binding is very weak ($\approx$ 4 meV) in comparison to organic materials. FWM studies have provided significant insight into the nature of the exciton response in GaAs [4, 8, 13, 68–72] as well as other material systems [74, 78–80]. In these experiments, the laser frequency is tuned below the band gap, such that primarily excitons are excited in the material. Since excitons have discrete electronic states, their optical response should resemble that of a homogeneously

broadened transition (*i.e.* free-polarization decay). In early experiments, a stronger exciton FWM signal for collinear polarized pulses than for cross-linearly polarized pulses [69, 121] contradicted the result expected from a non-interacting model of a homogeneously broadened system. However, more recent experiments revealed that both the coherence time as well as the resonance frequency of a transition depend strongly on the excitation density [4, 5, 82] and that this could explain the observed polarization dependence. The former is called excitation-induced dephasing (EID), and the latter is referred to as excitation-induced shift (EIS). The physical mechanism behind each of these interactions is explained as follows. In the case of EID, for increasing excitation density the probability of phase-breaking collisions between charges increases. This results in an increase in the dephasing rate that depends on the excitation density. EIS can be understood through a process known as dielectric screening. An isolated electron-hole pair can bind via the Coulomb interaction into an energetically-favourable bound state. The difference in energy between this bound state and free state is given by the binding energy of the electron and hole. When this electron-hole pair is now in the presence of other charges, dielectric screening of the Coulomb interaction in this system results in a decrease in the binding energy of the electron-hole pair, which in turn increases the resonant frequency of the optical transition.

If a broadband optical pulse is used to simultaneously excite exciton and free carrier transitions (a condition often satisfied in high speed optoelectronic devices) [6,8,13,71,72,78–80,85,86,88] and many-body interactions are neglected, the FWM response is comprised of two parts: (i) a long-lived free polarization decay corresponding to the exciton, and (ii) a photon echo corresponding to the continuum of electron-hole pair transitions above the band gap states [12]. However, with many-body interactions included the exciton response is modified considerably due to the presence of free-carriers. In previous FWM experiments where the laser was tuned above the band gap so that free-carrier transitions were excited together with the exciton transition, it was observed that the temporal width of the exciton FWM signal versus interpulse delay was significantly shorter than for resonant excitation, occurring over the same timescale as the pulse overlap. As well, despite being resonantly tuned to free-carrier states, the exciton dominated the FWM response [6, 8, 13, 68, 71, 72, 78, 79, 86]. (This

can be seen in Fig. 1.15 for experiments on bulk Ge). This phenomena was explained in terms of an exciton-carrier scattering process: the exciton polarization can diffract from the transient carrier grating associated with free carrier transitions. The associated exciton signal is strong when the two excitation pulses are overlapped in time. For nonzero delays, the grating tied to the free carrier population decays due to the range of optical transitions involved, which causes contributions at different energies to be out of phase. This decay of the free carrier population grating also causes decay of the exciton EID signal. Since exciton scattering with electron-hole pairs excited on the interband continuum transition is the source of the large exciton signal observed in FWM experiments [6] this phenomena is known as the continuum contribution to the exciton FWM response (CC).

Although many-body effects have been studied extensively in bulk GaAs using FWM, an ambiguity still exists as to whether the CC manifests with EID or EIS character. The small magnitude of the excitation-induced shift in conjunction with insufficient spectral resolution makes it difficult to distinguish these two effects using spectrally-resolved FWM. The main challenge with understanding many-body effects using FWM is that the phase of the FWM field is not measured. In contrast, 2DFTS fully characterizes the FWM field, allowing for the ready identification of many-body effects [88, 93, 95, 122]. In Fig. 1.17 is a composite image of two figures from Li *et al.* showing the calculated 2DFTS response for a GaAs multiple quantum well in the presence of different interactions [93]. In Fig. 1.17(a) is the 2DFTS response in the absence of interactions. The two peaks along the diagonal correspond to the response from the HH and LH exciton (with the former at lower energy). The off diagonal peaks correspond to coupling between the two exciton states due to the common ground state (*i.e.* the unexcited semiconductor). Due to the common ground state, absorption at one exciton resonance can lead to emission at the other exciton resonance.

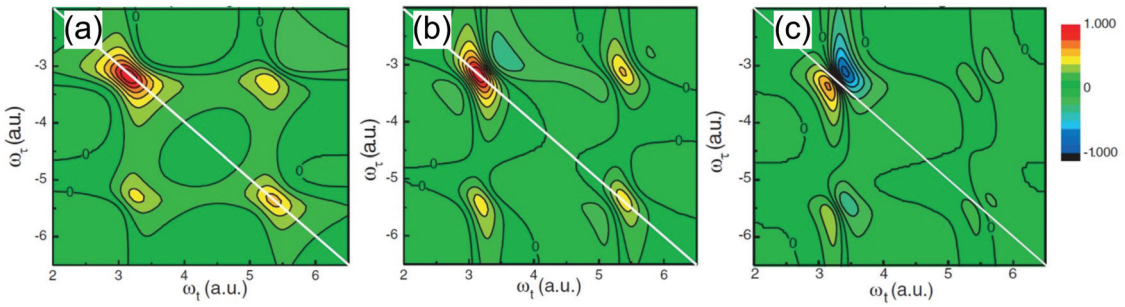

Figure 1.17: Calculated 2DFTS response of GaAs multiple quantum wells (a) in the absence of interactions, (b) EID only, and (c) EIS only. Modified with permission from Li *et al.* [93].

In Fig. 1.17(b) is the calculated 2DFTS response with only EID included. The increase in dephasing rate caused by EID results in a symmetrical narrowing of the exciton line shape. In Fig. 1.17(c) is the 2DFTS response with only EIS included. In contrast to the case of EID, EIS results in an asymmetrical cross-diagonal line shape that goes from positive to negative across the resonance. 2DFTS has yielded a bounty of information about many-body effects in GaAs quantum dots [90] and quantum wells [91–95, 123] but it has not been applied to bulk GaAs. Furthermore, existing 2DFTS experiments have focused on resonant excitation of excitons and coupling between HH and LH excitons. In this thesis work, SR-FWM and 2DFTS were used in conjunction with numerical modeling to investigate EID and EIS in bulk GaAs. In contrast to previous work, the experiments were carried out under conditions of broadband excitation of primarily free electron-hole pairs. This enables EID and EIS tied to the exciton-free carrier interactions to be studied, yielding new insight into these many-body interactions.

1.8 Summary of the Thesis

I have used three different experimental implementations of FWM to study the dynamics of electron-hole pair excitations in GaAs, LT-GaAs, and $CH_3NH_3PbI_3$.

In this thesis work, I designed and built a transient grating experiment using the boxcar geometry (shown in Fig. 1.1) to measure carrier transport in $CH_3NH_3PbI_3$. Measurement of the FWM signal lifetime as a function of grating period permitted

the extraction of the diffusion coefficient and recombination lifetime, which were in turn used to calculate the one-dimensional ambipolar diffusion length of electron-hole pairs. The almost 1 μm diffusion length was comparable to prior all-optical experiments using TAM that directly probe ambipolar carrier diffusion. This work was the first implementation of the transient grating technique on any material within the family of hybrid organic-inorganic solar cell materials. These experiments highlighted the ability of this method to extract the lifetime and diffusion length without the need for charge extraction layers or complicated modeling. Scanning electron microscopy images of the sample revealed a mean grain size of 250 nm, which in comparison to the large diffusion length suggested that grain boundaries do not impact carrier diffusion significantly. The results of this thesis work lay the groundwork for future experiments using this experimental approach on other perovskite materials. This work was published in Applied Physics Letters. The associated manuscript was reproduced in Chapter 4 with permission.

The work in this thesis builds upon recent studies of the FWM response of as-grown LT-GaAs by the author [8, 72]. In this work, LT-GaAs samples that were subjected to post-growth annealing for varying temperatures were studied using the nonlinear technique of spectrally-resolved FWM. Contributions from interband free carriers, excitons, and carriers in the Urbach band tail were observed in the FWM response. In contrast to the earlier studies by the author [8,72], the excitation density in these experiments was lower, resulting in a pronounced dip in the FWM exciton response that disappeared for samples annealed above 500°C. This observation suggested that the dip originates from interference between exciton and band tail states similar to that of a Fano resonance. FWM experiments for orthogonal linear pulse polarization revealed that the dip is associated with polarization interference between the exciton many-body signal and the Urbach band tail states. Spectral slices of the FWM signal at zero interpulse delay revealed a sharpening and blue shift of the FWM signal edge. The Urbach Energy was extracted for each of the annealed samples and was observed to remain constant for samples up to 500°C, and then drop to values similar to that of traditional high-temperature-grown GaAs. This work highlights the utility of FWM as a new probe of disorder in low-temperature-grown systems, complementing existing probes such as Auger spectroscopy, transmission

electron microscopy, and IR spectroscopy. This work will improve our understanding of disordered states in LT-GaAs, as well as other material systems that rely on low-temperature growth such as LT-InGaAs and LT-GaMnAs. This work is in preparation for submission. The associated manuscript is presented in Chapter 5.

In this thesis work, I have also applied FWM and 2DFTS to study exciton-exciton and exciton-carrier interactions in bulk GaAs. Prior to this thesis work, the continuum contribution to the exciton FWM response was taken to manifest solely through an EID mechanism since in FWM studies EID and EIS are impossible to separate. As well, determination of the strength of exciton-exciton and exciton-carrier scattering could only be made indirectly via prepulse experiments [4]. Using 2DFTS, I have measured the individual contributions to the FWM response from the heavy-hole and light-hole excitons, as well as the interband continuum for conditions of broadband excitation above the band gap. These conditions showcase nondegenerate interactions between bound excitons and unbound electron-hole pairs. These experiments also incorporated a separate detection of the real part of the complex four-wave mixing response for the first time in a bulk semiconductor. Using a multilevel model to account for the two exciton states and the interband continuum states, numerical calculations using the optical Bloch equations augmented with EID and EIS interactions were used to simulate the 2DFTS response of GaAs. It was found that exciton-carrier coupling was stronger than exciton-exciton by an order of magnitude. In addition, the manifestation of EID was found to be threefold stronger than EIS in the real part of the FWM spectrum for both exciton-exciton and exciton-carrier interactions. This thesis work has shown that interpretation of the 2DFTS response using conventional techniques (*i.e* based on the expectations for an isolated two-level system) is not sufficient, and that modeling is required. This work will aid in the understanding of future 2DFTS studies of exciton-carrier coupling in other materials. This work was published in Physical Review B. The associated manuscript was reproduced in Chapter 6 with permission.

The structure of the thesis is as follows. Chapter 2 contains a derivation of the results of four-wave mixing experiments based on the optical Bloch equations. Chapter 3 describes the experimental equipment and techniques used in this thesis work. The main findings of this thesis work are presented in Chapters 4 - 6. Chapter 4 presents

a study of charge carrier diffusion in the perovskite material $CH_3NH_3PbI_3$ using the transient grating technique. Chapter 5 presents a study of the coherent FWM response of LT-GaAs for a range of annealing temperatures, examining the influence of As-related defects on the nonlinear response. Chapter 6 presents a study of the leading many-body interactions in an optically-excited semiconductor using FWM and 2DFTS in bulk GaAs in conjunction with theoretical calculations. Finally, Chapter 7 summarizes this thesis work.

Chapter 2

Optical Bloch Equation Analysis of Four-Wave Mixing Experiments

2.1 Chapter Overview

In the most general form of a FWM experiment, three excitation pulses with electric fields $\vec{E_1}$, $\vec{E_2}$, $\vec{E_3}$ and wave vectors $\vec{k_1}$, $\vec{k_2}$, and $\vec{k_3}$ respectively generate a third-order macroscopic polarization in the sample, that emits radiation along the direction $\vec{k_3} + \vec{k_2} - \vec{k_1}$. Measurement of this signal can yield important properties of the material, such as the T_2 time, as well as type and strength of the optical transition in the material. The FWM emission can be calculated using the optical Bloch equations by performing an order expansion in the electric field. Such an analysis will aid in the interpretation of the experimental results in this thesis work. This analysis is presented in Sec. 2.2 for a three-pulse excitation scheme for a homogeneously broadened transition (*e.g.* exciton). Predicted results for time-integrated four-wave mixing (TI-FWM), and spectrally-resolved four-wave mixing (SR-FWM) experiments are discussed in Sec. 2.3 for a homogeneously broadened transition, and in Sec. 2.4 for an inhomogeneously broadened transition. Sec. 2.5 discusses the case when the complex FWM signal is measured using the experimental technique of two-dimensional Fourier transform spectroscopy (2DFTS). Next, an analysis using the optical Bloch equations augmented by additional scattering terms referred to as excitation-induced shift (EIS) and excitation-induced dephasing (EID) is presented in Sec. 2.6. EID and EIS are shown to lead to additional contributions to the FWM signal. Sec. 2.7 discusses the influence of the spin state of excited carriers on the four-wave mixing response. Finally, Sec. 2.8 discusses the case of simultaneous excitation of both exciton and interband continuum states.

2.2 FWM for a Two-Level System without Interactions

In the following treatment of light-matter interactions in a semiconductor, a semiclassical approach will be discussed with the end result being able to explain the results of FWM experiments. Within the density matrix approach, the dynamics for a closed system are given by the Liouville Equation:

$$\frac{\partial \rho}{\partial t} = \frac{1}{i\hbar}\left[H, \rho\right] \tag{2.1}$$

where H is the Hamiltonian describing the system and ρ is the density matrix. For a non-interacting two-level system, ρ is a 2×2 matrix where the diagonal elements correspond to the occupation of the excited or ground state, and the off-diagonal elements correspond to the coherence between the two states. In particular, the macroscopic polarization within the medium excited on the exciton transition (denoted by $P_{ex}(t)$) is related to the coherence $p_{ex}(t)$ by:

$$P_{ex}(t) = N\left(\mu_{ex} p^*_{ex}(t) + \mu^*_{ex} p_{ex}(t)\right) \tag{2.2}$$

where N is the number density of excitons in the ensemble and has units of cm^{-3}. The exciton occupation is also linked to a physically-meaningful term known as the exciton population density $N_{ex}(t)$, which is given as the product of the exciton number density N and the exciton occupation $n_{ex}(t)$.

The Hamiltonian describing a two-level system is given by:

$$H = H_0 + H_{\mathrm{int}} + H_R \tag{2.3}$$

H_0 is the unperturbed Hamiltonian for a two-level system, given by $H_0 = \hbar\omega_0$ (the ground state energy has been taken to equal zero) where ω_0 is the resonant frequency of the two-level system. H_{int} is the light-matter interaction Hamiltonian, which within a semiclassical picture is taken to be $H_{\mathrm{int}} = \vec{\mu}\cdot\vec{E}$, where $\vec{\mu}$ is the transition dipole moment of the two-level system and describes the coupling strength to the light field, and $\vec{E}$ is the electric field. H_R is the Hamiltonian describing relaxation of the system. In this thesis work, the phenomenological relaxation approximation was used to model system relaxation [12]. The rotating wave approximation is implemented by assuming the coherence, $p_{ex}(t)$ is a product of a slowly varying term and a term that oscillates

with the laser frequency ω, *i.e.*

$$p_{ex}(t) \rightarrow p_{ex}(t)e^{-i\omega t}. \tag{2.4}$$

Together with Eqn. 2.1, a series of differential equations can be derived for the occupation and coherence that fully describe the dynamics of a non-interacting two-level system (*e.g.* exciton). These are known as the optical Bloch equations (OBE) and are given as:

$$\begin{aligned} \left\{\tfrac{d}{dt} + \tfrac{1}{T_L}\right\} n_{ex}(t) &= -\left(\tfrac{i}{\hbar}\right)\left(\mu_{ex}E(\vec{R},t)p^*_{ex}(t) - p_{ex}(t)\mu_{ex}E^*(\vec{R},t)\right) \\ \left\{\tfrac{d}{dt} + i\Delta\omega + \tfrac{1}{T_2}\right\} p_{ex}(t) &= \left(\tfrac{i\mu_{ex}}{\hbar}\right) E(\vec{R},t)\left(1 - 2n_{ex}(t)\right). \end{aligned} \tag{2.5}$$

where μ_{ex} is the $\hat{y}$ component of the exciton dipole moment, $E(\vec{R},t)\hat{y}$ is the electric field of the laser pulse at $\vec{R}$, T_2 is the dephasing time of the exciton coherence $p_{ex}(t)$, $\Delta\omega = \omega_0 - \omega$ is the detuning of the exciton resonance frequency ω_0 from the laser center frequency ω, T_L is the population relaxation time, $n_{ex}(t)$ is the probability at time t that the exciton is populated.

In the most general form of a FWM experiment, the total laser field is the sum of three optical pulses propagating in the directions $\vec{k}_1$, $\vec{k}_2$, and $\vec{k}_3$. Taking $\vec{E_1}$, $\vec{E_2}$, and $\vec{E_3}$ to be polarized in $\hat{y}$ direction, the total laser field is given by:

$$\vec{E}(\vec{R},t) = E_1(t-t_1)e^{i\vec{k}_1\cdot\vec{R}}\hat{y} + E_2(t-t_2)e^{i\vec{k}_2\cdot\vec{R}}\hat{y} + E_3(t-t_3)e^{i\vec{k}_3\cdot\vec{R}}\hat{y} \tag{2.6}$$

where t_1, t_2, and t_3 correspond to the times of arrival of pulses 1, 2, and 3. $E_n(t-t_n)$ for $n = 1, 2, 3$ contain the time dependence of the pulse envelope as well as the fast variations tied to the carrier frequency, which is taken to be the same for each pulse. For the following discussion, we will consider the case when pulse 3 arrives after pulse 2 (*e.g.* $t_3 \geq t_2$). As well, since all pulse polarizations and dipole moments are oriented along $\hat{y}$, we will neglect indicating the direction for the rest of this development.

Due to the different propagation directions of the laser pulses, excitation of the system (described by the coherence and occupation $p_{ex}(t)$ and $n_{ex}(t)$ respectively) will depend on $\vec{R}$. This is taken into account by considering all of the spatial terms that contribute to the FWM process:

$$\begin{aligned} p_{ex}(t) = \;& p^{(1)}_{ex,1}(t)e^{i\vec{k}_1\cdot\vec{R}} + p^{(1)}_{ex,2}(t)e^{i\vec{k}_2\cdot\vec{R}} + p^{(1)}_{ex,3}(t)e^{i\vec{k}_3\cdot\vec{R}} \\ & + p^{(3)}_{ex,32-1}(t)e^{i(\vec{k}_3+\vec{k}_2-\vec{k}_1)\cdot\vec{R}} + p^{(3)}_{ex,1-2-3}(t)e^{i(\vec{k}_1-\vec{k}_2-\vec{k}_3)\cdot\vec{R}} \\ n_{ex}(t) = \;& n^{(0)}_{ex}(t) + n^{(2)}_{ex,1-2}(t)e^{i(\vec{k}_1-\vec{k}_2)\cdot R} + n^{(2)}_{ex,2-1}(t)e^{i(\vec{k}_2-\vec{k}_1)\cdot R} \end{aligned} \tag{2.7}$$

In the above, only terms up to third order in the light-matter interaction have been retained. The superscripts on each term indicate the order in the light-matter interaction. The exponential factors indicate the spatial dependence of the associated coherence or occupation term. For example, the term $p^{(1)}_{ex,1}(t)e^{i\vec{k}_1\cdot\vec{R}}$ corresponds to the first-order coherence generated by pulse 1 and is directed along $\vec{k_1}$(the number 1 in the subscript of $p^{(1)}_{ex,1}(t)$ also indicates the spatial direction of the coherence). From Eqn. 2.2, we see that the coherence excited along a particular direction functions as a source of electromagnetic radiation governed by Maxwell's equations. For example, the first-order polarization $P^{(1)}_{ex,1}(t)$ emits light in the same direction as the excitation pulse $\vec{k_1}$. Of particular interest to this thesis work is the FWM signal, which is emitted by the polarization in the $\vec{k}_3 + \vec{k_2} - \vec{k}_1$ direction and is determined by the coherence $p^{(3)}_{ex,32-1}$(the number $32-1$ in the subscript indicates that the coherence is directed along $\vec{k}_3 + \vec{k_2} - \vec{k}_1$).

In a FWM experiment, isolation of the spatial component $\vec{k_3} + \vec{k_2} - \vec{k_1}$ is achieved through selective positioning of the collection optics. The FWM signal can be calculated by inserting the spatial expansion in Eqn. 2.7 into the optical Bloch equations in Eqn. 2.5, and deriving a set of optical Bloch equations for each spatial component. This procedure results in a set of four differential equations, with the highest-order component $p^{(3)}_{ex,32-1}$ is given by:

$$\left\{\frac{d}{dt} + i\Delta\omega + \frac{1}{T_2}\right\} p^{(3)}_{ex,32-1}(t) = 2\left(\frac{i\mu_{ex}}{\hbar}\right) E_3(t-t_3) n^{(2)}_{ex,2-1}(t) \tag{2.8}$$

$p^{(3)}_{ex,32-1}(t)$ is driven by the second order occupation $n^{(2)}_{ex,2-1}$ and the third pulse (E_3). The driving term on the right hand side of Eqn. 2.8 stems from diffraction of E_3 from a grating in the exciton occupation, $n^{(2)}_{ex,2-1}(t)$. The equation of motion for $n^{(2)}_{ex,2-1}(t)$ is shown in Eqn. 2.8:

$$\left\{\frac{d}{dt} + \frac{1}{T_L}\right\} n^{(2)}_{ex,2-1}(t) = \left(\frac{i\mu_{ex}}{\hbar}\right)\left(E_2(t-t_2)p^{(1)*}_{ex,1}(t) + E^*_1(t-t_1)p^{(1)}_{ex,2}(t)\right) \tag{2.9}$$

Eqn. 2.9 shows that $n^{(2)}_{ex,2-1}(t)$ is driven by two coupling terms. The first term on the right hand side corresponds to interference of pulse E_2 with the linear polarization $p^{(1)}_{ex,1}(t)$ established by pulse E_1. The second term analagously stems from interference of pulse E_1 with the linear polarization $p^{(1)}_{ex,2}(t)$ established by pulse E_2. Physically, the electric field E_2 does work on the polarization $P^{(1)}_{ex,1}$, transferring energy to the system

and exciting a population of electron-hole pairs. The differential equation describing the linear polarization generated by each pulse (*i.e.* $p^{(1)}_{ex,n}(t)$, where $n = 1, 2$ indicates the pulse that generated that polarization) is given by:

$$\left\{\frac{d}{dt} + i\Delta\omega + \frac{1}{T_2}\right\} p^{(1)}_{ex,n}(t) = \left(\frac{i\mu_{ex}}{\hbar}\right) E_n(t - t_n) \quad n = 1, 2 \tag{2.10}$$

The coherence $p^{(3)}_{ex,32-1}(t)$, and thus the FWM signal, stems from a third-order light matter interaction which may be interpreted physically as diffraction of the third optical field E_3 from a grating in the excited occupation via the influence of the grating on the linear response (*i.e.* the index of refraction and the absorption).

In the limit where the pulse envelope is much shorter than the timescale of the relaxation dynamics, analytical solutions to the above set of equations can be found if the pulse envelopes of E_1, E_2, and E_3 are taken to be described by Dirac Delta functions. It should be noted that this approximation is not valid for many semiconductors due to their short dephasing times, which are comparable to the pulse duration. Despite this, the following development is useful for building intuition into the origin of the FWM response. In this case, we can write the electric field of each pulse as follows:

$$E_n(t - t_n) = \varepsilon_n \delta(t - t_n) e^{i\omega t_n} \quad n = 1, 2, 3 \tag{2.11}$$

The exponential factors in Eqn. 2.11 reflect the fact that each pulse is in phase at the time of arrival. In addition, we will make the following time variable substitutions:

$$\tau = t_2 - t_1 \quad T = t_3 - t_2 \quad t \to t - t_3. \tag{2.12}$$

The solution for $p^{(3)}_{ex,32-1}(t)$ is then given by:

$$\begin{aligned} p^{(3)}_{ex,32-1}(t) =& \xi e^{-(\frac{1}{T_2} + i\Delta\omega)t} \\ & \cdot \left[\begin{array}{l} \Theta(\tau)\Theta(T) e^{-(\frac{1}{T_2} - i\omega_0)\tau} e^{-\frac{T}{T_L}} \\ +\Theta(-\tau)\Theta(T + \tau) e^{(\frac{1}{T_2} - i\omega_0)\tau} e^{-\frac{T+\tau}{T_L}} \end{array} \right] \end{aligned} \tag{2.13}$$

where $\xi = -\frac{i\mu^3_{ex}}{\hbar^3}\varepsilon_3\varepsilon_2\varepsilon^*_1$. Eqn. 2.13 shows that there are two contributions to the coherence. For positive delay τ, the coherence $p^{(3)}_{ex,32-1}$ will only form following the arrival of pulse 3 (given by delay T). However, for negative delay τ a coherence $p^{(3)}_{ex,32-1}$ only exists when pulse 3 arrives after pulse 1. In both cases, *no coherence* is predicted for negative delay T within a non-interacting picture.

Depending on the experimental arrangement, $p^{(3)}_{32-1}(t)$ is measured either as a function of time (TR-FWM) or as a function of interpulse delay (TI-FWM). The TR-FWM signal may be obtained from Eqn. 2.8 using:

$$\mathrm{S_{TR}}(t) \propto |P_{ex}(t,\tau,T)|^2 \tag{2.14}$$

while the TI-FWM signal is obtained from:

$$\mathrm{S_{TI}}(\tau) = \int_{-\infty}^{\infty} \mathrm{d}t\, |P_{ex}(t,\tau,T)|^2 \tag{2.15}$$

When the spectral content of the FWM emission is measured, the experiment is referred to as SR-FWM. The SR-FWM signal is given as:

$$\mathrm{S_{SR}}\left(\omega_t,\tau,T\right) = \left| \int_{-\infty}^{\infty} \mathrm{d}t P_{ex}(t,\tau,T) e^{i\omega_t t} \right|^2 \tag{2.16}$$

where ω_t is the emission frequency, and is the Fourier component of the time variable t. In some of the experiments in this thesis work, two-pulse SR-FWM experiments were conducted. In contrast to the three-pulse case, only two pulses E_1 and E_2 are used to excite the material. Similar to three pulse FWM, the electric fields E_1 and E_2 excite a carrier grating within the sample. However, instead of a third optical pule diffracting off this grating, a portion of E_2 is diffracted, resulting in a FWM emission along the direction $2\vec{k_2} - \vec{k_1}$. The macroscopic polarization P_{ex} for this excitation geometry is simply found by taking the expression for the third order coherence in Eqn. 2.13 and having E_2 serve in the place of E_3 (*i.e.* $T = 0$, $\varepsilon_3 = \varepsilon_2$, and $\vec{k_3} = \vec{k_2}$).

2.3 Free Polarization Decay from a Homogeneously-Broadened Two-Level System

From Eqn. 2.13 and 2.14 for the two-level system case, we get

$$\mathrm{S_{TR}}(t) = N^2 |\mu_{ex}|^2 |\xi|^2 e^{-\frac{2t}{T_2}} \Theta(t) \left[\Theta(\tau)\Theta(T) e^{-\frac{2\tau}{T_2}} e^{-\frac{2T}{T_L}} + \Theta(-\tau)\Theta(T+\tau) e^{\frac{2\tau}{T_2}} e^{-\frac{2(T+\tau)}{T_L}} \right] \tag{2.17}$$

Using the result from Eqn. 2.17 in Eqn. 2.15 gives:

$$\mathrm{S_{TI}}(\tau) = 2N^2 |\mu_{ex}|^2 |\xi|^2 \left[\Theta(\tau)\Theta(T) e^{-\frac{2\tau}{T_2}} e^{-\frac{2T}{T_L}} + \Theta(-\tau)\Theta(T+\tau) e^{\frac{2\tau}{T_2}} e^{-\frac{2(T+\tau)}{T_L}} \right] \tag{2.18}$$

Eqn. 2.18 shows that no FWM signal is expected for negative delay T since diffraction of E_3 from the grating formed by E_1 and E_2 will not occur unless E_3 arrives after the grating is formed. For positive delay T, Eqn. 2.18 indicates that the FWM signal peaks at arrival of E_3 and exponentially decays as a function of delay τ at a rate $\frac{2}{T_2}$. This signal is commonly referred to as free-polarization decay, and describes the response of a two-level system in the absence of interactions.

Using Eqn. 2.13 and Eqn. 2.2, the SR-FWM emission for a homogeneously broadened transition is then given by:

$$\mathrm{S}_{\mathrm{SR,\ homo}}\left(\omega_t, \tau\right) = \left|\xi\right|^2 \Theta(\tau) e^{-\frac{2}{T_2}\tau} \frac{1}{\left(\frac{1}{T_2}\right)^2 + \left(\omega_0 - \omega_t\right)^2} \tag{2.19}$$

The SR-FWM signal for a homogeneously broadened transition has a Lorentzian spectral profile, and exhibits the same exponential decay observed in the time-integrated case and is shown in Fig. 2.1(a). Hence, SR-FWM is simply TI-FWM measured for each photon energy.

2.4 Photon Echo from an Inhomogeneously Broadened System

So far in this treatment of light-matter interactions, we have only considered the case of a homogeneously-broadened transition that is appropriate for discrete transitions in a semiconductor. However, if we would like to understand the response of a set of closely spaced transitions with a range of resonance frequencies (shown in Fig. 1.8(c)), such as for interband free-carrier transitions above the band gap, we need to examine the case of an inhomogeneously broadened transition. In this case, the net macroscopic polarization is a sum of the individual coherences (with associated transition energy and electron wave vector given by Eqn. 1.4) associated with each of these transitions. The TR-FWM signal is obtained by:

$$\mathrm{S}_{\mathrm{TR}}(t) \propto \left| \sum_k P_k^{(3)}(t, \tau, T) \right|^2 \tag{2.20}$$

where $P_k^{(3)}(t, \tau, T)$ is the macroscopic polarization associated with each two-level system with wave vector k. In contrast to a homogeneously-broadened transition that exhibits instantaneous decay after arrival of $\vec{E_3}$, Eqn. 2.20 yields a TR-FWM signal that reaches a maximum a time τ after arrival of E_3. (This is shown earlier in

Fig. 1.8(d)). This delayed response is commonly referred to as a photon-echo and has been observed for interband transitions above the band gap [13, 71]. The associated time integrated response can be found using Eqn. 2.15 and is given from:

$$\mathrm{S_{TI}}(\tau) \propto e^{-\frac{4\tau}{T_2}} e^{-\frac{2T}{T_L}} \left(1 + \mathrm{erf}\left(\frac{\delta\omega\tau}{\sqrt{\pi}}\right)\right) \tag{2.21}$$

where erf is the error function and $\delta\omega$ is the inhomogeneous bandwidth of excited states. Similar to Eqn. 2.18 for a homogeneously-broadened transition, Eqn. 2.21 shows that the TI-FWM signal for a continuum of transitions will also exhibit exponential decay for increasing pulse delay τ. However, the rate of decay is twice as fast for a continuum of transitions when compared to a discrete transition. This result in Eqn. 2.21 also indicates that the response of an inhomogeneously broadened system versus delay τ for a two pulse experiment in which T= 0 is peaked at positive delay by an amount that is determined by both T_2 and $\delta\omega$.

Using Eqn. 2.16 and the macroscopic polarization excited from an inhomogeneously-broadened transition, the SR-FWM signal is given by:

$$\mathrm{S_{SR,\ inhomo},m}\left(\omega_t, \tau, T\right) \propto \Theta(\tau)\Theta(T) e^{-\frac{2}{T_L}T} e^{-\frac{4}{T_2}\tau} e^{-\frac{(\omega_0-\omega_t)^2}{\delta\omega^2}} \tag{2.22}$$

In contrast to the homogeneously-broadened case, the SR-FWM signal for an inhomogeneously-broadened transition has a Gaussian spectral profile of width determined by the inhomogeneous broadening as shown in Fig. 2.1(b). The amplitude of the SR-FWM signal decays with the same rate $\frac{4}{T_2}$ as observed in TI-FWM.

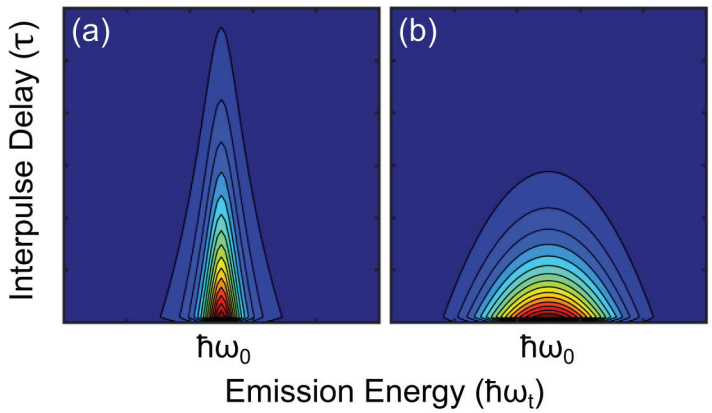

Figure 2.1: The SR-FWM signal as a function of interpulse delay τ and photon energy for (a) a homogeneously-broadened transition and (b) for an inhomogeneously-broadened transition excited by delta-shaped pulses.

2.5 Phase-Dependent Detection of the Complex FWM Response

We can extend the analytical result found for the FWM signal found in Sec. 2.2 to the case when the phase of the coherent FWM signal is measured, such as the case in a 2DFTS experiment. As was discussed in Sec. 1.6.2, the coherent polarization generated in the sample is measured using phase sensitive techniques (which will be discussed in further detail in Chapter 3).

Pulse ordering in a 2DFTS experiment is important as it ultimately determines what physical processes contribute to the FWM signal. In this development, we will restrict ourselves to the rephasing sequence ($T > \tau > 0$), the pulse arrangement used in this thesis work. In this case, the coherence found in Eqn. 2.28 simplifies to the following form:

$$p^{(3)}_{ex,32-1}(t) = \xi\Theta(\tau)\Theta(T)e^{-(\frac{1}{T_2}+i\Delta\omega)t}e^{-(\frac{1}{T_2}-i\omega_0)\tau}e^{-\frac{T}{T_L}} \tag{2.23}$$

In a 2DFTS experiment, the data is presented as a function of emission photon energy and absorption photon energy. The emission energy $\hbar\omega_t$ is tied to the real time emission of the FWM signal, and experimentally is measured using a monochromator. The absorption energy $\hbar\omega_\tau$ is obtained by measuring the phase of the FWM signal as a function of delay τ, and performing a Fourier transform at each emission energy. Analytically, the 2DFTS signal is found by performing a two-dimensional Fourier transform of the macroscopic polarization associated with the exciton coherence. The 2DTFS response for a homogeneously broadened transition in the absence of interaction (*i.e.* $\gamma_{\mathrm{EID}} = \gamma_{\mathrm{EIS}} = 0$) is given by [96]:

$$\mathrm{S}_{2\mathrm{D}}(\omega_t, \omega_\tau, T) \propto \left(\frac{1}{\frac{1}{T_2} + i(\omega_0 + \omega_\tau)}\right)\left(\frac{1}{\frac{1}{T_2} + i(\omega_0 - \omega_t)}\right) \tag{2.24}$$

The 2DFTS signal for a homogeneously broadened transition is a symmetrical Lorentzian function. An important consequence of Eqn. 2.24 is that the 2DFTS signal is peaked for a *negative* absorption energy $-\hbar\omega_\tau$, and stems from the electric field of E_1 being conjugated from that of E_2, resulting in a negative phase term. For inhomogeneously broadened transitions of the same form as the above, the 2DFTS signal can be obtained from:

$$\mathrm{S}_{2\mathrm{D}}(\omega_t, \omega_\tau, T) \propto \int_{-\infty}^{\infty} d\tau e^{i\omega_\tau\tau} \int_{-\infty}^{\infty} dt e^{i\omega_t t} P_{k,321*}(t, \tau, T)(i\omega_t) \tag{2.25}$$

2.6 Effect of Many-Body Interactions on the FWM Signal

As discussed in Sec. 1.7.4, excitation-induced dephasing (EID) and excitation-induced shift (EIS) are Coulomb-mediated processes. Numerous experiments [73, 74, 78–80] and theoretical treatments [6, 88] have shown that excitation-induced interactions are the leading many-body contribution to the FWM response in semiconductors. Although the optical Bloch equations cannot account for these effects, they can be suitably modified to reflect these interactions via the incorporation of a density-dependent dephasing rate $\frac{1}{T_2}$ and resonance frequency ω for excitons:

$$\tfrac{1}{T_2} = \tfrac{1}{T_2^0} + \gamma_{\mathrm{EID}} N_{ex} \quad \omega = \omega_0 + \gamma_{\mathrm{EIS}} N_{ex} \tag{2.26}$$

T_2^0 and ω_0 are the dephasing time and resonance frequency of excitons in the absence of an excited population. For example, experiments and complementary calculations on ZnSe quantum wells by Shacklette *et al.* revealed an EIS shift of 1.78 meV of the exciton resonance energy for comparable excitation densities used in this thesis work [88]. The coefficients γ_{EID} and γ_{EIS} quantify the strength of exciton-exciton interactions. The phenomenological approach to excitation-induced interactions contained in Eqn. 2.26 has been shown to account for many of reported trends in experimental observations [4, 88, 124]. To understand the influence of excitation-induced interactions on the FWM signal, we will look at the optical Bloch equation for $p^{(3)}_{ex,32-1}(t)$ with the inclusion of Eqn. 2.26. After performing an order expansion similar to that discussed in the previous section, the differential equation for $p^{(3)}_{ex,32-1}(t)$ is given by:

$$\begin{aligned}
&\left\{ \frac{d}{dt} + \frac{1}{T_2} + \gamma_{\mathrm{EID}} N_{ex}^{(0)} + i\Delta\omega + \gamma_{\mathrm{EIS}} N_{ex}^{(0)}(t) \right\} p^{(3)}_{ex,32-1}(t) \\
&= \left(\frac{i\mu_{ex}}{\hbar} \right) n^{(2)}_{ex,2-1}(t) E_3(t - t_3) - \left(\gamma_{\mathrm{EID}} + i\gamma_{\mathrm{EIS}} \right) p^{(1)}_{ex,3}(t) N^{(2)}_{ex,2-1}(t)
\end{aligned} \tag{2.27}$$

where $N_{ex}^{(0)}$ is the background density of excitons. In contrast to the non-interacting case, there are two driving terms on the right hand side of Eqn. 2.27. The first term appears in the absence of interactions (see Eqn. 2.7) and represents diffraction of E_3 from the occupation grating $n^{(2)}_{ex,2-1}$. The second term is an additional contribution to the FWM signal due to interactions. This additional signal stems from the diffraction

of the polarization $p^{(1)}_{ex,3}(t)$ generated by pulse E_3 (rather than pulse E_3 itself) from the grating in the total exciton density $N^{(2)}_{ex,2-1}(t) = N_{ex} n^{(2)}_{ex,2-1}(t)$. Using the change in temporal variables from Eqn. 2.12, the solution for δ-function pulses for $p^{(3)}_{ex,32-1}(t)$ is given by:

$$
\begin{aligned}
p^{(3)}_{ex,32-1}(t) = \xi e^{-(\frac{1}{T_2^0}+\gamma_{\mathrm{EID}}N^{(0)}_{ex}+i\left(\Delta\omega+\gamma_{\mathrm{EIS}}N^{(0)}_{ex}\right))t} & \\
\cdot \left[\begin{array}{l}
\Theta(\tau)\Theta(T) e^{-\left(\frac{1}{T_2^0}+\gamma_{\mathrm{EID}}N^{(0)}_{ex}-i(\omega_0+\gamma_{\mathrm{EIS}}N^{(0)}_{ex})\right)\tau} e^{-\frac{T}{T_L}} \\
+\Theta(-\tau)\Theta(T+\tau) e^{\left(\frac{1}{T_2^0}+\gamma_{\mathrm{EID}}N^{(0)}_{ex}+i(\omega_0+\gamma_{\mathrm{EIS}}N^{(0)}_{ex})\right)\tau} e^{-\frac{T+\tau}{T_L}}
\end{array} \right] & \\
+ T_L\left(\gamma_{\mathrm{EID}} + i\gamma_{\mathrm{EIS}}\right)\xi e^{-(\frac{1}{T_2^0}+\gamma_{\mathrm{EID}}N^{(0)}_{ex}+i\left(\Delta\omega+\gamma_{\mathrm{EIS}}N^{(0)}_{ex}\right))t} & \\
\cdot \left[\begin{array}{l}
\Theta(\tau)\Theta(T) e^{-\left(\frac{1}{T_2^0}+\gamma_{\mathrm{EID}}N^{(0)}_{ex}-i(\omega_0+\gamma_{\mathrm{EIS}}N^{(0)}_{ex})\right)\tau} \left(e^{-\frac{T}{T_L}} - e^{-\frac{t+T}{T_L}}\right) \\
+\Theta(-\tau)\Theta(T+\tau) e^{\left(\frac{1}{T_2^0}+\gamma_{\mathrm{EID}}N^{(0)}_{ex}+i(\omega_0+\gamma_{\mathrm{EIS}}N^{(0)}_{ex})\right)\tau} \left(e^{-\frac{T+\tau}{T_L}} - e^{-\frac{t+T+\tau}{T_L}}\right) \\
+\Theta(t+T)\Theta(\tau)\Theta(-T) e^{-\left(\frac{1}{T_2^0}+\gamma_{\mathrm{EID}}N^{(0)}_{ex}-i(\omega_0+\gamma_{\mathrm{EIS}}N^{(0)}_{ex})\right)\tau} \left(1 - e^{-\frac{t+T}{T_L}}\right) \\
+\Theta(t+T+\tau)\Theta(-\tau)\Theta(-T-\tau) e^{\left(\frac{1}{T_2^0}+\gamma_{\mathrm{EID}}N^{(0)}_{ex}+i(\omega_0+\gamma_{\mathrm{EIS}}N^{(0)}_{ex})\right)\tau} \left(1 - e^{-\frac{t+T+\tau}{T_L}}\right)
\end{array} \right]
\end{aligned}
\tag{2.28}
$$

The top term in Eqn. 2.28 represents the non-interacting solution found earlier in Eqn. 2.13 with the addition of density-dependent dephasing and resonance terms that depend on the background of excited excitons. The bottom term in Eqn. 2.28 corresponds to excitation-induced interactions and leads to the following phenomena i) coherence for negative T pulse delay and ii) slow rise of the magnitude of coherence in time.

The above development corresponds to the case of a homogeneously broadened transition. For an inhomogeneously broadened transition, the above result must be modified to contain the grating in the total population, summed over the range of frequencies involved in the optical transition. Additionally, the resulting third order polarization must be summed over frequency. It has been shown that the source terms tied to EID and EIS suffer from cancellation effects which dramatically suppress the resulting signal. As a result, EID and EIS signal contributions manifest strongly for a homogeneous transition, such as an exciton in a semiconductor.

2.7 Influence of the Spin State of the Excited Carriers

To properly account for the spin-state of the charge carriers in the above development, separate OBE's for each spin-state must be solved for the polarizations and occupations on each spin transition separately. Recall the optical selection rules for GaAs shown in Fig. 1.16. There are two allowed optical transitions between the HH valence band to conduction band, each dependent on the polarization of the laser pulse. For linearly polarized laser pulses, both of these transitions are excited leading to the creation of two population gratings, one for each spin state. For instance the grating in the total exciton population $N_{ex}^{(2)}$ in the OBE must include excitons from both spin states, *i.e.*:

$$N_{ex}^{(2)} = \sum_{s} N_s n_{ex,s}^{(2)} \tag{2.29}$$

where $n_{ex,s}^{(2)}$ is the occupation grating and N_s is the population density for each exciton spin state s. For collinear polarized pulses (*i.e.* $\vec{E_1} = E_1\hat{y}$, $\vec{E_2} = E_2\hat{y}$, $\vec{E_3} = E_3\hat{y}$) the population N_s and grating $n_{ex,s}^{(2)}$ are in phase for both spin states (s $= \sigma_1, \sigma_2$). In this case, the above OBE development that neglected spin is equivalent to the spin resolved case in describing excitation-induced effects. However, for cross-linearly polarized pulses (*i.e.* $\vec{E_1} = E_1\hat{y}$, $\vec{E_2} = E_2\hat{x}$, $\vec{E_3} = E_3\hat{x}$) the two exciton population gratings (corresponding to each spin state) are out of phase, *i.e.*

$$N_{ex}^{(2)} = N_{\sigma_1} n_{ex,\sigma_1}^{(2)} + N_{\sigma_2} n_{ex,\sigma_2}^{(2)} = 0 \tag{2.30}$$

For this reason, there is no EID or EIS contribution to the FWM signal for cross-linearly polarized pulses. However, the free-polarization decay expected from a non-interacting model is still present in the FWM signal as this stems from the diffraction of $\vec{E_3}$ from each of the exciton population gratings.

2.8 Simultaneous Excitation of Exciton and Continuum Transitions

So far in this chapter, we have only described the system dynamics of either a homogeneous or inhomogeneous optical transition. This is appropriate when the laser tuning and bandwidth are resonant with only one species and there is no strong coupling mechanism between species. However, a more complex situation unfolds for the case when wide-bandwidth optical pulses are used to simultaneously excite both exciton

and interband free-carrier transitions. In this case, we must apply the optical Bloch equations to each two-level system separately, then add up each of their respective polarization contributions to determine the overall FWM signal. This more involved treatment is further complicated by coupling between each of these two-level systems. The Coulomb interactions between excitons are strong for coupling between bound excitons, unbound excitons (*i.e.* electron-hole pairs excited above the band gap), or for the coupling between bound and unbound excitons. The energy-independent nature of this coupling process thus implies that excitation-induced shift and excitation-induced dephasing couple the polarization generated by interband continuum states to the polarization of exciton states and vice versa. The additional many-body signal at the exciton resulting from coupling to free-carrier transitions at higher energies is referred to as the continuum-contribution. This contribution results in an enhancement of the exciton FWM signal from that predicted from a non-interacting model due to diffraction of the exciton polarization from the total population grating on the interband continuum.

To gain some understanding of this process, we will consider the case of a two-pulse self-diffracted FWM experiment and follow the analytical treatment of Allan *et al.* [73] with the addition of excitation-induced shift. We consider the case of optical excitation above the band gap, such that the majority of the laser bandwidth energetically covers interband continuum states and only the low-energy tail is resonant with the exciton states. In this case, the density of excited free electron-hole pairs (n_k) in the system will be much larger than the density of excitons (n_{ex}), *i.e.*

$$N_k(t) \propto \sum_k n_k(t) \gg n_{ex}(t). \tag{2.31}$$

In this case, only the equations for the exciton coherence p_{ex} need to be solved as the exciton occupation, n_{ex} can be taken to be zero for all time. As well, since excitation-induced processes (EID, EIS) do not contribute significantly to the FWM response of an inhomogenously broadened transition, these interactions only need to be included in the optical Bloch equations for the exciton:

$$\left\{ \frac{d}{dt} + \frac{1}{T_{2,x}^0} + \gamma_{\mathrm{EID}} N + i\left(\omega_0 + \gamma_{\mathrm{EIS}} N\right) \right\} p_{ex} = \frac{i\mu_{ex}}{\hbar} E(t) \tag{2.32}$$

where $N = \sum_k N_k$ is the total population of excited continuum carriers only (since $N_{ex} \approx 0$). Physically, this excitation-induced signal stems from diffraction of the

first-order exciton polarization $p_{ex}^{(1)}$ generated by pulse E_3 from the total population grating in the continuum states $N^{(2)}$. The population grating only exists when the delay τ between pulses $\vec{E_1}$ and $\vec{E_2}$ is zero due to destructive interference since the grating at different k transitions are out of phase for $\tau \neq 0$.

To see that this is true, we can consider the solution to the optical Bloch equations for the population grating for a free carrier transition at a single k point:

$$n_k^{(2)}(t) = \mu_k^2 \varepsilon_1 \varepsilon_2 e^{-(\hbar\omega_x + \hbar\omega_k)\tau} e^{-\frac{1}{T_{2,k}}|\tau|} \left(\Theta(\tau)\Theta(t-\tau) + \Theta(-\tau)\Theta(t)\right) \tag{2.33}$$

where μ_k and $T_{2,k}$ are the dipole moment and dephasing time for each k state. Inspection of Eqn. 2.33 reveals that the population grating at a particular $\vec{k}$ persists for delays τ on a timescale set by $T_{2,k}$. Because the values for μ_k and $T_{2,k}$ do not vary significantly for optical transitions near the band gap, summation of Eqn. 2.33 over $\vec{k}$ results in a total population grating in the continuum states that exists only for $\tau = 0$, *i.e.*:

$$N^{(2)}(t) = \sum_{\vec{k}} n_k^{(2)} = \mu_k^2 \varepsilon_1 \varepsilon_2 \Theta(t-\tau)\delta(\tau) \tag{2.34}$$

where $\delta(\tau)$ corresponds to the delta function. In this case, third-order coherence at the exciton is given by:

$$p_{ex}^{(3)}(t) \propto \frac{\mu_{ex}\varepsilon_2}{\hbar} N^{(2)}(t) e^{-\left(\frac{1}{T_{2,x}^0} + \gamma_{\mathrm{EID}} N^{(0)} + i\left(\omega_0 + \gamma_{\mathrm{EIS}} N^{(0)}\right)t\right)} \Theta(t) \tag{2.35}$$

Unlike the free-polarization contribution which decays with delay at a timescale set by the coherence lifetime, Eqn. 2.35 reveals that the excitation-induced contribution to the exciton FWM signal only occurs when $\tau = 0$. For pulses with finite duration this excitation-induced contribution therefore *persists only for delays within the region of pulse overlap.*

The above development indicates that the dependence of the total FWM signal on the interpulse delay τ is modified by the inclusion of EID and EIS. The spectral content of the FWM emission is also changed in the presence of excitation-induced interactions. As seen in Sec. 2.3, the response of an exciton in a non-interacting model is that of a Lorentzian characterized by a width determined from the exciton dephasing time. In contrast, a Fourier transform of Eqn. 2.35 is a squared Lorentzian with a

width determined by both the excitation-induced dephasing rate and the excitation-induced shift in the presence of continuum carriers.

Summarizing the above development, the total FWM response is comprised of three components: i) Free-polarization decay at the exciton resonance ii) excitation-induced contributions to the exciton response that spectrally-sharpen the response as well as enhance the signal within the region of pulse overlap, and iii) a broadband photon-echo like response with a spectral width determined by the bandwidth of the excitation pulses. This predicted response has been observed in both GaAs [8, 13, 71, 72] and Ge [78–80] using SR-FWM techniques to separately measure the response of simultaneously-excited exciton and continuum states.

Chapter 3

Apparatus and Experimental Techniques

3.1 Overview

In this thesis work, the experimental technique of FWM was used to investigate charge carrier dynamics in GaAs, LT-GaAs, and $CH_3NH_3PbI_3$. The samples investigated in this work, including their production and preparation for optical experiments are described in Sec. 3.2. Sec. 3.3 describes the cryogenic cooling methods used in this work. Sec. 3.4 describes the methods used to measure and characterize femtosecond optical pulses. Sec. 3.5 describes the two-pulse self-diffracted FWM experiment used to understand the effects of annealing in LT-GaAs. The 2DFTS technique used to disentangle contributions from many-body effects to the coherent response of GaAs is described in Sec. 3.6. The transient grating experiment used to measure carrier transport in $CH_3NH_3PbI_3$ is discussed in Sec. 3.7.

3.2 Samples

3.2.1 GaAs and LT-GaAs

This thesis work involved the study of two GaAs thin film samples, one that was grown at 600°C and another grown at 250°C. Six segments of the LT-GaAs wafer were subsequently subdivided and subjected to annealing under different conditions. The samples were grown using molecular beam epitaxy by Jacek Furdyna's group at the University of Notre Dame. Beginning with a GaAs (001) substrate, a 100 nm buffer layer of GaAs was deposited, followed by 175 nm of $Al_{0.3}Ga_{0.7}As$, and then 800 nm of GaAs, which represents the thin film that four-wave experiments were carried out on. The four annealed samples were placed in an oven for 60 seconds for a given temperature under vacuum inside the growth chamber. The temperature used for annealing each of the LT-GaAs samples is shown in Table. 3.1.

Table 3.1: A table of the five LT-GaAs samples studied in this work and their corresponding annealing temperatures.

Sample	Annealing Temperature (°C)
LT-GaAs	As-Grown
LT-GaAs	400
LT-GaAs	500
LT-GaAs	550
LT-GaAs	600

To permit experiments in the transmission geometry, the samples were glued sample side down onto a 500 μm thick sapphire window using optical adhesive (Norland 61) that was transparent ($\geq$ 95% transmission) for the wavelengths used in this work. Examination of the sample-window interface revealed thin-film fringes suggesting that the layer of adhesive is very thin, with a thickness on the order of the wavelength of light. The optical adhesive was cured by exposing the sample to a UV light source (Electro-Lite 10 mW/cm^2 #82469) for an hour. The sample, together with the window, are shown schematically in Fig. 3.1. Removal of the GaAs substrate was required so that only the optical response of the GaAs thin film was probed. To achieve this, a combination of mechanical polishing as well as chemical etching was performed. First, the window was adhered to an aluminum puck using mounting wax (Buehler Mounting Wax #408150), which was then mounted into a six puck polishing head that also contained five sacrificial GaAs (001) wafer pieces that served to level the applied force from the polisher (Buehler Polisher/Grinder). The individual samples were polished sequentially (*i.e.* sacrificial GaAs wafers were used) instead of in parallel as individual polishing runs occasionally resulted in a large wedge on the sample surface, which led to a failed etching process and loss of the sample. Using 1200 grit (736 μm side) sandpaper, with an applied load force of 40 N, increments of 40 μm were polished until approximately 300 μm was removed from the substrate (See Fig. 3.1).

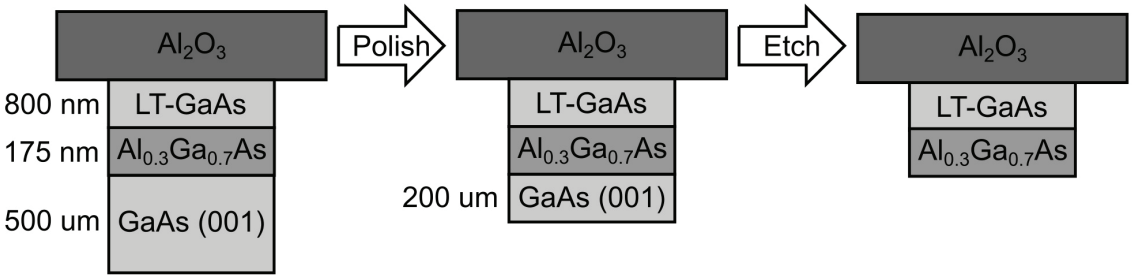

Figure 3.1: The three step process used to produce the GaAs samples for transmission measurements.

The remaining substrate was removed using chemical wet etching. The etchant solution used in this work was a 5:1 volumetric ratio of 6.3 M citric acid to 30% H_2O_2 as indicated by the etchant recipe provided by Eric J. Loren at the University of Iowa. Aqueous citric acid was produced the day prior to etching by dissolving 60.34 g of anhydrous citric acid in 50 mL of nanopure water. Using this solution, the GaAs substrate was removed at a rate of 20 μm/hour until the $Al_{0.3}Ga_{0.7}As$ stop-etch layer was reached (Fig. 3.1(c)), as indicated by the transition of the visual appearance of the substrate from a dull-grey to a mirror-like finish. Due to the lack of optical absorption for the photon energies probed in this work, the residual $Al_{0.3}Ga_{0.7}As$ present on the sample does not contribute to the FWM signal but only effects the surface quality of the sample. Finally, the sample was rinsed with nanopure water, followed by spectroscopic grade methanol to remove any remaining etchant.

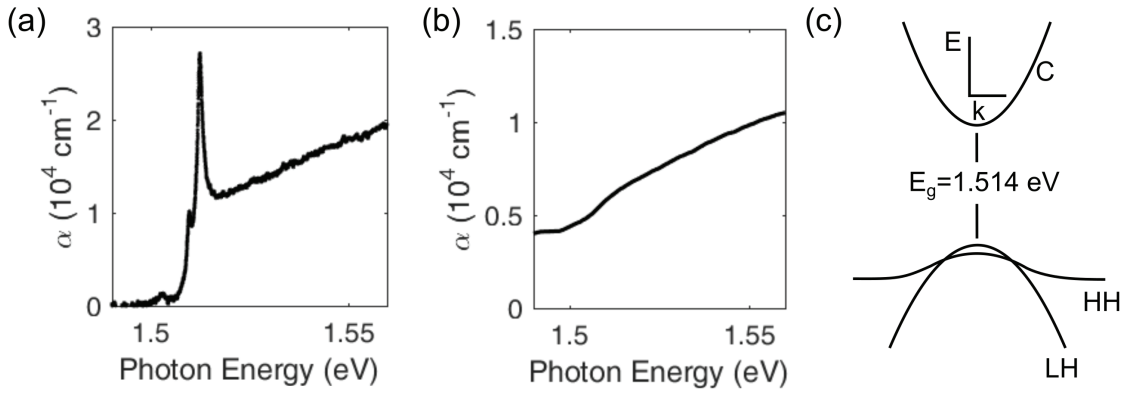

Figure 3.2: Linear absorption spectra for the (a) high-temperature-grown GaAs sample and (b) as-grown LT-GaAs sample studied in this work. (c) The electronic band structure of GaAs in the presence of biaxial tensile strain.

Linear transmission measurements were performed with the GaAs samples held at 10 K. For the high-temperature-grown sample, broad bandwidth optical pulses from a Ti:Sapphire laser were used to measure the transmission. To cover the range of photon energies displayed in Fig. 3.2(a), transmission measurements at several different laser centre wavelengths were performed, and the calculated absorption was stitched together. For the LT-GaAs sample, a tungsten lamp was used as a white light source. The raw transmission data for the LT-GaAs sample contained pronounced oscillations due to multiple reflections within the thin film. In order to extract the absorption coefficient a self-consistent model was used that takes into account the reflection losses at interfaces as well as the absorption in the material. Since the band width of the FWM signal was much smaller than the period of Fabry-Perot oscillations in the sample (*e.g.* 40 nm vs. 200 nm), interference effects in the FWM signal were negligible. The Fresnel coefficients for transmission and reflection at each interface were determined using the index of refraction for fused silica (cryostat window) [125], sapphire (substrate) [126], and bulk GaAs [127]. The absorption spectrum for GaAs grown at 600°C is shown in Fig. 3.2(a). The linear absorption spectrum for GaAs exhibits two peaks at photon energies of 1.5100 eV and 1.5125 eV corresponding to the light-hole and heavy-hole exciton resonances. Due to the larger thermal expansion coefficient of GaAs relative to the sapphire substrate, biaxial tensile strain developed in the GaAs sample upon being cooled to 10 K, resulting in the normally degenerate

light-hole and heavy-hole valence bands shifting and splitting [128, 129]. The band structure for GaAs (excluding the spin-orbit split-off band) in the presence of biaxial tensile strain is shown in Fig. 3.2(c).

3.2.2 $CH_3NH_3PbI_3$

Carrier transport was studied in methylammonium lead iodide perovskite ($CH_3NH_3PbI_3$). In this thesis work, the sample was produced by Charlotte Clegg of Ian Hill's research group at Dalhousie University using a modified sequential deposition procedure reported by Xiao *et al.* [29], and is described as follows. Under an argon atmosphere inside a glove box, a 1 M PbI_2 solution in diethylformamide (DMF) was stirred for 10 hours at a temperature of 70°C. It was then passed through a 0.45 μm pore polytetrafluoroethylene (PTFE) filter into a glass vial held at 70°C. 300 μL of the solution was cast onto a room temperature, stationary sapphire window, which was then spun at 4000 rpm for 1 minute. Any remaining solvent was removed by heating the substrate on a 70°C hotplate for 15 minutes. Next, 300 μL of methylammonium iodide solution in isopropanol was deposited onto the lead iodide film which was then spun at 3000 rpm for 1 minute. Finally, the sample was annealed at 100°C for 2 hours. X-ray diffraction (XRD) rocking curves of the perovskite film revealed a full conversion to tetragonal phase perovskite, with no residual lead iodide as determined by the lack of an XRD peak at 12.5 degrees [130]. The resulting thin film had a thickness of 305 nm, determined by removing a thin strip of perovskite from a companion sample, and measuring the indentation using a profilometer (Bruker Dektak). Prior to removal from the glove box, the samples were mounted onto a cold finger tip inside a Janis instruments ST-300 liquid helium flow-through cryostat under an argon atmosphere and subsequently sealed to prevent air contamination of the film. Prior to the experiment, the cryostat was evacuated to 10^{-6} Torr.

The linear absorption spectrum of the $CH_3NH_3PbI_3$ sample is shown in Fig. 3.3. The absorbance data (which was used to calculate the absorption coefficient) was collected by Sam A. March, and published in March *et al.* [130]. Linear transmission measurements were performed to obtain the absorbance using a CARY UV-VIS spectrometer with the sample held at room temperature. The spectrometer calculates the

absorbance spectrum $A(\omega)$ using the following equation:

$$A(\omega) = -\log_{10}\left(\frac{I_{out}}{I_{in}}\right) \tag{3.1}$$

I_{in} and I_{out} represent the intensity of light measured before and after the sample. Since the sample resides on a substrate inside an evacuated cryostat, the measured absorbance includes reflections from interfaces (*e.g.* cryostat windows, sample, substrate, etc.) and so these must be taken into account. Using a similar procedure as described in Sec. 3.2.1 for GaAs, the linear absorption spectrum for $CH_3NH_3PbI_3$ was calculated based upon the reported index of refraction for another $CH_3NH_3PbI_3$ sample [131] and from the measured absorbance spectrum. The linear absorption spectrum for the $CH_3NH_3PbI_3$ sample studied in this work is shown in Fig. 3.3.

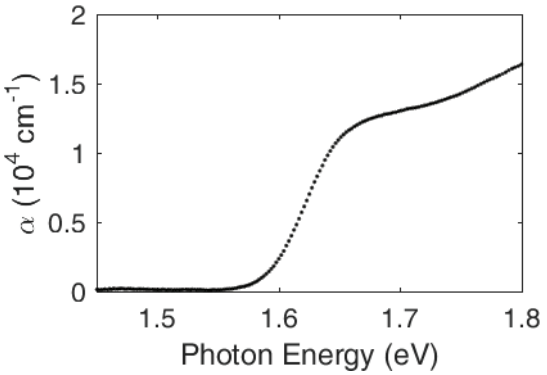

Figure 3.3: Calculated linear absorption spectrum for the $CH_3NH_3PbI_3$ sample studied in this work with the substrate held at 300K.

3.3 Sample Cooling

For the experiments conducted using the two-pulse and three-pulse FWM experiments, the samples were held in a Janis Instruments ST-300 liquid helium flow-through cryostat that was evacuated to 10^{-6} Torr prior to and during experiments. For the experiments conducted using the two-dimensional Fourier transform spectroscopy (2DFTS) setup at West Virginia University, a Montana Instruments closed-cycle liquid helium cryocooler was used that was also evacuated to 10^{-6} Torr during experiments.

3.4 Pulse Measurement, Characterization, and Optimization

To investigate the rapid dynamics of charge carriers in a semiconductor, very short optical pulses are required. A Ti:Sapphire oscillator was used to generate optical pulses with widths in the range of 25-35 fs. Conventional electronics (e.g. photodetectors) are too slow to directly measure the pulse duration on such a short timescale, and so zero-background autocorrelation techniques were used to measure and optimize the pulse duration.

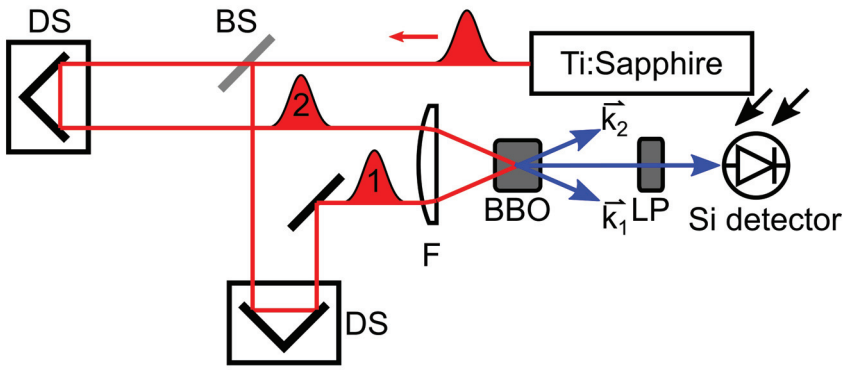

Figure 3.4: A schematic of the experiment used to measure the zero-background autocorrelation. The labels are: BBO - Beta-barium borate, BS - beamsplitter, M - mirror, LP - Low-pass filter, DS - Delay Stage.

If two optical fields with electric fields $\vec{E_1}$ and $\vec{E_2}$, wave vectors $\vec{k_1}$ and $\vec{k_2}$, and angular frequencies ω_1 and ω_2 respectively are focused together onto a material with a strong optical nonlinearity (χ_2), mixing between the two beams leads to the generation of a signal with frequency $\omega_1 + \omega_2$ that emits along $\vec{k_2} + \vec{k_1}$. This is known as sum-frequency generation, and for two optical pulses this only occurs when both beams are spatially- and temporally-overlapped on the nonlinear material. A schematic of the autocorrelation setup used is shown in Fig. 3.4. Since the pulses $\vec{E_1}$ and $\vec{E_2}$ are derived from the same laser source, $\omega_1 = \omega_2 = \omega$. The nonlinear crystal used in this thesis work was a 100 μm thick beta-barium borate (BBO) crystal which was cut for phase matching at 800 nm at normal incidence. Optimization of this signal provides an avenue to ensure beam overlap and temporal characterization. A low-pass filter placed after the BBO crystal removed any scattered light at the fundamental

frequency prior to measurement on the Si photodiode.

In addition to alignment purposes, the sum-frequency generated light can be used for pulse characterization. The sum-frequency signal (*i.e.* autocorrelation) is given as the cross-correlation of the pulse intensity envelopes:

$$\mathrm{S_{auto}}(\tau) = \int_{-\infty}^{\infty} dt\, |E_1(t)|^2\, |E_2(t-\tau)|^2\,. \tag{3.2}$$

The width of the autocorrelation is related to the width of the optical pulses that generated it. For two pulses with Gaussian envelope, the autocorrelation signal is also Gaussian with a FWHM that is 1.414 times larger than the actual pulse FWHM. There are also second harmonic pulses generated by each of the two pulses $\vec{E_1}$ and $\vec{E_2}$ separately. If the two beams were incident on the sample in a collinear geometry, these single-beam second harmonic signals would represent a background. In the noncollinear geometry shown in Fig. 3.4, these single-beam second harmonic signals are not detected because they propagate with directions $\vec{k_1}$ and $\vec{k_2}$. By detecting only the signal along $\vec{k_2} + \vec{k_1}$, this background signal is avoided. For this reason, this technique is called the "zero-background" technique.

3.4.1 Excited Carrier Density

The excited carrier density is calculated based on the number of photons in an optical pulse, which is determined based on the absorbed laser power P_{abs} (determined by measuring the laser power before and after the sample using a power meter) and the excited volume in the sample. For a laser producing pulses with a repetition rate R_{rep}, the energy per pulse is given by $P_{\mathrm{abs}}/R_{\mathrm{rep}}$. The number of photons in each pulse is determined by taking the ratio of the energy per pulse with the energy per photon (*i.e.* $\hbar\omega_0$, where ω_0 is the centre frequency of the laser pulse). For an optical transition it takes one photon to excite one electron-hole pair, and so the number of photons indicates the number of excited electron-hole pairs. For a sample with thickness L, and a laser beam spot area A, the electron-hole pair density per unit volume is given by:

$$N_{ex} = \frac{P_{\mathrm{abs}}}{R_{\mathrm{rep}}\hbar w_0 AL}. \tag{3.3}$$

3.4.2 Laser Spot Size Measurement

The laser spot size (w) is an important parameter as it is required to determine the carrier density excited by an optical pulse. In the experiments conducted in this thesis, the laser spot size was measured using the knife edge technique. A simple schematic of this arrangement is shown in Fig. 3.5(a). A razor blade was mounted onto a translation stage, which was located at the focal point of the lens. A power meter located after the knife edge but in the beam path measured the transmitted beam power as the knife edge was translated perpendicularly into the beam path. If the laser spot size is assumed to have a Gaussian transverse intensity profile, and the knife edge translates in the x direction, the transmitted power $P(x_k)$ at a given knife edge position x_k is given by:

$$P(x_k) = P_0 \int_{-\infty}^{\infty} dy \int_{-\infty}^{x_k} dx e^{-\frac{2(x^2+y^2)}{w^2}} \tag{3.4}$$

where P_0 is the transmitted power in the absence of a knife edge. The solution to the above integral is given by:

$$P(x) = \frac{P_0}{2}\left(1 + \text{erf}\left(\frac{\sqrt{2}x}{w}\right)\right) \tag{3.5}$$

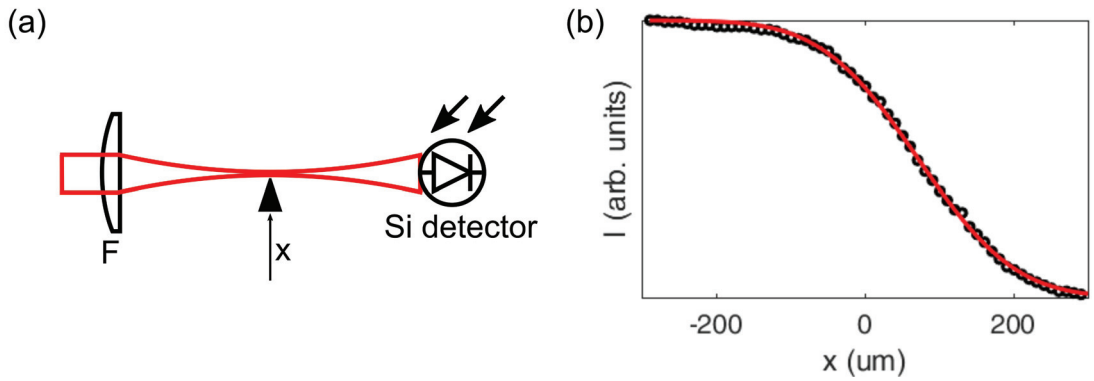

Figure 3.5: (a) A schematic of the knife edge experiment. (b)Transmitted laser power as a function of knife edge position (x).

3.4.3 Pulse Compression

The temporal resolution in a transient FWM experiment is limited by the temporal width of the optical pulses. Interaction of the light pulse with optical elements in the

setup (*e.g.* lenses) causes a temporal distortion of the pulse envelope. This is called group-velocity dispersion (GVD) and causes a frequency dependent phase shift of different frequency components in the optical pulse. In normal media, GVD is positive and so lower frequency components of light will travel faster than higher frequency components, resulting in a temporal broadening of the optical pulse. The positive GVD introduced by optical elements can be compensated by introducing negative GVD using an apparatus commonly known as a prism compressor. A schematic of such an arrangement used in this thesis work is shown in Fig. 3.6. Negative GVD is introduced to the pulse by forcing lower frequency components to travel longer path lengths, such that on recombination the mutual phase between individual components is minimized.

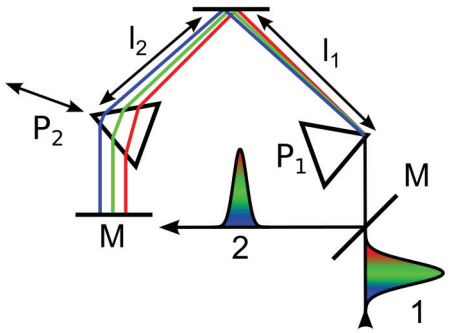

Figure 3.6: A schematic diagram of the prism compressor. Optical pulse 1 has accrued positive GVD, resulting in lower frequency (*e.g.* red) traveling ahead of higher frequency (*e.g.* blue) components, as shown pictorially. After emergence from the prism compressor, the pulse duration is shortened due to realignment of different spectral components in time.

The optimum amount of GVD compensation introduced by the prism compressor was obtained when the autocorrelation width, and thus the pulse width, was at a minimum. Shown in Fig. 3.6 is a schematic of the prism compressor used in this thesis work. A prism compressor introduces both positive and negative GVD to the optical pulse through careful positioning of prism P_2: (i) Positive GVD is added by changing the path length of different frequency components through the prism (which is performed by translating the prism laterally across the beam direction) ; and (ii) Negative GVD is added by changing the path length l_2 of the different frequency components in air. For the two-pulse FWM experiments conducted in this work,

near time-bandwidth limited Gaussian pulses of ≈ 29 fs width were obtained.

3.5 Two-Pulse Self-Diffracted FWM

As discussed in Sec. 1.6, three pulses $\vec{E_1}$, $\vec{E_2}$, and $\vec{E_3}$ of the same centre frequency with wave vectors $\vec{k_1}$, $\vec{k_2}$, and $\vec{k_3}$ are used to excite electron-hole pairs in a semiconductor. In a two-pulse self-diffracted FWM experiment, only two pulses are used to excite the sample. Similar to the process described earlier, the first two pulses $\vec{E_1}$ and $\vec{E_2}$ generate a carrier grating within the sample. However, instead of a third optical pulse diffracting off this grating, a $\vec{E_2}$ plays the role of $\vec{E_3}$ as well, emitting a fourth field along the direction $2\vec{k_2} - \vec{k_1}$.

A full diagram of the two-pulse SR-FWM experiment is shown in Fig. 3.7. The output beam of the laser was first passed through a prism compressor (PC). The laser was then focused onto a pinhole which functions as spatial filter. In optical experiments it is desirable to have a laser beam with a transverse intensity profile (*i.e.* transverse to the propagation direction) that is Gaussian in shape. This corresponds to the fundamental transverse electric mode (TEM_{00}). The pinhole diameter (50 μm) was chosen to match the Gaussian beam spot size, such that higher order TEM modes would be blocked and only the TEM_{00} mode would transmit. The beam was then split into two beams $\vec{E_1}$ and $\vec{E_2}$ using a 50/50 beamsplitter designed for low GVD for 800 nm pulses. The two beams were sent down two different paths, each of which contains a retroreflector and a method of changing the path length. A fixed translation stage (mechanical delay stage) in the path of $\vec{E_1}$ was used for coarse adjustment of the delay τ. The delay between pulses $\vec{E_1}$ and $\vec{E_2}$ was varied using the rapid-scan technique. For adjustments of the path of $\vec{E_2}$, a retroreflector was glued onto the cone of a speaker. The speaker was driven to oscillate so that the optical path delay in $\vec{E_2}$ was rapidly varied. The frequency of speaker oscillation was much smaller than the beam repetition rate so that at each instance of pulse delay, the FWM signal would be averaged over many optical excitations to improve the signal-to-noise. Spatial and temporal alignment of the two optical beams was performed using the autocorrelation procedure discussed earlier in this chapter. The two excitation beams $\vec{E_1}$ and $\vec{E_2}$ were redirected to an equivalent focus point using a pick-off mirror (labeled PO in Fig. 3.7).

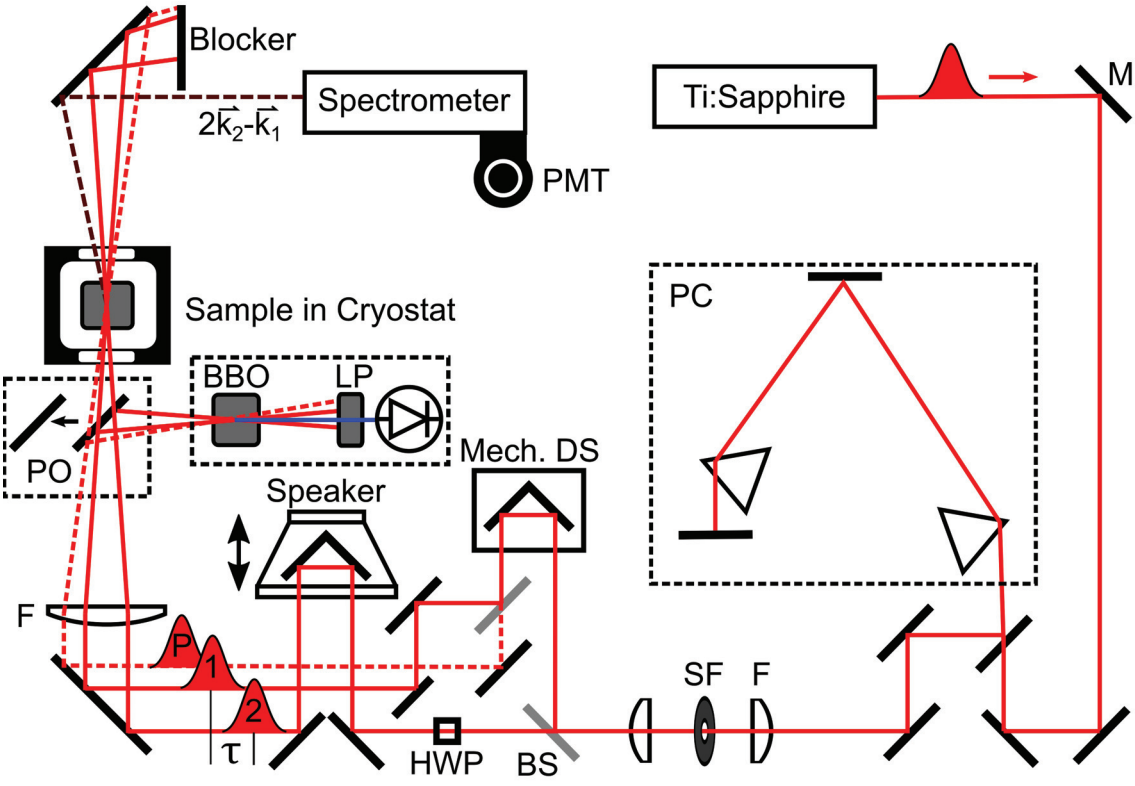

Figure 3.7: A schematic diagram of the two-pulse SR-FWM apparatus used in this thesis. The prism compressor (PC) and autocorrelator described earlier are enclosed in the black dashed boxes. The labels in the figure correspond to: Mirror (M), Lens of focal length F (F), Beta-barium borate (BB0), low-pass filter (LP), beamsplitter (BS), pick-off mirror (PO). The FWM signal (dark red dashed line) generated by pulses 1 and 2 propagates along the $2\vec{k}_2 - \vec{k}_1$ direction into the spectrometer. In some experiments in this thesis work, a prepulse (P) that was temporally coincident with pulse 1 was used and is shown offset in the figure for clarity. In addition, a half-wave plate (HWP) place in the pulse 2 path was used to rotate the linear polarization of $\vec{E}_2$.

The FWM signal along $2\vec{k}_2 - \vec{k}_1$ was collimated, and then focused into the entrance slit of a Czerny Turner type monochromator (Oriel Cornerstone 260). The operation of this type of monochromator is described as follows: the entrance slit functions as a point source. A parabolic mirror placed after the entrance slit collimates and directs the light towards a diffraction grating. The individual wavelength components diffracted from the grating are refocused by a second parabolic mirror onto the exit slit such that only a narrow range of wavelengths (≈ 1 nm for the slit widths used in these experiments) emerges from the monochromator. To change the wavelength of

light emitted by the monochromator, the angle of the diffraction grating is changed such that the desired wavelength component diffracted by the grating is focused onto the exit slit.

Calibration of the monochromator was achieved by aligning a Helium-Neon laser source collinearly with the FWM beam and into the monochromator. A helium-neon laser produces a spectrally-narrow emission centred at 632.8 nm. The wavelength of light emitted at the output slit of the monochromator is determined by the angle of the diffraction grating. If the angle of incidence on the input slit is not normal, the desired wavelength set by the controller will differ from the wavelength at the output slit. To perform the calibration, the monochromator output was measured as a function of the wavelength (read out using the hand-held controller unit) and the offset was determined using the known wavelength of the He-Ne laser.

Due to the nonlinearity of the FWM process, the generated signal was very weak ($\approx 1 - 10$ nW for LT-GaAs samples) and required the use of a sensitive photodetector. In these experiments, a photomultiplier tube was used to measure the spectrally-resolved signal from the output of the monochromator. The operation of a photomultiplier tube is based on two material interactions: the photoelectric effect and secondary emission. In the photoelectric effect, a photon with energy sufficient to overcome the work function of a material can cause the excitation and emission of an electron. Secondary emission corresponds to the process which primary mobile electrons of sufficient energy strike a material inducing the emission of many secondary electrons. In a photomultiplier tube, the first of these two effects occurs when incident photons strike a photocathode resulting in emission of electrons. These electrons gain kinetic energy as they are propelled towards the first of a series of dynodes via the application of a large potential. At each metal plate, secondary electrons are generated that are propelled to the next metal plate in the series, resulting in a cascaded secondary emission process that strongly amplifies the small number of electrons excited by the incident weak optical signal.

For selected experiments, in addition to the excitation pulses $\vec{E_1}$ and $\vec{E_2}$ a third pulse with unique wave vector $\vec{k_{pp}}$ was used to excite the sample. The third beam does not contribute to grating formation but serves to inject a population of excited carriers. These type of experiments are commonly referred to as prepulse experiments,

and are useful for studying many-body effects. Experimentally, a prepulse experiment is realized by focusing a third optical pulse with electric field $\vec{E_{PP}}$ such that $\vec{k_{pp}} \neq \vec{k_1}, \vec{k_2}, 2\vec{k_2} - \vec{k_1}$ and measuring the FWM signal along the two-pulse path $2\vec{k_2} - \vec{k_1}$. In this work, the prepulse beam line was created by placing a beam splitter in the beam path of $\vec{E_1}$ and is shown in Fig. 3.7 by the red dashed line. The mutual delay between $\vec{E_1}$ and $\vec{E_P}$ was changed by varying the path length of $\vec{E_P}$ using a micrometre-controlled delay stage. Spatial and temporal alignment of all three beams was achieved using the autocorrelation technique described in Sec. 3.4.

3.6 Two-Dimensional Fourier Transform Spectroscopy

As discussed in Sec. 1.6.2, two-dimensional Fourier transform spectroscopy (2DFTS) is an enhanced version of a three-pulse FWM experiment. Three pulses of the same centre frequency with wave vectors $\vec{k_1}$, $\vec{k_2}$, and $\vec{k_3}$ are used to excite electron-hole pairs in a semiconductor. In contrast to conventional FWM experiments where only the intensity of the signal is measured, in a 2DFTS experiment both the amplitude and phase of the coherent signal are measured. The experimental setup used for this thesis work was built and maintained by Brian Wilmer and Alan D. Bristow at West Virginia University. In particular, a variant of a 2DFTS setup, called the Multidimensional Optical Nonlinear SpecTRometer (MONSTR) was used for these experiments.

The MONSTR was originally designed and built by Alan D. Bristow and Steven T. Cundiff [132]. The MONSTR circumvents the complexity and large optical bench real estate requirements of existing setups by using a folded geometry, which doubles to increase the phase stability between optical pulses. The use of delay stages provides access to long relaxation times suitable for studies in most semiconductor systems, and interferometric feedback loops connected to adjustable mirrors provided the necessary phase stabilization. A computer-assisted design drawing of the MONSTR is shown in Fig. 3.8(a) (adapter from [132]).

The complex FWM signal was measured using an optical heterodyne detection scheme. For a reference pulse with electric field $E_0(t)$ and signal with field $E(t)$ both with the same polarization, their respective frequency compositions are given by their corresponding Fourier transformed counterparts $E_0(\omega)$ and $E(\omega)$. The optical

heterodyne signal $S(\omega)$ measured on a photodetector is given as the square-modulus of the sum of their fields:

$$S(\omega) = |E_0(\omega)|^2 + |E(\omega)|^2 + 2\mathrm{Re}\left\{E_0^*(\omega)E(\omega)\right\} \tag{3.6}$$

where Re is the real part of $E_0^*(\omega)E(\omega)$. The first two terms in Eqn. 3.6 represent the individual power spectrum of the reference and the signal pulse. However, the last term is proportional to the cosine of the phase difference between the reference and the signal [133]. In the experiment, the heterodyne signal was realized by first interfering the FWM field with a delayed reference pulse on a beam splitter (these are labeled 4 and R on Fig. 3.8(b) respectively). A condition on the reference pulse is that its pulse bandwidth must entirely cover the range of frequencies that span the FWM signal. Next, the interference signal $(4 + R)$ was collimated and focused into a 1-metre spectrometer (SPEX 1702), where the spectral content of this interference (*i.e.* spectral interferogram) was simultaneously measured over a 20 nm wavelength window using a thermoelectrically-cooled charge-coupled device (Andor iDus 420). In a 2DFTS experiment, the power spectrum of the optical pulse and FWM signal were measured separately so that phase information could be extracted using Eqn. 3.6.

Precise knowledge of the phase of the three excitation beams and the reference beam are required to obtain the complex FWM emission. In practice, mechanical noise such as table vibrations stemming from sources external to the lab (*e.g.* people walking in the corridor, road construction), as well as thermal noise such as turbulent air currents and inconsistent air conditioning control lead to alterations in the optical path lengths causing changes in the relative pulse delays. To achieve precise phase control between optical pulses, the phase of the optical pulses were maintained using active-phase stabilization techniques.

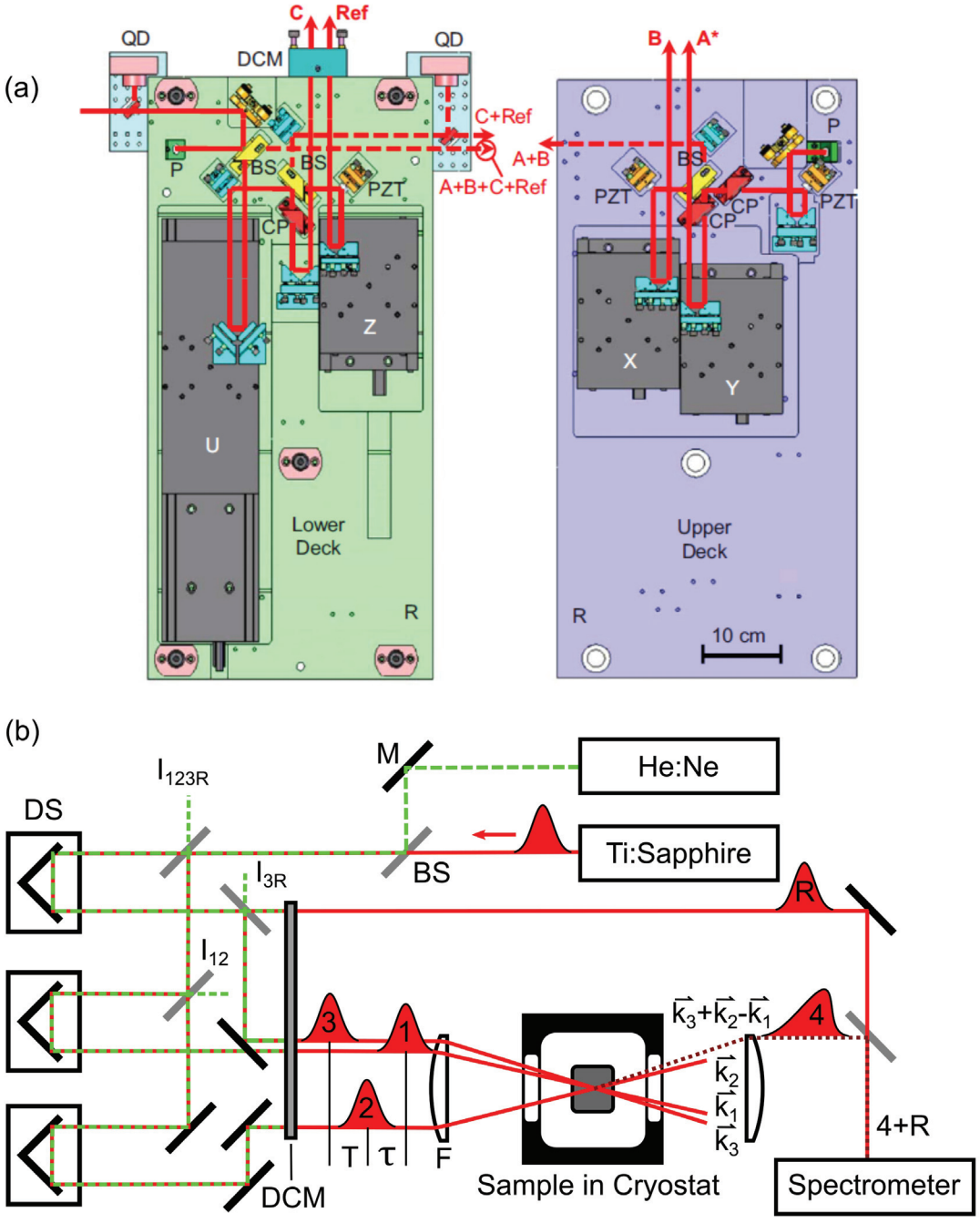

Figure 3.8: (a) Computer-aided design drawing of the MONSTR apparatus used in these experiments. The MONSTR is made up of two metal slabs which serve as optical benches. Shown is a schematic of the lower deck (left hand side) and upper deck (right hand side), which are stacked in experiment. Modified with permission from Bristow *et al.* [132] (b) A schematic representation of the 2DFTS experiment. A HeNe laser beam collinear with Ti:Sapphire beam was reflected by a dichroic mirror and used to interferometrically monitor the optical path delay in each delay path.

Active-phase stabilization was realized experimentally by integrating Michelson interferometers into each of the optical paths controlling pulses $\vec{E}_1$, $\vec{E}_2$, $\vec{E}_3$, and R as well as mounting a piezoelectric transducer onto the end mirror in each interferometer. This is shown in Fig. 3.8(b). A piezoelectric device is a device in which an applied voltage can distort a material via the piezoelectric effect. In these experiments, coarse adjustment of the pulse delay was performed by computer controlled delay stages, where as fine control was achieved using piezoelectric transducers. The laser source used to provide active feedback to the piezoelectric transducers was a Helium Neon laser (He:Ne) that aligned collinearly with the Ti:Sapphire laser. The interference signal between path lengths 1 and 2 (I_{12}), 3 and R (I_{3R}), as well as all four beams (I_{123R}) were monitored using Si photodiodes.

As the mutual delay between the two arms is changed, the intensity of the interference pattern will vary. In these experiments, the coarse delay was changed using a computer controlled delay stage in half-wavelength steps (for $\lambda_c = 632$ nm, this corresponds to 316 nm, or ≈ 1 fs) so that the measured interferometric signal will always remain a maximum due to constructive interference. The error between the interferometric signal and the desired delay was minimized using an proportional, integral, and derivative (PID) controller. Due to the mechanical and thermal noise described earlier, the optical path delay will change resulting in the interferometric signal drifting away from its peak intensity (*i.e.* the interferometric signal will be a maximum when the optical path delay is zero). This error is used as a source term by the PID loop to drive the piezoelectric-controlled mirrors so that the desired path delay is recovered. Using this arrangement, an optical path length stability of $\lambda/100$ was achieved.

3.7 Transient Grating Technique

The experimental arrangement for transient grating experiments is illustrated in Fig. 3.9. Laser pulses generated by a Ti:Sapphire laser system are split into three optical pulses $\vec{E}_1$, $\vec{E}_2$, and $\vec{E}_3$ that are separated by delays τ and T and focused onto the sample. As discussed in Sec. 1.6, interference of $\vec{E}_2$ from the polarization induced by $\vec{E}_1$ leads to the generation of a periodic carrier grating laterally across the sample, that can be visualized as an optical grating. Measurement of the FWM

signal stemming from the diffraction of $\vec{E}_3$ off this grating versus T provides a direct measurement of carrier transport.

In these experiments, the intensity of the FWM emission was measured using a Si photodiode as a function of pulse delay τ and T. At each delay T, the pulse delay τ was rapidly varied using a retroreflector attached to a speaker cone. The delay T was varied using a computer controlled delay stage. In a transient grating experiment, the FWM signal is normally measured as a function of T for $\tau = 0$ delay so that the grating strength is at a maximum. To improve the signal-to-noise in these experiments, the FWM signal was measured over a broad range of delay τ such that any background light measured along the FWM direction could be determined. This was achieved by examining the measured signal for $\tau > 4T_2$ where no FWM signal is expected to be measured. This provided an offset which was subtracted from the overall FWM intensity.

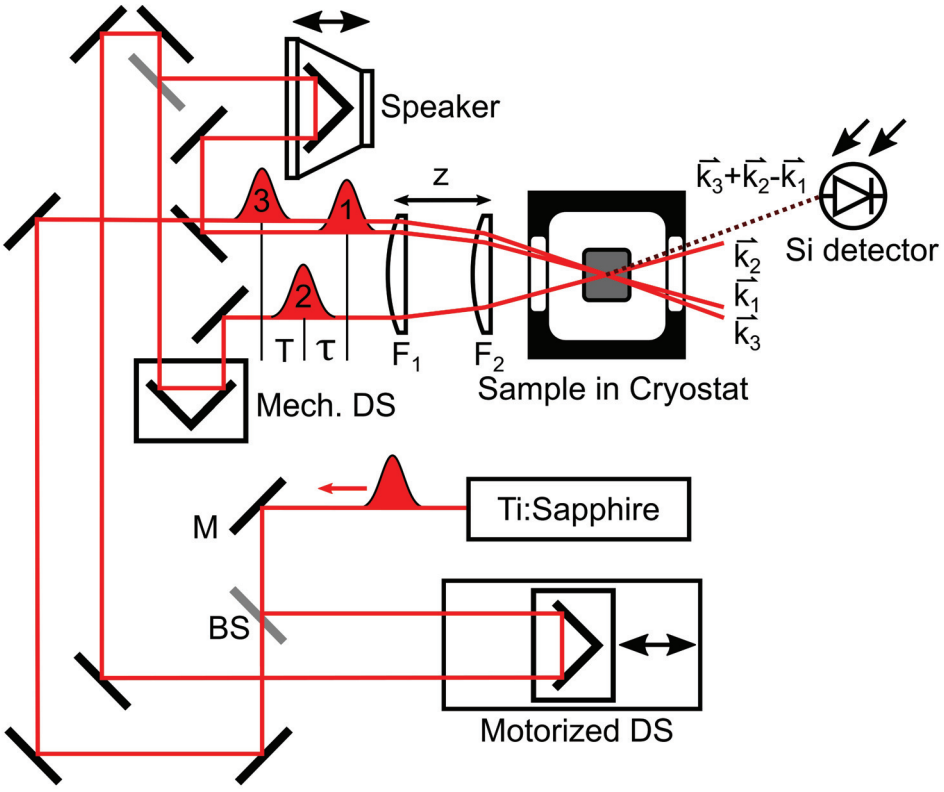

Figure 3.9: A schematic diagram of the three-pulse FWM apparatus used in this thesis.

Precise control over the grating period is required in transient grating measurements to permit extraction of carrier diffusion. In addition, to improve the accuracy and precision of the diffusion length estimate, numerous grating periods are necessary, requiring experimental flexibility to adjust the incident laser angle without modifying the beam overlap on the sample. To achieve this we utilized a paired-lens arrangement, as shown in Fig. 3.9, that allowed the grating period to be varied between 4.2 μm and 6.7 μm. By changing the distance z between a plano-convex lens with focal length $F_1 = 40$ cm and a fixed plano-convex lens with focal length $F_2 = 20$ cm, the effective focal length, and in turn the angle of incidence could be controlled. For the experiments presented in this thesis work, the angle was calculated based on the measured distance between the lens, F_2, and the sample, as well as the beam separation from the optical axis at lens F_2, which was taken as half of the distance between beams $\vec{E_1}$ and $\vec{E_2}$. To complement these measurements, a calculation using ray matrices was performed, and the resulting expression for the angle of incidence between the last lens and the sample is given by,

$$\theta = \left(\frac{1}{F_2} + \frac{1 - z/F_2}{F_1} \right) l \tag{3.7}$$

where l is half the distance between the collimated beams $\vec{E_1}$ and $\vec{E_2}$ incident on lens F_1. The results of these calculations alongside the measured values are plotted in Fig. 3.10. Knowledge of the laser spot size is critical in determining the density of photoexcited carriers in the sample. The beam diameter for a Gaussian shaped beam is given by:

$$\text{Beam Diameter} = \left(\frac{4\lambda}{\pi} \right) \left(\frac{1}{\theta} \right) \tag{3.8}$$

Since the beam diameter changes with the angle of incidence θ, the beam power was suitably modified to maintain a constant intensity on the sample.

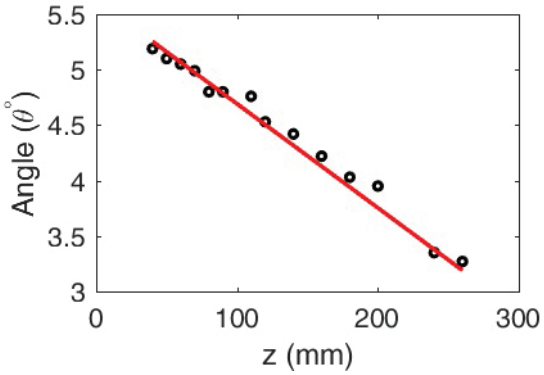

Figure 3.10: Measured values of the angle between the three pulses and the optical axis. The solid red line is the result shown in Eqn. 3.7.

Chapter 4

Carrier Diffusion in Thin-Film $CH_3NH_3PbI_3$ Perovskite Measured using Four-Wave Mixing

Authors: D. Webber[1], C. Clegg[1], A. W. Mason[1], S. A. March, I. G. Hill[1], K. C. Hall[1]

[1] Department of Physics and Atmospheric Science, Dalhousie University, Halifax, Nova Scotia B3H4R2, Canada

Reprinted with permission from Applied Physics Letters 111, , 121905 (2017).

Daniel Webber developed the techniques, performed the experiments, and the data analysis. Allister Mason assisted with data collection. Charlotte Clegg and Ian Hill developed and produced the sample. Daniel Webber and Kimberley C. Hall conceived the direction for research. Daniel Webber and Kimberley C. Hall wrote the manuscript with input from all authors. Section titles were added to the original manuscript to aid the reader.

4.1 Abstract

We report the application of femtosecond four-wave mixing (FWM) to the study of carrier transport in solution-processed $CH_3NH_3PbI_3$. The diffusion coefficient was extracted through direct detection of the lateral diffusion of carriers utilizing the transient grating technique, coupled with simultaneous measurement of decay kinetics exploiting the versatility of the boxcar excitation beam geometry. The observation of exponential decay of the transient grating versus interpulse delay indicates diffusive transport with negligible trapping within the first nanosecond following excitation. The in-plane transport geometry in our experiments enabled the diffusion length to be compared directly with the grain size, indicating that carriers move across multiple grain boundaries prior to recombination. Our experiments illustrate the broad utility of FWM spectroscopy for rapid characterization of macroscopic film transport properties.

4.2 Introduction

Organo-lead trihalide perovskites possess a unique combination of electronic and optical properties, making them attractive for applications in light-emitting diodes, [134, 135] lasers, [136–138] optical sensors, [139–141] and most notably high performance solar cells where the efficiencies have rapidly increased, reaching over 22% in just a few years. [19] In addition, these hybrid perovskites can be solution-processed and applied as thin films to a variety of substrates, [142, 143] pointing to the potential for large-scale, low-cost solar cell production using *e*.g. spray, blade or slot die coating techniques. [31, 144–147] The transport properties of electrons and holes within the perovskite absorber material are crucial to the performance of photovoltaics and other optoelectronic technologies using these materials. The first observation of micron-scale carrier diffusion lengths in $CH_3NH_3PbI_{3-x}Cl_x$ [21, 26, 148] stimulated a comprehensive research effort aimed at understanding the nature of carrier transport. [99–109, 149–151] Carrier mobilities and/or diffusion lengths have been studied using electrical techniques (*e.g.* AC Photo Hall, [100] space-charge-limited current, [99] impedance spectroscopy, [101], and spatially-resolved electron-beam-induced current [102]) as well as optical techniques that rely on electrical contacts such as photoluminescence quenching [21, 26] and scanning photocurrent microscopy. [149, 151] Some of these techniques offer the ability to probe transport in a working solar cell device, however imperfectly characterized interface energetics and ambiguities tied to the model-dependent extraction of transport characteristics impede the determination of the physical processes limiting device performance.

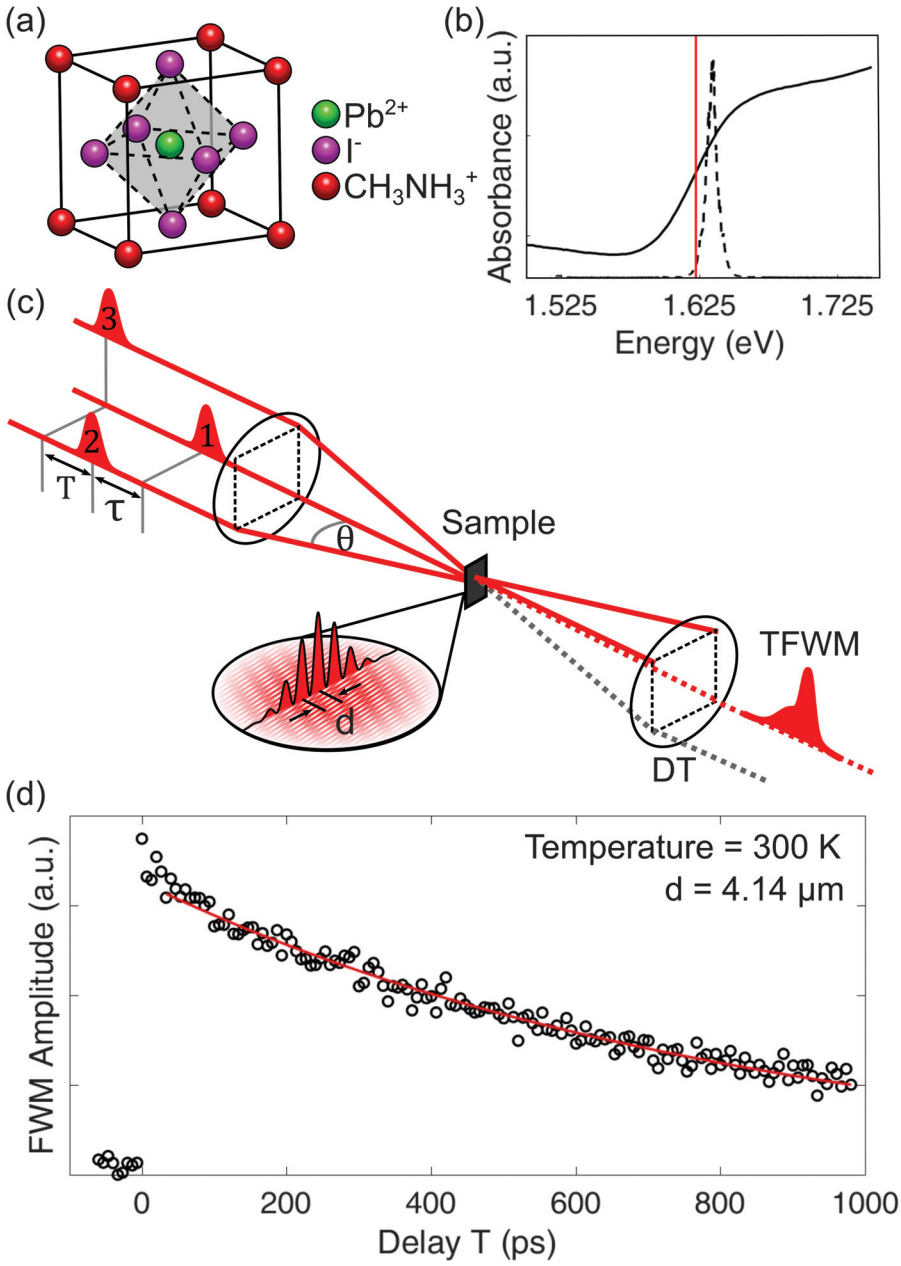

Figure 4.1: (color online) (a) The crystal structure of $CH_3NH_3PbI_3$. (b) The linear absorption spectrum for the pervoskite sample at 300 K (solid curve) alongside the laser pulse spectrum (dashed curve). The red vertical line indicates the band gap of $CH_3NH_3PbI_3$. [152] (c) A schematic of the FWM setup showing the boxcar geometry. (d) FWM signal as a function of delay T at 300 K for d = 4.14 μm. The solid curve is a least-squares fit to Eqn. 4.1.

All-optical techniques provide an effective approach to studying carrier transport within a wide range of photovoltaic materials as no carrier extraction layers or ohmic contacts are required. Time-domain terahertz spectroscopy (TDTHz) and time-resolved microwave conductivity (TRMC) have provided valuable insight into carrier scattering processes in the organometal halide perovskites in recent years. [106, 108, 109, 153] For such techniques, the quantitative determination of mobility requires modeling of the Drude response of the multi-component carrier system. Transient absorption microscopy [103] provides a more direct, all-optical probe of carrier transport. In this technique, carrier motion away from the laser excitation spot is imaged as a function of time after excitation using a diffraction-limited focusing geometry, enabling the influence of variations in sample morphology on the local transport characteristics to be assessed. A complementary all-optical technique that probes carrier transport on macroscopic length scales, while also relying on the direct detection of the spatial motion of carriers, would provide a valuable characterization tool for the rapid survey of photovoltaic materials.

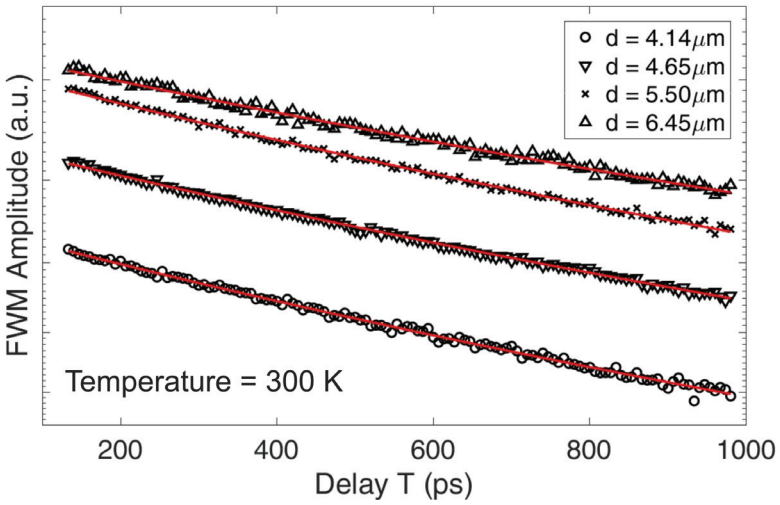

Figure 4.2: (color online) FWM signal intensity on a logarithmic scale as a function of delay T for a range of grating constants. The sample temperature is 300 K. The solid curves are fits using Eqn. 4.1.

Here we apply femtosecond four-wave mixing (FWM) to investigate carrier transport in $CH_3NH_3PbI_3$, highlighting the utility of this technique for application to a

wide range of organic-inorganic perovskites. Our experiments illustrate several advantages of this approach: (i) it involves a direct measurement of the ambipolar diffusion coefficient without any need for modeling; (ii) it is an all-optical (contactless) technique, applicable to the survey of a wide range of photovoltaic materials; (iii) the carrier lifetime may be accessed through fitting the grating period dependence or directly through differential transmission with the same apparatus, exploiting the versatility of the boxcar geometry; (iv) diffusive and trap-limited transport are easily distinguished through the interpulse delay dependence of the four-wave mixing signal; and (v) the in-plane transport configuration enables the motion of carriers to be directly compared with grain sizes and allows anisotropy of transport characteristics [149] to be evaluated through simple rotation of the sample. As an additional feature, transport may be studied using this technique with high time resolution at low carrier densities ($\sim 10^{15}$ to 10^{16} cm^{-3}), reflective of solar cell operating conditions. Our experimental results on solution-processed $CH_3NH_3PbI_3$ indicate diffusive transport within the first nanosecond following excitation, with a diffusion coefficient (D) of 1.7 $\pm$ 0.1 cm^2 s^{-1} and diffusion length (L_D) of 0.95 $\pm$ 0.07 μm. As this technique probes the ambipolar diffusion length, which is dominated by the transport of the slower carrier type (electrons or holes), the observation of L_D $\sim$four times larger than the measured average grain size of 250 nm indicates that defects tied to grain boundaries have a limited impact on transport, in agreement with recent experiments [100,149] and theoretical predictions of predominantly shallow traps. [154,155] The application of nonlinear optical FWM techniques to the study of transport in $CH_3NH_3PbI_3$ presented here builds upon recent studies of carrier-carrier interactions and exciton localization in this material using a two-pulse degenerate FWM configuration, [130, 156] as well as measurements of the third-order nonlinear susceptibility in perovskite thin films. [157]

4.3 Materials and Methods

4.3.1 Transient Grating Technique

In the four-wave mixing experiments, three noncollinear optical pulses with electric fields $\vec{E}_1(t)$, $\vec{E}_2(t\text{-}\tau)$, and $\vec{E}_3(t\text{-}(\tau+T))$ with corresponding wavevectors $\vec{k_1}$, $\vec{k_2}$, and $\vec{k_3}$

were focused onto the sample in a noncollinear boxcar geometry, [123] resulting in a fourth field emitted in the phase-matched direction $\vec{k_3} + \vec{k_2} - \vec{k_1}$ (See Fig. 4.1(c)). Interference between pulses $\vec{E}_1(t)$ and $\vec{E}_2(t\text{-}\tau)$ creates a periodic spatial modulation of the carrier density in the material, forming a transient grating. The grating undergoes decay due to recombination and lateral carrier transport in the material. A third delayed pulse $\vec{E}_3(t\text{-}(\tau+T))$, was used to probe the grating modulation depth by monitoring the diffracted signal as a function of time delay T between pulses $\vec{E}_2$ and $\vec{E}_3$. Provided carrier transport is diffusive, [2, 158] the FWM signal decays exponentially versus T, [2, 97] with the signal intensity proportional to:

$$I(T) \propto \exp\left(-T/T_s\right). \tag{4.1}$$

and the decay constant T_s determined by:

$$\frac{1}{T_s} = \frac{2}{T_L} + \frac{8\pi^2 D}{d^2}, \tag{4.2}$$

In Eqn. 4.2, T_L is the carrier lifetime, D is the ambipolar diffusion coefficient, λ is the center wavelength of the laser pulse, and the grating constant $d = \frac{\lambda}{2\sin(\theta/2)}$, where θ is the angle between the two incident beams. The slope of a linear fit of the inverse grating decay time versus $\frac{8\pi^2}{d^2}$ yields the ambipolar diffusion coefficient D, while the offset yields the carrier lifetime. The experimental boxcar geometry also permits differential transmission (DT) measurements using the same apparatus for a separate verification of the carrier lifetime. In this case, $\vec{E}_1(t)$ was blocked, $\vec{E}_2(t\text{-}\tau)$ served as the pump pulse (setting $\tau = 0$), and $\vec{E}_3(t\text{-}T)$ attenuated by approximately $100\times$ served as the probe pulse.

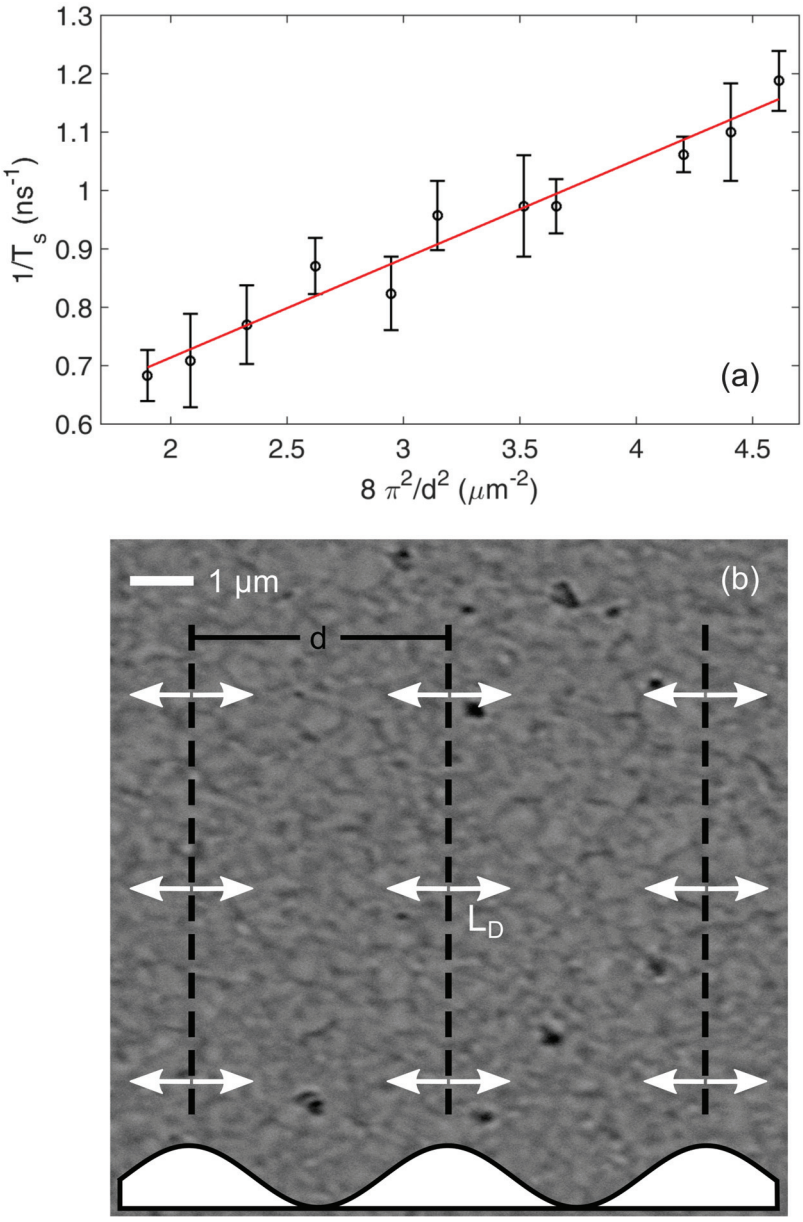

Figure 4.3: (color online) (a) Inverse signal decay time T_s^{-1} as a function of $8\pi^2/d^2$ measured at 300 K. The solid line is a fit of the data to Eqn. 4.2, yielding the parameters $D = 1.7$ cm^2 s^{-1} and $T_L = 5.3$ ns. (b) Scanning electron microscopy image of the $CH_3NH_3PbI_3$ sample. The initial spatial variation of the carrier distribution for a grating period of d = 4.14 μm is represented by the white filled region at the bottom, and the white arrows (with a magnitude equal to the measured diffusion length) represent diffusive carrier motion driven by the concentration gradient.

4.3.2 Experiment Details

The laser source used in these experiments was a Ti:sapphire oscillator producing 120 fs pulses with a bandwidth of ∼10 meV. The grating period d was varied by controlling the angle θ between the beams $\vec{E}_1(t)$ and $\vec{E}_2(t\text{-}\tau)$ by changing the effective focal length of a two-lens system. The excitation density in the sample was held constant as a function of d by measuring the beam diameter (150 - 200 μm) for each lens configuration and adjusting the laser power using neutral density filters to maintain a constant pulse fluence. All three optical pulses were s-polarized. At each delay T, the FWM signal as a function of the delay τ between $\vec{E}_1(t)$ and $\vec{E}_2(t\text{-}\tau)$ was detected with a fast amplified photodiode using a rapid scan technique mediated by a retroreflector attached to a vibrating speaker cone. This allowed the FWM signal at $\tau = 0$ fs to be easily separated from scattered light sources propagating along the same direction. The delay T between $\vec{E}_2(t\text{-}\tau)$ and $\vec{E}_3(t\text{-}(\tau+T))$ was varied using a computer-controlled delay stage.

4.3.3 Sample

The $CH_3NH_3PbI_3$ sample under investigation in this work was prepared using a modified sequential deposition procedure described in detail in Ref. [156]. A 1M PbI_2 solution in dimethylformamide was cast onto a sapphire substrate, and spun at 4000 rpm for 60 seconds. Next, an equal volume of methylammonium iodide was cast and spun at 3000 rpm for 60 seconds. The resulting film was annealed at 100°C resulting in a 305 nm thick layer of $CH_3NH_3PbI_3$. Scanning electron microscopy (SEM) measurements showed good uniformity, and x-ray diffraction (XRD) indicated full conversion to perovskite with no residual lead iodide. For the XRD and SEM studies, the exposure of the sample to air was limited to 1-2 hours. The linear absorption spectrum of a companion sample prepared at the same time using an identical procedure was measured with a Cary UV-Vis spectrometer, and is shown alongside the laser spectrum in Fig. 4.1(b). For all FWM experiments, exposure to air was avoided by mounting the sample in a compact optical cryostat within an argon glove box and sealing prior to transport to the FWM apparatus.

4.4 Results and Discussion

4.4.1 Transient Grating Results: Evidence of Ambipolar Carrier Diffusion

Fig. 4.1(d) shows the FWM signal at $\tau = 0$ fs versus pulse delay T at 300 K for a grating period of d = 4.14 μm. For these experiments, the laser was tuned to 760 nm, exciting unbound electron-hole pairs with energies within ∼10 meV of the band gap (Fig. 4.1(b)). [159] The excitation density was 1.6×10^{16} cm^{-3}. With the exception of the region of overlap of the excitation laser pulses, the four-wave mixing signal exhibits exponential decay over the full measurement range of 1 ns. The red curve in Fig. 4.1(d) shows a fit to Eqn. 4.1, yielding a grating decay time of $T_s = 840$ ps. Fig. 4.2 shows a logarithmic plot of the FWM signal as a function of delay for grating constants d = 4.14, 4.65, 5.50, and 6.45 μm. As shown by the quality of the linear fits, the FWM signal decays exponentially in all cases. The inverse decay time T_s^{-1} is plotted versus $8\pi^2/d^2$ in Fig. 4.3. The error bars represent the standard deviation of ten delay scans taken for each grating constant. The solid line in Fig. 4.3 is a linear fit using Eqn. 4.2. The slope (intercept) yields the ambipolar diffusion coefficient (carrier lifetime), corresponding to $D = 1.7 \pm 0.1$ cm^2 s^{-1} and $T_L = 5.3 \pm 0.5$ ns. As a self-consistency check, differential transmission measurements were also carried out using the same apparatus for the same total excitation carrier density (Fig. 4.4). These measurements yield a carrier lifetime of $T_L = 5.4 \pm 0.2$ ns, in good agreement with the value of 5.3 ns obtained from fitting the transient grating results. Using a one dimensional diffusion model, for which $L_D = \sqrt{DT_L}$, these fit results yield a diffusion length of 0.95 ± 0.07 μm. This value is in line with measurements of the ambipolar diffusion length on similar films using transient absorption microscopy techniques. [103]

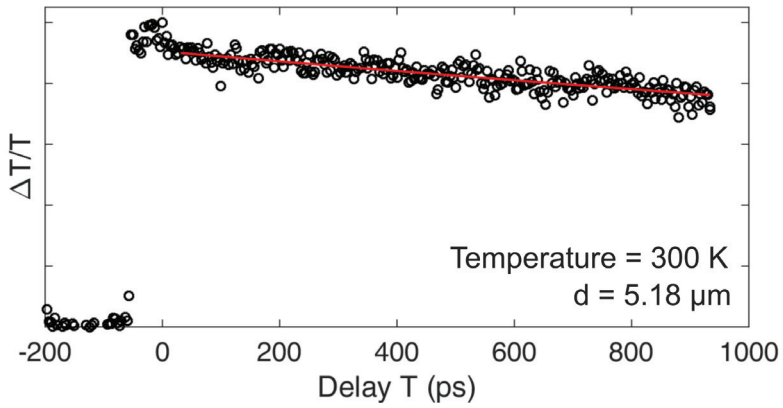

Figure 4.4: (color online) Results of differential transmission measurements using the same FWM boxcar apparatus on the $CH_3NH_3PbI_3$ sample under the same experimental conditions. The solid curve shows the result of a least-squares fit of the measured signal to an exponential decay, yielding $T_L = 5.4$ ns.

The good agreement between the experimental results and Eqn. 4.1 and 4.2 over the full range of accessible delays indicates that carrier transport is within the diffusive regime. Carrier trapping, which would lead to subdiffusive behavior, [160] therefore has a negligible influence on the carrier kinetics within the first nanosecond after excitation. This is in agreement with studies of $CH_3NH_3PbI_3$ thin films using transient absorption microscopy, [103] in which a diffusive model accounted for the spatiotemporal carrier occupation over a 3 ns time interval after excitation. (Similar to the case of transient absorption microscopy, the time scale over which transport may be probed using four-wave mixing is ∼1 ns, dictated by the length of the optical delay stage.) Using broadband THz spectroscopy, Valverde-Chavez *et al.* observed a rapid initial decay of mobility on a subpicosecond time scale in single crystal $CH_3NH_3PbI_3$ attributed to the charging of trap states and/or a charge-mediated phonon scattering mechanism. [108] The experiments in Ref. [108] were carried out at a much larger excited carrier density ($\sim 10^{18}$ cm^{-3}), suggesting that these charge-mediated effects turn on under stronger excitation conditions than our experiments.

4.4.2 Influence of Grain Size on Carrier Transport

Scanning electron microscopy measurements on the same $CH_3NH_3PbI_3$ film used for FWM experiments are shown in Fig. 4.3(b). A spatial Fourier analysis indicates the

presence of grains up to 500 nm in diameter, with a mean grain size of 250 nm. The observation of L_D $\sim$4 $\times$ larger than the mean grain diameter, together with the fact that this ambipolar diffusion length is limited by the slower carrier species, [158] indicates that grain boundaries do not constitute a significant barrier to carrier motion. This result is in agreement with recent measurements on solution processed $CH_3NH_3PbI_3$ using AC Photo Hall [100] and photocurrent imaging techniques [149] as well as theoretical calculations suggesting that the most prevalent point defects represent shallow traps and that grain boundaries have a relatively benign effect. [154, 155] In addition, screening by the methylammonium ions may play a role in reducing the rate of trapping by charged defects, [100] in line with the recently proposed large polaron model of carrier transport in perovskites. [120]

Reported values of the diffusion length in solution processed methylammonium lead iodide films have varied over the range 0.1 to 23 μm. [21,26,100–104,107,109,149] Differences in both the microstructure of the film and the optically-excited carrier density contribute to this broad range of values as these together dictate the carrier lifetime. [151] The application of a variety of experimental techniques to extract the transport characteristics also plays an important role in the observed variability. For instance, photoluminescence-based techniques only probe the transport of radiative species, TRMC and TDTHz techniques measure the sum of the electron and hole mobilities (μ_e+μ_h), AC Photo Hall measurements detect μ_h-μ_e, and TA microscopy and the FWM technique applied in this work both probe the ambipolar diffusion coefficient ($\mu_a = \frac{2\mu_e\mu_h}{\mu_e+\mu_h}$). In addition, while techniques that rely on electrical contacts can offer the advantage of probing transport in a working device, [102] uncertainties tied to the energetics of the contact interfaces can significantly influence the extracted results for L_D. [98] This highlights the need for a survey tool for probing transport in a wide range of photovoltaic materials such as the FWM transient grating technique presented here. We note that a steady-state photocarrier grating method relying on a change of photocurrent induced by interference of continuous wave laser beams [161,162] was recently applied to organic-inorganic perovskite films. [105] In contrast to the approach used in Ref. [105], the transient grating technique applied in this work does not require electrical contacts to the sample and provides access to dynamic information about the photocarrier response.

4.5 Conclusions

In conclusion, we have applied the all-optical four-wave mixing transient grating technique using a boxcar geometry to the study of carrier transport in a solution processed film of $CH_3NH_3PbI_3$, illustrating the power and flexibilty of this approach for application to emerging photovoltaic materials based on the organic-inorganic family of perovskites. Our experiments yield values for the carrier lifetime of 5.3 ± 0.5 ns and the ambipolar diffusion coefficient of 1.7 ± 0.1 cm^2 s^{-1}, corresponding to a diffusion length of 0.95 ± 0.07 μm. These fit values are obtained from the measured transient grating signal without the need for modeling, a consequence of the direct optical detection of the spatial motion of carriers. As four-wave mixing probes the transport of all electron-hole pair species within the optically-coupled region of the band structure, the transport properties of low-energy unbound electron-hole pairs studied here could be extended to excitons and band tail states by varying the wavelength of the excitation source. Our experiments show that this method provides a valuable rapid survey tool for probing macroscopic transport properties in the hybrid perovskites.

This research is supported by the Natural Sciences and Engineering Research Council of Canada, the Canada Foundation for Innovation, and the Canada Research Chairs program.

Chapter 5

Control of the Urbach band tail and Interband Dephasing Time with Post-Growth Annealing in Low-Temperature-Grown GaAs

Authors: D. Webber[1], X. Liu[2], M. Dobrowolska[2], J. K. Furdyna[2], K. C. Hall[1]

[1] Department of Physics and Atmospheric Science, Dalhousie University, Halifax, Nova Scotia B3H4R2, Canada

[2] Department of Physics, University of Notre Dame, Notre Dame, Indiana 46556, USA

Daniel Webber developed the control software, performed the experiments, and the data analysis. Xinyu Liu, Margaret Dobrowolska, and Jacek Furdyna grew and produced the samples. Daniel Webber and Kimberley C. Hall conceived the direction for research. Daniel Webber and Kimberley C. Hall wrote the manuscript, which has been submitted to Applied Physics Letters Materials.

5.1 Abstract

Femtosecond four-wave mixing experiments on low-temperature-grown (LT-) GaAs for a range of post-growth annealing temperatures indicate that the free carrier dephasing time is limited by scattering with As point defects for annealing temperatures below 550°C and that the Urbach band tail abruptly diminishes above 550°C due to the conversion of As-related point defects to As clusters. Our experiments also indicate a complex interplay of polarization source terms associated with the exciton and Urbach band tail for annealing temperatures below 550°C. These experiments shed light on the carrier dynamics and ultrafast nonlinear optical properties of LT-GaAs.

5.2 Introduction

GaAs grown at substrate temperatures in the range 200-300°C has found a variety of applications in optoelectronics, including fast photodetectors, [38, 46, 163] THz photonic sources and detectors, [52,53,164–167] and laser modelocking elements. [48] The unique characteristics of this material that make it attractive for such applications (semi-insulating conductivity, [36] short carrier lifetime, [38,168–170] and large band edge optical nonlinearity, [40]) stem from the incorporation of up to 0.6% excess arsenic during growth. [61] This excess arsenic leads to a high density of As_i and As_{Ga} point defects and associated midgap states [36, 61] as well as local potential fluctuations that lead to spatially localized states below the band gap (the *so-called* Urbach band tail). [59] The point defects lead to rapid trapping of band electrons [171] and pin the Fermi level in the gap resulting in semi-insulating behaviour. [36,62] The band tail states contribute to a large optical nonlinearity in the vicinity of the band gap due to the spatial localization of the electron and hole wavefunctions. [40]

In addition to these beneficial properties, the high density of defects also leads to undesirable effects. For instance, the optical promotion of carriers from the mid-gap states to the conduction band results in strong broad-band absorption that obscures the optical band edge. [58] In addition, the band tail states have been shown to reduce the rate of carrier relaxation due to a decreased cross section for trapping into the midgap defect levels, limiting the overall speed of the material response. [40] A good understanding of the defect landscape is therefore essential to optimize the material properties of LT-GaAs and related low-temperature-grown semiconductors for applications.

Post-growth annealing provides a means to control the optoelectronic properties of LT-GaAs. [36,58,61,62,110–114] A variety of techniques have been used to study the point defect density as a function of the growth and annealing temperature, including Hall effect, [36] electron paramagnetic resonance, [111] Auger spectroscopy, [61] positron annihilation, [112] and scanning tunneling microscopy. [113,114] These studies have shown that annealing reactions involving defect complexes of As_{Ga}, As_i, and V_{Ga} promote the diffusion of As_i and the resulting reduction in point defect density through the formation of As precipitates. [61,171,172] Much less is known about the influence of annealing on the Urbach band tail. This is due primarily to the

need to apply nonlinear optical spectroscopy, [40] which enables the band tail states to be isolated from the strong defect-induced absorption that dominates the linear optical response of LT-GaAs. [8, 58, 72]

Here we report the application of four-wave mixing (FWM) spectroscopy to study the influence of annealing on the optical properties of LT-GaAs. Our experiments show an increase in the interband dephasing time (T_2) with annealing temperature (T_a) up to 500°C. This indicates that arsenic point defects contribute strongly to carrier scattering in weakly-annealed LT-GaAs films. These scattering processes are diminished with annealing due to the reduction in the As_i and As_{Ga} point defects as precipitates begin to form, which has been found to occur for T_a as low as 300°C. [36, 173] The Urbach energy (E_U) was extracted in our experiments from the low-energy tail of the FWM spectrum for a range of T_a values. An abrupt decrease in E_U to values characteristic of high-temperature-grown GaAs was observed at $T_a = 550$°C, suggesting that the material must enter the regime of large arsenic cluster formation ($\geq$5 nm) [173] in order to diminish the local potential fluctuations responsible for band tail states. By extending our earlier FWM studies of as-grown films of LT-GaAs [8, 72] to lower excitation powers, our experiments also reveal a dip in the FWM response in the vicinity of the exciton. This dip is found to be insensitive to laser tuning and disappears when the sample is annealed at 550°C, indicating that it is tied to the coexistence of band tail and exciton signal contributions, reminiscent of a Fano resonance. [174] Polarization-dependent and prepulse FWM experiments indicate that this dip results from polarization interference between the exciton signal and the continuum of transitions within the Urbach band tail. Our experiments show that FWM spectroscopy provides a sensitive probe of the defect distribution in low-temperature-grown semiconductors, providing an avenue for tailoring these defects for applications such as saturable absorbers and THz switching devices.

5.3 Experimental Methods

The samples under investigation in this work are GaAs epilayers grown by molecular beam epitaxy on semi-insulating GaAs substrates held at 250°C. The As_2 to Ga equivalent pressure ratio during growth was 10:1 and the growth rate was 12 nm/minute. After growth, the LT-GaAs samples were mounted on a molybdenum substrate holder

using indium and annealed under high vacuum for 30 seconds inside the MBE chamber for temperatures T_a = 400°C to 600°C. For reference experiments, a companion GaAs epilayer grown at 600°C (HT-GaAs) was also prepared. For all samples a 175 nm $Al_{0.27}Ga_{0.73}As$ stop-etch layer was deposited prior to growth of the 800 nm thick GaAs epilayer to enable experiments in the transmission geometry. The samples were glued face down to sapphire windows using Norland optical adhesive, and the substrates were removed using mechanical polishing followed by wet etching.

Spectrally-resolved four-wave mixing experiments were carried out in the two-pulse self-diffraction geometry with the samples held at 80 K in an optical cryostat. The laser source used for these experiments was a mode-locked Ti:Sapphire oscillator producing tunable pulses with a duration of 25-30 fs. In the four-wave mixing experiments, two pulses $\vec{E_1}(t)$ and $\vec{E_2}(t-\tau)$ with wavevectors $\vec{k_1}$ and $\vec{k_2}$ are used to excite the sample, resulting in a spatially-modulated carrier density that leads to a transient optical grating. The FWM signal corresponds to self-diffraction of $\vec{E_2}$ from the transient carrier grating, which generates a field that propagates along the direction $2\vec{k_2} - \vec{k_1}$. Pulse $\vec{E_2}$ was approximately 4 times more intense than $\vec{E_1}$, and the total carrier density excited by the two excitation pulses was $\sim 1\times10^{16}$ cm^{-3}. The two excitation pulses were either both s-polarized (YY) or pulse $\vec{E_2}$ was rotated by 90 degrees (XY). The FWM signal was passed through a 0.25 m monochromator and measured as a function of interpulse delay (τ) and photon energy using a photomultiplier detector.

5.4 Results and Discussion

The FWM response of the LT-GaAs samples is shown in Fig. 5.1(a)-(e), together with the response of the HT-GaAs reference sample in Fig. 5.1(f). For these results, the excitation laser was tuned to 1.520 eV. The FWM signal for the LT-GaAs samples for $T_a \leq 500$°C contains two main features: *(i)* a peak associated with the exciton resonance (at approximately 1.5 eV, [8, 72]); and *(ii)* a signal originating from the optically-excited interband continuum transitions at higher detection energies. The exciton response is peaked at zero delay, while the peak position of the interband response moves to larger values of interpulse delay as T_a is increased. In addition, the FWM signal drops off slowly on the low-energy side of the exciton in the as-grown

sample, indicating a coherent response from the Urbach band tail. A pronounced dip is also observed on the high-energy side of the exciton in the LT-GaAs samples for $T_a \leq 500°C$. This feature is highlighted in Fig. 5.2, which shows the FWM spectrum from the as-grown LT-GaAs sample, alongside the response from HT-GaAs.

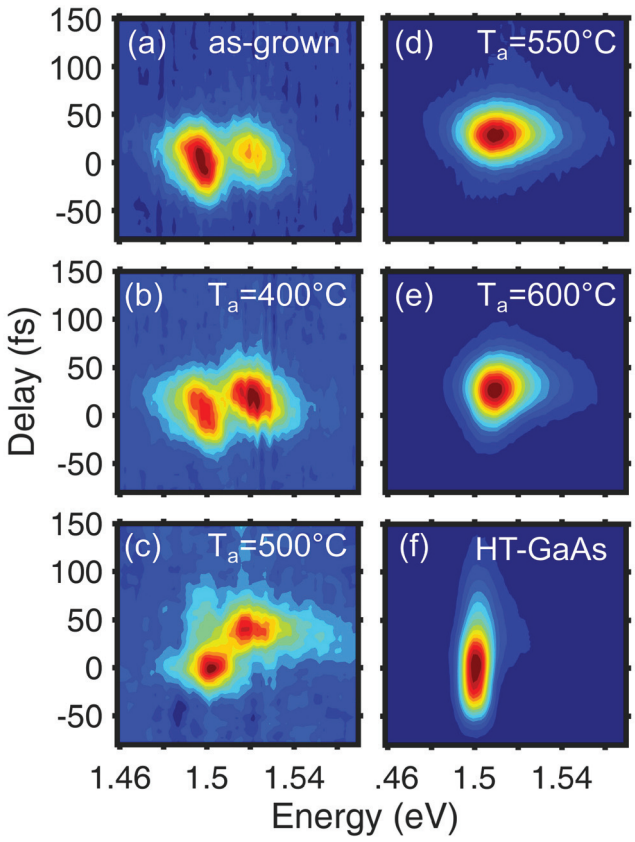

Figure 5.1: (color online) FWM results at T = 80 K for near resonant excitation for (a-e) LT-GaAs annealed at different temperatures and (f) HT-GaAs. The FWM data is presented as a function of delay between pulses E_1 and E_2 and detected photon energy.

An abrupt change in the signal characteristics occurs at an annealing temperature of 550°C: The interband continuum response grows substantially relative to the exciton signal, and the band tail contribution is strongly reduced. In the sample annealed at 600°C, the exciton response is apparent only as a shoulder for low energies in the vicinity of zero delay. The response in HT-GaAs includes a strong exciton peak at zero delay and an interband continuum response that peaks at positive delay values and higher energies, consistent with earlier FWM studies on high-temperature-grown semiconductors. [80,85] No evidence of an Urbach band tail is observed in the results

from HT-GaAs, reflecting the low defect density in this sample.

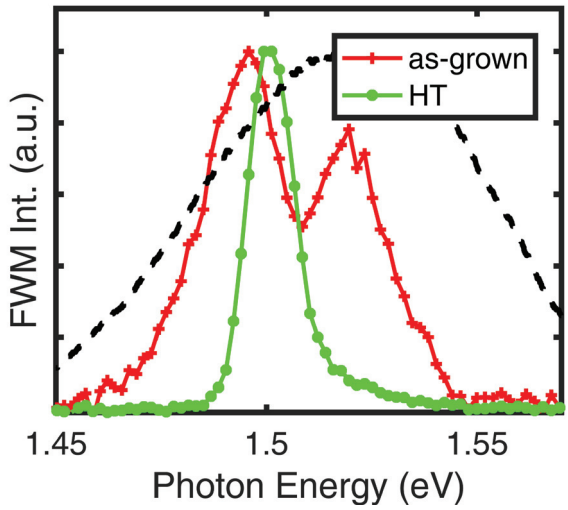

Figure 5.2: (color online) Normalized spectral cuts of the FWM contour plots shown in Fig. 5.1 for as-grown LT-GaAs and HT-GaAs at $\tau = 25$ fs. The laser spectrum is indicated by the black dashed curve.

A smooth transition in the optical joint density of states is expected between the interband continuum and the band tail contributions to the absorption in LT-GaAs. As a result, the dip on the high-energy side of the exciton peak in Fig. 5.2 is not expected. The spectral location of the dip does not change as the laser is tuned to higher or lower energies, as shown in Fig. 5.4(c) and (d) for the as-grown sample. The dip was observed for all samples with annealing temperature below 550°C, but is absent for higher annealing temperatures. (The results of corresponding measurements of the FWM signal from the sample with $T_a = 600$°C are shown in Fig. 5.4(e) and (f).) These findings suggest that the presence of this dip is linked to the interplay of the exciton and band tail responses.

The above assertion can be verified by carrying out experiments that suppress the exciton feature. In previous FWM experiments on LT-GaAs, the exciton signal was identified as resulting from excitation-induced dephasing (EID), [8] through which non-degenerate Coulomb interactions of excitons with carriers excited on the interband continuum lead to diffraction of the exciton polarization from a grating in the total free carrier population. [6, 74, 80, 85] Such an EID signal is only present at zero delay due to interference of signal contributions from population gratings over a

range of transition energies in the interband continuum. This exciton signal may be suppressed by either exposing the sample to a prepulse (which excites additional carriers that screen the EID coefficient [4,73,121]) or by using cross-polarized excitation (which eliminates the free carrier population grating due to the phase shift between grating contributions corresponding to carriers with opposite spin [121]). The results of these experiments are shown in Fig. 5.5. The node is observed to vanish with the reduction of the exciton signal. This points to destructive interference between the exciton and band tail four-wave mixing responses as the origin of the observed dip. A similar effect was observed in experiments at the spin-orbit split-off exciton in InP, where the role of the band tail continuum was played by interband transitions associated with the heavy-hole and light-hole valence bands. [74]

Disorder in the crystal structure leads to local potential fluctuations and an associated quasi-continuum of weakly-bound energy states in the vicinity of the band extrema. These band tails result in an absorption edge that is well described by $\alpha(\omega) \propto e^{\frac{\hbar\omega-\hbar\omega_0}{E_U}}$, [59] where $\alpha(\omega)$ is the absorption coefficient at frequency ω, $\hbar\omega_0$ is the effective band gap of the disordered crystal, and E_U is the Urbach energy. Assuming that the dipole moment of the band tail transitions is approximately constant over the energy range probed, the Urbach energy may be extracted from the slope of the natural logarithm of the low energy tail of the FWM signal. The zero-delay FWM spectrum for the LT-GaAs samples is shown in Fig. 5.3(a). For these results, the center of the excitation laser pulses was tuned 30 meV below the band gap. Extracted values of E_U for each sample are plotted in Fig. 5.3(b). The Urbach energy is observed to be relatively constant for temperatures ≤ 500°C, and abruptly decrease at $T_a = 550$°C. The dashed line in Fig. 5.3(b) shows the Urbach energy reported previously for GaAs, [64, 175] which is consistent with the value extracted in this work for the HT-GaAs reference sample. Our results indicate that, for T_a above 550°C, the Urbach energy is similar to the value in HT-GaAs.

The four-wave mixing signal from the interband continuum may be treated as a photon echo, characteristic of an inhomogeneously-broadened transition. [1] The peak position of such a photon echo signal versus interpulse delay is determined by both the degree of inhomogeneous broadening ($\delta\omega$, dictated by the laser pulse spectrum and the effective band gap) and the dephasing time (T_2). Since T_2 is comparable to $\delta\omega^{-1}$

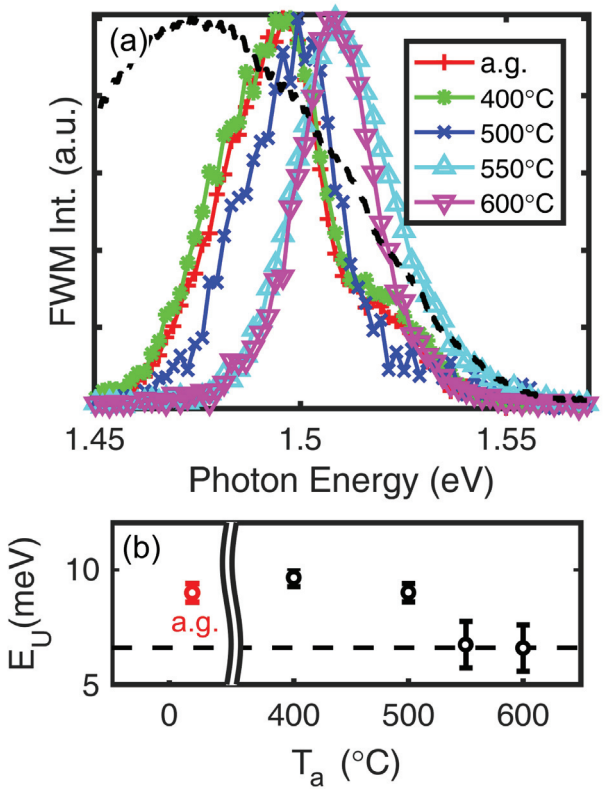

Figure 5.3: (a) Normalized spectral cuts of the FWM signal at $\tau = 0$ fs for LT-GaAs at different annealing temperatures. The black dashed line is the laser spectrum used for these measurements. (b) Extracted values for the Urbach energy E_U as a function of annealing temperature (T_a). The black dashed line is the value for E_U for HT-GaAs from Ref. [64].

in the case considered here, [13] an increase in T_2 leads to a shift in the peak FWM signal to larger values of interpulse delay. Our observation of a shift in the interband continuum response to larger delay values in LT-GaAs between the results for the as-grown sample, and the samples annealed at 400°C and 500°C therefore reflects an annealing-induced increase of the interband dephasing time. Since the density of As_i and As_{Ga} point defects and/or defect complexes is reduced with annealing, our results indicate that these defects play a role in free carrier dephasing in weakly-annealed LT-GaAs for the conditions considered here (80 K, 1×10^{16} cm^{-3}). The peak position of the photon echo response in LT-GaAs saturates for T_a larger than 550°C at a value similar to that observed for HT-GaAs. This suggests that defect-related scattering has been reduced below the rate of carrier scattering with phonons and other carriers

for $T_a \geq 550°C$.

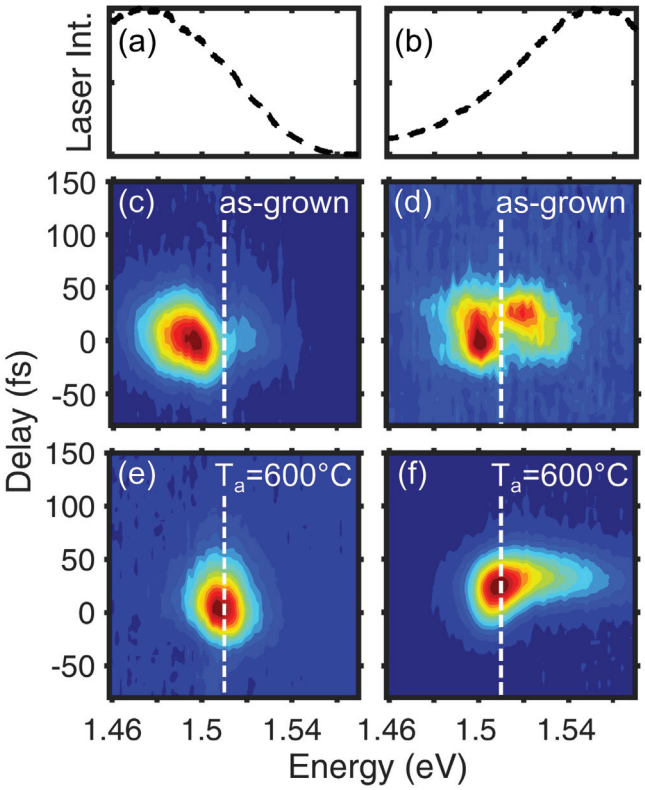

Figure 5.4: (a,b) The laser spectrums for red-tuned and blue-tuned excitation respectively. FWM results for (c,d) as-grown LT-GaAs and (e,f) LT-GaAs annealed at 600°C for the two laser tunings in (a,b) respectively. The white dashed line at a photon energy of 1.510 eV highlights the dip in the spectrum for as-grown LT-GaAs, which disappears with annealing for $T_a \geq 550°C$.

Our observations of an increase in the dephasing time for free carriers and a reduction in the Urbach energy with annealing in LT-GaAs are consistent with the reduction in the density of As_{Ga} and As_i point defects. As_i and V_{Ga} have been found to assist the diffusion of As_i defects at temperatures as low as 300°C. [36, 173] The increase in T_2 observed here for $T_a \leq 500°$ likely reflects an increase in the rate of diffusion of these point defects with temperature in the regime in which precipitates are beginning to form. [173] Our experiments, which highlight the high sensitivity of the interband dephasing time in LT-GaAs to changes in the density of point defects, indicate that scattering with these defects is a key factor in carrier relaxation and

transport in LT-GaAs subject to annealing at temperatures below 500°C. Our observation of a higher threshold annealing temperature for the reduction in the Urbach energy indicates that a substantial fraction of the point defects must be replaced by As clusters in order to significantly alter the potential landscape experienced by carriers in the crystal. The mean precipitate diameter was observed in Ref. [173] to increase sharply to values exceeding 5 nm for anneal temperatures exceeding 550°C. The formation of As clusters at the expense of point defects reduces the density of localization centers and thereby decreases the density and energetic extent of the band tail states. A faster evolution of the defect distribution with higher annealing temperatures [36, 173, 176] may have contributed to the abruptness in the change of the Urbach energy with annealing temperature observed here, in line with earlier studies of the influence of annealing on the linear absorption spectrum and carrier lifetime in LT-GaAs. [58, 65, 176]

We note that Segschneider *et al.* detected band tail states in an LT-GaAs sample that had been annealed at 600°C using nonlinear pump probe spectroscopy. [40] The persistence of the band tail in the experiments of Ref. [[40]] despite the high temperature used for annealing likely reflects the lower growth temperature of 200°C for the sample studied, which together with the annealing temperature determines the post-annealing defect density. [173, 177]

5.5 Conclusions

In summary, we have applied four-wave mixing spectroscopy to study the influence of annealing on the band edge optical properties and carrier kinetics in LT-GaAs. Our experiments indicate that the interband dephasing time is limited by scattering with As-related point defects for annealing temperatures below 500°C, while for higher temperatures the dephasing rate is in line with the value in high-temperature-grown GaAs, known from previous studies to be limited by scattering by phonons and other carriers. These findings therefore shed light on the scattering dynamics limiting carrier mobility in annealed LT-GaAs films, in which annealing temperatures as low as 400°C may offer the best compromise between resistivity and trapping time for application to THz sources and detectors. [178] Our experiments indicate an abrupt reduction in the Urbach energy for an annealing temperature of 550°C to values in line

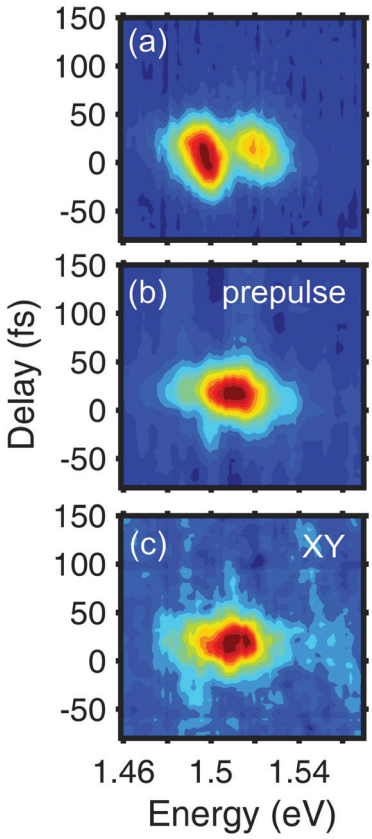

Figure 5.5: (color online) FWM results in as-grown LT-GaAs for (a) two-pulse excitation. (b) Same conditions as in (a) but in the presence of a temporally coincident prepulse. The power of the prepulse beam was comparable to the power in each of the two excitation beams. (c) Same conditions as (a) but for cross-linearly polarized pulses (XY).

with GaAs grown at elevated temperatures. The evolution of the Urbach energy with annealing temperature may be accounted for by the conversion of As-related point defects to As clusters, which eliminates the potential fluctuations responsible for the band tail states. Our experiments also reveal evidence of interference of four-wave mixing polarization source terms associated with the exciton and Urbach band tail. These findings shed light on the optical properties and carrier scattering processes in low-temperature-grown GaAs and will aid in the optimization of this materials as well as related low-temperature-grown materials for applications in optoelectronics.

This research is supported by the Natural Sciences and Engineering Research Council of Canada, the Nova Scotia Research and Innovation Program, and the National Science Foundation (Grant DMR1400432).

Chapter 6

Signatures of four-particle correlations associated with exciton-carrier interactions in coherent spectroscopy on bulk GaAs

Authors: D. Webber[1], B. L. Wilmer[2], X. Liu[3], M. Dobrowolska[3], J. K. Furdyna[3], A. D. Bristow[2], K. C. Hall[1]

[1] Department of Physics and Atmospheric Science, Dalhousie University, Halifax, Nova Scotia B3H4R2, Canada

[2] Department of Physics and Astronomy, West Virginia University, Morgantown, West Virginia 26506-6315, USA

[3] Department of Physics, University of Notre Dame, Notre Dame, Indiana 46556, USA

Daniel Webber used the 2DFTS experimental apparatus built by Brian L. Wilmer and Alan. D. Bristow to carry out 2DFTS experiments on GaAs. Daniel Webber developed the optical Bloch equation computer code and used it to carry out the theoretical simulations and the data analysis. Xinyu Liu, Margaret Dobrowolska, and Jacek Furdyna grew and produced the samples. Daniel Webber and Kimberley C. Hall conceived the direction for research. Daniel Webber and Kimberley C. Hall wrote the manuscript with input from all authors.

6.1 Abstract

Transient four-wave mixing studies of bulk GaAs under conditions of broad bandwidth excitation of primarily interband transitions have enabled four-particle correlations tied to degenerate (exciton-exciton) and nondegenerate (exciton-carrier) interactions to be studied. Real two-dimensional Fourier-transform spectroscopy (2DFTS) spectra

reveal a complex response at the heavy-hole exciton emission energy that varies with the absorption energy, ranging from dispersive on the diagonal, through absorptive for low-energy interband transitions to dispersive with the opposite sign for interband transitions high above band gap. Simulations using a multilevel model augmented by many-body effects provide excellent agreement with the 2DFTS experiments and indicate that excitation-induced dephasing (EID) and excitation-induced shift (EIS) affect degenerate and nondegenerate interactions equivalently, with stronger exciton-carrier coupling relative to exciton-exciton coupling by approximately an order of magnitude. These simulations also indicate that EID effects are three times stronger than EIS in contributing to the coherent response of the semiconductor.

6.2 Introduction

The strong, long-range Coulomb interaction between electrons has a profound influence on the optical response of a variety of material systems, including biological photosynthetic complexes [179, 180], organic polymer systems [181] and semiconductor heterostructures [12]. The need to unravel these so-called *many-body* effects, which play a crucial role in a variety of optoelectronic devices such as photodetectors and solar cell technologies, has led to a comprehensive research effort spanning more than two decades [6, 73, 74, 85, 88, 93, 94, 123, 182–187]. Semiconductor materials provide an excellent model system for studying Coulomb correlations, in which the interactions between bound electron-hole pairs called excitons may be studied using coherent optical techniques such as time-resolved four-wave mixing (TFWM). In such experiments, correlations between electron-hole pairs lead to additional contributions to the measured optical signal, [12] providing a means to separate out the influences of different types of interactions [6, 73, 74, 85, 88, 185]. The development of 2DFTS techniques [188], in which measurement of the phase of the four-wave mixing signal allows correlations at different absorption and emission frequencies to be identified [132, 189], have enabled the further separation of these signal contributions providing additional insight into many-body interactions [93, 94, 123, 182, 186, 187]. In recent years, a complex hierarchy of correlations involving successively larger numbers of particles have been revealed using these powerful spectroscopy techniques [180, 182–184].

Existing experiments have primarily focused on exciton-exciton interactions in semiconductor quantum wells [88, 93–95, 123, 182, 184, 187, 190] in which excitonic resonances involving the heavy-hole and light-hole valence bands are separated in energy but linked to a common ground state via the shared conduction band levels. Recent studies have revealed bound biexciton states [184,191], enabled the separation of coherent and incoherent contributions to the many-body related signals [95], and have indicated the dominance of effects beyond the Hartree-Fock approximation in the coherent response of the semiconductor [123]. Much less attention has been paid to nondegenerate four-particle correlations involving excitons and unbound electron-hole pairs [70, 73, 74, 85, 186], yet for excitation with broad bandwidth laser pulses such effects strongly dominate the overall coherent emission. This was apparent from early TFWM studies that revealed a dramatic enhancement of the exciton response when unbound electron-hole pairs are simultaneously excited [70]. Coupling of the exciton to unbound electron-hole pairs at higher energies was found to account for this enhancement of the exciton signal [6,85], although the relative importance of EID and EIS was not clear. 2DFTS studies were able to spectrally separate the exciton signal contributions tied to exciton-exciton and exciton-carrier interactions [186], but the relative importance of various coupling effects to the measured signals remained unclear [182, 186].

Here we report TFWM and 2DFTS experiments on bulk GaAs with the laser pulses energetically tuned above the band gap to elucidate the nature of exciton-continuum interactions. A strong enhancement of the exciton response in TFWM is observed, and the 2DFTS results indicate separate contributions to the exciton signal tied to degenerate and nondegenerate many-body interactions, consistent with previous reports [70, 73, 186, 192]. The real part of the rephasing 2DFTS signal reveals a rich dispersive structure that was not evident in earlier 2DFTS studies of the exciton-continuum coupling because only the amplitude spectra were detected [91,186] or the signal was measured over a narrower range of energies [94, 95]. This complex spectral structure prevents a simple assignment of EID and EIS effects to different parts of the spectra, as has been done in previous experiments under resonant excitation of the exciton [182]. Simulations of the measured 2DFTS results using a density matrix treatment within a multi-level model augmented with a phenomenological treatment

of many-body effects [193] provide excellent agreement with both the amplitude and real 2DFTS spectra, including the observed dependence on excited carrier density. The multi-level scheme includes strain-split heavy- and light-hole excitons and a broad continuum of states that is capable of modeling unexplored non-degenerate 2DFTS contributions. Our simulations indicate that EID and EIS coupling affects degenerate and nondegenerate interactions equivalently, and that exciton-continuum coupling via these effects is an order of magnitude stronger than exciton-exciton coupling, in agreement with past prepulse TFWM experiments [4]. For the conditions of our experiments under short pulse excitation of primarily continuum states, four-particle interactions tied to EID have a three-fold stronger influence on the coherent response of the semiconductor than EIS.

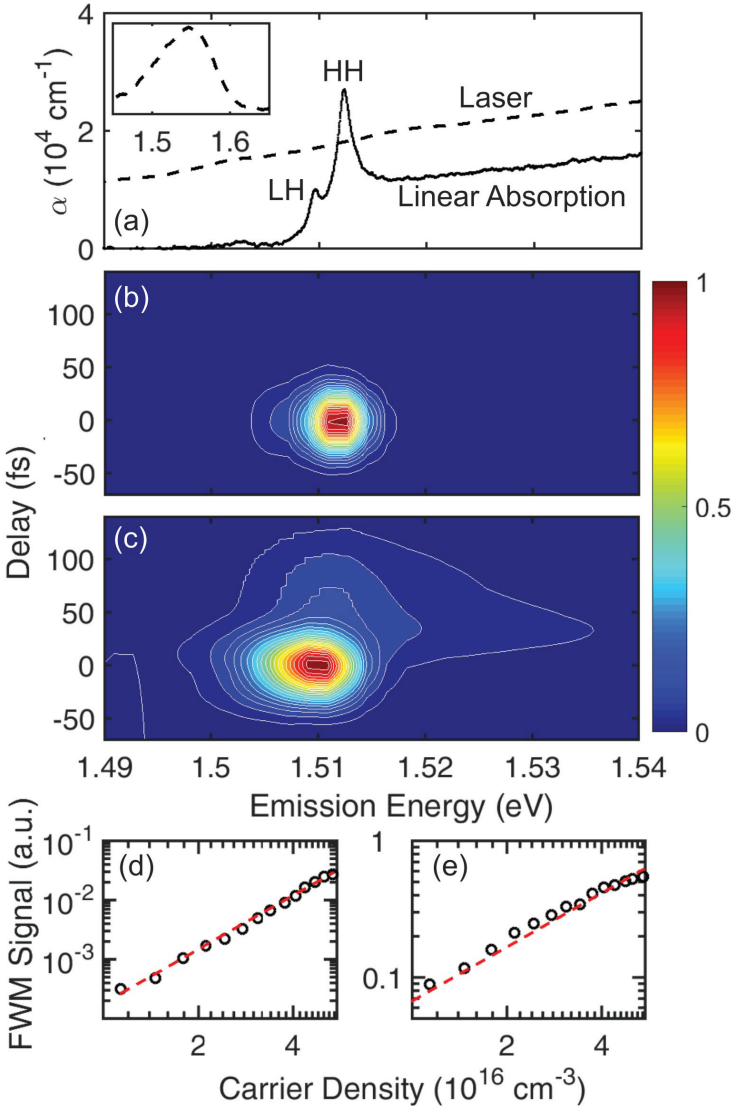

Figure 6.1: (color online) (a) Linear absorption (solid curve) of the GaAs sample showing the heavy-hole exciton (HH) and light-hole exciton (LH) resonances together with the laser spectrum (dashed) used in the TFWM experiments. Inset: Laser spectrum plotted over a wider energy range. (b) TFWM results at 10 K as a function of time delay (τ) between $\vec{E}_1$ and $\vec{E}_2$ and detection photon energy for an excited carrier density of $8.0 \times 10^{15}\text{cm}^{-3}$; (c) Same as (b) for a density of $5.4 \times 10^{16}\text{cm}^{-3}$; (d) The four-wave mixing signal as a function of density for a detection photon energy within the interband continuum at 1.53 eV; (e) Same as (d) for detection at the exciton peak. The red dashed line in (d,e) is a fit to a power law, showing cubic scaling for the interband continuum signal and weaker scaling for the exciton response.

6.3 Materials and Methods

6.3.1 TFWM

In a TFWM experiment, three optical pulses with wavevectors $\vec{k}_1$, $\vec{k}_2$, and $\vec{k}_3$ are focused onto the sample, generating a third-order nonlinear polarization that emits light in the direction $\vec{k}_3$+$\vec{k}_2$-$\vec{k}_1$. The spectral and temporal composition of this signal contains a wealth of information about the optical transitions within the sample that are in resonance with the laser pulse. For instance, measurement of the signal as a function of the time delay between the excitation pulses and the detection photon energy may be used to determine the coherence lifetime of excitons and unbound electron-hole pairs [4, 194], to gain insight into the optical joint density of states of doped semiconductors [13, 71], and to study many-body interactions between excited electron-hole pairs [6, 8, 74, 85]. The high sensitivity of this technique to many-body effects stems from polarization diffraction contributions to the measured signal tied to Coulomb-induced coupling of the polarization on a given optical transition to other transitions [12]. TFWM has been used extensively to study the nonlinear optical response of semiconductor systems over the past two decades [4, 6, 8, 13, 70–74, 79, 85, 88, 185, 194–196].

Two-pulse, degenerate spectrally-resolved four-wave mixing experiments were carried out on a bulk GaAs sample held at 10 K using 1.55 eV, 30 fs pulses with a full-width at half maximum bandwidth of 78 meV. The laser spectrum is shown in Fig. 6.1(a). Two collinearly-polarized excitation pulses $\vec{E}_1$ and $\vec{E}_2$ with wavevectors $\vec{k}_1$ and $\vec{k}_2$ were focused onto the sample in the self-diffraction geometry (i.e. $\vec{k}_3$=$\vec{k}_2$). The four-wave mixing signal emitted along ($2\vec{k}_2$-$\vec{k}_1$) was spectrally resolved using a 0.25 m monochromator, and the intensity was measured as a function of the delay between the two excitation pulses using a photomultiplier tube. The excitation carrier density was estimated using the measured spot size of 70 μm and by measuring the fraction of transmitted power through the sample from both beams taking into account reflections from the cryostat windows. Further details regarding the TFWM setup are provided in Ref. [197].

6.3.2 2DFTS

Two-dimensional Fourier-transform spectroscopy is an enhanced version of a three-pulse spectrally-resolved four-wave mixing experiment. In contrast to a standard TFWM experiment where the intensity of the four-wave mixing emission is measured, in a 2DFTS experiment both the amplitude and phase of the coherent emission are detected using spectral interferometry techniques [133]. By Fourier transforming the coherently detected signal as a function of the time delay between the first and second pulses (the so-called one-quantum rephasing geometry [132]), one can measure correlations between contributions to the signal at different absorption and emission frequencies. This enables the separation of signals tied to coupling of resonances via a common ground state [198], and many-body effects tied to degenerate and nondegenerate interactions [182, 186]. 2DFTS can also reveal the degree of homogeneous and inhomogeneous broadening of excitonic resonances [92, 199], separate excitonic and biexcitonic contributions to the measured response [123, 184] and detect Raman coherences [198]. Several experimental approaches have been implemented to achieve the necessary phase stability between pulses, including pulse shaping [189], diffractive optics [200], and active interferometric feedback loops utilizing a collinear continuous-wave laser [132].

Two-dimensional Fourier transform spectroscopy experiments were conducted on the GaAs sample using a multidimensional optical nonlinear spectrometer (MONSTR). More information about this technique, which utilizes three active interferometric feedback loops for phase-stability, can be found in Ref. [132]. The process for retrieval of the global phase of the four-wave mixing signal is described in Ref. [201]. Three optical pulses, $\vec{E}_1$,$\vec{E}_2$, and $\vec{E}_3$ with wavevectors $\vec{k}_1$, $\vec{k}_2$, and $\vec{k}_3$ were focused onto the sample that was held at 10 K in a closed cycle optical cryostat. Experiments were performed with either parallel linear (XXX) or cross linear (XYY) polarization configurations. For these experiments, the center photon energy of the laser pulse was 1.527 eV with a bandwidth of 19 meV and a pulse duration of approximately 100 fs. The four-wave mixing signal emitted along $\vec{k}_3$+$\vec{k}_2$-$\vec{k}_1$ was heterodyne detected with a known local oscillator, and the resulting spectral interferogram was measured using a 1 m monochromator. The delay between $\vec{E}_2$ and $\vec{E}_3$ was held fixed at T = 200 fs.

6.3.3 Samples

The sample investigated in this work was a GaAs epilayer grown by molecular beam epitaxy on a semi-insulating GaAs substrate held at 600°C. Prior to deposition of the 800 nm GaAs layer, a 175 nm AlGaAs stop-etch layer was deposited onto the substrate to permit experiments in the transmission geometry. The sample was glued top side down onto a c-cut sapphire window and the substrate was removed using a combination of mechanical polishing and wet-etching. The linear absorption spectrum of the GaAs sample at 10 K was measured by taking the ratio of the incident and transmitted light using a tunable modelocked Ti:Sapphire oscillator as the excitation source. The spectra at each laser tuning were detected using a 0.75 m monochromator and photomultiplier tube detector. The absorption coefficient was extracted from the raw transmission data using a self-consistent model that incorporates multiple reflections within the sample layer. The sample exhibits two peaks at 1.5100 eV and 1.5125 eV, corresponding to the light-hole and heavy-hole exciton resonances, respectively. Due to differing thermal expansion coefficients of GaAs and the sapphire substrate, which were bonded at room temperature, biaxial tensile strain is produced in the GaAs layer at low temperature, lifting the degeneracy of the valence bands [128, 129].

6.4 Numerical Simulations

We have done numerical simulations of the 2DFTS response of the bulk GaAs sample using a multilevel model [193] within the density matrix approach in the rotating wave approximation. The multilevel system under study is shown pictorially in Fig. 6.2(b). For the linearly-polarized excitation conditions considered here, the strain-split heavy-hole and light-hole exciton resonances (at energies $\hbar\omega_{\mathrm{LH}}$ and $\hbar\omega_{\mathrm{HH}}$) form an effective three-level system due to the shared conduction band states. The interband transitions above the band gap are approximated using ten resonances of varying energy ($\hbar\omega_C$), with each resonance separated by 1.8 meV. The effects of excitation-induced dephasing and excitation-induced shift on the exciton resonances were modeled using

a dephasing rate and resonance frequency that depend on the total excited electron-hole population:

$$\begin{aligned} \frac{1}{T_2} &= \frac{1}{T_2^0} + \gamma_{\mathrm{EID}}^{\mathrm{X}} N_{\mathrm{X}} + \gamma_{\mathrm{EID}}^{\mathrm{C}} N_{\mathrm{C}} \\ \omega &= \omega_0 + \gamma_{\mathrm{EIS}}^{\mathrm{X}} N_{\mathrm{X}} + \gamma_{\mathrm{EIS}}^{\mathrm{C}} N_{\mathrm{C}} \end{aligned} \tag{6.1}$$

where T_2^0 and ω_0 are the exciton dephasing time and resonance frequency in the absence of excitation, N_X is the sum of the heavy-hole and light-hole exciton densities, N_C is the total unbound electron-hole pair density, and $\gamma_{\mathrm{EID/EIS}}^{\mathrm{X}}$ and $\gamma_{\mathrm{EID/EIS}}^{\mathrm{C}}$ are the coefficients representing the strength of exciton-exciton and exciton-continuum coupling. The strength of many-body interactions was assumed to be equal for the heavy-hole and light-hole excitons, and larger for coupling of each exciton transition to the interband continuum than for exciton-exciton coupling to reflect a stronger measured exciton scattering rate involving free carriers [4]. This treatment of many-body effects incorporates degenerate and nondegenerate coupling as each excitonic transition is coupled to the heavy-hole and light-hole exciton populations and to population on the full bandwidth of continuum transitions. A population relaxation time of 15 ps was assumed for all transitions, and a value of T_2^0 of 1 ps was used for the excitonic transitions [4] and 120 fs for the continuum transitions [13]. The many-body coupling coefficients $\gamma_{\mathrm{EID}}^{\mathrm{C,X}}$ and $\gamma_{\mathrm{EIS}}^{\mathrm{C,X}}$ were taken as adjustable parameters in fitting the experimental 2DFTS results.

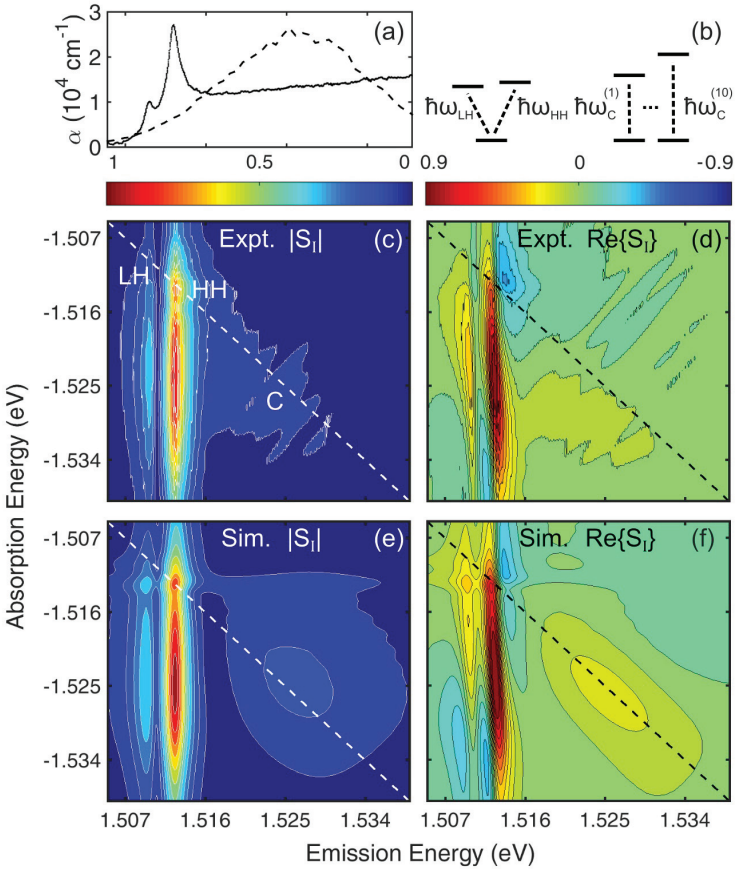

Figure 6.2: (color online) (a) Linear absorption (solid curve) with the laser spectrum (dashed) used in the 2DFTS experiments. (b) The strain-split heavy-hole and light-hole excitons were modeled as a three-level system with transition energies $\hbar\omega_{HH}$ and $\hbar\omega_{LH}$, respectively. The interband transitions were modeled as ten independent equally-spaced two-level systems with transition energies $\hbar\omega_C^{(1)}..\hbar\omega_C^{(10)}$. (c)/(d) Experimental results for the amplitude (c) and real part (d) of the 2DFTS signal. These data were taken with parallel polarizations in the two input excitation pulses (e)/(f) Simulation results for the amplitude (e) and real part (f) of the 2DFTS signal using the optimum EID and EIS parameters.

In a four-wave mixing experiment, only a single spatial component of the total polarization is measured (e.g. along $\vec{k}_3$+$\vec{k}_2$-$\vec{k}_1$). In the simulation, the four-wave mixing signal was extracted from the polarization through projection of this spatial

component [196]. To achieve this, the light field was taken as:

$$\begin{aligned} E(\vec{r},t) = \; & e^{i\vec{k_1}\cdot\vec{r}}\left[E_0(t) + E_0(t-\tau)e^{i\omega\tau}e^{i\phi}\right. \\ & \left. + E_0(t-T)e^{i\omega T}e^{i\psi}\right] + \text{c.c.}, \end{aligned} \tag{6.2}$$

where c.c. denotes the complex conjugate of the first term, E_0 is the pulse envelope (taken to be Gaussian with a pulse width of 100 fs), and $\hbar\omega$ is the energy of the laser pulse (1.527 eV). The light field depends only on two phase factors $\phi = (\vec{k_2} - \vec{k_1}) \cdot \vec{r}$ and $\psi = (\vec{k_3} - \vec{k_1}) \cdot \vec{r}$. The four-wave mixing signal is then given by:

$$P(t,\tau) = \frac{1}{4\pi^2}\sum_{x=1}^{4}\sum_{y=1}^{4} P(t,\tau,\phi_x,\psi_y)e^{i\phi_x}e^{i\psi_y}. \tag{6.3}$$

$P(t,\tau,\phi_x,\psi_y)$ is the macroscopic polarization (determined from the density matrix components) at each delay τ and each combination of phase angles ϕ_x and ψ_y. For computational convenience, the phase was taken discretely as $\phi_x = \pi x/2$ and $\psi_y = \pi y/2$. A Fourier transform of the four-wave mixing signal with respect to time and delay yields the emission and absorption frequency axes, respectively.

6.5 Results and Discussion

6.5.1 TFWM on Bulk GaAs: Exciton Enhancement Through Nondegenerate Interactions

Results of spectrally-resolved TFWM experiments for an excitation density of 8.0×10^{15} cm^{-3} are shown in Fig. 6.1(b). The contour scale indicates the amplitude of the four-wave mixing signal as a function of delay between the two excitation pulses and the emission energy. The laser excitation spectrum for these experiments is shown in Fig. 6.1(a), together with the linear absorption spectrum of the sample. A single peak is observed at approximately 1.512 eV tied to the combined response of the heavy-hole and light-hole excitons, which are not separately detected due to the limited resolution of the measurements. The most notable aspect of these results is that the exciton peak strongly dominates the nonlinear optical response of the bulk GaAs sample even though the laser spectrum is tuned above the exciton resonance, exciting primarily the continuum of unbound electron-hole pair transitions. The exciton response persists only for a narrow range of delay values centered at zero delay,

with a full width at half maximum similar to the pulse autocorrelation, despite being spectrally narrow in comparison to the pulse bandwidth.

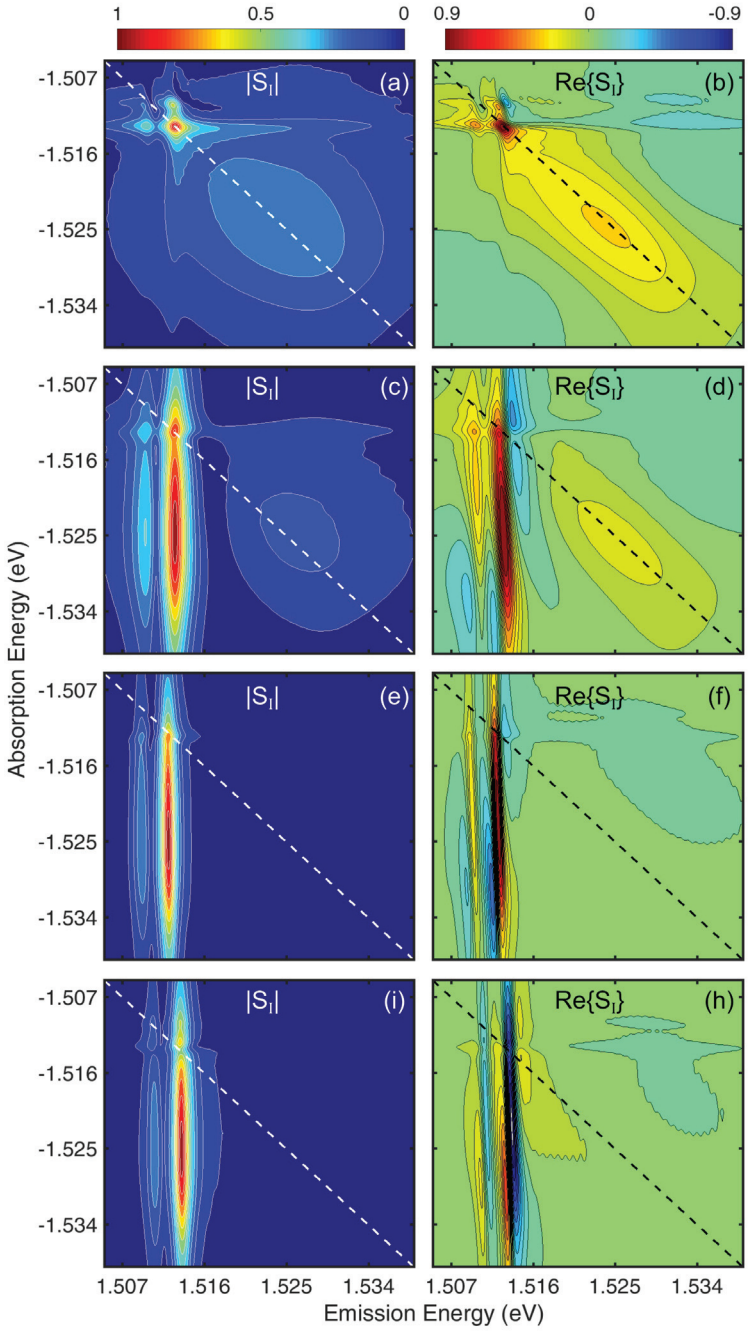

Figure 6.3: (color online) Simulation results of the normalized 2DFTS signal for varying levels of EID and EIS. (a,b) Amplitude and real part of the calculated 2DFTS signal with no EID or EIS. (c,d) Simulated results with no EIS with EID coefficients governing exciton-exciton and exciton-continuum interactions of $\gamma^{\mathrm{X}}_{\mathrm{EID}}=0.27\times10^{-4}$ cm^3 s^{-1} and $\gamma^{\mathrm{C}}_{\mathrm{EID}}=3.6\times10^{-4}$ cm^{3}s^{-1}, respectively. (e,f) Simulated results for no EID, but including EIS with the same magnitude of coupling coefficients as in (c,d) with a negative sign. (i,h) Same as (e,f), but with positive values for the EIS coefficients.

The interband continuum response at emission energies above the exciton resonance is only detectable above the noise floor of the experiments for larger excited carrier densities. Fig. 6.1(c) shows the results for a density of 5.4×10^{16} cm^{-3}. The continuum response peaks at positive delay values, as expected for a simple inhomogeneously-broadened transition [1]. The continuum response scales as the cube of the intensity over several orders of magnitude [(Fig. 6.1(d)], verifying that the system response is within the $\chi^{(3)}$ regime at these excitation densities. A sub-cubic scaling at the exciton is expected for all densities due to the influence of many-body effects, [73, 195] in line with the results in Fig. 6.1(e). The general features of these results are consistent with earlier studies using TFWM in GaAs and other bulk and quantum well semiconductor systems [8, 70, 72–74, 79, 85].

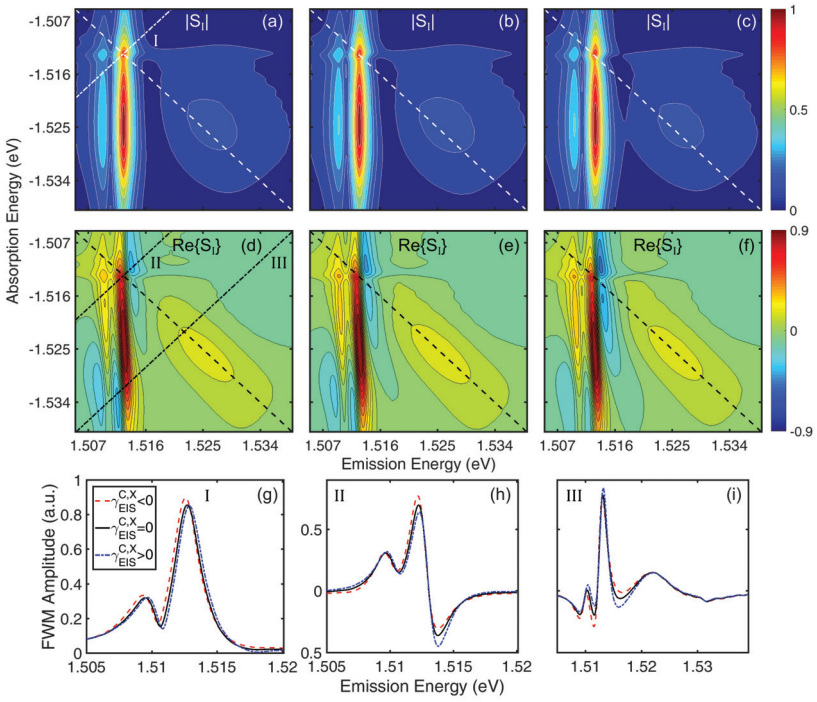

Figure 6.4: (color online) Simulation results of the normalized 2DFTS signal for varying levels of EIS with the EID coefficients held constant at the optimum values. (a) Simulated results with negative EIS coefficients three times smaller in magnitude than the EID coefficients; (b) Simulated results without EIS added. (c) Same as (a) with positive EIS coefficients. (d-f) Real part of 2DFTS signal shown in (a-c). Cross diagonal slices of the amplitude and real 2DFTS spectra are plotted along lines I, II, and III as a function of emission energy in (g), (h), and (i) respectively.

The observed exciton enhancement in TFWM under broad bandwidth excitation is caused by nondegenerate coupling of the exciton to the unbound electron-hole pair population, which leads to contributions to the measured signal emitted at the exciton energy induced by absorption at energies within the interband continuum. [6] Due to the inability to separate signals tied to absorption at different energies in TFWM, this physical understanding of the observed four-wave mixing response only emerged through detailed theoretical calculations [6], and two-color TFWM experiments [85]. The associated exciton signal has been referred to as the *continuum contribution* (CC) [6], and is larger the broader the bandwidth of continuum transitions excited. The short duration of the exciton response versus the delay between the two excitation pulses is caused by interference of signal contributions involving interband excitations at different energies, which is constructive only in the vicinity of zero delay where a net grating in the total free carrier population summed over energy exists [6, 85].

The type of exciton-continuum coupling included in the original treatments of the CC signal at the exciton was EID [6], however the role of EIS was highlighted in later experiments in semiconductor quantum wells [88]. EID and EIS are both caused by four-particle correlations that lead to renormalization of the exciton self-energy, with EIS (EID) tied to the real part (imaginary part) [94, 182]. (While local field contributions tied to polarization-polarization interactions may also contribute, the associated four-wave mixing signal was found to be weaker than the EID/EIS contributions for the broadband excitation conditions considered here [79].) For the case of nondegenerate coupling, the four-particle correlations are between bound excitons and unbound electron-hole pairs excited on the continuum of interband transitions. The CC signals tied to EID and EIS will both be emitted at the exciton energy and persist for a narrow range of pulse delays around zero delay (dictated by the existence of a net population grating of free carriers). As a result, it is not possible to disentangle the contributions of EID and EIS in TFWM. Since EID and EIS contributions to the four-wave mixing polarization are 90 degrees out of phase [93], studies of the exciton response using 2DFTS techniques provide a means of elucidating the relative importance of these two processes. The detection of the real part of the 2DFTS spectrum, together with modeling via separately adjustable EID and EIS coupling strengths provides insight into the manifestation of these effects.

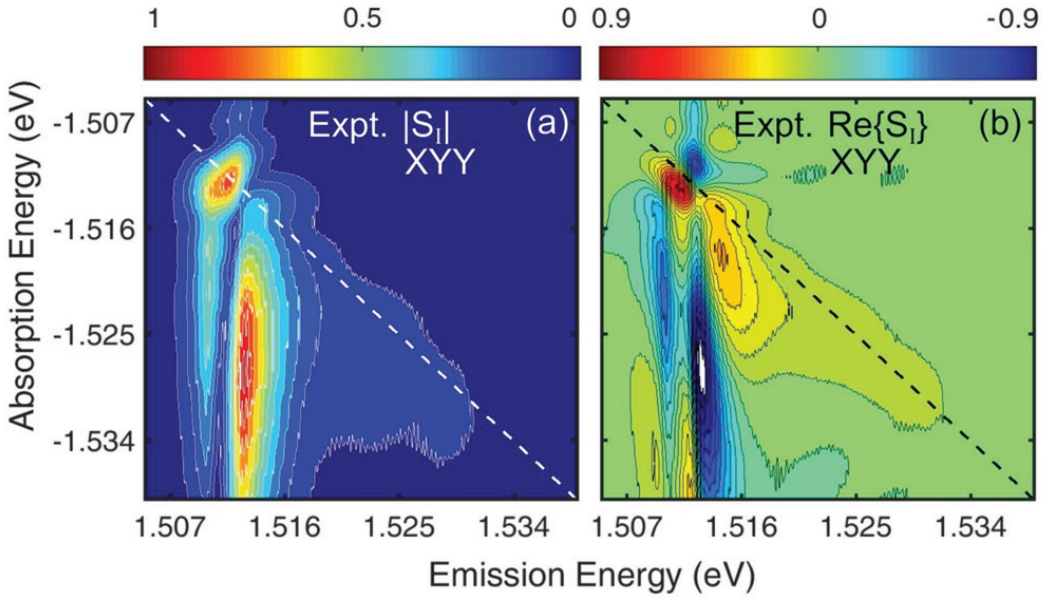

Figure 6.5: (color online) Results of 2DFTS experiments for the same conditions as in Fig. 2. taken with orthogonal linear excitation pulse polarizations, showing the (a) magnitude and (b) real part of the 2DFTS spectrum. The overall magnitude of the signal strength, which is displayed here using a normalized contour scale, is reduced relative to the results in Fig. 2(c)/(d) by approximately 6 times.

6.5.2 2DFTS Results: Separation of Signals Tied to Exciton-Exciton and Exciton-Continuum Coupling

The results of 2DFTS experiments conducted on the bulk GaAs sample are shown in Fig. 2(c) and Fig. 2(d) for the normalized amplitude and real part of the rephasing four-wave mixing response (S_I), respectively. These results correspond to an excited carrier density of 1.6×10^{16} cm^{-3}. As in the TFWM experiments, the laser energy is tuned above the exciton resonance to excite primarily continuum transitions, as shown in Fig. 6.2(a). The amplitude 2DFTS spectrum in Fig. 6.2(c) is composed of two primary features: (i) vertical stripes at emission energies of 1.5100 eV and 1.5125 eV, corresponding to the light-hole and heavy-hole exciton resonances; and (ii) a broad-band response at energies above the exciton resonances that resides along the diagonal axis. The heavy-hole exciton response is stronger than the light-hole response due to the weaker oscillator strength of the light-hole transitions and the greater degree of overlap of the laser pulse spectrum with the HH exciton resonance. The broad band

response is due to the continuum of interband transitions, with a signal that covers an energy range similar to the laser spectrum.

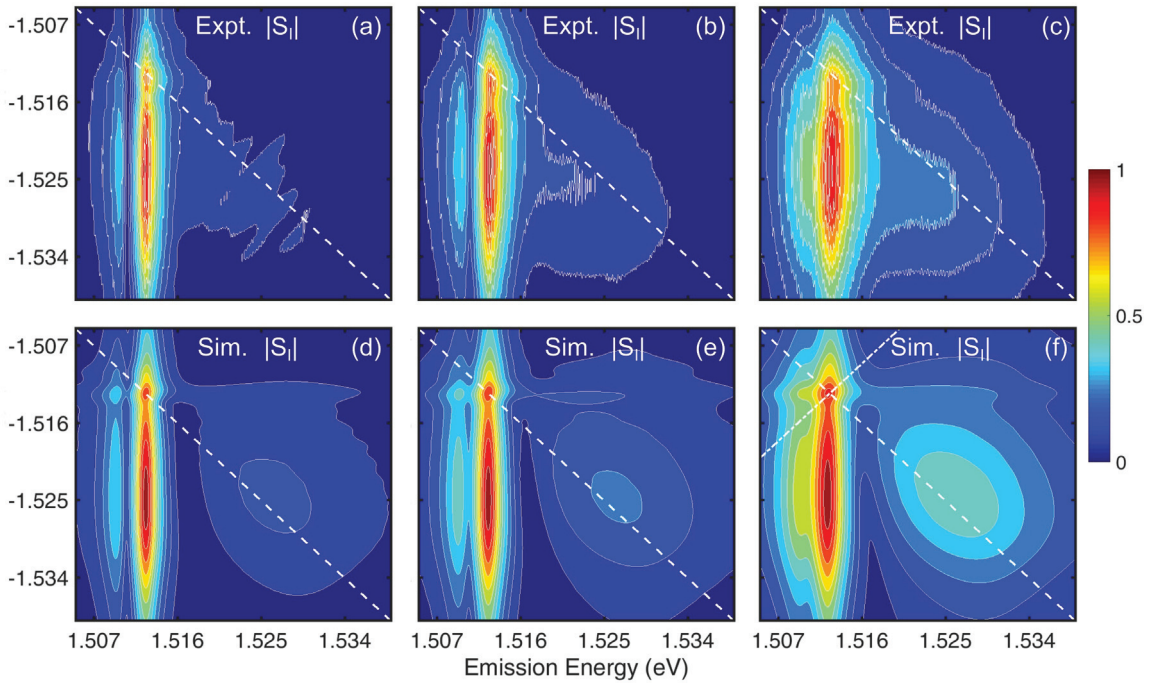

Figure 6.6: (color online) Normalized amplitude results of 2DFTS experiments and simulations for varying excited carrier density. (a-c) Results of 2DFTS experiments for excited carrier densities of 1.6×10^{16} cm^{-3}, 3.2×10^{16} cm^{-3}, and 8.0×10^{16} cm^{-3} respectively. (d-f) Simulation results for the same excited carrier densities as (a-c).

The two vertical stripes corresponding to emission at the light-hole and heavy-hole exciton resonances consist of a number of spectrally distinct contributions along the absorption axis. There are peaks along the diagonal tied to resonant absorption and emission at the exciton resonances as well as discrete off-diagonal peaks tied to coupling between the heavy-hole and light-hole excitons. The latter coupling effects have been studied extensively using 2DFTS techniques [93, 94, 123, 187]. The vertical stripes at larger absorption energies are caused by absorption within the interband continuum followed by emission at the exciton resonances. These signals correspond to the CC that leads to strong enhancement of the excitons in TFWM experiments when the continuum of interband transitions is excited together with the excitons, as discussed in Sec. 6.3.1. The ability to separate absorption and emission pathways in 2DFTS permits the separation of the discrete resonance contributions and the CC.

Table 6.1: Many-body coefficients ($\gamma^{X}_{EID/EIS}$ and $\gamma^{C}_{EID/EIS}$) found in numerical simulations of the 2DFTS results to provide the best agreement with the experimental data.

Coefficients	Exciton-Exciton	Exciton-Continuum
γ_{EID} ($cm^3\ s^{-1}$)	0.27×10^{-4}	3.6×10^{-4}
γ_{EIS} ($cm^3\ s^{-1}$)	0.09×10^{-4}	1.2×10^{-4}

Based on the observed amplitudes, the CC strongly dominates the overall four-wave mixing response for conditions of broad bandwidth excitation of primarily continuum transitions, a result that is consistent with conclusions based on prior TFWM experiments [8, 70, 72–74, 79, 85].

The real part of the 2DFTS spectrum in Fig. 6.2(d) reveals a complex spectral structure that varies along the absorption energy axis. Focusing on the signal emitted at the HH exciton resonance, the spectral shape on the diagonal is dispersive in nature, in agreement with previous work, [93–95] while for higher absorption energies the lineshape evolves from a primarily absorptive response to a dispersive structure as the absorption energy increases. The dispersive structure at high energies within the continuum is 180° out of phase with the exciton response on the diagonal. The vertical stripe feature associated with the CC in Fig. 6.2(c) and Fig. 6.2(d) was observed previously in rephasing 2DFTS experiments on GaAs systems but the variation in the spectral structure for absorption energies within the continuum in Fig. 6.2(d) was not evident either because only the amplitude spectrum was detected [91, 186] or the signal was measured over a narrower range of energies [94, 95]. The dispersive lineshapes we observe for absorption at high energies within the continuum in this work were also not seen in recent experiments on InSe films [192]. Unraveling the spectral structure within the CC in Fig. 6.2(d) would provide insight into exciton-continuum interactions within the optically excited semiconductor.

The different lineshape of the HH exciton emission on the diagonal and for higher absorption energies makes it tempting to conclude that the primary coupling mechanism influencing the HH exciton emission differs for degenerate and nondegenerate interactions. In two-quantum studies on GaAs quantum wells [182], the dispersive

structure at the exciton was attributed to EIS and the absorptive shape in the continuum was attributed to EID since these two types of interactions within a simple two-level system analysis are known to generate polarization responses that are 90° out of phase [88]. The variation in spectral shape for varying absorption energy in Fig. 6.2(d) makes such conclusions more difficult to draw. While the dominance of the CC contribution to the overall four-wave mixing response of the GaAs sample is clear, supporting numerical simulations are needed to identify the relevant coupling mechanisms within the system of bound and unbound electron-hole pairs.

6.5.3 Simulations of 2DFTS Experimental Results

Simulations of the 2DFTS results were carried out for varying strengths of EID and EIS. The simulation results corresponding to the optimum coupling parameters are shown in Fig. 6.2(e) and Fig. 6.2(f) for the amplitude and real 2DFTS spectra, respectively. The evolution of the dispersive structure at the HH exciton detection energy with increasing absorption energy is well reproduced in the simulated results. The optimum many-body coefficients tied to EID were found to be $\gamma_{\mathrm{EID}}^{\mathrm{X}}$=0.27×10^{-4} cm^3 s^{-1} and $\gamma_{\mathrm{EID}}^{\mathrm{C}}$=3.6×10^{-4} cm^{3}s^{-1}. These values indicate an approximately ten-fold larger rate of exciton-continuum scattering than exciton-exciton scattering, consistent with the experimental results in Ref. [4]. The optimum values of the EIS coefficients were found to be smaller than the EID coefficients by the same ratio for the exciton-exciton and exciton-continuum interactions, corresponding to a factor of approximately three. EIS therefore plays a smaller role than EID in the coherent response of the exciton. It is notable that good agreement is obtained for the full range of emission and detection energies using the same relative strengths of EID and EIS describing both degenerate and nondegenerate interactions, indicating that exciton-exciton and exciton-continuum interactions are governed by the same coupling mechanisms.

In order to gain insight into the spectral dependence of the signal contributions tied to EID and EIS, simulations were carried out with EID or EIS alone [Fig. 6.3] or by varying the level of EIS in the presence of EID held fixed at the optimum value [Fig. 6.4]. The vertical stripe associated with the CC is observed in the calculated amplitude 2DFTS results with a similar spectral shape for any combination of EID and/or EIS, but the real 2DFTS spectra vary considerably in their qualitative features

as the relative amounts of the two physical effects are varied. At the exciton resonance on the diagonal, EID alone is sufficient to recover the dispersive structure observed in many past experiments [93–95]. Simulations incorporating a similar phenomenological treatment of EID and EIS were carried out in Ref [93] considering only the discrete exciton transitions, which were excited resonantly in that work. They found a dispersive feature was only produced at the exciton when EIS was included. The simulations in Fig. 6.3 and Fig. 6.4 show that a simple separation of signal characteristics tied to EID and EIS is not possible under nonresonant excitation conditions, for which continuum states are excited together with the exciton.

The spectral structure of the calculated 2DFTS response with varying absorption energies agrees qualitatively with the measured results when EID alone is included in the simulations. For the signal emitted at the heavy-hole exciton, EID reproduces both the correct sign of dispersion and the relative degrees of dispersion (*i. e.* the magnitude of the negative features relative to the positive ones) for absorption at the exciton and within the interband continuum. Changes in the magnitude of the EID coefficient affect the overall linewidth of the exciton resonance, and the optimum values provide good agreement with the experimental exciton linewidth. For a positive value of the EIS coefficient and no EID included (Fig. 6.3(h)), the calculated spectra are in very poor agreement with the experimental results. When only EIS is included with a negative sign for the EIS coupling coefficient (Fig. 6.3(f)), the qualitative shape of the spectra is correct, but the line width of the exciton resonance is smaller than in the experiment and the relative magnitudes of the negative dip at the exciton and continuum absorption energies are reversed.

The agreement between the measured results and the calculations including EID improves with the addition of a small amount of EIS with a negative sign in the coefficients. The variations in the signal characteristics with changes in the magnitude and sign of the EIS coefficients with the EID coefficients held at the optimum values are highlighted in Fig. 6.4 through cross diagonal cuts at the exciton resonance in the amplitude 2DFTS response (Fig. 6.4(g)), at the exciton resonance in the real 2DFTS response (Fig. 6.4(h)), and at absorption energies corresponding to the CC response in the real 2DFTS results (Fig. 6.4(i)). The cross diagonal cut at the exciton in Fig. 6.4(g) shows that a positive (negative) value of the EIS coefficient shifts

the HH exciton resonance to higher (lower) energies along the emission axis. In the real 2DFTS spectra, EIS has the effect of increasing or decreasing the amount of asymmetry in the dispersive peak at the HH exciton emission energy. In the experimental results, the HH exciton resonance peak is centered on the diagonal in the amplitude 2DFTS response. The simulations produce a centered exciton peak for negative EIS coupling coefficients three times smaller than the corresponding EID coefficients, reflecting the dominant role played by EID in the coherent response of the semiconductor.

6.5.4 Polarization dependence

The results of 2DFTS experiments under the same conditions as Fig. 6.2 but with cross linearly polarized excitation pulses are shown in Fig. 6.5. The most notable difference in the signal for the XYY polarization configuration relative to that for XXX is a sharp reduction (by approximately six times) in the overall signal magnitude. Since the EID and EIS interactions are independent of the spin states of the carriers, the associated signal contributions are known to vanish for cross linearly polarized excitation pulses due to the absence of a grating in the total carrier population summed over spin [185]. The large drop in signal amplitude we observe is consistent with the removal of the dominant EID and EIS contributions to the FWM response for the case of parallel input pulse polarizations, and is in line with Ref.([123]) in which a similar nine-fold reduction in signal strength was reported under conditions of resonant excitation of excitons. This drop in overall signal amplitude is accompanied by a more prominent diagonal continuum response relative to the other features in the 2DFTS spectra, an observation that is most clear in the real spectrum in Fig. 6.5(b) and is expected from simple simulations with no EID or EIS contributions [186]. The real part spectrum in Fig. 6.5(b) also indicates a vertical stripe tied to residual exciton-continuum coupling, but the associate signal is out of phase with the EID/EIS signal in Fig. 6.2(d). This residual source of non-degenerate interactions is assumed to be tied to exchange coupling (*i.e.* terms included at the level of the Hartree-Fock approximation). We also note that the horizontal elongation in the vicinity of the diagonal exciton peaks in Fig. 6.5(a) and the associated negative dip to the lower left of the exciton peaks in Fig. 6.5(b) are consistent with

previous single quantum [94, 123] and two-quantum [182, 184] studies under resonant excitation of excitons, and are tied to exciton-biexciton transitions [191]. Transitions involving biexciton states become comparable in magnitude to the exciton responses in the orthogonal linear polarization geometry due to the suppression of the much stronger EID and EIS signal contributions [94, 123, 182, 184].

6.5.5 Dependence on Excited Carrier Density

The dependence of the four-wave mixing signal on excited carrier density is shown in Fig. 6.6. The amplitude 2DFTS results for densities of 1.6×10^{16}, 3.2×10^{16}, and 8.0×10^{16} cm^{-3} are shown in Fig. 6.6(a) - Fig. 6.6(c), respectively. The dominant effect of increasing the carrier density is an increase of the linewidth of the exciton along the emission axis, reflecting the strong role played by EID in the exciton response. At the highest carrier density probed, the collision-induced broadening is sufficient that the energetically split heavy-hole and light-hole exciton peaks merge. In addition to the observed broadening, the strength of the interband continuum response on the diagonal is enhanced relative to the exciton four-wave mixing signal. The slower growth of the exciton signal with increasing carrier density relative to the interband response is also caused by EID. As discussed previously [73,195] this sub-cubic scaling behavior of the exciton is caused by the larger total dephasing rate of the exciton at higher densities, which reduces the time-integrated signal. The simulated 2DFTS results for the optimum EID and EIS coupling parameters provide good agreement with the measured carrier density dependence, as shown in Fig. 6.6(d)-Fig. 6.6(f). Since the EID coefficient is held constant in the simulations, the good agreement suggests that screening of the EID coefficient is negligible at the carrier densities considered here.

6.6 Conclusions

In summary, TFWM and 2DFTS experiments were carried out on bulk GaAs to elucidate the nature of exciton-carrier interactions. TFWM results for broadband excitation of primarily interband transitions indicated a strong enhancement of the exciton emission in TFWM, a result that was shown using 2DFTS to result from nondegenerate four-particle correlations between bound and unbound electron-hole

pairs. Real 2DFTS spectra revealed a complex dispersive structure: For emission at the heavy-hole exciton, the discrete response on the diagonal was primarily dispersive, in agreement with previous work, but for absorption within the interband continuum, the response at low-energies was primarily absorptive and at high energies dispersive with a 180° phase shift relative to absorption at the exciton. Despite these differences, simulations based on a simple multilevel model augmented by many-body effects provide excellent agreement with the experiments and show that the same physical effects govern exciton-exciton and exciton-continuum interactions. We find that the spectral features are qualitatively captured considering coupling via excitation-induced dephasing alone, with a three-fold weaker EIS included to enhance the quantitative agreement. The EID coupling parameters governing exciton-exciton and exciton-continuum interactions determined from fitting the experimental 2DFTS spectra are in line with values found in past TFWM experiments. Such excellent agreement is only obtained by including strain-split heavy- and light-hole excitons and a broad continuum of states.

Our findings highlight the importance of simulations in determining the operative many-body effects when continuum transitions are excited together with the exciton, as a simple assessment of the relative role of different coupling mechanisms is not possible using a discrete resonance analysis and identification of the measured lineshapes. While the excellent agreement obtained using the phenomenological treatment of many-body effects used here illustrates the power of these simple approaches for determining the dominant interactions, a full many-body calculation using a microscopic model such as dynamics-controlled truncation [202, 203] would aid in the interpretation of the effects observed. In addition, extension of the 2DFTS experiments reported here to larger waiting times [95] would provide useful verification of the interpretation presented here, in which only exciton renormalization tied to population terms were needed to account for the experimental observations. Our findings provide new insight into the role of many-body interactions in the coherent optical response of semiconductors.

The work performed at Dalhousie University was supported by the Natural Sciences and Engineering Research Council of Canada and the Walter C. Sumner Foundation. Work at West Virginia University was supported by the West Virginia Higher

Education Policy Commission (HEPC.dsr.12.29) and the National Science Foundation (CBET-1233795). Work at the University of Notre Dame was supported by the National Science Foundation (Grant DMR1400432).

Chapter 7

Conclusion

FWM is a powerful tool used to study light matter interactions in semiconductor materials. This thesis work has built upon approximately two decades of studies on traditional semiconductor materials using the conventional two pulse self-diffraction four-wave mixing technique providing a host of information regarding dephasing processes and yielding important insight into the interactions between charge carriers during the coherent ultrafast regime. This progress in understanding has supported the development of a wide range of optoelectronic devices using traditional semiconductors, including photodetectors and solar cell materials. This thesis work has served to extend the above body of work in two primary ways: (i) To exploit the power and flexibility of four-wave mixing to examine the optical properties of newer semiconductor materials (applied to the study of transport in $CH_3NH_3PbI_3$ in the support of the development of solar cell technology using organic-inorganic perovskite and LT-GaAs to support the optimization of the broader class of low-temperature grown semiconductor materials in optoelectronics); and (ii) To further the understanding of many-body effects through the application of the newer variant of this technique (the phase sensitive approach 2DFTS) to probe nondegenerate many-body interactions in a bulk semiconductor system. This thesis work has therefore exploited the versatility of FWM as a tool to study a wide range of phenomena in condensed matter systems in support of their applications in semiconductor technology.

Charge carrier transport in $CH_3NH_3PbI_3$ was studied in the the first project of this thesis work using a variant of FWM known as the transient grating technique. $CH_3NH_3PbI_3$ has recently garnered significant interest as a solar cell absorber material, in part due to the long micron-scale diffusion lengths in this material. The use of three optical pulses allowed for the direct measurement of the ambipolar diffusion coefficient and population lifetime of photoexcited charge carriers in $CH_3NH_3PbI_3$,

without the need for complex modeling or charge extraction layers used in other measurement techniques. The calculated ambipolar diffusion length of ≈ 1 um was found to be consistent with recent all-optical studies in this material. Scanning electron microscopy images of the sample indicated a mean grain size that was four times smaller than the diffusion length, suggesting that grain boundaries do not play a significant role in the carrier transport properties. The findings of this work highlight the strength of this technique as a transport measurement tool for solar cell materials, and will stimulate future studies on other materials within the family of hybrid organic-inorganic perovskites using this approach.

In the second project of this thesis work, FWM was used to measure the coherent response of LT-GaAs that had been annealed over a range of temperatures. Due to the short carrier lifetimes and meteoric increase in resistivity with annealing temperature in these materials, annealed LT-GaAs is the material of choice in the design of ultrafast optoelectronic devices. Previous FWM experiments on as-grown LT-GaAs (*i.e.* no annealing) have shown that the coherent response near the band edge is composed of contributions from interband free-carrier, exciton, and Urbach band tail states associated with defect-induced disorder. In this thesis work, the FWM response of annealed LT-GaAs has shown a similar FWM response that is sensitively linked to annealing temperature. In particular, a dip in the exciton FWM response was observed for annealing temperatures up to 500°C and was associated with interference between the many-body exciton signal and continuum of states associated with band tails. For temperatures exceeding 500°C, the disappearance of the exciton dip was found to be consistent with the decrease in FWM band tail response and was linked to the decrease in As point defects. The Urbach energy, which empirically quantifies the magnitude of disorder in the system, was extracted from the FWM response and was found to decrease to GaAs values for temperatures exceeding 500°C. Since FWM is a nonlinear spectroscopic technique, the ability to clearly resolve the Urbach band tail will be beneficial for studying other highly disordered materials utilizing low temperature growth.

FWM is the technique of choice for studying many-body effects in semiconductors. Many-body effects encompass a hierarchy of different interactions between charge carriers after the photoexcitation of electron-hole pairs. The third project of this thesis

examined the role of excitation-induced phenomena in the interaction between free electron-hole pairs (carriers) and bound electron-hole pairs (excitons) in GaAs using two experimental variants of FWM; two-pulse self-diffracted FWM and 2DFTS. A plethora of studies in the past using FWM have provided considerable insight into the nature of these interactions, however the work presented in this thesis is the first application of 2DFTS to this problem. Using a multilevel model to describe the electronic structure, numerical simulations using the optical Bloch equations augmented by these interactions indicated that exciton-carrier scattering dominates over exciton-exciton scattering, and that excitation-induced dephasing manifests more strongly in the real part of the four-wave mixing signal than excitation-induced shift. The findings of this project also demonstrated that the conventional means of interpreting 2DFTS results using a simple two-level model is not sufficient, and that simulations are required to disentangle various contributions to the FWM response.

Future directions for the three projects presented in this thesis work are described as follows. Extension of carrier diffusion measurements in Chapter 4 to perovskite materials produced using different deposition techniques would be beneficial in understanding the impact these various methods have on the charge transport properties. In addition, the extension of these methods to two-dimensional materials will aid in their incorporation into solar cell devices. The work on LT-GaAs presented in Chapter 5 could be extended by measuring the FWM response of band tail states as a function of excitation density. These measurements will permit identification of the third-order dielectric susceptibility of band tail states, which will be beneficial for devices that utilize the optical nonlinearity such as all-optical switches. Finally, the work presented in Chapter 6 using 2DFTS to study exciton-exciton and exciton-continuum scattering could be extended to similar studies on materials within the organic-inorganic family of perovskites. For instance, recent FWM studies on $CH_3NH_3PbI_3$ indicated weaker many-body interactions than GaAs [156]. It would be interesting to investigate the strength of many-body coupling (including exciton-continuum interactions) in 2D perovskites, in which the screening properties tied to the organic constituents are expected to differ from that in bulk perovskites.

Bibliography

[1] T. Yajima and Y. Taira. Spatial optical coupling of picosecond light pulses and transverse relaxation effect in resonant media. *J. Phys. Soc. Jpn.*, 47:1620, 1979.

[2] J. R. Salcedo, A. E. Siegman, D. D. Dlott, and M. D. Fayer. Dynamics of energy transport in molecular crystals: The picosecond transient-grating method. *Phys. Rev. Lett.*, 41:131–134, Jul 1978.

[3] Y. M. Wong and V. M. Kenkre. Extension of exciton-transport theory for transient grating experiments into the intermediate coherence domain. *Phys. Rev. B*, 22:3072–3077, Sep 1980.

[4] L. Schultheis, J. Kuhl, A. Honold, and C. W. Tu. Ultrafast phase relaxation of excitons via exciton-exciton and exciton-electron collisions. *Phys. Rev. Lett.*, 57:1635–1638, Sep 1986.

[5] A. Honold, L. Schultheis, J. Kuhl, and C. W. Tu. Collision broadening of two-dimensional excitons in a GaAs single quantum well. *Phys. Rev. B*, 40:6442–6445, Sep 1989.

[6] K. El Sayed, D. Birkedal, V. G. Lyssenko, and J. M. Hvam. Continuum contribution to excitonic four-wave mixing due to interaction-induced nonlinearities: A numerical study. *Phys. Rev. B*, 55:2456–2465, Jan 1997.

[7] Otfried Madelung. *Semiconductors - Basic Data*. Spring, Springer-Verlag, Tiergartenstrasse 17, D-69121 Heidelberg, Germany, 1996.

[8] D. Webber, L. Hacquebard, X. Liu, M. Dobrowolska, J. K. Furdyna, and K. C. Hall. Role of many-body effects in the coherent dynamics of excitons in low-temperature-grown GaAs. *Applied Physics Letters*, 107(14):–, 2015.

[9] R. J. Elliott. Intensity of optical absorption by excitons. *Phys. Rev.*, 108:1384–1389, Dec 1957.

[10] Hartmut Haug and Stephan Koch. *Quantum Theory of the Optical and Electronic Properties of Semiconductors*. World Scientific Publishing Co. Pte. Ltd., Singapore, 1990.

[11] William D Callister and David G Rethwisch. *Materials science and engineering*, volume 5. John Wiley & Sons NY, 2011.

[12] Jagdeep Shah. *Ultrafast Spectroscopy of Semiconductors and Semiconductor Nanostructures*. Springer, Springer-Verlag, Tiergartenstrasse 17, D-69121 Heidelberg, Germany, 1996.

[13] M. Yildirim, S. March, R. Mathew, A. Gamouras, X. Liu, M. Dobrowolska, J. K. Furdyna, and K. C. Hall. Interband dephasing and photon echo response in GaAsMnAs. *Applied Physics Letters*, 101(6):062403, 2012.

[14] RJ Nelson and RG Sobers. Minority-carrier lifetimes and internal quantum efficiency of surface-free GaAs. *Journal of Applied Physics*, 49(12):6103–6108, 1978.

[15] JS Weiner and PY Yu. Free carrier lifetime in semi-insulating GaAs from time-resolved band-to-band photoluminescence. *Journal of applied physics*, 55(10):3889–3891, 1984.

[16] Helen D Megaw. Origin of ferroelectricity in barium titanate and other perovskite-type crystals. *Acta Crystallographica*, 5(6):739–749, 1952.

[17] D. Weber. Ch3nh3pbx3 a pb(ii)-system with cubic perovskite structure. *Z. Naturforsch*, 33b:1443–1445, 1978.

[18] Akihiro Kojima, Kenjiro Teshima, Yasuo Shirai, and Tsutomu Miyasaka. Organometal halide perovskites as visible-light sensitizers for photovoltaic cells. *Journal of the American Chemical Society*, 131(17):6050–6051, 2009. PMID: 19366264.

[19] National Renewable Energy Laboratory. Best research-cell efficiencies. *NREL*, 2016. Available at http://www.nrel.gov/pv/assets/images/efficiency_chart.jpg.

[20] Stefaan De Wolf, Jakub Holovsky, Soo-Jin Moon, Philipp Lper, Bjoern Niesen, Martin Ledinsky, Franz-Josef Haug, Jun-Ho Yum, and Christophe Ballif. Organometallic halide perovskites: Sharp optical absorption edge and its relation to photovoltaic performance. *The Journal of Physical Chemistry Letters*, 5(6):1035–1039, 2014. PMID: 26270984.

[21] Samuel D. Stranks, Giles E. Eperon, Giulia Grancini, Christopher Menelaou, Marcelo J. P. Alcocer, Tomas Leijtens, Laura M. Herz, Annamaria Petrozza, and Henry J. Snaith. Electron-hole diffusion lengths exceeding 1 micrometer in an organometal trihalide perovskite absorber. *Science*, 342(6156):341–344, 2013.

[22] Atsuhiko Miyata, Anatolie Mitioglu, Paulina Plochocka, Oliver Portugall, Jacob Tse-Wei Wang, Samuel D. Stranks, Henry J. Snaith, and Robin J. Nicholas. Direct measurement of the exciton binding energy and effective masses for charge carriers in organic-inorganic tri-halide perovskites. *Nat Phys*, 11(7):582–587, Jul 2015. Article.

[23] A. Poglitsch and D. Weber. Dynamic disorder in methylammoniumtrihalogenoplumbates (ii) observed by millimeterwave spectroscopy. *The Journal of Chemical Physics*, 87(11):6373–6378, 1987.

[24] Wissam A. Saidi and Joshua J. Choi. Nature of the cubic to tetragonal phase transition in methylammonium lead iodide perovskite. *The Journal of Chemical Physics*, 145(14):144702, 2016.

[25] Tze Chien Sum and Nripan Mathews. Advancements in perovskite solar cells: photophysics behind the photovoltaics. *Energy Environ. Sci.*, 7:2518–2534, 2014.

[26] Guichuan Xing, Nripan Mathews, Shuangyong Sun, Swee Sien Lim, Yeng Ming Lam, Michael Grätzel, Subodh Mhaisalkar, and Tze Chien Sum. Long-range balanced electron- and hole-transport lengths in organic-inorganic $CH_3NH_3PbI_3$. *Science*, 342(6156):344–347, 2013.

[27] Joseph S Manser and Prashant V Kamat. Band filling with free charge carriers in organometal halide perovskites. *Nature Photonics*, 8(9):737–743, 2014.

[28] T. Umebayashi, K. Asai, T. Kondo, and A. Nakao. Electronic structures of lead iodide based low-dimensional crystals. *Phys. Rev. B*, 67:155405, Apr 2003.

[29] Zhengguo Xiao, Cheng Bi, Yuchuan Shao, Qingfeng Dong, Qi Wang, Yongbo Yuan, Chenggong Wang, Yongli Gao, and Jinsong Huang. Efficient, high yield perovskite photovoltaic devices grown by interdiffusion of solution-processed precursor stacking layers. *Energy Environ. Sci.*, 7:2619–2623, 2014.

[30] Kyeongil Hwang, Yen-Sook Jung, Youn-Jung Heo, Fiona H. Scholes, Scott E. Watkins, Jegadesan Subbiah, David J. Jones, Dong-Yu Kim, and Doojin Vak. Toward large scale roll-to-roll production of fully printed perovskite solar cells. *Advanced Materials*, 27(7):1241–1247, 2015.

[31] Stefano Razza, Francesco Di Giacomo, Fabio Matteocci, Lucio Cin, Alessandro Lorenzo Palma, Simone Casaluci, Petra Cameron, Alessandra D'Epifanio, Silvia Licoccia, Andrea Reale, Thomas M. Brown, and Aldo Di Carlo. Perovskite solar cells and large area modules (100cm2) based on an air flow-assisted pbi2 blade coating deposition process. *Journal of Power Sources*, 277:286 – 291, 2015.

[32] Moritz H Futscher and Bruno Ehrler. Efficiency limit of perovskite/si tandem solar cells. *ACS Energy Letters*, 1(4):863–868, 2016.

[33] Kevin A Bush, Axel F Palmstrom, J Yu Zhengshan, Mathieu Boccard, Rongrong Cheacharoen, Jonathan P Mailoa, David P McMeekin, Robert LZ Hoye, Colin D Bailie, Tomas Leijtens, et al. 23.6%-efficient monolithic perovskite/silicon tandem solar cells with improved stability. *Nature Energy*, 2:17009, 2017.

[34] J. C. M. Hwang, H. Temkin, T. M. Brennan, and R. E. Frahm. Growth of highpurity GaAs layers by molecular beam epitaxy. *Applied Physics Letters*, 42(1):66–68, 1983.

[35] W. I. Wang, R. F. Marks, and L. Vina. Highpurity GaAs grown by molecular-beam epitaxy. *Journal of Applied Physics*, 59(3):937–939, 1986.

[36] D. C. Look, D. C. Walters, G. D. Robinson, J. R. Sizelove, M. G. Mier, and C. E. Stutz. Annealing dynamics of molecular-beam epitaxial GaAs grown at 200°C. *Journal of Applied Physics*, 74(1):306–310, 1993.

[37] F. W. Smith, H. Q. Le, V. Diadiuk, M. A. Hollis, A. R. Calawa, S. Gupta, M. Frankel, D. R. Dykaar, G. A. Mourou, and T. Y. Hsiang. Picosecond GaAsbased photoconductive optoelectronic detectors. *Applied Physics Letters*, 54(10):890–892, 1989.

[38] S. Gupta, M. Y. Frankel, J. A. Valdmanis, J. F. Whitaker, G. A. Mourou, F. W. Smith, and A. R. Calawa. Subpicosecond carrier lifetime in GaAs grown by molecular beam epitaxy at low temperatures. *Applied Physics Letters*, 59(25):3276–3278, 1991.

[39] E. S. Harmon, M. R. Melloch, J. M. Woodall, D. D. Nolte, N. Otsuka, and C. L. Chang. Carrier lifetime versus anneal in low temperature growth GaAs. *Applied Physics Letters*, 63(16):2248–2250, 1993.

[40] G. Segschneider, T. Dekorsy, H. Kurz, R. Hey, and K. Ploog. Energy resolved ultrafast relaxation dynamics close to the band edge of low-temperature grown GaAs. *Applied Physics Letters*, 71(19):2779–2781, 1997.

[41] S. D. Benjamin, H. S. Loka, A. Othonos, and P. W. E. Smith. Ultrafast dynamics of nonlinear absorption in low temperature grown GaAs. *Applied Physics Letters*, 68(18):2544–2546, 1996.

[42] S Marcinkevicius, A Krotkus, R Viselga, U Olin, and C Jagadish. Non-thermal photoexcited electron distributions in non-stoichiometric GaAs. *Semiconductor Science and Technology*, 12(4):396, 1997.

[43] M. Stellmacher, J. Nagle, J. F. Lampin, P. Santoro, J. Vaneecloo, and A. Alexandrou. Dependence of the carrier lifetime on acceptor concentration in GaAs grown at low-temperature under different growth and annealing conditions. *Journal of Applied Physics*, 88(10):6026–6031, 2000.

[44] M. Mikulics, S. Wu, M. Marso, R. Adam, A. Forster, A. van der Hart, P. Kordos, H. Luth, and R. Sobolewski. Ultrafast and highly sensitive photodetectors with recessed electrodes fabricated on low-temperature-grown GaAs. *Photonics Technology Letters, IEEE*, 18(7):820–822, April 2006.

[45] Marc Currie, Fabio Quaranta, Adriano Cola, Eric M. Gallo, and Bahram Nabet. Low-temperature grown GaAs heterojunction metal-semiconductor-metal photodetectors improve speed and efficiency. *Applied Physics Letters*, 99(20):–, 2011.

[46] Marc Currie, Pouya Dianat, Anna Persano, Maria Concetta Martucci, Fabio Quaranta, Adriano Cola, and Bahram Nabet. Performance enhancement of a GaAs detector with a vertical field and an embedded thin low-temperature grown layer. *Sensors*, 13(2):2475, 2013.

[47] Jiun-Cheng Wang, Chi-Kuang Sun, and Juen-Kai Wang. Nonlinear pulse-shaping phenomena of semiconductor saturable absorber mirror. *Applied Physics Letters*, 89(23):–, 2006.

[48] Xiaomin Liu, Edik U. Rafailov, Daniil Livshits, and Dmitry Turchinovich. Quantum well saturable absorber mirror with electrical control of modulation depth. *Applied Physics Letters*, 97(5):–, 2010.

[49] E. Peytavit, C. Coinon, and J.-F. Lampin. A metal-metal fabryprot cavity photoconductor for efficient GaAs terahertz photomixers. *Journal of Applied Physics*, 109(1):–, 2011.

[50] E. Peytavit, S. Lepilliet, F. Hindle, C. Coinon, T. Akalin, G. Ducournau, G. Mouret, and J.-F. Lampin. Milliwatt-level output power in the sub-terahertz range generated by photomixing in a GaAs photoconductor. *Applied Physics Letters*, 99(22):–, 2011.

[51] E. A. Michael and M. Mikulics. Losses from long-living photoelectrons in terahertz-generating continuous-wave photomixers. *Applied Physics Letters*, 100(19):–, 2012.

[52] T. Ackemann, M. Alduraibi, S. Campbell, S. Keatings, P. Luke Sam, H. Fraser, A. S. Arnold, E. Riis, and M. Missous. Diamond heat sinking of terahertz antennas for continuous-wave photomixing. *Journal of Applied Physics*, 112(12):–, 2012.

[53] Jan-Martin Rmer, Frank Ospald, Georg von Freymann, and Ren Beigang. Generation and detection of terahertz radiation up to 4.5thz by low-temperature grown GaAs photoconductive antennas excited at 1560nm. *Applied Physics Letters*, 103(2):–, 2013.

[54] Eicke R. Weber Maria Kaminska. Low temperature GaAs: Electrical and optical properties. *Materials Science Forum*, 83-87:1033–1044, 1992.

[55] M. Luysberg, H. Sohn, A. Prasad, P. Specht, Z. Liliental-Weber, E. R. Weber, J. Gebauer, and R. Krause-Rehberg. Effects of the growth temperature and As/Ga flux ratio on the incorporation of excess as into low temperature grown GaAs. *Journal of Applied Physics*, 83(1):561–566, 1998.

[56] Shantanu Gupta, John F Whitaker, and Gerard A Mourou. Ultrafast carrier dynamics in III-V semiconductors grown by molecular-beam epitaxy at very low substrate temperatures. *IEEE Journal of Quantum Electronics*, 28(10):2464–2472, 1992.

[57] JI Landman, CG Morgan, JT Schick, P Papoulias, and A Kumar. Arsenic interstitials and interstitial complexes in low-temperature grown GaAs. *Physical Review B*, 55(23):15581, 1997.

[58] D Streb, M Ruff, SU Dankowski, P Kiesel, M Kneissl, S Malzer, UD Keil, and GH Döhler. Optical characterization of low temperature grown GaAs by transmission measurements above the band gap. *Journal of Vacuum Science & Technology B: Microelectronics and Nanometer Structures Processing, Measurement, and Phenomena*, 14(3):2275–2277, 1996.

[59] Sajeev John, Costas Soukoulis, Morrel H. Cohen, and E. N. Economou. Theory of electron band tails and the urbach optical-absorption edge. *Phys. Rev. Lett.*, 57:1777–1780, Oct 1986.

[60] S. U. Dankowski, D. Streb, M. Ruff, P. Kiesel, M. Kneissl, B. Knpfer, G. H. Dhler, U. D. Keil, C. B. So/renson, and A. K. Verma. Above band gap absorption spectra of the arsenic antisite defect in low temperature grown GaAs and alGaAs. *Applied Physics Letters*, 68(1):37–39, 1996.

[61] M Stellmacher, R Bisaro, P Galtier, J Nagle, K Khirouni, and J C Bourgoin. Defects and defect behaviour in GaAs grown at low temperature. *Semiconductor Science and Technology*, 16(6):440, 2001.

[62] X. Liu, A. Prasad, W. M. Chen, A. Kurpiewski, A. Stoschek, Z. LilientalWeber, and E. R. Weber. Mechanism responsible for the semiinsulating properties of lowtemperaturegrown GaAs. *Applied Physics Letters*, 65(23):3002–3004, 1994.

[63] K. S. Burch, J. Stephens, R. K. Kawakami, D. D. Awschalom, and D. N. Basov. Ellipsometric study of the electronic structure of $ga_{1-x}mn_xAs$ and low-temperature GaAs. *Phys. Rev. B*, 70:205208, Nov 2004.

[64] M. D. Sturge. Optical absorption of gallium arsenide between 0.6 and 2.75 ev. *Phys. Rev.*, 127:768–773, Aug 1962.

[65] Doo-Hyeb Youn, Seung-Hwan Lee, Han-Cheol Ryu, Se-Young Jung, Seung-Bum Kang, Min-Hwan Kwack, Sungil Kim, Sang-Kuk Choi, Mun-Cheol Baek, Kwang-Yong Kang, Chang-Seop Kim, Ki-Ju Yee, Young-Bin Ji, Eui-Su Lee, Tae-In Jeon, Seong-Jin Kim, Sanjeev Kumar, and Gil-Ho Kim. Effects of post-growth annealing on the structure and electro-optical properties of low-temperature grown GaAs. *Journal of Applied Physics*, 103(12):123528, 2008.

[66] SS Prabhu, SE Ralph, MR Melloch, and ES Harmon. Carrier dynamics of low-temperature-grown GaAs observed via THz spectroscopy. *Applied physics letters*, 70(18):2419–2421, 1997.

[67] H Němec, A Pashkin, P Kužel, M Khazan, S Schnüll, and I Wilke. Carrier dynamics in low-temperature grown GaAs studied by terahertz emission spectroscopy. *Journal of Applied Physics*, 90(3):1303–1306, 2001.

[68] A. Lohner, K. Rick, P. Leisching, A. Leitenstorfer, T. Elsaesser, T. Kuhn, F. Rossi, and W. Stolz. Coherent optical polarization of bulk GaAs studied by femtosecond photon-echo spectroscopy. *Phys. Rev. Lett.*, 71:77–80, Jul 1993.

[69] Hailin Wang, Kyle Ferrio, Duncan G. Steel, Y. Z. Hu, R. Binder, and S. W. Koch. Transient nonlinear optical response from excitation induced dephasing in GaAs. *Phys. Rev. Lett.*, 71:1261–1264, Aug 1993.

[70] M. U. Wehner, D. Steinbach, and M. Wegener. Ultrafast coherent transients due to exciton-continuum scattering in bulk GaAs. *Phys. Rev. B*, 54:R5211–R5214, Aug 1996.

[71] M. Yildirim, S. March, R. Mathew, A. Gamouras, X. Liu, M. Dobrowolska, J. K. Furdyna, and K. C. Hall. Electronic structure of $Ga_{1-x}Mn_xAs$ probed by four-wave mixing spectroscopy. *Phys. Rev. B*, 84:121202, Sep 2011.

[72] D. Webber, M. Yildirim, L. Hacquebard, S. March, R. Mathew, A. Gamouras, X. Liu, M. Dobrowolska, J. K. Furdyna, and K. C. Hall. Observation of the exciton and urbach band tail in low-temperature-grown GaAs using four-wave mixing spectroscopy. *Applied Physics Letters*, 105(18):–, 2014.

[73] G. R. Allan and H. M. van Driel. Coherence dynamics of excitons and continuum excitations in inp. *Phys. Rev. B*, 59:15740, 1999.

[74] K. C. Hall, G. R. Allan, H. M. van Driel, T. Krivosheeva, and W. Pötz. Coherent response of spin-orbit split-off excitons in inp: Isolation of many-body effects through interference. *Phys. Rev. B*, 65:201201(R), 2002.

[75] Claus Dornfeld and Joern M Hvam. Optical nonlinearities and phase coherence in CdSe studied by transient four-wave mixing. *IEEE Journal of Quantum Electronics*, 25(5):904–912, 1989.

[76] VG Lyssenko, J Erland, I Balslev, K-H Pantke, BS Razbirin, and JM Hvam. Nature of nonlinear four-wave-mixing beats in semiconductors. *Physical Review B*, 48(8):5720, 1993.

[77] J Erland, K-H Pantke, V Mizeikis, VG Lyssenko, and Jørn Märcher Hvam. Spectrally resolved four-wave mixing in semiconductors: influence of inhomogeneous broadening. *Physical Review B*, 50(20):15047, 1994.

[78] T. Rappen, U. Peter, M. Wegener, and W. Schäfer. Coherent dynamics of continuum and exciton states studied by spectrally resolved fs four-wave mixing. *Phys. Rev. B*, 48:4879–4882, Aug 1993.

[79] T. Rappen, U. Peter, G. Mohs, W. Schäfer, and M. Wegener. Coherent dynamics of continuum and bound states in germanium. *Semicond. Sci. Technol.*, 9:422, 1994.

[80] Thomas Rappen, Ulf-Gereon Peter, Martin Wegener, and Wilfried Schäfer. Polarization dependence of dephasing processes: A probe for many-body effects. *Physical Review B*, 49(15):10774, 1994.

[81] K. Leo, M. Wegener, J. Shah, D. S. Chemla, E. O. Göbel, T. C. Damen, S. Schmitt-Rink, and W. Schäfer. Effects of coherent polarization interactions on time-resolved degenerate four-wave mixing. *Phys. Rev. Lett.*, 65:1340–1343, Sep 1990.

[82] Dai-Sik Kim, Jagdeep Shah, J. E. Cunningham, T. C. Damen, Wilfried Schäfer, Michael Hartmann, and Stefan Schmitt-Rink. Giant excitonic resonance in time-resolved four-wave mixing in quantum wells. *Phys. Rev. Lett.*, 68:1006–1009, Feb 1992.

[83] Dai-Sik Kim, Jagdeep Shah, TC Damen, W Schäfer, F Jahnke, S Schmitt-Rink, and K Köhler. Unusually slow temporal evolution of femtosecond four-wave-mixing signals in intrinsic gaas quantum wells: Direct evidence for the dominance of interaction effects. *Physical review letters*, 69(18):2725, 1992.

[84] S. T. Cundiff, H. Wang, and D. G. Steel. Polarization-dependent picosecond excitonic nonlinearities and the complexities of disorder. *Phys. Rev. B*, 46:7248–7251, Sep 1992.

[85] S. T. Cundiff, M. Koch, W. H. Knox, J. Shah, and W. Stolz. Optical coherence in semiconductors: Strong emission mediated by nondegenerate interactions. *Phys. Rev. Lett.*, 77:1107–1110, Aug 1996.

[86] D. Birkedal, V. G. Lyssenko, J. M. Hvam, and K. El Sayed. Continuum contribution to excitonic four-wave mixing due to interaction-induced nonlinearities. *Phys. Rev. B*, 54:R14250–R14253, Nov 1996.

[87] T Rappen, G Mohs, and M Wegener. Polariton dynamics in quantum wells studied by femtosecond four-wave mixing. *Physical Review B*, 47(15):9658, 1993.

[88] Justin M. Shacklette and Steven T. Cundiff. Role of excitation-induced shift in the coherent optical response of semiconductors. *Phys. Rev. B*, 66:045309, Jul 2002.

[89] X Chen, Wojciech J Walecki, O Buccafusca, David N Fittinghoff, and Arthur L Smirl. Temporally and spectrally resolved amplitude and phase of coherent four-wave-mixing emission from gaas quantum wells. *Physical Review B*, 56(15):9738, 1997.

[90] Steven T. Cundiff. Optical two-dimensional Fourier transform spectroscopy of semiconductor nanostructures. *J. Opt. Soc. Am. B*, 29(2):A69–A81, Feb 2012.

[91] I. Kuznetsova, T. Meier, S. T. Cundiff, and P. Thomas. Determination of homogeneous and inhomogeneous broadening in semiconductor nanostructures by two-dimensional Fourier-transform optical spectroscopy. *Phys. Rev. B*, 76:153301, Oct 2007.

[92] Alan D. Bristow, Tianhao Zhang, Mark E. Siemens, Steven T. Cundiff, and R. P. Mirin. Separating homogeneous and inhomogeneous line widths of heavy- and light-hole excitons in weakly disordered semiconductor quantum wells. *The Journal of Physical Chemistry B*, 115(18):5365–5371, 2011. PMID: 21384940.

[93] Xiaoqin Li, Tianhao Zhang, Camelia N. Borca, and Steven T. Cundiff. Many-body interactions in semiconductors probed by optical two-dimensional Fourier transform spectroscopy. *Phys. Rev. Lett.*, 96:057406, Feb 2006.

[94] Tianhao Zhang, Irina Kuznetsova, Torsten Meier, Xiaoqin Li, Richard P. Mirin, Peter Thomas, and Steven T. Cundiff. Polarization-dependent optical 2D Fourier transform spectroscopy of semiconductors. *Proceedings of the National Academy of Sciences*, 104(36):14227–14232, 2007.

[95] Daniel B. Turner, Patrick Wen, Dylan H. Arias, Keith A. Nelson, Hebin Li, Galan Moody, Mark E. Siemens, and Steven T. Cundiff. Persistent exciton-type many-body interactions in GaAs quantum wells measured using two-dimensional optical spectroscopy. *Phys. Rev. B*, 85:201303, May 2012.

[96] Mark E. Siemens, Galan Moody, Hebin Li, Alan D. Bristow, and Steven T. Cundiff. Resonance lineshapes in two-dimensional Fourier transform spectroscopy. *Opt. Express*, 18(17):17699–17708, Aug 2010.

[97] H. Schwab, K.-H. Pantke, J. M. Hvam, and C. Klingshirn. Measurements of exciton diffusion by degenerate four-wave mixing in $cds_{1-x}se_x$. *Phys. Rev. B*, 46:7528–7532, Sep 1992.

[98] Gary Hodes and Prashant V. Kamat. Understanding the implication of carrier diffusion length in photovoltaic cells. *The Journal of Physical Chemistry Letters*, 6(20):4090–4092, 2015. PMID: 26722782.

[99] Dong Shi, Valerio Adinolfi, Riccardo Comin, Mingjian Yuan, Erkki Alarousu, Andrei Buin, Yin Chen, Sjoerd Hoogland, Alexander Rothenberger, Khabiboulakh Katsiev, Yaroslav Losovyj, Xin Zhang, Peter A. Dowben, Omar F. Mohammed, Edward H. Sargent, and Osman M. Bakr. Low trap-state density and long carrier diffusion in organolead trihalide perovskite single crystals. *Science*, 347(6221):519–522, 2015.

[100] Y Chen, HT Yi, X Wu, R Haroldson, YN Gartstein, YI Rodionov, KS Tikhonov, A Zakhidov, X-Y Zhu, and V Podzorov. Extended carrier lifetimes and diffusion in hybrid perovskites revealed by hall effect and photoconductivity measurements. *Nature communications*, 7, 2016.

[101] Victoria Gonzalez-Pedro, Emilio J. Juarez-Perez, Waode-Sukmawati Arsyad, Eva M. Barea, Francisco Fabregat-Santiago, Ivan Mora-Sero, and Juan Bisquert. General working principles of ch3nh3pbx3 perovskite solar cells. *Nano Letters*, 14(2):888–893, 2014. PMID: 24397375.

[102] Eran Edri, Saar Kirmayer, Sabyasachi Mukhopadhyay, Konstantin Gartsman, Gary Hodes, and David Cahen. Elucidating the charge carrier separation and working mechanism of $CH_3NH_3PbI_3$- xclx perovskite solar cells. *Nature communications*, 5:3461, 2014.

[103] Zhi Guo, Joseph S Manser, Yan Wan, Prashant V Kamat, and Libai Huang. Spatial and temporal imaging of long-range charge transport in perovskite thin films by ultrafast microscopy. *Nature communications*, 6:7471, 2015.

[104] Yu Li, Weibo Yan, Yunlong Li, Shufeng Wang, Wei Wang, Zuqiang Bian, Lixin Xiao, and Qihuang Gong. Direct observation of long electron-hole diffusion distance in $CH_3NH_3PbI_3$ perovskite thin film. *Scientific reports*, 5, 2015.

[105] Gede W. P. Adhyaksa, Leon W. Veldhuizen, Yinghuan Kuang, Sarah Brittman, Ruud E. I. Schropp, and Erik C. Garnett. Carrier diffusion lengths in hybrid perovskites: Processing, composition, aging, and surface passivation effects. *Chemistry of Materials*, 28(15):5259–5263, 2016.

[106] Carlito S. Ponseca, Tom J. Savenije, Mohamed Abdellah, Kaibo Zheng, Arkady Yartsev, Tobjrn Pascher, Tobias Harlang, Pavel Chabera, Tonu Pullerits, Andrey Stepanov, Jean-Pierre Wolf, and Villy Sundstrm. Organometal halide perovskite solar cell materials rationalized: Ultrafast charge generation, high and microsecond-long balanced mobilities, and slow recombination. *Journal of the American Chemical Society*, 136(14):5189–5192, 2014. PMID: 24654882.

[107] Christian Wehrenfennig, Giles E. Eperon, Michael B. Johnston, Henry J. Snaith, and Laura M. Herz. High charge carrier mobilities and lifetimes in organolead trihalide perovskites. *Advanced Materials*, 26(10):1584–1589, 2014.

[108] David A. Valverde-Chavez, Carlito S. Ponseca, Constantinos C. Stoumpos, Arkady Yartsev, Mercouri G. Kanatzidis, Villy Sundstrom, and David G. Cooke. Intrinsic femtosecond charge generation dynamics in single crystal $CH_3NH_3PbI_3$. *Energy Environ. Sci.*, 8:3700–3707, 2015.

[109] Eline M. Hutter, Giles E. Eperon, Samuel D. Stranks, and Tom J. Savenije. Charge carriers in planar and meso-structured organicinorganic perovskites: Mobilities, lifetimes, and concentrations of trap states. *The Journal of Physical Chemistry Letters*, 6(15):3082–3090, 2015. PMID: 26267206.

[110] N Hozhabri, S-H Lee, and K Alavi. Infrared measurements in annealed molecular beam epitaxy GaAs grown at low temperature. *Applied physics letters*, 66(19):2546–2548, 1995.

[111] M Kaminska, Z Liliental-Weber, ER Weber, T George, JB Kortright, FW Smith, B-Y Tsaur, and AR Calawa. Structural properties of as-rich GaAs grown by molecular beam epitaxy at low temperatures. *Applied Physics Letters*, 54(19):1881–1883, 1989.

[112] J Gebauer, R Krause-Rehberg, S Eichler, M Luysberg, H Sohn, and ER Weber. Ga vacancies in low-temperature-grown GaAs identified by slow positrons. *Applied physics letters*, 71(5):638–640, 1997.

[113] RM Feenstra, JM Woodall, and GD Pettit. Observation of bulk defects by scanning tunneling microscopy and spectroscopy: Arsenic antisite defects in GaAs. *Physical review letters*, 71(8):1176, 1993.

[114] Adrian Díaz Alvarez, Tao Xu, Goezde Tuetuencueoglu, Thomas Demonchaux, Jean-Philippe Nys, Maxime Berthe, Federico Matteini, Heidi A Potts, David Troadec, Gilles Patriarche, et al. Nonstoichiometric low-temperature grown GaAs nanowires. *Nano letters*, 15(EPFL-ARTICLE-214110):6440–6445, 2015.

[115] MO Manasreh, David C Look, KR Evans, and CE Stutz. Infrared absorption of deep defects in molecular-beam-epitaxial GaAs layers grown at 200°C: Observation of an el2-like defect. *Physical Review B*, 41(14):10272, 1990.

[116] I Kostakis and M Missous. Optimization and temperature dependence characteristics of low temperature $In_{0.3}GaAs_{0.7}As$ and $In_{0.53}GaAs_{0.47}As$-$In_{0.52}Al_{0.48}As$ semiconductor terahertz photoconductors. *AIP Advances*, 3(9):092131, 2013.

[117] Leon N. Cooper. Bound electron pairs in a degenerate fermi gas. *Phys. Rev.*, 104:1189–1190, Nov 1956.

[118] J. Frenkel. On the transformation of light into heat in solids. ii. *Phys. Rev.*, 37:1276–1294, May 1931.

[119] X.-Y. Zhu and V. Podzorov. Charge carriers in hybrid organicinorganic lead halide perovskites might be protected as large polarons. *The Journal of Physical Chemistry Letters*, 6(23):4758–4761, 2015. PMID: 26575427.

[120] Haiming Zhu, Kiyoshi Miyata, Yongping Fu, Jue Wang, Prakriti P. Joshi, Daniel Niesner, Kristopher W. Williams, Song Jin, and X.-Y. Zhu. Screening in crystalline liquids protects energetic carriers in hybrid perovskites. *Science*, 353(6306):1409–1413, 2016.

[121] Y. Z. Hu, R. Binder, S. W. Koch, S. T. Cundiff, H. Wang, and D. G. Steel. Excitation and polarization effects in semiconductor four-wave-mixing spectroscopy. *Phys. Rev. B*, 49:14382–14386, May 1994.

[122] J. M. Shacklette and S. T. Cundiff. Nonperturbative transient four-wave-mixing line shapes due to excitation-induced shift and excitation-induced dephasing. *J. Opt. Soc. Am. B*, 20(4):764–769, Apr 2003.

[123] Alan D. Bristow, Denis Karaiskaj, Xingcan Dai, Richard P. Mirin, and Steven T. Cundiff. Polarization dependence of semiconductor exciton and biexciton contributions to phase-resolved optical two-dimensional Fourier-transform spectra. *Phys. Rev. B*, 79:161305, Apr 2009.

[124] L Bányai, QT Vu, B Mieck, and H Haug. Ultrafast quantum kinetics of time-dependent rpa-screened coulomb scattering. *Physical review letters*, 81(4):882, 1998.

[125] IH Malitson. Interspecimen comparison of the refractive index of fused silica. *Josa*, 55(10):1205–1209, 1965.

[126] Irving H Malitson. Refraction and dispersion of synthetic sapphire. *JOSA*, 52(12):1377–1379, 1962.

[127] DD Sell, HC Casey Jr, and KW Wecht. Concentration dependence of the refractive index for n-and p-type GaAs between 1.2 and 1.8 eV. *Journal of Applied Physics*, 45(6):2650–2657, 1974.

[128] C. M. N. Mateo, A. T. Garcia, F. R. M. Ramos, K. I. Manibog, and A. A. Salvador. Strain-induced splitting of the valence band in epitaxially lifted-off GaAs films. *J. Appl. Phys.*, 101:073519, 2007.

[129] B. L. Wilmer, D. Webber, J. M. Ashley, K. C. Hall, and A. D. Bristow. Role of strain on the coherent properties of GaAs excitons and biexcitons. *Phys. Rev. B*, 96:075207, 2016.

[130] S. A. March, C. Clegg, D. B. Riley, **Webber, D.**, I. G. Hill, and K. C. Hall. Simultaneous observation of free and defect-bound excitons in $CH_3NH_3PbI_3$ using four-wave mixing spectroscopy. *Nature Scientific Reports*, 6:39139, December 2016.

[131] Philipp Loper, Michael Stuckelberger, Bjoern Niesen, Jérémie Werner, Miha Filipic, Soo-Jin Moon, Jun-Ho Yum, Marko Topic, Stefaan De Wolf, and Christophe Ballif. Complex refractive index spectra of $CH_3NH_3PbI_3$ perovskite thin films determined by spectroscopic ellipsometry and spectrophotometry. *The journal of physical chemistry letters*, 6(1):66–71, 2014.

[132] A. D. Bristow, D. Karaiskaj, X. Dai, T. Zhang, C. Carlsson, K. R. Hagen, R. Jimenez, and S. T. Cundiff. A versatile ultrastable platform for optical multidimensional Fourier-transform spectroscopy. *Rev. Sci. Instrum.*, 80:073108, 2009.

[133] L. Lepetit, G. Cheriaux, and M. Joffre. Linear techniques of phase measurement by femtosecond spectral interferometry for applications in spectroscopy. *J. Opt. Soc. Am. B*, 12:2467, 1995.

[134] Zhi-Kuang Tan, Reza Saberi Moghaddam, May Ling Lai, Pablo Docampo, Ruben Higler, Felix Deschler, Michael Price, Aditya Sadhanala, Luis M. Pazos, Dan Credgington, Fabian Hanusch, Thomas Bein, Henry J. Snaith, and Richard H. Friend. Bright light-emitting diodes based on organometal halide perovskite. *Nat Nano*, 9(9):687–692, Sep 2014. Letter.

[135] Young-Hoon Kim, Himchan Cho, Jin Hyuck Heo, Tae-Sik Kim, NoSoung Myoung, Chang-Lyoul Lee, Sang Hyuk Im, and Tae-Woo Lee. Multicolored organic/inorganic hybrid perovskite light-emitting diodes. *Advanced Materials*, 27(7):1248–1254, 2015.

[136] Felix Deschler, Michael Price, Sandeep Pathak, Lina E. Klintberg, David-Dominik Jarausch, Ruben Higler, Sven Httner, Tomas Leijtens, Samuel D. Stranks, Henry J. Snaith, Mete Atatre, Richard T. Phillips, and Richard H. Friend. High photoluminescence efficiency and optically pumped lasing in solution-processed mixed halide perovskite semiconductors. *The Journal of Physical Chemistry Letters*, 5(8):1421–1426, 2014. PMID: 26269988.

[137] Haiming Zhu, Yongping Fu, Fei Meng, Xiaoxi Wu, Zizhou Gong, Qi Ding, Martin V. Gustafsson, M. Tuan Trinh, Song Jin, and X.-Y. Zhu. Lead halide perovskite nanowire lasers with low lasing thresholds and high quality factors. *Nat Mater*, 14(6):636–642, Jun 2015. Article.

[138] Yongping Fu, Haiming Zhu, Alex W. Schrader, Dong Liang, Qi Ding, Prakriti Joshi, Leekyoung Hwang, X-Y. Zhu, and Song Jin. Nanowire lasers of formamidinium lead halide perovskites and their stabilized alloys with improved stability. *Nano Letters*, 16(2):1000–1008, 2016. PMID: 26727024.

[139] Letian Dou, Yang Micheal Yang, Jingbi You, Ziruo Hong, Wei-Hsuan Chang, Gang Li, and Yang Yang. Solution-processed hybrid perovskite photodetectors with high detectivity. *Nature communications*, 5:5404, 2014.

[140] Yanjun Fang and Jinsong Huang. Resolving weak light of sub-picowatt per square centimeter by hybrid perovskite photodetectors enabled by noise reduction. *Advanced Materials*, 27(17):2804–2810, 2015.

[141] Rui Dong, Yanjun Fang, Jungseok Chae, Jun Dai, Zhengguo Xiao, Qingfeng Dong, Yongbo Yuan, Andrea Centrone, Xiao Cheng Zeng, and Jinsong Huang. High-gain and low-driving-voltage photodetectors based on organolead triiodide perovskites. *Advanced Materials*, 27(11):1912–1918, 2015.

[142] Pablo Docampo, James M Ball, Mariam Darwich, Giles E Eperon, and Henry J Snaith. Efficient organometal trihalide perovskite planar-heterojunction solar cells on flexible polymer substrates. *Nature communications*, 4, 2013.

[143] Yaowen Li, Lei Meng, Yang Michael Yang, Guiying Xu, Ziruo Hong, Qi Chen, Jingbi You, Gang Li, Yang Yang, and Yongfang Li. High-efficiency robust

perovskite solar cells on ultrathin flexible substrates. *Nature communications*, 7, 2016.

[144] Alexander T. Barrows, Andrew J. Pearson, Chan Kyu Kwak, Alan D. F. Dunbar, Alastair R. Buckley, and David G. Lidzey. Efficient planar heterojunction mixed-halide perovskite solar cells deposited via spray-deposition. *Energy Environ. Sci.*, 7:2944–2950, 2014.

[145] Jong H. Kim, Spencer T. Williams, Namchul Cho, Chu-Chen Chueh, and Alex K.-Y. Jen. Enhanced environmental stability of planar heterojunction perovskite solar cells based on blade-coating. *Advanced Energy Materials*, 5(4):1401229–n/a, 2015. 1401229.

[146] Yehao Deng, Edwin Peng, Yuchuan Shao, Zhengguo Xiao, Qingfeng Dong, and Jinsong Huang. Scalable fabrication of efficient organolead trihalide perovskite solar cells with doctor-bladed active layers. *Energy Environ. Sci.*, 8:1544–1550, 2015.

[147] Mike Hambsch, Qianqian Lin, Ardalan Armin, Paul L. Burn, and Paul Meredith. Efficient, monolithic large area organohalide perovskite solar cells. *J. Mater. Chem. A*, 4:13830–13836, 2016.

[148] Constantinos C. Stoumpos, Christos D. Malliakas, and Mercouri G. Kanatzidis. Semiconducting tin and lead iodide perovskites with organic cations: Phase transitions, high mobilities, and near-infrared photoluminescent properties. *Inorganic Chemistry*, 52(15):9019–9038, 2013. PMID: 23834108.

[149] Shuhao Liu, Lili Wang, Wei-Chun Lin, Sukrit Sucharitakul, Clemens Burda, and Xuan P. A. Gao. Imaging the long transport lengths of photo-generated carriers in oriented perovskite films. *Nano Letters*, 16(12):7925–7929, 2016. PMID: 27960525.

[150] Qingfeng Dong, Yanjun Fang, Yuchuan Shao, Padhraic Mulligan, Jie Qiu, Lei Cao, and Jinsong Huang. Electron-hole diffusion lengths ¿ 175 m in solution-grown $CH_3NH_3PbI_3$ single crystals. *Science*, 347(6225):967–970, 2015.

[151] Octavi E. Semonin, Giselle A. Elbaz, Daniel B. Straus, Trevor D. Hull, Daniel W. Paley, Arend M. van der Zande, James C. Hone, Ioannis Kymissis, Cherie R. Kagan, Xavier Roy, and Jonathan S. Owen. Limits of carrier diffusion in n-type and p-type $CH_3NH_3PbI_3$ perovskite single crystals. *The Journal of Physical Chemistry Letters*, 7(17):3510–3518, 2016. PMID: 27525491.

[152] Jacky Even, Laurent Pedesseau, and Claudine Katan. Analysis of multivalley and multibandgap absorption and enhancement of free carriers related to exciton screening in hybrid perovskites. *The Journal of Physical Chemistry C*, 118(22):11566–11572, 2014.

[153] Liang Luo, Long Men, Zhaoyu Liu, Yaroslav Mudryk, Xin Zhao, Yongxin Yao, Joong M. Park, Ruth Shinar, Joseph Shinar, Kai-Ming Ho, Ilias E. Perakis, Javier Vela, and Jigang Wang. Ultrafast terahertz snapshots of excitonic rydberg states and electronic coherence in an organometal halide perovskite. *Nature Communications*, 8:15565 EP –, Jun 2017. Article.

[154] Wan-Jian Yin, Tingting Shi, and Yanfa Yan. Unique properties of halide perovskites as possible origins of the superior solar cell performance. *Advanced Materials*, 26(27):4653–4658, 2014.

[155] Wan-Jian Yin, Tingting Shi, and Yanfa Yan. Unusual defect physics in $CH_3NH_3PbI_3$ perovskite solar cell absorber. *Applied Physics Letters*, 104(6):063903, 2014.

[156] Samuel A. March, Drew B. Riley, Charlotte Clegg, Daniel Webber, Xinyu Liu, Margaret Dobrowolska, Jacek K. Furdyna, Ian G. Hill, and Kimberley C. Hall. Four-wave mixing in perovskite photovoltaic materials reveals long dephasing times and weaker many-body interactions than GaAs. *ACS Photonics*, 4(6):1515–1521, 2017.

[157] Justin C. Johnson, Zhen Li, Paul F. Ndione, and Kai Zhu. Third-order nonlinear optical properties of methylammonium lead halide perovskite films. *J. Mater. Chem. C*, 4:4847–4852, 2016.

[158] Brian A. Ruzicka, Lalani K. Werake, Hassana Samassekou, and Hui Zhao. Ambipolar diffusion of photoexcited carriers in bulk GaAs. *Applied Physics Letters*, 97(26):262119, 2010.

[159] Based on the measured laser spectrum, optical absorbance, and band gap, we estimate that over 95% of absorbed photons excite unbound electron-hole pairs.

[160] Gleb M Akselrod, Parag B Deotare, Nicholas J Thompson, Jiye Lee, William A Tisdale, Marc A Baldo, Vinod M Menon, and Vladimir Bulovic. Visualization of exciton transport in ordered and disordered molecular solids. *Nature communications*, 5:3646, 2014.

[161] D. Ritter, K. Weiser, and E. Zeldov. Steadystate photocarrier grating technique for diffusionlength measurement in semiconductors: Theory and experimental results for amorphous silicon and semiinsulating GaAs. *Journal of Applied Physics*, 62(11):4563–4570, 1987.

[162] I. Balberg, A. E. Delahoy, and H. A. Weakliem. Ambipolar diffusion length measurements on hydrogenated amorphous silicon pin structures. *Applied Physics Letters*, 53(20):1949–1951, 1988.

[163] E Peytavit, S Formont, and J-F Lampin. GaAs fabry-perot cavity photoconductors: Switching with picojoule optical pulses. *Electronics Letters*, 49(3):207–208, 2013.

[164] Samir Rihani, Richard Faulks, Harvey Beere, Hideaki Page, Ian Gregory, Michael Evans, David A Ritchie, and Michael Pepper. Effect of defect saturation on terahertz emission and detection properties of low temperature GaAs photoconductive switches. *Applied Physics Letters*, 95(5):051106, 2009.

[165] T Kataoka, K Kajikawa, J Kitagawa, Y Kadoya, and Y Takemura. Improved sensitivity of terahertz detection by GaAs photoconductive antennas excited at 1560 nm. *Applied Physics Letters*, 97(20):201110, 2010.

[166] Oday Mazin Abdulmunem, Norman Born, Martin Mikulics, Jan Christof Balzer, Martin Koch, and Sascha Preu. High accuracy terahertz time-domain system for reliable characterization of photoconducting antennas. *Microwave and Optical Technology Letters*, 59(2):468–472, 2017.

[167] P Uhd Jepsen, David G Cooke, and Martin Koch. Terahertz spectroscopy and imaging–modern techniques and applications. *Laser & Photonics Reviews*, 5(1):124–166, 2011.

[168] Nathan P Wells, Paul M Belden, Joseph R Demers, and William T Lotshaw. Transient reflectivity as a probe of ultrafast carrier dynamics in semiconductors: A revised model for low-temperature grown GaAs. *Journal of Applied Physics*, 116(7):073506, 2014.

[169] M Uemura, K Honda, Y Yasue, SL Lu, P Dai, and A Tackeuchi. Picosecond spin relaxation in low-temperature-grown GaAs. *Applied Physics Letters*, 104(12):122403, 2014.

[170] Fan Zheng-Fu, Tan Zhi-Yong, Wan Wen-Jian, Xing Xiao, Lin Xian, Jin Zuan-Ming, Cao Jun-Cheng, and Ma Guo-Hong. Study on ultrafast dynamics of low-temperature grown GaAs by optical pump and terahertz probe spectroscopy. *ACTA PHYSICA SINICA*, 66(8), 2017.

[171] Arūnas Krotkus. Semiconductors for terahertz photonics applications. *Journal of Physics D: Applied Physics*, 43(27):273001, 2010.

[172] MR Melloch, N Otsuka, JM Woodall, AC Warren, and JL Freeouf. Formation of arsenic precipitates in GaAs buffer layers grown by molecular beam epitaxy at low substrate temperatures. *Applied physics letters*, 57(15):1531–1533, 1990.

[173] I. S. Gregory, C. M. Tey, A. G. Cullis, M. J. Evans, H. E. Beere, and I. Farrer. Two-trap model for carrier lifetime and resistivity behavior in partially annealed GaAs grown at low temperature. *Phys. Rev. B*, 73:195201, May 2006.

[174] Ugo Fano. Effects of configuration interaction on intensities and phase shifts. *Physical Review*, 124(6):1866, 1961.

[175] S. R. Johnson and T. Tiedje, 1995. Temperature dependence of the Urbach edge in GaAs.

[176] R. Yano, Y. Hirayama, S. Miyashita, N. Uesugi, and S. Uehara. Arsenic pressure dependence of carrier lifetime and annealing dynamics for low-temperature grown GaAs studied by pumpprobe spectroscopy. *Journal of Applied Physics*, 94(6):3966–3971, 2003.

[177] K. A. McIntosh, K. B. Nichols, S. Verghese, and E. R. Brown. Investigation of ultrashort photocarrier relaxation times in low-temperature-grown GaAs. *Applied Physics Letters*, 70(3):354–356, 1997.

[178] I. S. Gregory, C. Baker, W. R. Tribe, M. J. Evans, H. E. Beere, E. H. Linfield, A. G. Davies, and M. Missous. High resistivity annealed low-temperature GaAs with 100 fs lifetimes. *Applied Physics Letters*, 83(20):4199–4201, 2003.

[179] G. S. Engel, T. R. Calhoun, E. L. Read, T.-K. Ahn, T. Mancal, Y.-C. Cheng, R. E. Blankenship, and G. R. Fleming. Evidence for wavelike energy transfer through quantum coherence in photosynthetic systems. *Nature*, 446:782, 2007.

[180] D. Abramavicius, D. V. Voronine, and S. Mukamel. Double-quantum resonances and exciton scattering in coherent 2d spectroscopy of photosynthetic complexes. *Proc. Natl. Acad. Sci.*, 105:8525, 2008.

[181] J. Clark, C. Silva, R. H. Friend, and F. C. Spano. Role of intermolecular coupling in the photophysics of disordered organic semiconductors: aggregate emission in regioregular polythiophene. *Phys. Rev. Lett.*, 98:206406, 2007.

[182] K. W. Stone, D. B. Turner, K. Gundogdu, S. T. Cundiff, and K. A. Nelson. Exciton-exciton correlations revealed by two-quantum, two-dimensional Fourier transform optical spectroscopy. *Acc. Chem. Res.*, 42:1452, 2009.

[183] A. E. Almand-Hunter, H. Li, S. T. Cundiff, M. Mootz, M. Kira, and S. W. Koch. Quantum droplets of electrons and holes. *Nature*, 506:471, 2014.

[184] K. W. Stone, K. Gundogdu, D. B. Turner, X. Li, S. T. Cundiff, and K. A. Nelson. Two-quantum 2d ft electronic spectroscopy of biexcitons in GaAs quantum wells. *Science*, 324:1169, 2009.

[185] H. Wang, K. Ferrio, D. G. Steel, Y. Z. Hu, R. Binder, and S. W. Koch. Transient nonlinear optical response from excitation induced dephasing in GaAs. *Phys. Rev. Lett.*, 71:1261, 1993.

[186] C. N. Borca, T. Zhang, X. Li, and S. T. Cundiff. Optical two-dimensional Fourier transform spectroscopy of semiconductors. *Chem. Phys. Lett.*, 416:311, 2005.

[187] D. Karaiskaj, A. D. Bristow, L. Yang, X. Dai, R. P. Mirin, S. Mukamel, and S. T. Cundiff. Two-quantum many-body coherences in two-dimensional Fourier-transform spectra of exciton resonances in semiconductor quantum wells. *Phys. Rev. Lett.*, 104:117401, 2010.

[188] S. T. Cundiff. Optical three dimensional coherent spectroscopy. *Phys. Chem. Chem. Phys.*, 16:8193, 2014.

[189] J. C. Vaughan, T. Hornung, K. W. Stone, and K. A. Nelson. Coherently controlled ultrafast four-wave mixing spectroscopy. *J. Phys. Chem. A*, 111:4873, 2007.

[190] G. Nardin, G. Moody, R. Singh, T. M. Autry, H. Li, F. Morier-Genoud, and S. T. Cundiff. Coherent excitonic coupling in an asymmetric double InGaAs quantum well arises from many-body effects. *Phys. Rev. Lett.*, 112:046402, 2014.

[191] H. Wang, K. B. Ferrio, D. G. Steel, P. R. Berman, Y. Z. Hu, R. Binder, and S. W. Koch. Transient four-wave-mixing line shapes: Effects of excitation-induced dephasing. *Phys. Rev. A*, 49:R1551–R1554, Mar 1994.

[192] P. Dey, J. Paul, N. Glinkin, Z. D. Kovalyuk, Z. R. Kudrynskyi, A. H. Romero, and D. Karaiskaj. Mechanism of excitonic dephasing in layered inse crystals. *Phys. Rev. B*, 89:125128, 2014.

[193] H. Wang, K. B. Ferrio, D. G. Steel, P. R. Berman, Y. Z. Hu, R. Binder, and S. W. Koch. Transient four-wave-mixing line shapes: Effects of excitation-induced dephasing. *Phys. Rev. A*, 49:R1551, 1994.

[194] W. A. Hugel, M. F. Heinrich, M. Wegener, Q. T. Vu, L. Banyai, and H. Haug. Photon echos from semiconductor band-to-band continuum transitions in the regime of coulomb quantum kinetics. *Phys. Rev. Lett.*, 83:3313, 1999.

[195] J. M. Shacklette and S.T. Cundiff. Nonperturbative transient four-wave-mixing line shapes due to excitation-induced shift and excitation-induced dephasing. *J. Opt. Soc. Am. B.*, 20:764, 2003.

[196] L. Banyai, D. B. Tran, Thoai, E. Reitsamer, H. Haug, D. Steinbach, M. U. Wehner, M. Wegener, T. Marschner, , and W. Stolz. Exciton-klo-phonon quantum kinetics: Evidence of memory effects in bulk GaAs. *Phys. Rev. Lett.*, 75:2188, 1995.

[197] D. Webber, T. de Boer, M. Yildirim, S. March, R. Mathew, A. Gamouras, X. Liu, M. Dobrowolska, J. K. Furdyna, and K. C. Hall. Measurement of coherence decay in gamnas using femtosecond four-wave mixing. *J. Visualized Exp.*, 82:e51094, 2013.

[198] S. T. Cundiff. Optical two-dimensional Fourier transform spectroscopy of semiconductor nanostructures. *J. Opt. Soc. Am. B*, 29:A69, 2012.

[199] I. Kuznetsova, T. Meier, S. T. Cundiff, and P. Thomas. Determination of homogeneous and inhomogeneous broadening in semiconductor nanostructures by two-dimensional Fourier-transform optical spectroscopy. *Phys. Rev. B*, 76:153301, 2007.

[200] M. L. Cowan, J.P. Ogilvie, and R.J.D. Miller. Two-dimensional spectroscopy using diffractive optics based phased-locked photon echoes. *Chem. Phys. Lett.*, 386:184, 2004.

[201] A. D. Bristow, D. Karaiskaj, X. Dai, and S. T. Cundiff. All-optical retrieval of the global phase for two-dimensional Fourier-transform spectroscopy. *Opt. Exp.*, 16:18017, 2008.

[202] V. M. Axt and A. Stahl. A dynamics-controlled truncation scheme for the hierarchy of density-matrices in semiconductor optics. *Z. Phys. B.*, 93:195, 1994.

[203] M. Lindberg, Y. Z. Hu, R. Binder, and S. W. Koch. $\chi^{(3)}$ formalism in optically-excited semiconductors and its applications in 4-wave-mixing spectroscopy. *Phys. Rev. B.*, 50:18060, 1994.

Appendix A

Discussion of Experimental Uncertainties

A discussion of the experimental uncertainties in this thesis work are presented here. In particular, the procedure on how the uncertainties in Chapter 6 were obtained are described in this appendix.

The strength of the four-wave mixing signal is very weak, and in most cases, can be easily obscured by background light or scattered light from surfaces. In the experiments presented in thesis work, the power of the four-wave mixing signal was on the order of 1-100 nW for all samples. In comparison, the excitation laser power was on the order of 1 - 100 mW. For these reasons, scattered light that travels along the four-wave mixing signal direction posed the biggest challenge in improving the signal-to-noise of these experiments. Careful alignment of collection optics, low-light conditions in the laboratory environment, as well as careful positioning of the focused laser beams on the sample helped to minimize these additional sources of light.

In Chapter 6, the spectrally-integrated intensity of the four-wave mixing signal was measured using a photodiode at each pulse delay T. Ambient light in the room, as well as scattered light lead to a DC background superimposed over the four-wave mixing signal. An estimate of the DC offset was performed by measuring the four-wave mixing signal as a function of delays τ and T. As discussed in Chapter 2, no four-wave mixing signal is expected for either a homogeneous or inhomogeneous transition for $\tau > 5T_2$ where T_2 is the coherence lifetime. For the sample used in these experiments, $T_2 \approx 200fs$, and so by measuring the light along the four-wave mixing signal path at the these long delays, an estimate of the background signal was obtained for each delay T.

To improve the estimate of T_s, ten measurements of the four-wave mixing signal as a function of delay τ and T were performed for each grating period d. A value of T_s for each grating period was obtained by performing a least squares fit of each data set, and then averaging the set of extracted T_s values. The uncertainty on $\overline{T_s}$ was dictated

by the standard deviation of the set since the uncertainty of the fitting routine was found to be much smaller in comparison. The main reason for this uncertainty stems from the finite range of the delay stage, which was not large enough to cover the entire decay of the four-wave mixing signal with respect to T.

The uncertainty on the ambipolar diffusion length L_D was determined through error propagation. Recall the definition of diffusion length

$$\mathrm{L_D} = \sqrt{DT_L} \tag{A.1}$$

where D and T_L are the ambipolar diffusion coefficient and carrier lifetime. The respective error on each of these terms is given by δD and δT_L and were determined from the root-mean-square error of the linear fitting routine used to fit the data presented in Fig. 4.3. The error on L_D was then computed using the following relation:

$$\delta\mathrm{L_D} = \mathrm{L_D}\frac{1}{2}\left(\frac{\delta D}{D} + \frac{\delta T_L}{T_L}\right) \tag{A.2}$$

Appendix B

Choice of Ordinary Differential Integrator for Simulating the Optical Bloch Equations

In this thesis work, the optical Bloch equations were numerically calculated using an ordinary differential equation (ODE) integrator. The numerical technique used was an 8^{th} order Runge-Kutta (RK) algorithm and was chosen based on it providing the best available performance. In this Appendix, a brief overview of numerical integration techniques is explained, as well as the justification for the use of the Runge Kuttaexplained.

The simplest form of Runge-Kutta is the first-order method, also known as the Euler method. If $y(t)$ is a smooth function and its dynamics are described by a corresponding first-order differential equation (described by $\dot{y}(t) = f(t, y)$), the solution to $y(t)$ at some time Δt later is found by forward propagation:

$$y(t + \Delta t) = y(t) + \Delta t f(t, y(t)) \tag{B.1}$$

The solution to $y(t)$ is found by iteratively solving Eqn. B.1 over the desired time range. The Euler method is an approximation to the analytical solution, and relies on the use of a small enough time step Δt so that rapid fluctuations in $y(t)$ are not missed. Because of this point, many iterations have to be performed adding to the overall computation time. An improvement over this method is to increase the accuracy of the forward propagation by computing the slope at the midpoint $(t+\frac{1}{2}\Delta t)$ using the estimate of $y(t)$ at the midpoint as determined by Eqn. B.1. For this reason, this approach is said to be a second-order Runge-Kutta, and the solution to $y(t)$ at a time step later is given by:

$$y(t + \Delta t) = y(t) + \Delta t f(t + \frac{1}{2}\Delta t, y(t) + \frac{1}{2}\Delta t f(t, y(t))) \tag{B.2}$$

Despite Eqn. B.2 requiring more computation time per iteration than Eqn. B.1, the second-order approach is an overall improvement over the first-order approximation

since the truncation error approaches zero faster for decreasing step size, and subsequently leads to less computation time. Following this approach, one can obtain a set of equations for higher-order Runge-Kutta until the desired tradeoff between time taken to compute each iteration and the time taken over all iterations is minimized.

So far, discussion has focused on techniques that utilize a fixed time step. However, improvements in computation time can be had when the time step is allowed to vary such that the truncation error is within a certain tolerance. These methods are called adaptive step size routines, and for functions that contain both slowly-varying and fast-varying regions it can lead to a significant decrease in computation time. For example, a rapidly-varying function will require a fine time step to capture all of the salient features but once the integrator reaches a region of slow variation, the time step can be increased so that the computation can be done faster.

The program used to simulate the 2DFTS response was written by the author in the MATLAB programming environment. Three ODE integrators were tested prior to computation of the results presented in Chapter 4 and are called ODE23, ODE45, and ODE87. ODE23, ODE45, and ODE87 are third, fifth, and eighth-order adaptive stepsize Runge-Kutta algorithms respectively. To determine which integrator provided the optimal performance in calculating the optical Bloch equations, the time-resolved four-wave mixing emission was calculated for the same multilevel model presented in Chapter 4 with similar excitation conditions (*e.g.* pulse ordering, pulse delay T) and system relaxation properties (*e.g.* T_2, T_L). In the below figure is a plot of the time-resolved four-wave mixing signal for each integrator alongside the reference, which was calculated using the ODE87 integrator with a very high tolerance (10^{-15}).

Each of the integrators reasonably estimated the reference signal. The tolerance was adjusted such that the root mean signal error was the same for each integrator (≤ 0.05). The amount of tolerance and average computation time taken to perform each calculation is listed in the following table:

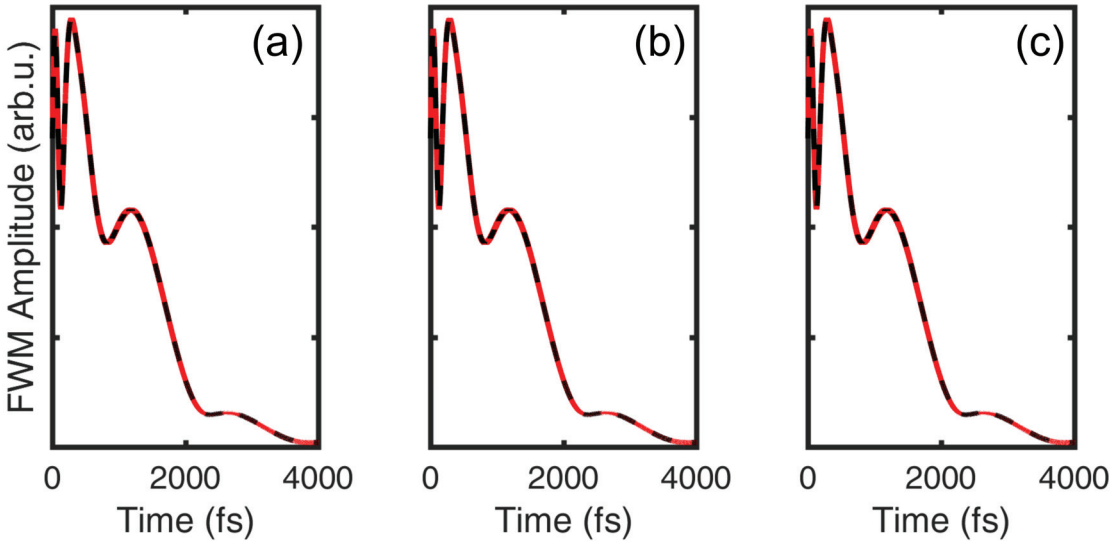

Figure B.1: The time-resolved four-wave mixing signal alongside the reference signal (black dashed line) calculated with (a) ODE23, (b) ODE45, (c) ODE87.

Integrator	Tolerance ($\times 10^{-8}$)	Computation Time (s)
ODE23	1	4.2
ODE45	0.1	1.7
ODE87	1	1.2

The ODE87 integrator performed the best out of the three integrators tested in this work.

Appendix C

Bányai Projection Method

Extraction of the FWM signal emitted along $\vec{k_3} + \vec{k_2} - \vec{k_1}$ from the optical Bloch equations was obtained using the Bányai projection method [196] which was extended by the author to the case of three pulse excitation.

Within the rotating wave approximation, the electric field can be rewritten as:

$$E(\vec{R}, t) = e^{i(\vec{k}_1 \cdot \vec{R} - \omega(t-t_1))} \left[E_1(t-t_1) + E_2(t-t_2) e^{i(\psi+\omega\tau))} + E_3(t-t_3) e^{i(\phi+\omega T)} \right] \quad \text{(C.1)}$$

The light field depends on two phase factors $\phi = (\vec{k_2} - \vec{k_1}) \cdot \vec{R}$ and $\psi = (\vec{k_3} - \vec{k_1}) \cdot \vec{R}$. The FWM signal can be obtained from the expression,

$$P(t, \tau) = \int_0^{2\pi} \int_0^{2\pi} d\phi d\psi P(t, \tau, \phi, \psi) e^{in\phi} e^{im\psi} \quad \text{(C.2)}$$

where $P(t, \tau, \phi, \psi)$ is the macroscopic polarization determined from the density matrix components at each delay τ and each combination of phase angles ϕ and ψ. To obtain the FWM signal stemming from the polarization emitted in the $\vec{k_3} + \vec{k_2} - \vec{k_1}$ direction, integers $n = m = 1$ such that the overall phase has the matching spatial component $\vec{k_3} + \vec{k_2} - \vec{k_1}$. The polarization $P(\vec{r}, t, \tau, \phi, \psi)$ produced by the three light fields is composed of an infinite combination of different spatial combinations (*e.g* $\vec{k_1}$, $\vec{k_2} - \vec{k_3}$, $2\vec{k_2}$ etc.) but only one combination of spatial directions matches the direction of the FWM signal. In this case, we see that the terms $P(\vec{r}, t, \tau, \phi, \psi)$ and $e^{in\phi} e^{im\psi}$ are only not orthogonal for when $n = m = 1$ (or in other words, Eqn. C.2 is only nonzero when $n = m = 1$).

Following Bányai *et al.*, the integrals in Eqn. C.2 are replaced as a summation for several discrete values of the phase angles ψ, ϕ. For the two-pulse case in Bányai *et al.* [196] four ϕ angles equally spaced between 0 and 2π were used to calculate the FWM signal. For the three pulse case, four values of ϕ and four values of ψ were used, for a total calculation count of sixteen. The calculated polarization $P(\vec{k}_{32-1}t, \tau)$

along $\vec{k}_{32-1}$ is then given by Eqn. 6.3.

$$P(t,\tau) = \sum_{x=1}^{4}\sum_{y=1}^{4} P(t,\tau,\phi,\psi)e^{i\phi_x}e^{i\psi_y} \tag{C.3}$$

Appendix D

Derivation of the Ambipolar Diffusion Equation

In this section, a derivation of the ambipolar diffusion equation is presented. As discussed earlier, ambipolar transport governs the motion of an electron-hole pair through a semiconductor. To determine the equation of motion, we need to consider first the motion of an electron and hole separately. Consider an electron distribution in one dimension given by $n(x,T)$. The flow of electrons (the number of electrons per m^2s) at $x = 0$ is given by:

$$\frac{1}{2}\frac{\frac{n(-l,T)+n(0,T)}{2}l - \frac{n(0,T)+n(l,T)}{2}l}{\frac{l}{v_{th}}} \tag{D.1}$$

where l_e is the mean-free path of electrons, and v_{th} is the thermal velocity of the electrons. $n(\pm l,T)$ can be Taylor expanded to yield:

$$n(\pm l,T) = n(0,T) + \left.\frac{\delta n(x,T)}{\delta x}\right|_{x=0}(\pm l) \tag{D.2}$$

The flow of electron-hole pairs is given by:

$$-\frac{l_e v_{th}}{2}\frac{\delta n(x,T)}{\delta x} \tag{D.3}$$

Define the electron diffusion coefficient as $D_e = \frac{l_e v_{th}}{2}$, and describe the flow in terms of the current density $J(x,t)$ and one obtains Fick's law:

$$J_n = eD_e\frac{\delta n(x,T)}{\delta x}. \tag{D.4}$$

Similarly, using the same procedure as above for a hole distribution $p(x,t)$, one obtains:

$$J_p = -eD_h\frac{\delta p(x,T)}{\delta x}. \tag{D.5}$$

We will now consider a current density J_e through a volume of cross-sectional area A and infinitesimal small length dx, including the effects of recombination. The rate of charge transfer to and from the volume is given by:

$$Adx\frac{dn(x,T)}{dT} = \frac{J_n(x,T)A}{e} - \frac{J_n(x+dx,T)A}{e} - R_n(x,t)Adx \tag{D.6}$$

where R_n is the rate of electron recombination. If relaxation $R_n(x,t)$ is taken to be in the low-level injection regime, then $R_n(x,t) = \frac{n(x,T)}{T_e}$ where T_e is the electron recombination time. With this approximation, simplification of the above gives:

$$\frac{dn(x,T)}{dT} = \frac{1}{e}\frac{\delta J_n(x,T)}{\delta x} - \frac{n(x,T)}{T_n} \tag{D.7}$$

Combining Eqn. D.5 and D.7 results in the following equation describing diffusion of electrons:

$$\frac{dn(x,T)}{dT} = D_e\frac{\partial n^2(x,T)}{\partial x^2} - \frac{n(x,T)}{T_e} \tag{D.8}$$

and similarly for holes:

$$\frac{dp(x,T)}{dT} = D_h\frac{\partial p^2(x,T)}{\partial x^2} - \frac{p(x,T)}{T_h} \tag{D.9}$$

Optical excitation leads to the generation of excess electrons and holes in addition to what is already present in the system (*i.e.* $n = n_0 + \delta n$, where δn is the excess number of electrons excited). Since optical excitation leads to the generation of electron-hole pairs, $\delta_n = \delta_p = \zeta$, and they will recombine with each other at the same rate, *i.e.*

$$\frac{n(x,T)}{T_e} = \frac{p(x,T)}{T_h} = R \tag{D.10}$$

We will now multiply the diffusion equation for the total number of electrons (holes), given by Eqn. D.8 (Eqn. D.9) by their respective mobilities μ_e (μ_h) and number of electrons (holes), and then add the two equations together to yield:

$$(\mu_e n + \mu_h p)\frac{d\zeta(x,T)}{dT} = (\mu_e n D_e + \mu_h n D_h)\frac{\partial\zeta(x,T)^2}{\partial x^2} - (\mu_e n + \mu_h p)R \tag{D.11}$$

This can be rearranged into the following form:

$$\frac{d\zeta(x,T)}{dT} = D_a\frac{\partial\zeta(x,T)^2}{\partial x^2} - R \tag{D.12}$$

where $D_a = \frac{(\mu_e n D_e + \mu_h p D_h)}{(\mu_e n + \mu_h p)}$ is called the ambipolar diffusion coefficient. If relaxation is primarily due to electron-hole pair recombination, then $R = \frac{\zeta(x,T)}{T_L}$ were T_L is the recombination lifetime. Therefore the above can be written again to yield:

$$\frac{d\zeta(x,T)}{dT} = D_a\frac{\partial^2\zeta(x,T)}{\partial x^2} - \frac{\zeta(x,T)}{T_L} \tag{D.13}$$

Which is the same result presented in Chapter 1.

Appendix E

Rights and Permissions

AIP PUBLISHING LLC LICENSE TERMS AND CONDITIONS

Oct 02, 2017

This Agreement between Daniel Webber ("You") and AIP Publishing LLC ("AIP Publishing LLC") consists of your license details and the terms and conditions provided by AIP Publishing LLC and Copyright Clearance Center.

License Number	4200910058645
License date	Oct 02, 2017
Licensed Content Publisher	AIP Publishing LLC
Licensed Content Publication	Journal of Applied Physics
Licensed Content Title	Annealing dynamics of molecular-beam epitaxial GaAs grown at 200 °C
Licensed Content Author	D. C. Look, D. C. Walters, G. D. Robinson, et al
Licensed Content Date	Jul 1, 1993
Licensed Content Volume	74
Licensed Content Issue	1
Type of Use	Thesis/Dissertation
Requestor type	Student
Format	Print and electronic
Portion	Figure/Table
Number of figures/tables	1
Title of your thesis / dissertation	TRANSIENT FOUR-WAVE MIXING STUDIES OF GaAs, LOW-TEMPERATURE-GROWN GaAs, AND CH3NH3PbI3
Expected completion date	Dec 2017
Estimated size (number of pages)	190
Requestor Location	Daniel Webber Dept. of Physics Dalhousie University Halifax, NS B3H4R2 Canada Attn: Daniel Webber
Billing Type	Invoice
Billing Address	Daniel Webber Dept. of Physics Dalhousie University Halifax, NS B3H4R2 Canada Attn: Daniel Webber
Total	0.00 USD

Terms and Conditions

AIP Publishing LLC -- Terms and Conditions: Permissions Uses

AIP Publishing hereby grants to you the non-exclusive right and license to use and/or distribute the Material according to the use specified in your order, on a one-time basis, for the specified term, with a maximum distribution equal to the number that you have ordered. Any links or other content accompanying the Material are not the subject of this license.

1. You agree to include the following copyright and permission notice with the reproduction of the Material:"Reprinted from [FULL CITATION], with the permission of AIP Publishing." For an article, the credit line and permission notice must be printed on the first page of the article or book chapter. For photographs, covers, or tables, the notice may appear with the Material, in a footnote, or in the reference list.
2. If you have licensed reuse of a figure, photograph, cover, or table, it is your responsibility to ensure that the material is original to AIP Publishing and does not contain the copyright of another entity, and that the copyright notice of the figure, photograph, cover, or table does not indicate that it was reprinted by AIP Publishing, with permission, from another source. Under no circumstances does AIP Publishing purport or intend to grant permission to reuse material to which it does not hold appropriate rights.
   You may not alter or modify the Material in any manner. You may translate the Material into another language only if you have licensed translation rights. You may not use the Material for promotional purposes.
3. The foregoing license shall not take effect unless and until AIP Publishing or its agent, Copyright Clearance Center, receives the Payment in accordance with Copyright Clearance Center Billing and Payment Terms and Conditions, which are incorporated herein by reference.
4. AIP Publishing or Copyright Clearance Center may, within two business days of granting this license, revoke the license for any reason whatsoever, with a full refund payable to you. Should you violate the terms of this license at any time, AIP Publishing, or Copyright Clearance Center may revoke the license with no refund to you. Notice of such revocation will be made using the contact information provided by you. Failure to receive such notice will not nullify the revocation.
5. AIP Publishing makes no representations or warranties with respect to the Material. You agree to indemnify and hold harmless AIP Publishing, and their officers, directors, employees or agents from and against any and all claims arising out of your use of the Material other than as specifically authorized herein.
6. The permission granted herein is personal to you and is not transferable or assignable without the prior written permission of AIP Publishing. This license may not be amended except in a writing signed by the party to be charged.
7. If purchase orders, acknowledgments or check endorsements are issued on any forms containing terms and conditions which are inconsistent with these provisions, such inconsistent terms and conditions shall be of no force and effect. This document, including the CCC Billing and Payment Terms and Conditions, shall be the entire agreement between the parties relating to the subject matter hereof.

This Agreement shall be governed by and construed in accordance with the laws of the State of New York. Both parties hereby submit to the jurisdiction of the courts of New York County for purposes of resolving any disputes that may arise hereunder.

V1.1

Questions? customercare@copyright.com or +1-855-239-3415 (toll free in the US) or +1-978-646-2777.

AIP PUBLISHING LLC LICENSE TERMS AND CONDITIONS

Oct 02, 2017

This Agreement between Daniel Webber ("You") and AIP Publishing LLC ("AIP Publishing LLC") consists of your license details and the terms and conditions provided by AIP Publishing LLC and Copyright Clearance Center.

License Number	4200901461633
License date	Oct 02, 2017
Licensed Content Publisher	AIP Publishing LLC
Licensed Content Publication	Journal of Vacuum Science & Technology B
Licensed Content Title	Optical characterization of low temperature grown GaAs by transmission measurements above the band gap
Licensed Content Author	D. Streb, M. Ruff, S. U. Dankowski, et al
Licensed Content Date	May 1, 1996
Licensed Content Volume	14
Licensed Content Issue	3
Type of Use	Thesis/Dissertation
Requestor type	Student
Format	Print and electronic
Portion	Figure/Table
Number of figures/tables	1
Title of your thesis / dissertation	TRANSIENT FOUR-WAVE MIXING STUDIES OF GaAs, LOW-TEMPERATURE-GROWN GaAs, AND CH3NH3PbI3
Expected completion date	Dec 2017
Estimated size (number of pages)	190
Requestor Location	Daniel Webber Dept. of Physics Dalhousie University Halifax, NS B3H4R2 Canada Attn: Daniel Webber
Billing Type	Invoice
Billing Address	Daniel Webber Dept. of Physics Dalhousie University Halifax, NS B3H4R2 Canada Attn: Daniel Webber
Total	0.00 USD

Terms and Conditions

American Vacuum Society -- Terms and Conditions: Permissions Uses

American Vacuum Society ("AVS") hereby grants to you the non-exclusive right and license to use

and/or distribute the Material according to the use specified in your order, on a one-time basis, for the specified term, with a maximum distribution equal to the number that you have ordered. Any links or other content accompanying the Material are not the subject of this license.

1. You agree to include the following copyright and permission notice with the reproduction of the Material:"Reprinted with permission from [FULL CITATION]. Copyright [PUBLICATION YEAR], American Vacuum Society." For an article, the copyright and permission notice must be printed on the first page of the article or book chapter. For photographs, covers, or tables, the copyright and permission notice may appear with the Material, in a footnote, or in the reference list.
2. If you have licensed reuse of a figure, photograph, cover, or table, it is your responsibility to ensure that the material is original to AVS and does not contain the copyright of another entity, and that the copyright notice of the figure, photograph, cover, or table does not indicate that it was reprinted by AVS, with permission, from another source. Under no circumstances does AVS, purport or intend to grant permission to reuse material to which it does not hold copyright.
3. You may not alter or modify the Material in any manner. You may translate the Material into another language only if you have licensed translation rights. You may not use the Material for promotional purposes. AVS reserves all rights not specifically granted herein.
4. The foregoing license shall not take effect unless and until AVS or its agent, Copyright Clearance Center, receives the Payment in accordance with Copyright Clearance Center Billing and Payment Terms and Conditions, which are incorporated herein by reference.
5. AVS or the Copyright Clearance Center may, within two business days of granting this license, revoke the license for any reason whatsoever, with a full refund payable to you. Should you violate the terms of this license at any time, AVS, American Vacuum Society, or Copyright Clearance Center may revoke the license with no refund to you. Notice of such revocation will be made using the contact information provided by you. Failure to receive such notice will not nullify the revocation.
6. AVS makes no representations or warranties with respect to the Material. You agree to indemnify and hold harmless AVS, American Vacuum Society, and their officers, directors, employees or agents from and against any and all claims arising out of your use of the Material other than as specifically authorized herein.
7. The permission granted herein is personal to you and is not transferable or assignable without the prior written permission of AVS. This license may not be amended except in a writing signed by the party to be charged.
8. If purchase orders, acknowledgments or check endorsements are issued on any forms containing terms and conditions which are inconsistent with these provisions, such inconsistent terms and conditions shall be of no force and effect. This document, including the CCC Billing and Payment Terms and Conditions, shall be the entire agreement between the parties relating to the subject matter hereof.

This Agreement shall be governed by and construed in accordance with the laws of the State of New York. Both parties hereby submit to the jurisdiction of the courts of New York County for purposes of resolving any disputes that may arise hereunder.

Questions? customercare@copyright.com or +1-855-239-3415 (toll free in the US) or +1-978-646-2777.

AMERICAN PHYSICAL SOCIETY LICENSE TERMS AND CONDITIONS

Oct 02, 2017

This Agreement between Daniel Webber ("You") and American Physical Society ("American Physical Society") consists of your license details and the terms and conditions provided by American Physical Society and Copyright Clearance Center.

License Number	4200901307674
License date	Oct 02, 2017
Licensed Content Publisher	American Physical Society
Licensed Content Publication	Physical Review B
Licensed Content Title	Mechanism of excitonic dephasing in layered InSe crystals
Licensed Content Author	P. Dey et al.
Licensed Content Date	Mar 31, 2014
Licensed Content Volume	89
Type of Use	Thesis/Dissertation
Requestor type	Student
Format	Print, Electronic
Portion	image/photo
Number of images/photos requested	1
Portion description	Figure 3 (c).
Rights for	Main product
Duration of use	Life of Current Edition
Creation of copies for the disabled	no
With minor editing privileges	no
For distribution to	Worldwide
In the following language(s)	Original language of publication
With incidental promotional use	no
The lifetime unit quantity of new product	0 to 499
The requesting person/organization is:	Daniel Webber (PhD Candidate)
Order reference number	
Title of your thesis / dissertation	TRANSIENT FOUR-WAVE MIXING STUDIES OF GaAs, LOW-TEMPERATURE-GROWN GaAs, AND CH3NH3PbI3
Expected completion date	Dec 2017
Expected size (number of pages)	190
Requestor Location	Daniel Webber Dept. of Physics Dalhousie University

	Halifax, NS B3H4R2 Canada Attn: Daniel Webber
Billing Type	Invoice
Billing Address	Daniel Webber Dept. of Physics Dalhousie University Halifax, NS B3H4R2 Canada Attn: Daniel Webber
Total	0.00 USD

Terms and Conditions

Terms and Conditions

The American Physical Society (APS) is pleased to grant the Requestor of this license a non-exclusive, non-transferable permission, limited to [**print** and/or **electronic** format, depending on what they chose], provided all criteria outlined below are followed.

1. You must also obtain permission from at least one of the lead authors for each separate work, if you haven't done so already. The author's name and affiliation can be found on the first page of the published Article.
2. For electronic format permissions, Requestor agrees to provide a hyperlink from the reprinted APS material using the source material's DOI on the web page where the work appears. The hyperlink should use the standard DOI resolution URL, http://dx.doi.org/{DOI}. The hyperlink may be embedded in the copyright credit line.
3. For print format permissions, Requestor agrees to print the required copyright credit line on the first page where the material appears: "Reprinted (abstract/excerpt/figure) with permission from [(FULL REFERENCE CITATION) as follows: Author's Names, APS Journal Title, Volume Number, Page Number and Year of Publication.] Copyright (YEAR) by the American Physical Society."
4. Permission granted in this license is for a one-time use and does not include permission for any future editions, updates, databases, formats or other matters. Permission must be sought for any additional use.
5. Use of the material does not and must not imply any endorsement by APS.
6. Under no circumstance does APS purport or intend to grant permission to reuse materials to which it does not hold copyright. It is the requestors sole responsibility to ensure the licensed material is original to APS and does not contain the copyright of another entity, and that the copyright notice of the figure, photograph, cover or table does not indicate that it was reprinted by APS, with permission from another source.
7. The permission granted herein is personal to the Requestor for the use specified and is not transferable or assignable without express written permission of APS. This license may not be amended except in writing by APS.
8. You may not alter, edit or modify the material in any manner.
9. You may translate the materials only when translation rights have been granted.
10. You may not use the material for promotional, sales, advertising or marketing purposes.
11. The foregoing license shall not take effect unless and until APS or its agent, Copyright Clearance Center (CCC), receives payment in full in accordance with CCC Billing and Payment Terms and Conditions, which are incorporated herein by reference.
12. Should the terms of this license be violated at any time, APS or CCC may revoke the license with no refund to you and seek relief to the fullest extent of the laws of the USA. Official written notice will be made using the contact information provided with the permission request. Failure to receive such notice will not nullify revocation of the permission.

13. APS reserves all rights not specifically granted herein.
14. This document, including the CCC Billing and Payment Terms and Conditions, shall be the entire agreement between the parties relating to the subject matter hereof.

Other Terms and Conditions

Version 1.1

Questions? customercare@copyright.com or +1-855-239-3415 (toll free in the US) or +1-978-646-2777.

AIP PUBLISHING LLC LICENSE TERMS AND CONDITIONS

Oct 02, 2017

This Agreement between Daniel Webber ("You") and AIP Publishing LLC ("AIP Publishing LLC") consists of your license details and the terms and conditions provided by AIP Publishing LLC and Copyright Clearance Center.

License Number	4200900992769
License date	Oct 02, 2017
Licensed Content Publisher	AIP Publishing LLC
Licensed Content Publication	Applied Physics Letters
Licensed Content Title	Role of many-body effects in the coherent dynamics of excitons in low-temperature-grown GaAs
Licensed Content Author	D. Webber, L. Hacquebard, X. Liu, et al
Licensed Content Date	Oct 5, 2015
Licensed Content Volume	107
Licensed Content Issue	14
Type of Use	Thesis/Dissertation
Requestor type	Author (original article)
Format	Print and electronic
Portion	Figure/Table
Number of figures/tables	1
Title of your thesis / dissertation	TRANSIENT FOUR-WAVE MIXING STUDIES OF GaAs, LOW-TEMPERATURE-GROWN GaAs, AND CH3NH3PbI3
Expected completion date	Dec 2017
Estimated size (number of pages)	190
Requestor Location	Daniel Webber Dept. of Physics Dalhousie University Halifax, NS B3H4R2 Canada Attn: Daniel Webber
Billing Type	Invoice
Billing Address	Daniel Webber Dept. of Physics Dalhousie University Halifax, NS B3H4R2 Canada Attn: Daniel Webber
Total	0.00 USD

Terms and Conditions

AIP Publishing LLC -- Terms and Conditions: Permissions Uses

AIP Publishing hereby grants to you the non-exclusive right and license to use and/or distribute

the Material according to the use specified in your order, on a one-time basis, for the specified term, with a maximum distribution equal to the number that you have ordered. Any links or other content accompanying the Material are not the subject of this license.

1. You agree to include the following copyright and permission notice with the reproduction of the Material:"Reprinted from [FULL CITATION], with the permission of AIP Publishing." For an article, the credit line and permission notice must be printed on the first page of the article or book chapter. For photographs, covers, or tables, the notice may appear with the Material, in a footnote, or in the reference list.
2. If you have licensed reuse of a figure, photograph, cover, or table, it is your responsibility to ensure that the material is original to AIP Publishing and does not contain the copyright of another entity, and that the copyright notice of the figure, photograph, cover, or table does not indicate that it was reprinted by AIP Publishing, with permission, from another source. Under no circumstances does AIP Publishing purport or intend to grant permission to reuse material to which it does not hold appropriate rights.
   You may not alter or modify the Material in any manner. You may translate the Material into another language only if you have licensed translation rights. You may not use the Material for promotional purposes.
3. The foregoing license shall not take effect unless and until AIP Publishing or its agent, Copyright Clearance Center, receives the Payment in accordance with Copyright Clearance Center Billing and Payment Terms and Conditions, which are incorporated herein by reference.
4. AIP Publishing or Copyright Clearance Center may, within two business days of granting this license, revoke the license for any reason whatsoever, with a full refund payable to you. Should you violate the terms of this license at any time, AIP Publishing, or Copyright Clearance Center may revoke the license with no refund to you. Notice of such revocation will be made using the contact information provided by you. Failure to receive such notice will not nullify the revocation.
5. AIP Publishing makes no representations or warranties with respect to the Material. You agree to indemnify and hold harmless AIP Publishing, and their officers, directors, employees or agents from and against any and all claims arising out of your use of the Material other than as specifically authorized herein.
6. The permission granted herein is personal to you and is not transferable or assignable without the prior written permission of AIP Publishing. This license may not be amended except in a writing signed by the party to be charged.
7. If purchase orders, acknowledgments or check endorsements are issued on any forms containing terms and conditions which are inconsistent with these provisions, such inconsistent terms and conditions shall be of no force and effect. This document, including the CCC Billing and Payment Terms and Conditions, shall be the entire agreement between the parties relating to the subject matter hereof.

This Agreement shall be governed by and construed in accordance with the laws of the State of New York. Both parties hereby submit to the jurisdiction of the courts of New York County for purposes of resolving any disputes that may arise hereunder.

V1.1

Questions? customercare@copyright.com or +1-855-239-3415 (toll free in the US) or +1-978-646-2777.

AMERICAN PHYSICAL SOCIETY LICENSE TERMS AND CONDITIONS

Oct 23, 2017

This Agreement between Daniel Webber ("You") and American Physical Society ("American Physical Society") consists of your license details and the terms and conditions provided by American Physical Society and Copyright Clearance Center.

License Number	4215030119173
License date	Oct 23, 2017
Licensed Content Publisher	American Physical Society
Licensed Content Publication	Physical Review Letters
Licensed Content Title	Many-Body Interactions in Semiconductors Probed by Optical Two-Dimensional Fourier Transform Spectroscopy
Licensed Content Author	Xiaoqin Li et al.
Licensed Content Date	Feb 7, 2006
Licensed Content Volume	96
Type of Use	Thesis/Dissertation
Requestor type	Student
Format	Print, Electronic
Portion	image/photo
Number of images/photos requested	2
Portion description	Figure 4 Figure 5
Rights for	Main product
Duration of use	Life of Current Edition
Creation of copies for the disabled	no
With minor editing privileges	no
For distribution to	Worldwide
In the following language(s)	Original language of publication
With incidental promotional use	no
The lifetime unit quantity of new product	0 to 499
The requesting person/organization is:	Daniel Webber/Dalhousie University
Order reference number	
Title of your thesis / dissertation	TRANSIENT FOUR-WAVE MIXING STUDIES OF GaAs, LOW-TEMPERATURE-GROWN GaAs, AND CH3NH3PbI3
Expected completion date	Dec 2017
Expected size (number of pages)	190
Requestor Location	Daniel Webber Dept. of Physics

	Dalhousie University Halifax, NS B3H4R2 Canada Attn: Daniel Webber
Billing Type	Invoice
Billing Address	Daniel Webber Dept. of Physics Dalhousie University Halifax, NS B3H4R2 Canada Attn: Daniel Webber
Total	0.00 CAD

Terms and Conditions

Terms and Conditions

The American Physical Society (APS) is pleased to grant the Requestor of this license a non-exclusive, non-transferable permission, limited to [**print** and/or **electronic** format, depending on what they chose], provided all criteria outlined below are followed.

1. You must also obtain permission from at least one of the lead authors for each separate work, if you haven't done so already. The author's name and affiliation can be found on the first page of the published Article.
2. For electronic format permissions, Requestor agrees to provide a hyperlink from the reprinted APS material using the source material's DOI on the web page where the work appears. The hyperlink should use the standard DOI resolution URL, http://dx.doi.org/{DOI}. The hyperlink may be embedded in the copyright credit line.
3. For print format permissions, Requestor agrees to print the required copyright credit line on the first page where the material appears: "Reprinted (abstract/excerpt/figure) with permission from [(FULL REFERENCE CITATION) as follows: Author's Names, APS Journal Title, Volume Number, Page Number and Year of Publication.] Copyright (YEAR) by the American Physical Society."
4. Permission granted in this license is for a one-time use and does not include permission for any future editions, updates, databases, formats or other matters. Permission must be sought for any additional use.
5. Use of the material does not and must not imply any endorsement by APS.
6. Under no circumstance does APS purport or intend to grant permission to reuse materials to which it does not hold copyright. It is the requestors sole responsibility to ensure the licensed material is original to APS and does not contain the copyright of another entity, and that the copyright notice of the figure, photograph, cover or table does not indicate that it was reprinted by APS, with permission from another source.
7. The permission granted herein is personal to the Requestor for the use specified and is not transferable or assignable without express written permission of APS. This license may not be amended except in writing by APS.
8. You may not alter, edit or modify the material in any manner.
9. You may translate the materials only when translation rights have been granted.
10. You may not use the material for promotional, sales, advertising or marketing purposes.
11. The foregoing license shall not take effect unless and until APS or its agent, Copyright Clearance Center (CCC), receives payment in full in accordance with CCC Billing and Payment Terms and Conditions, which are incorporated herein by reference.
12. Should the terms of this license be violated at any time, APS or CCC may revoke the license with no refund to you and seek relief to the fullest extent of the laws of the USA. Official written notice will be made using the contact information provided with the

permission request. Failure to receive such notice will not nullify revocation of the permission.
13. APS reserves all rights not specifically granted herein.
14. This document, including the CCC Billing and Payment Terms and Conditions, shall be the entire agreement between the parties relating to the subject matter hereof.

Other Terms and Conditions

Version 1.1

Questions? customercare@copyright.com or +1-855-239-3415 (toll free in the US) or +1-978-646-2777.

AMERICAN PHYSICAL SOCIETY LICENSE TERMS AND CONDITIONS

Nov 05, 2017

This Agreement between Daniel Webber ("You") and American Physical Society ("American Physical Society") consists of your license details and the terms and conditions provided by American Physical Society and Copyright Clearance Center.

License Number	4222530928071
License date	Nov 05, 2017
Licensed Content Publisher	American Physical Society
Licensed Content Publication	Physical Review B
Licensed Content Title	Polarization dependence of dephasing processes: A probe for many-body effects
Licensed Content Author	Thomas Rappen et al.
Licensed Content Date	Apr 15, 1994
Licensed Content Volume	49
Type of Use	Thesis/Dissertation
Requestor type	Student
Format	Print, Electronic
Portion	image/photo
Number of images/photos requested	1
Portion description	Figure 1
Rights for	Main product
Duration of use	Life of Current Edition
Creation of copies for the disabled	no
With minor editing privileges	no
For distribution to	Worldwide
In the following language(s)	Original language of publication
With incidental promotional use	no
The lifetime unit quantity of new product	0 to 499
The requesting person/organization is:	Daniel Webber
Order reference number	
Title of your thesis / dissertation	TRANSIENT FOUR-WAVE MIXING STUDIES OF GaAs, LOW-TEMPERATURE-GROWN GaAs, AND CH3NH3PbI3
Expected completion date	Dec 2017
Expected size (number of pages)	190
Requestor Location	Daniel Webber Dept. of Physics

	Dalhousie University Halifax, NS B3H4R2 Canada Attn: Daniel Webber
Billing Type	Invoice
Billing Address	Daniel Webber Dept. of Physics Dalhousie University Halifax, NS B3H4R2 Canada Attn: Daniel Webber
Total	0.00 USD

Terms and Conditions

Terms and Conditions

The American Physical Society (APS) is pleased to grant the Requestor of this license a non-exclusive, non-transferable permission, limited to [**print** and/or **electronic** format, depending on what they chose], provided all criteria outlined below are followed.

1. You must also obtain permission from at least one of the lead authors for each separate work, if you haven't done so already. The author's name and affiliation can be found on the first page of the published Article.
2. For electronic format permissions, Requestor agrees to provide a hyperlink from the reprinted APS material using the source material's DOI on the web page where the work appears. The hyperlink should use the standard DOI resolution URL, http://dx.doi.org/{DOI}. The hyperlink may be embedded in the copyright credit line.
3. For print format permissions, Requestor agrees to print the required copyright credit line on the first page where the material appears: "Reprinted (abstract/excerpt/figure) with permission from [(FULL REFERENCE CITATION) as follows: Author's Names, APS Journal Title, Volume Number, Page Number and Year of Publication.] Copyright (YEAR) by the American Physical Society."
4. Permission granted in this license is for a one-time use and does not include permission for any future editions, updates, databases, formats or other matters. Permission must be sought for any additional use.
5. Use of the material does not and must not imply any endorsement by APS.
6. Under no circumstance does APS purport or intend to grant permission to reuse materials to which it does not hold copyright. It is the requestors sole responsibility to ensure the licensed material is original to APS and does not contain the copyright of another entity, and that the copyright notice of the figure, photograph, cover or table does not indicate that it was reprinted by APS, with permission from another source.
7. The permission granted herein is personal to the Requestor for the use specified and is not transferable or assignable without express written permission of APS. This license may not be amended except in writing by APS.
8. You may not alter, edit or modify the material in any manner.
9. You may translate the materials only when translation rights have been granted.
10. You may not use the material for promotional, sales, advertising or marketing purposes.
11. The foregoing license shall not take effect unless and until APS or its agent, Copyright Clearance Center (CCC), receives payment in full in accordance with CCC Billing and Payment Terms and Conditions, which are incorporated herein by reference.
12. Should the terms of this license be violated at any time, APS or CCC may revoke the license with no refund to you and seek relief to the fullest extent of the laws of the USA. Official written notice will be made using the contact information provided with the

permission request. Failure to receive such notice will not nullify revocation of the permission.
13. APS reserves all rights not specifically granted herein.
14. This document, including the CCC Billing and Payment Terms and Conditions, shall be the entire agreement between the parties relating to the subject matter hereof.

Other Terms and Conditions

Version 1.1

Questions? customercare@copyright.com or +1-855-239-3415 (toll free in the US) or +1-978-646-2777.

AIP PUBLISHING LLC LICENSE TERMS AND CONDITIONS

Nov 06, 2017

This Agreement between Daniel Webber ("You") and AIP Publishing LLC ("AIP Publishing LLC") consists of your license details and the terms and conditions provided by AIP Publishing LLC and Copyright Clearance Center.

License Number	4223130402780
License date	Nov 06, 2017
Licensed Content Publisher	AIP Publishing LLC
Licensed Content Publication	Review of Scientific Instruments
Licensed Content Title	A versatile ultrastable platform for optical multidimensional Fourier-transform spectroscopy
Licensed Content Author	A. D. Bristow, D. Karaiskaj, X. Dai, et al
Licensed Content Date	Jul 1, 2009
Licensed Content Volume	80
Licensed Content Issue	7
Type of Use	Thesis/Dissertation
Requestor type	Student
Format	Print and electronic
Portion	Figure/Table
Number of figures/tables	2
Title of your thesis / dissertation	TRANSIENT FOUR-WAVE MIXING STUDIES OF GaAs, LOW-TEMPERATURE-GROWN GaAs, AND CH3NH3PbI3
Expected completion date	Dec 2017
Estimated size (number of pages)	190
Requestor Location	Daniel Webber Dept. of Physics Dalhousie University Halifax, NS B3H4R2 Canada Attn: Daniel Webber
Billing Type	Invoice
Billing Address	Daniel Webber Dept. of Physics Dalhousie University Halifax, NS B3H4R2 Canada Attn: Daniel Webber
Total	0.00 USD

Terms and Conditions

AIP Publishing LLC -- Terms and Conditions: Permissions Uses

AIP Publishing hereby grants to you the non-exclusive right and license to use and/or distribute

AIP PUBLISHING LLC LICENSE TERMS AND CONDITIONS

Nov 06, 2017

This Agreement between Daniel Webber ("You") and AIP Publishing LLC ("AIP Publishing LLC") consists of your license details and the terms and conditions provided by AIP Publishing LLC and Copyright Clearance Center.

License Number	4223130402780
License date	Nov 06, 2017
Licensed Content Publisher	AIP Publishing LLC
Licensed Content Publication	Review of Scientific Instruments
Licensed Content Title	A versatile ultrastable platform for optical multidimensional Fourier-transform spectroscopy
Licensed Content Author	A. D. Bristow, D. Karaiskaj, X. Dai, et al
Licensed Content Date	Jul 1, 2009
Licensed Content Volume	80
Licensed Content Issue	7
Type of Use	Thesis/Dissertation
Requestor type	Student
Format	Print and electronic
Portion	Figure/Table
Number of figures/tables	2
Title of your thesis / dissertation	TRANSIENT FOUR-WAVE MIXING STUDIES OF GaAs, LOW-TEMPERATURE-GROWN GaAs, AND CH3NH3PbI3
Expected completion date	Dec 2017
Estimated size (number of pages)	190
Requestor Location	Daniel Webber Dept. of Physics Dalhousie University Halifax, NS B3H4R2 Canada Attn: Daniel Webber
Billing Type	Invoice
Billing Address	Daniel Webber Dept. of Physics Dalhousie University Halifax, NS B3H4R2 Canada Attn: Daniel Webber
Total	0.00 USD

Terms and Conditions

AIP Publishing LLC -- Terms and Conditions: Permissions Uses

AIP Publishing hereby grants to you the non-exclusive right and license to use and/or distribute

AMERICAN PHYSICAL SOCIETY LICENSE TERMS AND CONDITIONS

Dec 13, 2017

This Agreement between Daniel Webber ("You") and American Physical Society ("American Physical Society") consists of your license details and the terms and conditions provided by American Physical Society and Copyright Clearance Center.

License Number	4247150136885
License date	Dec 13, 2017
Licensed Content Publisher	American Physical Society
Licensed Content Publication	Physical Review B
Licensed Content Title	Measurements of exciton diffusion by degenerate four-wave mixing in ${\mathrm{CdS}}_{1\mathrm{\ensuremath{-}}\mathit{x}}$${\mathrm{Se}}_{\mathit{x}}$
Licensed Content Author	H. Schwab et al.
Licensed Content Date	Sep 15, 1992
Licensed Content Volume	46
Type of Use	Thesis/Dissertation
Requestor type	Student
Format	Print, Electronic
Portion	image/photo
Number of images/photos requested	1
Portion description	Figure 2
Rights for	Main product
Duration of use	Life of Current Edition
Creation of copies for the disabled	no
With minor editing privileges	no
For distribution to	Worldwide
In the following language(s)	Original language of publication
With incidental promotional use	no
The lifetime unit quantity of new product	0 to 499
The requesting person/organization is:	Daniel Webber

Order reference number	
Title of your thesis / dissertation	TRANSIENT FOUR-WAVE MIXING STUDIES OF GaAs, LOW-TEMPERATURE-GROWN GaAs, AND CH3NH3PbI3
Expected completion date	Dec 2017
Expected size (number of pages)	190
Requestor Location	Daniel Webber Dept. of Physics Dalhousie University Halifax, NS B3H4R2 Canada Attn: Daniel Webber
Billing Type	Invoice
Billing Address	Daniel Webber Dept. of Physics Dalhousie University Halifax, NS B3H4R2 Canada Attn: Daniel Webber
Total	0.00 CAD

Terms and Conditions

Terms and Conditions

The American Physical Society (APS) is pleased to grant the Requestor of this license a non-exclusive, non-transferable permission, limited to [**print** and/or **electronic** format, depending on what they chose], provided all criteria outlined below are followed.

1. You must also obtain permission from at least one of the lead authors for each separate work, if you haven't done so already. The author's name and affiliation can be found on the first page of the published Article.
2. For electronic format permissions, Requestor agrees to provide a hyperlink from the reprinted APS material using the source material's DOI on the web page where the work appears. The hyperlink should use the standard DOI resolution URL, http://dx.doi.org/{DOI}. The hyperlink may be embedded in the copyright credit line.
3. For print format permissions, Requestor agrees to print the required copyright credit line on the first page where the material appears: "Reprinted (abstract/excerpt/figure) with permission from [(FULL REFERENCE CITATION) as follows: Author's Names, APS Journal Title, Volume Number, Page Number and Year of Publication.] Copyright (YEAR) by the American Physical Society."
4. Permission granted in this license is for a one-time use and does not include permission for any future editions, updates, databases, formats or other matters. Permission must be sought for any additional use.
5. Use of the material does not and must not imply any endorsement by APS.
6. Under no circumstance does APS purport or intend to grant permission to reuse materials to which it does not hold copyright. It is the requestors sole responsibility to ensure the licensed material is original to APS and does not contain the copyright of another entity, and that the copyright notice of the figure, photograph, cover or table does not indicate that it was reprinted by APS, with permission from another source.
7. The permission granted herein is personal to the Requestor for the use specified and is not transferable or assignable without express written permission of APS. This license may not be amended except in writing by APS.
8. You may not alter, edit or modify the material in any manner.
9. You may translate the materials only when translation rights have been granted.
10. You may not use the material for promotional, sales, advertising or marketing purposes.

11. The foregoing license shall not take effect unless and until APS or its agent, Copyright Clearance Center (CCC), receives payment in full in accordance with CCC Billing and Payment Terms and Conditions, which are incorporated herein by reference.
12. Should the terms of this license be violated at any time, APS or CCC may revoke the license with no refund to you and seek relief to the fullest extent of the laws of the USA. Official written notice will be made using the contact information provided with the permission request. Failure to receive such notice will not nullify revocation of the permission.
13. APS reserves all rights not specifically granted herein.
14. This document, including the CCC Billing and Payment Terms and Conditions, shall be the entire agreement between the parties relating to the subject matter hereof.

Other Terms and Conditions

Version 1.1

Questions? customercare@copyright.com or +1-855-239-3415 (toll free in the US) or +1-978-646-2777.

AMERICAN PHYSICAL SOCIETY LICENSE TERMS AND CONDITIONS

Dec 13, 2017

This Agreement between Daniel Webber ("You") and American Physical Society ("American Physical Society") consists of your license details and the terms and conditions provided by American Physical Society and Copyright Clearance Center.

License Number	4247150930364
License date	Dec 13, 2017
Licensed Content Publisher	American Physical Society
Licensed Content Publication	Physical Review B
Licensed Content Title	Ultrafast coherent transients due to exciton-continuum scattering in bulk GaAs
Licensed Content Author	M. U. Wehner, D. Steinbach, and M. Wegener
Licensed Content Date	Aug 15, 1996
Licensed Content Volume	54
Type of Use	Thesis/Dissertation
Requestor type	Student
Format	Print, Electronic
Portion	image/photo
Number of images/photos requested	1
Portion description	Figure 1
Rights for	Main product
Duration of use	Life of Current Edition
Creation of copies for the disabled	no
With minor editing privileges	no
For distribution to	Worldwide
In the following language(s)	Original language of publication
With incidental promotional use	no
The lifetime unit quantity of new product	0 to 499
The requesting person/organization is:	Daniel Webber
Order reference number	
Title of your thesis / dissertation	TRANSIENT FOUR-WAVE MIXING STUDIES OF GaAs, LOW-TEMPERATURE-GROWN GaAs, AND CH3NH3PbI3
Expected completion date	Dec 2017
Expected size (number of pages)	190
Requestor Location	Daniel Webber Dept. of Physics

	Dalhousie University Halifax, NS B3H4R2 Canada Attn: Daniel Webber
Billing Type	Invoice
Billing Address	Daniel Webber Dept. of Physics Dalhousie University Halifax, NS B3H4R2 Canada Attn: Daniel Webber
Total	0.00 CAD

Terms and Conditions

Terms and Conditions

The American Physical Society (APS) is pleased to grant the Requestor of this license a non-exclusive, non-transferable permission, limited to [**print** and/or **electronic** format, depending on what they chose], provided all criteria outlined below are followed.

1. You must also obtain permission from at least one of the lead authors for each separate work, if you haven't done so already. The author's name and affiliation can be found on the first page of the published Article.
2. For electronic format permissions, Requestor agrees to provide a hyperlink from the reprinted APS material using the source material's DOI on the web page where the work appears. The hyperlink should use the standard DOI resolution URL, http://dx.doi.org/{DOI}. The hyperlink may be embedded in the copyright credit line.
3. For print format permissions, Requestor agrees to print the required copyright credit line on the first page where the material appears: "Reprinted (abstract/excerpt/figure) with permission from [(FULL REFERENCE CITATION) as follows: Author's Names, APS Journal Title, Volume Number, Page Number and Year of Publication.] Copyright (YEAR) by the American Physical Society."
4. Permission granted in this license is for a one-time use and does not include permission for any future editions, updates, databases, formats or other matters. Permission must be sought for any additional use.
5. Use of the material does not and must not imply any endorsement by APS.
6. Under no circumstance does APS purport or intend to grant permission to reuse materials to which it does not hold copyright. It is the requestors sole responsibility to ensure the licensed material is original to APS and does not contain the copyright of another entity, and that the copyright notice of the figure, photograph, cover or table does not indicate that it was reprinted by APS, with permission from another source.
7. The permission granted herein is personal to the Requestor for the use specified and is not transferable or assignable without express written permission of APS. This license may not be amended except in writing by APS.
8. You may not alter, edit or modify the material in any manner.
9. You may translate the materials only when translation rights have been granted.
10. You may not use the material for promotional, sales, advertising or marketing purposes.
11. The foregoing license shall not take effect unless and until APS or its agent, Copyright Clearance Center (CCC), receives payment in full in accordance with CCC Billing and Payment Terms and Conditions, which are incorporated herein by reference.
12. Should the terms of this license be violated at any time, APS or CCC may revoke the license with no refund to you and seek relief to the fullest extent of the laws of the USA. Official written notice will be made using the contact information provided with the

permission request. Failure to receive such notice will not nullify revocation of the permission.
13. APS reserves all rights not specifically granted herein.
14. This document, including the CCC Billing and Payment Terms and Conditions, shall be the entire agreement between the parties relating to the subject matter hereof.

Other Terms and Conditions

Version 1.1

Questions? customercare@copyright.com or +1-855-239-3415 (toll free in the US) or +1-978-646-2777.